Numerical investigation of MPD thrusters using a density-based method with semi-discrete central-upwind schemes for MHD equations

Vom Fachbereich Produktionstechnik

der

UNIVERSITÄT BREMEN

zur Erlangung des Grades

Doktor-Ingenieur

genehmigte

Dissertation

von

M. Sc. Charles Chelem Mayigué

Gutachter: Prof. Dr. Claus Lämmerzahl
Prof. Dr. Claus Braxmaier

Tag der mündlichen Prüfung: 05 September 2018

Declaration of Authorship

I, Charles CHELEM MAYIGUE, declare that this thesis titled, "Numerical investigation of MPD thrusters using a density-based method with semi-discrete central-upwind schemes for MHD equations" and the work presented in it are my own. I confirm that:

- This work was done wholly in candidature for a research degree at the University of Bremen.
- Where any part of this thesis has previously been submitted for a degree or any other qualification at the University of Bremenor any other institution, this has been clearly stated.
- Where I have consulted the published work of others, this is always clearly attributed.
- Where I have quoted from the work of others, the source is always given. With the exception of such quotations, this thesis is entirely my own work.
- I have acknowledged all main sources of help.
- Where the thesis is based on work done by myself jointly with others, I have made clear exactly what was done by others and what I have contributed myself.

Signed:

Date:September 10, 2018

Dedicated to Mefand Christine gone too soon...
... Thanks, Mom

"*Earth is the cradle of humanity, but one cannot live in a cradle forever*"

Konstantin Tsiolkovsky, 1911

Abstract

The magnetohydrodynamic (MHD) equations which combines the Navier-Stokes equations with the Maxwell equations are essential for the investigations of many research areas as earth's core modelling, metal casting, fusion devices and electrical and aerospace devices. In the present work, the central-upwind schemes proposed by Kurganov, Noelle and Petrova (Kurganov, Noelle, and Petrova, 2001) for hydrodynamics are extended and combined with the divergence cleaning method of Dedner (Dedner et al., 2002) in order to investigate the performance of the self-field and applied magneto-plasma dynamic thrusters which still involving some outstanding problems. This new algorithm is developed for the single temperature, ideal and resistive MHD equations in a finite volume discretization framework with Gaussian integration. The electrical conductivity is predicted according to the Spitzer-Härm formulation and the real gas ratio of specific heats proposed by Sankaran is implemented for higher discharge current. To improve the quality of the solution, the limiter function of first and second order interpolation scheme is used.

The accuracy and the robustness of the obtained solver are demonstrated through numerical simulations of ideal MHD benchmark problems. first, the ability of the developed code to handle shocks, rarefactions and contact discontinuities is tested with the Brio-Wu shock-tube problem. The Minmod and the Van Albada limiter functions has been found to perform better than the other limiter used and the obtained results agree well with both the analytic and the simulations results of previous work. Secondly, the complex and multiple shock interactions and the transition from smooth to turbulent flow involved in the Orszag-Tang vortex problem is well described by the present code and the comparison with the WENO-5 scheme of Shen (Shen, Zha, and Huerta, 2012) shows good agreement. Lastly, The ability to described the interaction of an denser cloud with a MHD shock is tested by simulating the 2D cloud-shock interaction problem. The main phases of the interaction are well captured by the solver and the temporal progression of the density contour is in accordance with those obtained by Xisto (Xisto, Pascoa, and Oliviera, 2014).

The ability of the developed resistive solver to deal with plasma flow acceleration is tested by simulating the well experimental investigated thrusters: The full scale benchmark thruster and the extended anode thruster of Princeton. The results show good agreement with the experimental and simulations results of previous work (Boyle, 1974; Lapointe, 1991; Lapointe, 1992; Sankaran, Choueiri, and Jardin, 2005) for discharge current less than the critical current just before the beginning of the onset phenomenon. Simulations are also conducted on the Villani-H thruster to determine the effect of geometric changes over the thruster performance and a first designing attempts is proposed according to the stability analysis.

Confident with the results obtained with ideal and resistive MHD problems, the present code is extended to applied-field MPD thrusters. The purpose is to achieve a high thrust level required for space missions with less input power than with self-field MPD thrusters and thus avoid the onset instabilities. For the verification of the code, the NASA Lewis Research Center's (NASALeRC) MPD thruster is chosen because of its wide range of experimental data bank. The method presented

reproduce the theory of thrust production and plasma acceleration. Some difficulties as the limitation of the maximum rotational speed and the depletion of the plasma density on the anode surface have been captured. Moreover, the present density-based method compares very well with experimental data of Myers (Myers, 1990) and simulations of Mikellides (Mikellides, Turchi, and Roderick, 2000).

Zusammenfassung

Im Rahmen dieser Arbeit wird auf der Basis von Zentral-Differenzen-Schemata nach Kurganov und Tadmor ein dichtebasiertes Finite-Volumen-Verfahren entwickelt, mittels dem elektromagnetische Triebwerkssysteme mit dem Ziel zukünftiger Deep-Space-Missionen weiterentwickelt werden sollen. Aus diesem Grund wird ein bereits existierendes Simulationspaket zur Beschreibung kompressibler Strömungen auf Basis der Navier-Stokes-Gleichungen um den Einfluss elektromagnetischer Felder erweitert, mit den Maxwell-Gleichungen der Elektrodynamik gekoppelt und mit der Divergenz-Reinigungsmethode nach Dedner kombiniert. Aufgrund der kontinuumsmechanischen Beschreibung des Plasmaflusses wird die elektrische Leitfähigkeit durch die Spitzer-Harm-Formulierung berechnet und das von Sankaran vorgeschlagene reale Gasverhältnis der spezifischen Erwärmung für einen höheren Entladestrom implementiert. Um die Qualität der Lösung zu verbessern, werden sogenannte Limiter-Funktionen verwendet. Die Genauigkeit und die Robustheit dieses neuen Solvers werden durch numerische Simulationen von idealen Magnetohydrodynamik(MHD)-Benchmark-Problemen wie dem Brio-Wu-Stoßwellenproblem, dem Orszag-Tang-Wirbelproblem und dem 2D-Cloud-Shock-Wechselwirkungsproblem demonstriert. Danach werden die Eigenschaften des in dieser Arbeit entwickelten, resistiven Solvers anhand einer Simulationen der Beschleunigung voll-ionisierter «single-temperature»-Argonplasmaströmungen innerhalb von Magneto-Plasmadynamischen Eigenfeld-(MPD-)Triebwerken getestet, welche bereits experimentell durch Wissenschaftler der Priceton University untersucht wurden. Überzeugt von den Ergebnissen, die mit idealen und resistiven MHD-Problemen erzielt wurden, wurde der vorliegende Code für Fremdfeld-MPD-Triebwerke mit extern anliegendem, magnetischem Feld erweitert. Der Zweck dieser Fremdfeld-MPD-Triebwerke ist es, mit einer geringeren Eingangsleistung als bei Eigenfeld-MPD-Triebwerken stabil ein hohes Schubniveau zu erreichen. Diese Energieeinsparung ist für reale Weltraummissionen zwingend erforderlich. Die vorgestellte Methode reproduziert die Theorie der Schubproduktion und der Plasmabeschleunigung. Komplexe Phänomene, wie die Begrenzung der maximalen Rotationsgeschwindigkeit und der Inhomogenitäten der Plasmadichte auf der Anodenoberfläche, wurden verifiziert und beschrieben. Darüber hinaus stimmen die resultieren Simulationsergebnisse des vorliegenden dichtebasierten Verfahrens sehr gut mit experimentellen Daten bekannter Vorarbeiten überein.

Acknowledgements

Glory be to God, who made this happen. Thank you for being the light which shows me the path.

At the end of my journey as PhD student, I want to show my gratitude to some people I encountered during my thesis work and who contributed to make all this possible.

First, I want to thank my advisor and mentor PD. Dr.-Ing. habil. Rodion Groll, who gave me the great opportunity to come and work in ZARM (Center of Applied Space Technology and Microgravity) at the University of Bremen. Every discussion we had taught me something new and made me feel more confident day after day. You had this unique ability to make me give the best of myself and to stretch my limits forward. I learnt a lot from the researcher, the lecturer and most importantly from the good person you are. So thank you Rodion.

Special thanks to Prof. Dr. rer. nat. Claus Lämmerzahl, who accepted to supervise this work and for his help with all the administrative procedures. Thank you for receiving me at ZARM and for providing for me, as the director of the institute as I entered the doors of the Fallturm for my first time, a comfortable and adequate environment which made this work easier.

I would like to say thank you to Prof. Dr.-Ing. habil. Michael Dreyer who gave me my chance by forwarding my PhD position seeker's mail to Rodion. This action was in my head during all my time in ZARM and always remembered me how much one anodin action can radically change a life, my life. Thank you so much.

The former TFD (Thermo-Fluid Dynamics) team member. Stephan, Kristopher, Claudia and Andre who where there when I first arrived. The support and advice you gave me, after leaving the team, was priceless.

The current fellow PhD students. Juan, with whom I spent a lot of time until I could start my first simulation with OpenFOAM. Till, the man without whom I would never have been able to progress as far as I have and who always found the way to make me laugh even in the darkest OpenFOAM moments. Thank you for introducing me to the German culture. Juan, Till and Peng, I will never forget the help and support that all of you gave me, especially at the beginning. Additionally,

I would like to thank my colleagues from the space science and fluid dynamics research groups: Ertan, Zeli, Max. Thank you for your support. You were always there for me when I needed you the most even for personal matter. Our students in TFD, Björn and Christoph "der Starke" who taught me many things about everything: German language, LaTex, Software installation, electronics, cars and so much more. Thank you "Jungs".

I would also like to thank all the administrative staff of ZARM. You have my entire gratitude.

Thanks to the IT team of ZARM and most particularly to Mr. Thorsten Coordes for his advice and help with the HLRN applications.

This research was made possible by the understanding of the University of Maroua, my employer, which endorsed my PhD time abroad as an internship and gave me all the support I needed.

Pr. Pemha Elkana and Dr. Obounou Marcel of the University of Yaounde 1 and Pr. Mouangue Ruben of the University of Ngaoundéré. The men who guided my first foot steps in CFD (Computational Fluid Dynamics). I owe you all a lot.

Special thanks to my parents and my siblings for staying by my side supporting me since the beginning of my arduous long journey in the world of sciences.

My wife Kissi, who supported me from the first day we met till now and joined me in Germany so we could become a true and strong family. I will never be able to thank you enough for your sacrifice and for enduring my absence for long. This thesis is a fruit of your effort and patience. You and Prince are all I have in this world.

My old friends, Abdou, Amos, Larissa. Thank you for your encouragements over all these years.

Special thanks go to:

Family Godrati in Münster to make me feel at home. You were my family during these years.

My German teachers at Kapito Sprachschule in Münster: Bernadette, Jörg and Jildiz. You were the starting point of all this. Thank you for your patience.

The International office with all the senior citizen of the University of Bremen. Thank you for what you did for me and for what you are doing every single day for all the foreign students. I will miss the weekly "Cafe international".

The Mountain of God church. Thanks to Pastor Beauty and Pastor Robert for their guidance and care.

Lastly and most importantly, this work was funded by the *Deutscher Akademischer Austauschdienst* (DAAD) through the "Research grants for doctoral candidates and young academics and scientists" programme with the grant number 57076385 as well as by the *North-German Supercomputing Alliance* (HLRN) which provided the computational resources for the numerical simulations with the Grant numbers hbi00027 and hbi00030.

Contents

List of Figures

List of Tables

List of Abbreviations

AFMPDT	**A**pplied-**F**ield **M**agneto-**P**lasma **D**ynamic **T**hruster
CFD	**C**omputational **F**luid **D**ynamics
CFL	**C**ourant-**F**riedrichs-**L**ewy
CMFD	**C**omputational **M**agneto-**F**luid **D**ynamics
EP	**E**lectric **P**ropulsion
MHD	**M**agneto**H**ydro**D**ynamics
MPD	**M**agneto-**P**lasma **D**ynamic
SFMPDT	**S**elf-**F**ield **M**agneto-**P**lasma **D**ynamic **T**hruster
SIMPDT	**S**elf-**I**nduced **M**agneto-**P**lasma **D**ynamic **T**hruster

Physical Constants

Speed of Light	$c = 2.997\,924\,58 \times 10^{8}\,\mathrm{m\,s^{-1}}$
Permittivity in vacuum	$\epsilon_0 = 8.854\,19 \times 10^{-12}\,\mathrm{A\,s\,V^{-1}\,m^{-1}}$
Magnetic permeability of free space	$\mu_0 = 1.2566 \times 10^{-6}\,\mathrm{kg\,m\,s^{-2}\,A^{-2}}$
Boltzmann constant	$k_B = 1.380\,648\,8 \times 10^{-23}\,\mathrm{kg\,m^2\,s^{-2}\,K^{-1}}$
Acceleration due to gravity	$g = 9.81\,\mathrm{m\,s^{-2}}$
Ideal ratio of specific heats for Argon	$\gamma = 1.666$
Mass of Argon ion	$\gamma = 6.6335 \times 10^{-26}\,\mathrm{kg}$
Mass of electron	$m_e = 9.109\,382\,91 \times 10^{-31}\,\mathrm{kg}$
Charge of electron	$q_e = -1.602\,176\,565 \times 10^{-19}\,\mathrm{C}$
Argon first ionization potential	$\phi_i = 25.216 \times 10^{-19}\,\mathrm{kg\,m^2\,s^{-2}}$
Prandtl number	$P_r = 0.67$
Universel gas constant	$R_0 = 8.314\,462\,1\,\mathrm{J\,K^{-1}\,mol^{-1}}$

List of Symbols

Indexes

a	anode/atomic
A	Alfvèn
ap	applied
c	critical/cathode/convective
d	diffusive
ex	exhaust
f	final/cell face
h	heavy particle (neutral and ion)
i	initial/induced/ion/ionization
m	magnetic/magnetosonic
max	maximum
n	neutral
p	propellant
ref	reference
s	species/sutherland/spacecraft
sh	sheath
th	thermal
$visc$	viscous

Variables	**Physical value**	**Unit**
a	speed of sound	$\mathrm{m\,s^{-1}}$
b	body force per unit mass	$\mathrm{N\,kg^{-1}}$
$\mathbf{B}, B$	magnetic flux density/magnetic induction	T
c_p	specific heat capacity at constant pressure	$\mathrm{J\,kg^{-1}\,K^{-1}}$
c_v	specific heat capacity at constant volume	$\mathrm{J\,kg^{-1}\,K^{-1}}$
e	electron/internal energy per unit mass	$\mathrm{J\,kg^{-1}}$
$\mathbf{E}$	electric field	$\mathrm{V\,m^{-1}}$
E	total energy per unit mass	$\mathrm{J\,kg^{-1}}$
$\mathbf{F}, f$	Force/thrust	N
h	cell size /enthalpy	m/J
$\mathbf{H}$	magnetic field/Hartmann number	$\mathrm{A\,m^{-1}}$
I	current intensity	A
I_{sp}	specific impulse	s
$\mathbf{J}, j$	current density	$\mathrm{A\,m^{-3}}$
k	thermal conductivity	$\mathrm{m^2\,s^{-1}}$
l, L	distance/the Lundquist number	m
m	mass	kg
$\dot{m}$	mass flow rate	$\mathrm{kg\,s^{-1}}$
$M, \mathbf{M}$	Mach number/Magnetization	$\mathrm{A\,m^{-1}}$

P	power	W ($\mathrm{J\,s^{-1}}$)
p	pressure	Pa
P_{over}	overall pressure	Pa
Q	source term or sink term/heat energy per unit mass	$\mathrm{J\,kg^{-1}}$
R	specific gas constant	$\mathrm{J\,K^{-1}\,mol^{-1}}$
Re	Reynolds number	
$\mathbf{R}_e$	force density due to collisions	$\mathrm{N\,m^{-3}}$
t	time	s
T	temperature	K
$\mathbf{U}, U, v$	velocity	$\mathrm{m\,s^{-1}}$
V	volume/electric voltage	$\mathrm{m^3}$ / V
W	work done per unit mass	$\mathrm{J\,kg^{-1}}$
$+/pos$	fast/right	
$-/neg$	slow/left	

Greeks

ω	angular frequency	$\mathrm{s^{-1}}$
θ	angle/azimuthal component	rad
β	plasma beta	
η	efficiency	
ξ	dimensionless current	
ρ	mass density	$\mathrm{kg\,m^{-3}}$
μ	dynamic viscosity	$\mathrm{N\,s\,m^{-2}}$
λ_D	Debye length	m
σ	electrical conductivity	$\mathrm{S\,m^{-1}}$
τ	viscous stress tensor	$\mathrm{N\,m^{-2}}$
γ	adiabatic index	
$ln\Lambda$	Coulomb logarithm	
Λ	interaction length	
Γ	diffusivity	
χ	shock strength parameter	
ϕ	first ionization potential	$\mathrm{kg\,m^2\,s^{-2}}$

Chapter 1

Introduction and objectives

The magnetohydrodynamic (MHD) equations combine the Euler equations of gas dynamics and the Maxwell's equations of electrodynamics. These equations describe electrically conducting fluids, which include space physics plasmas. Due to the highly non linear nature of these equations, it is usually impossible to find analytical solutions to the MHD system of equations. With the rise of the computer performance and the high cost of high-power experimental facilities, MHD numerical simulation has in recent years become a popular means by which the magnetoplasma dynamic (MPD) thrusters involving magnetohydrodynamic equations are solved. But until now most of the developed MHD code remain very difficult to handle and often expensive, even with the help of supercomputers. One possible way to overcome these issues is to employ advanced and reliable simulation methods which can be improved and used more easily. The contribution of this thesis is the development of a density-based central-upwind MHD code relevant for MHD application simulations such as MPD thrusters.

1.1 Magnetohydrodynamic applications

MHD has a wide range of application in plasma physics performed in laboratory to aid in the understanding of plasmas, as well as to test and help expand plasma theory. The progress in plasma research has led to some important applications. In this section, some applications and notions deducted from (Bittencourt, 2004; Goebel and Katz, 2008; Sutton and Biblarz, 2010; Messerschmid and Fasoulas, 2011) will be presented.

1.1.1 Controlled thermonuclear fusion

The most important application of man-made MHD is in the control of thermonuclear fusion reactions, which holds a vast potential for the generation of power. Nuclear fusion is the process whereby two light nuclei combine to form a heavier one, the total final mass being slightly less than the total initial mass. The mass difference (Δm) appears as energy (ΔE) according to Einstein's famous law $\Delta E = \Delta m c^2$ (Valtonen et al., 2016) where c denotes the speed of light. The nuclear fusion reaction is the source of energy in the stars, including the sun. The confinement of the hot plasma in this case is provided by the self-gravity of the stars. The basic problem in achieving controlled fusion is to generate a plasma at very high temperatures and hold its particles together long enough for a substantial number of fusion reactions to take place. The need for high temperature come from

the fact that, in order to undergo fusion, the positively charged nuclei must come very close together, which require sufficient kinetic energy to overcome the electrostatic coulomb reaction. Many confinement schemes have been suggested and built to use some type of magnetic configuration. The main experimental efforts for achieving plasma conditions for fusion can be grouped into four approaches: Open systems (magnetic mirrors), closed systems (toruses), theta pinch devices and the laser-pellet fusion (see (Bittencourt, 2004) and the references therein for more details).

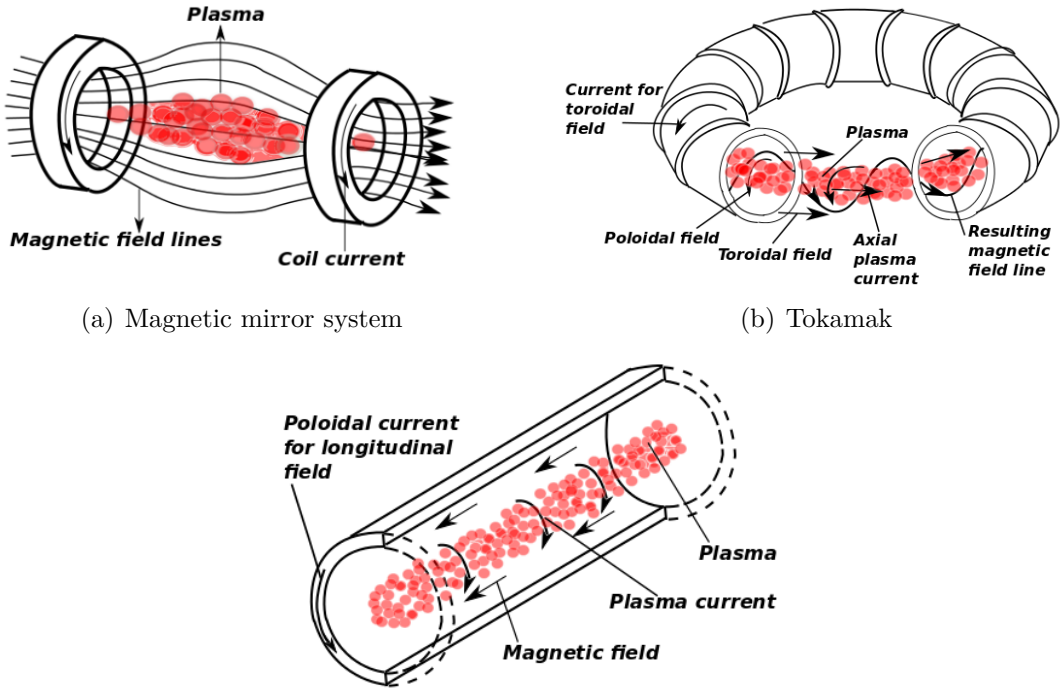

(a) Magnetic mirror system

(b) Tokamak

(c) Linear θ pinch

FIGURE 1.1: Schematic diagram showing magnetic field configurations of some basic schemes for plasma confinement according to (Bittencourt, 2004)

The mirror machines are linear devices with an axial magnetic field to keep the particles away from the wall, and with magnetic mirrors (regions of converging magnetic field lines) at the ends to prevent particles from escaping. In the Tokamak, which is one of the closed systems, a poloidal field produced by an internal plasma current is superposed on the toroidal field. In the theta pinch devices, a plasma current in the azimuthal direction and a longitudinal magnetic field produces a force that compresses the cross-sectional area of the plasma (see Fig. 1.1). Since controlled nuclear fusion can provide an almost limitless source of energy, it is certainly one of the most important scientific challenges man faces today, and its achievement will cause an enormous impact on our civilization.

1.1.2 MHD generator

The MHD energy generator converts the kinetic energy of a dense plasma flowing across a magnetic field into electrical energy. The basic principle of this devices is

as follow: A plasma flows with velocity **U** (along the x direction) across an applied magnetic field **B** (in y direction). The Lorentz force ($q(\mathbf{U} \times \mathbf{B})$) causes the ions to drift upward (in z direction) and the electrons downward, so that if electrodes are placed in the walls of the channel and connected to an external circuit, then a current density $\mathbf{J} = \sigma E_{ind} = \sigma \mathbf{U} \times \mathbf{B}$ (Bittencourt, 2004) (where σ denotes the plasma conductivity and E_{ind} is the induced electric field) flows across the plasma stream in the z direction. This current density, in turn, produces a force density $\mathbf{J} \times \mathbf{B}$ (in the x direction), which decelerates the flowing plasma. The net result is the conversion of some of the plasma kinetic energy entering the generator into electrical energy that can be applied to an external load. This process has the advantage that it operates without the inefficiency of a heat cycle.

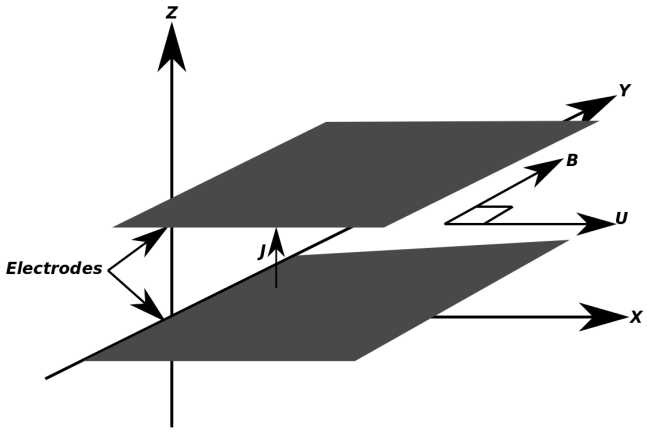

FIGURE 1.2: Diagram illustrating the basic principle of the MHD energy generator as seen in (Bittencourt, 2004)

1.1.3 Electric propulsion technologies: Plasma propulsion

The electric propulsion (EP) is a class of space devices used for spacecraft propulsion during interplanetary missions. They make use of electrical power to ionize and accelerate a neutral gas (propellant) by the means of electrical discharge and/or electromagnetic force. The basic idea behind the EP technologies is that the used neutral gas or propellant (plasma, ions) is electrically accelerated and propelled outside the thruster with much higher exhaust velocities and then, according to the rocket equation of Tsiolkovsky (Messerschmid and Fasoulas, 2011) (see the next section), results in a reduction of the amount of propellant required for a given space mission compared to the classical chemical propulsion. The use of electrical power generate body force which act directly on the propellant stream and makes the overall system more mass efficient (See Fig.1.3). The propellant used in EP thrusters varies with the type of thruster. From a rare gas such as Xenon and Argon to liquid metal. In the next section, an overview of the EP type is given.

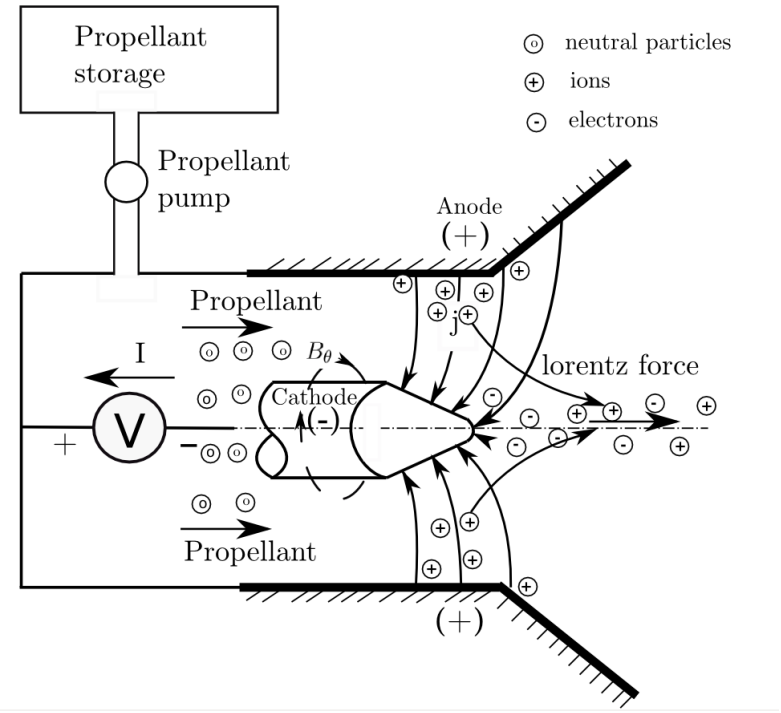

FIGURE 1.3: Diagram of an EP thruster: the magnetoplasmadynamic thruster

1.2 Electric propulsion type

In chemical rocket engines, the velocity with which the heated propellant is ejected from the thruster (the exhaust velocity) is limited by the chemical energy stored in the propellant's chemical bounds and released by the combustion reaction within the engine. By using an alternative source of energy, namely an external electric generator, the propellant gas can be accelerated to higher velocities with low fuel consumption. Thus, to obtain an optimal exhaust velocity, it is then recommended to increase the energy consumption. The choice of an optimal exhaust velocity thus depends on the specific power of the electric generator, on the mission duration, and on the total impulse needed for the mission. The higher the specific power of the generator, the higher the optimal exhaust velocity will be.

Since the beginning of the research on electric propulsion, several electric systems have been investigated and generally described in terms of the acceleration method used to produce the thrust. These methods can be easily separated into three fundamental types: electrothermal, electrostatic and electromagnetic (Goebel and Katz, 2008; Sutton and Biblarz, 2010). The three categories of EP thrusters are described in the following:

Electrothermal propulsion

In the electrothermal thrusters, the propellant is heated electrically and expanded thermodynamically; i.e., the gas is accelerated to supersonic speeds through a converging-diverging nozzle, as in the chemical propulsion. Two main systems can

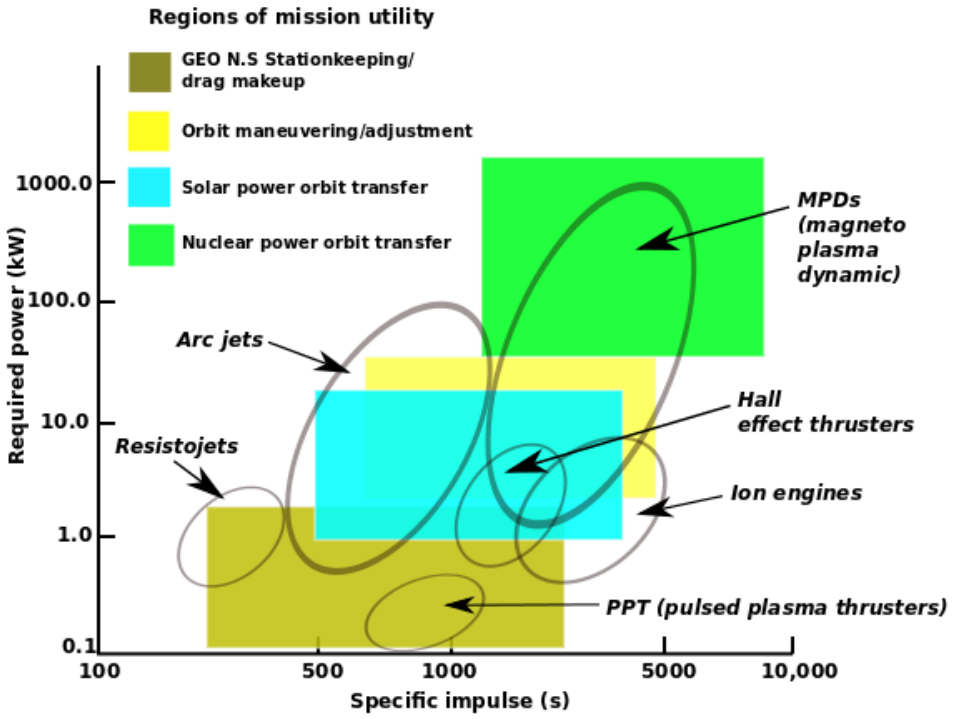

FIGURE 1.4: Diagram of the approximated operational regions for EP systems as a function of the power required and the specific impulse as seen in (Sutton and Biblarz, 2010)

be included in this category:

a) Resistojet

These are the simplest type of EP devices. The technology is based on radiation heat exchange, where a propellant flows over an ohmically heated refractory-metal surface which can consist of different types, such as coils of heated wires, heated hollow tubes or heated cylinders. The heated propellant is then directed and expelled through a nozzle which, like in the chemical propulsion (CP), accelerates it to higher velocities. The available materials limit the maximum gas temperature of a resistojet and materials like tungsten, tantalum and platinum have been used with these systems. The resistojet technology has specific impulse values similar to CP systems but much lower thrust values. However these systems have the advantage of being less complex than the chemical ones. Virtually any propellant can be used with this type of technology which made resistojets to be proposed for manned long-duration deep space mission, where the spacecraft's waste products like H_2O or CO_2 could be used as propellants. These devices have already been implemented in several missions such as the Satcom 1-R, Meteor 3-1, and Iridium spacecrafts.

b) Arcjet

An arcjet is also an electrothermal thruster that heats the propellant by passing it through a high current arc in line with the nozzle feed system. While there is an

electric discharge involved in the propellant path, plasma effects are insignificant in the exhaust velocity because the propellant is weakly ionized. The specific impulse (Isp) is limited by thermal heating to less than 700 s for easily stored propellants.

Electrostatic propulsion

Electrostatic propulsion uses a high voltage electrostatic field to accelerate ions to large exhaust velocities. The acceleration is achieved by the acceleration of the electrostatic fields on non-neutral or charged propellant particles such as atomic ions, droplets, or colloids. For this category, we can distinguish:

a) Ion thruster
The ion thrusters employs a variety of plasma generating methods to ionize a large fraction of propellant. A biased grids is used to electrostatically extract ions from the plasma and accelerate them to high velocity at voltages up to and exceeding 10 kV. Ion thrusters feature the highest efficiency (from 60% to over 80%) and very high Isp (from 2000 to over 10000 s) compared to other thruster types.

b) Hall thruster
The Hall thruster is a type of electrostatic propulsion system in which the propellant is accelerated by an electric field. A transverse magnetic field is used to trap electrons, which then ionize propellant. The produced ions are efficiently accelerate to produce thrust and then neutralize in the plume. Hall thruster's efficiency and Isp are somewhat less than that achievable in ion thrusters, but the thrust at a given power is higher and the device is much simpler and requires fewer power supplies to operate.

Electromagnetic propulsion

Acceleration is achieved by the interaction of electric and magnetic fields within a plasma. Moderately dense plasmas are high-temperature or non-equilibrium gases, electrically neutral and reasonably good conductors of electricity.

a) Pulsed plasma thruster
A pulsed plasma thruster (PPT) is an electromagnetic thruster that utilizes a pulsed discharge to ionize a fraction of a solid propellant ablated into a plasma arc, and electromagnetic effects in the pulse to accelerate the ions to high exit velocity. The pulse repetition rate is used to determine the thrust level.

b) Magnetoplasmadynamic thruster
The magnetoplasmadynamics (MPD) thrusters use a very high current arc between an anode and cathode to ionize a significant fraction of the propellant, and then electromagnetic forces (Lorentz $\mathbf{J} \times \mathbf{B}$ forces) in the plasma discharge to accelerate the highly ionized plasmas. Since both the current and the magnetic field are usually generated by the plasma discharge, MPD thrusters tend to operate at very high powers in order to generate sufficient force for high specific impulse operation, and thereby also generate high thrust compared to the other technologies described above. Among the various types of thrusters mentioned previously, this thesis

focuses only on MPD thrusters. MPDT thrusters promise a wide range of thrust levels (from 100 mN to 100 N) (Kodys and Choueiri, 2005) depending on the power level, along with exhaust velocities (from 10 km/s up to 100 km/s with hydrogen) a high thrust efficiency, ($10 - 25$ % with argon and up to 60% with lithium propellant), and the ability to process hundreds of kW to multi MW of power in a single compact device (see Fig.1.3). In Chap.4, the MPD thrusters will be described in more details as they are of particular interest for this thesis and the applications of the present developed numerical techniques are focused on their study.

1.3 Advantages and performance parameters of electric propulsion

MPD thrusters like other electric thrusters use the same propulsion principle as the chemical rockets which is to accelerate the mass and eject it from the space engine. The ejected mass is dominantly composed of energetic charged particles which permit the electric thrusters to perform better than other types of thrusters and modify the conventional way some performance parameters are evaluated. For a given rocket velocity increment Δv, electric thrusters provide higher exhaust velocities than chemical rockets and thus are suitable for deep space missions and also reduce the cost and the vehicle size. These advantages of electric thrusters over chemical thrusters are clearly demonstrated through the rocket equation of Tsiolkovsky (Messerschmid and Fasoulas, 2011).

1.3.1 Tsiolkovsky's rocket equation

The propellant (with mass m_p) carried onboard of the spacecraft (with mass M_s) which moves with velocity v, is accelerated and ejected outside of the vehicle with the exhaust velocity v_{ex} in the reference frame of the spacecraft. Thus, from the conservation of momentum, we have:

$$m_p v_{ex} = M_s \frac{dv}{dt} \tag{1.1}$$

The thrust on the spacecraft which is equal to the mass of the vehicle times its variation in velocity, is equal and opposite to the variation in time of the momentum of the propellant

$$F = M_s \frac{dv}{dt} = -\frac{d}{dt}(m_p v_{ex}) = -v_{ex}\frac{dm_p}{dt} \tag{1.2}$$

During the thrusting operation, the propellant is consumed and the total mass of spacecraft changes as:

$$\frac{dM_s}{dt} = \frac{d(m_d + m_p)}{dt} = \frac{dm_p}{dt} \tag{1.3}$$

where m_d is the delivered mass of the spacecraft without propellant so that, the mass of the spacecraft at any time of operation is equal to: $M_s(t) = m_d + m_p$. Now, substituting Eq.1.3 into Eq.1.2 and Eq.1.1, gives

$$M_s \frac{dv}{dt} = -v_{ex} \frac{dM_s}{dt} \tag{1.4}$$

which can be writen as:

$$dv = -v_{ex} \frac{dM_s}{M_s} \tag{1.5}$$

By integrating Eq.1.5 across a straight line from spacecraft initial velocity, v_i, to the final velocity v_f, corresponding to the mass change of $m_d + m_p$ and m_d respectively, we have:

$$v_i - v_f = \Delta v = v_{ex} ln(\frac{m_d}{m_d + m_p}) = (I_{sp} * g) ln(\frac{m_d}{m_d + m_p}) \tag{1.6}$$

where $\Delta v = v_i - v_f$ is the change in velocity of the spacecraft during the entire mission or the velocity increment and $I_{sp} = \frac{v_{ex}}{g}$ is the specific impulse and one of the most important performance parameter of the thruster which will be shown in the next section with $g = 9.81 m/s^2$, the acceleration by gravity.

According to Eq.1.6, the initial spacecraft mass ($M_s(t = 0) = m_d + m_p$) can be reduced by increasing the I_{sp} of the thruster for a given mission with a required velocity increment Δv. Reducing the initial spacecraft mass $M_s(t = 0)$ reduces the launch vehicle size and cost. That is why electric propulsion systems are recommended for High delta-v missions instead of conventional chemical propulsion systems because they exhibit much higher exhaust velocities and I_{sp}.

From Eq.1.6, the required propellant mass can be evaluated:

$$m_p = m_d[e^{\Delta v / v_{ex}} - 1] = m_d[e^{\Delta v / (I_{sp} * g)} - 1] \tag{1.7}$$

The above relation between the amount of propellant required to perform a given mission and its exhaust velocity shows that the propellant mass increases exponentially with Δv required. Thus, thrusters which exhibit higher value of propellant exhaust velocity compared to the mission Δv will have a very small propellant mass compared to the delivered spacecraft mass m_d. While the chemical thrusters are limited by the energy contained in the electrical force linking the atoms of the propellant used, Electric thrusters separate the propellant from the energy source and thus are not subject to the same limitations.

It is clear from the equations above that, for a given total velocity increment, the needed mass of propellant decreases when the propellant velocity increases. For this reason, electric thrusters can allow a considerable reduction of the needed propellant mass, with respect to chemical thrusters (the propellant velocity in electrical thrusters can be as large as 20 or more km/s in chemical engines). Reduced propellant mass can significantly decrease the launch mass of spacecraft or satelite, leading to important saving costs. In general, electric propulsion (EP) encompasses any propulsion technology in which electricity is used to increase the propellant exhaust velocity. There are many figures of merit for electric thrusters, but mission and application planners are primarily interested in thrust F, specific

impulse I_{sp} and total efficiency in relating the performance of the thruster to the delivered mass and change in the spacecraft velocity during thrust periods. The thruster performance can then be evaluate through some output parameters specific for the electric propulsion which are extrapolated from the final solution. The thrust is directly related to the propellant mass flow rate $\dot{m}$ and to the exhaust velocity and is given by (Messerschmid and Fasoulas, 2011):

$$F_{total} = \dot{m} v_{ex} \tag{1.8}$$

The electromagnetic component of the total thrust is calculated with the volume integral of the axial component of the Lorentz force,

$$F_{EM} = \int_V (J \times B)_x dV \tag{1.9}$$

The thermal contribution of the total thrust can be easily calculated as the difference between total and electromagnetic thrust,

$$F_{thermal} = F_{total} - F_{EM} \tag{1.10}$$

The specific impulse is evaluated in the following way,

$$I_{sp} = \frac{F_{total}}{\dot{m} g} = \frac{v_{ex}}{g} \tag{1.11}$$

The efficiency of the self-field MPD thruster is the ratio of the output power and the the input power,

$$\eta_{eff} = \frac{Power_{output}}{Power_{input}} = \frac{F_{total}^2}{2\dot{m} I (V + V_{sh})} \tag{1.12}$$

Here, V and V_{sh}, are the electrical voltage across the plasma and the electrode sheath voltage respectively. V can be calculated as the line integral of Ohm's law from anode to cathode (Eq. 1.13). The electrode sheath is not included in the present code.

$$V = \int E dl = \int (\frac{J}{\sigma} - U \times B) dl \tag{1.13}$$

Naturally, spacecraft designers are concerned about providing the electrical power that the thruster requires to produce a given thrust, as well as with dissipating the thermal power that the thruster generates as waste heat. An electric thruster can achieve specific impulses in the range of $1500 - 8000\ s$ (i.e. velocity of the propellant on the order of $15 - 30\ km/s$) as indicated in Table. 1.1. This is much higher than the specific impulse of conventional chemical engines. Table. 1.1 compares performance values of different electric propulsion systems with chemical rockets. On the other hand the thrust of electric thrusters is generally less than thrust of chemical thruster, on the order of $100\ mN$. In fact, it is not possible to supply them with electric power in the same order as that available from chemical or nuclear reactions and that is why EP are well-suited for space applications where gravitational forces are weaker than on Earth (micro-gravity environments) such as satellite repositioning, station keeping and orbit transfer. Nevertheless, EP thrusters also have the potential for deep space missions because of it's large total impulse. Indeed, the Deep Space 1 was the first interplanetary

TABLE 1.1: Typical performance of various electric propulsion systems (VanGilder, 2000)

Thruster	Thrust [mN]	Specific Impulse [s]	Thruster Efficiency [%]	Input Power [kW]
Chemical rocket	$4,000 - 400,000$	$200 - 400$	≈ 50	100
Resistojet	$2 - 100$	$200 - 300$	$200 - 300$	1
Ion thruster	$0.01 - 200$	$1500 - 5000$	$60 - 80$	$1 - 10$
Hall thruster	$0.01 - 2000$	$2000 - 5000$	$30 - 50$	$1 - 30$
AFMPD thruster	$0.001 - 2000$	$1000 - 8000$	$30 - 50$	$0.1 - 200$

spacecraft to use an ion propulsion system, delivered by the Nasa Solar Electric Propulsion Technology Application Readiness (NSTAR) program, for the primary delta-V manoeuvre (Plok et al., 1999). In this thesis we are focussed on the MPD thrusters as the exhibit highest specific impulse values for a large spectrum of space missions than other EP system as presented in Fig.1.4 and they will be described in more details in Chap.4.

1.4 Previous Computational efforts on MHD

All the before mentioned applications of sec.1.1 involve problems that require solutions of the MHD equations. Numerical efforts to solve them have advanced more lazily than experimental research. The main reason of that was due to lack of the computational resources necessary to properly model the highly non linear and interactive physics involved in the thrusters. To find the first attempt of simulation of plasma flow in a MPD thruster, we have to look back to the end of the sixties with the work of Burshlinkskii and Morozov (Brushlinski, Gerlakh, and Morozov, 1967; Brushlinski and Morozov, 1968; Brushlinski, Gerlakh, and Morozov, 1968) with the simulation of a two-dimensional unsteady plasma flow with finite conductivity in the presence of the Hall effect. The results of density and current in coaxial devices were in good agreement with experiment, despite the fact that their model had to be very simple due to the limitation of computational resources available at that time. In fact, the energy equation was not implemented and the electrical conductivity was assumed constant and uniform.
With the improvement of computational power, several methods have been developed for the prediction of the plasma flowfields inside the MPD thrusters. Over the past decades, to efficiently solve the ideal MHD equations, numerical methods have been extended from hydrodynamics to MHD. The most popular so far are the Riemann solvers (Brio and Wu, 1988). They are: the Roe's approximation Riemann solver (Roe, 1981), the generalized Godunov's method introduced by Colella

(Colella and Woodward, 1984) and known as Piecewise Parabolic Method (PPM) in which the states of the adjacent cells are assumed to be parabolic, the Essentially Non-Oscillatory (ENO) schemes developed by Harten and Osher (Harten et al., 1997), the approximate Riemann solver devised by Harten, Lax, Van Leer (HLL) (Harten, Lax, and Leer, 1983) and it's variants (HLLE, HLLEM, HLLEC) which are generated using the fastest leftward and the fastest rightward moving characteristics. Due to their robustness and accuracy to capture all the discontinuities, these solvers were regarded in the past as the best candidates to handle the MHD equations (Roe, 1981). Besides the Riemann solvers, we have the central schemes (Nessyahu and Tadmor, 1990) which do not involve Riemann solvers at the cell interface or characteristic decomposition. Nessyahu (Nessyahu and Tadmor, 1990) proposed the more robust Lax-Friedrichs (LxF) solver which is simpler. Here, no Riemann solvers are solved and hence field-by-field decomposition is avoided. However, the use of high-resolution MUSCL-type interpolants to deal with the excessive numerical viscosity is needed. Inspired by Nessyahu and Tadmor's new central schemes (Nessyahu and Tadmor, 1990), Kurganov (Nessyahu and Tadmor, 1990) introduced a family of new second-order Godunov-type central schemes for one-dimensionsional systems of conservation laws whose construction is based on the maximal one-sided local speeds of propagation and aim to reduce the implementation complexity and computation time by using a partially characteristic decomposition. Jiang (Jiang et al., 1998) proposed a procedure in which staggered spatial grids are converted into non-staggered schemes and used this to construct a new family of non-staggered, central schemes for hyperbolic conservation laws while retaining the desirable properties of simplicity and high-resolution. Theses schemes do not involve Riemann solvers. In order to reduce computational time, Constantin and Kurganov (Constantin and Kurganov, 2006) proposed a new version of the Central-Upwind schemes in which second-order limiters are applied near shock waves only, while in the rest of computational domain, an unlimited fifth order reconstruction is employed and coupled with a shock detection algorithm. All these previous schemes seem to be more dissipative. Because of this, Kurganov and Lin (Kurganov and Lin, 2006) proposed a modification of one-dimensional and semi-discrete Central-Upwind schemes to decrease the numerical dissipation present on the staggered Central Schemes. The simplicity, versatility and robustness of the non-oscillatory central schemes had encouraged many researchers to investigate the possibility to extend these central schemes to the MHD equations, since the wave structure of the MHD equations is similar to the wave structure of the Euler equations. Recently, Baldas (Baldás, Tadmor, and Wu, 2004) made use of family high-resolution, non-oscillatory central schemes for the approximate solution of the one- and two-dimensional MHD equations. To improve the efficiency and versatility of the previous developed fully-discrete MHD central schemes, they proposed a semi-discrete formulation which retains the simplicity of the fully-discrete staggered schemes (Baldás and Tadmor, 2006). With the intention to satisfy the solenoidal property of the magnetic field and avoid the resolution of the Riemann problems at the cell interfaces, Touma and Arminjon (Touma and Arminjon, 2006) proposed three-dimensional central finite volume methods based on the Lax-Friedrichs and Nessyahu-Tadmor one-dimensional central finite difference schemes (Nessyahu and Tadmor, 1990). The methods had demonstrated it's

accuracy and efficiency to solve the hyperbolic conservation laws and in particular the MHD equations. However, they are based on the staggered grids and involve Riemann problems. Thus, Touma proposed later a switch from the staggered central schemes to the second-order, non-oscillatory, unstaggered central schemes (UCS) (Touma, 2009), by using implicitly ghost staggered grid cells to bypass the resolution of the Riemann problems arising at the cell interfaces. Shengtai Li (Li, 2008) extended the central finite volume schemes of Liu (Liu et al., 2007) on overlapping cells to MHD equations. F. Li (Li, Xu, and Yakovlev, 2011) extended the original central discontinuous Galerkin methods for hyperbolic conservation laws to MHD equations with accurate divergence-free magnetic fields. Greenshields (Greenshields et al., 2010) described the implementation of semi-discrete, non-staggered central schemes methods in finite volume and indicated that the method is competitive and relatively simple and well suited for the finite volumes. As described above, a lot of work have been done concerning computational MHD. However, until now many of them remain complex black boxes, are based on a complex process of characteristic decomposition and Jacobian evaluation making them difficult to implement and are also computationally expensive, especially for multidimensional problems (Roe and Balsara, 1996). Inspired by some modern MHD extended upwind schemes such as the E-CUSP (Energy-convective upwind and split pressure) method of Shen at al. (Shen, Zha, and Huerta, 2012), the AUSM-MHD of Xisto (Xisto, Pascoa, and Oliviera, 2014; Xisto, Pascoa, and Oliviera, 2013; Xisto et al., 2012) and the modified E-CUSP MHD method of Huazheng (Huazheng and Xueshang, 2015), the present work extends the Godunov-type central-upwind scheme of Greenshields (Greenshields et al., 2010) to the ideal and then to the resistive MHD equations by using the schemes of Kurganov and Tadmor (Kurganov, Noelle, and Petrova, 2001; Kurganov and Tadmor, 2000) which are based on the volumetric fluxes evaluation associated with the local magnetosonic speed of MHD waves propagation and do not involve Riemann's solver and characteristic decomposition making them simple to implement and also computational inexpensive.

1.5 Objectives of the present work and structure of the thesis

The ultimate goal of the present work is the prediction of the plasma flow inside MPD thrusters. To do so, it is indispensable to have a robust computational model in with the current and the flow are solved in a consistent manner. The main goal is subdivided as follow:

1.5.1 Extension of the central-upwind flux calculation schemes from Euler equations to the MHD equations

In this thesis the open-source software *OpenFOAM*® (*OpenFOAM version 2.3.0*) is used as developer tool in order to take advantage of several numerical features and improvements concerning the numerical methods for Euler and Navier-Stokes equations. The conservative formulation of equation, used in *OpenFOAM*®,

makes the application of boundary conditions much easier and consistent with both the flux based numerical method already implemented in *OpenFOAM*® and the finite volume cell centered storage of variables. Beside these advantages, the density-based central-upwind schemes (Kurganov, Noelle, and Petrova, 2001; Kurganov and Tadmor, 2000) are strong and accurate numerical techniques which have been tested and used for several compressible flow benchmark problems with shocks and for a wide range of Mach number (Greenshields et al., 2010). All this make them the suitable candidate for an extension to MHD plasma simulation. The extension is achieved by solving the induction equation in iteratively and in a conservative manner as the flow equations (conservation of mass, momentum and energy). The magnetic field and the Alfvèn wave effects are taken into account in the flow equations and in the flux calculation scheme respectively. This part of the thesis work is organized as follow: Chap.2 is completely dedicated to the physical model and the transport properties we used and the descriptions of the equations governing the flow. The resistive MHD and the ideal MHD equations which form the core of the current model are developed and presented. In Chap.3, the density-based method is developed and presented.

1.5.2 Validation of the developed MHD code

Before using the developed density-based MHD code for the simulation of MPD thruster plasma flows, its validation is necessary. First in Chap.3, the ideal version of the present code is verified against one or two dimensional ideal MHD test problems for which either analytical solutions exist or the simulated variable distributions are well known. Thus, the different test used in this work are: The one dimensional shock tube problem of Sod (Sod, 1978) for testing the ability of a MHD code to accurately describe the shocks, rarefactions, contact discontinuities and compound waves of MHD. The two dimensional Orszag-Tang vortex problem (Shen, Zha, and Huerta, 2012; Baldás and Tadmor, 2005) very useful in describing local supersonic regions in a turbulent, compressible, dissipative conducting fluid. Finally the two dimensional cloud-shock interaction test (Xisto, Pascoa, and Oliviera, 2014) is used to test the ability of the present solver to simulate the interaction between a MHD shock and a high density cloud. Secondly in Chap.5 the resistive version of the aforementioned MHD code is tested against experimental data and other MHD code for plasma MPD thrusters. The chosen MPDT thrusters for verification are: The Princeton's Full Scale Benchmark Thruster (PFSBT) (Boyle, 1974; Burton, Clark, and Jahn, 1983), the Extended Anode Thruster (PEAT) (Lapointe, 1991; Lapointe, 1992) and the Villani-H thruster (Villani, 1982; Sankaran, 2005; Ahangar, Ebrahimi, and Shams, 2014).

1.5.3 Numerical investigation on the performance of MPD thrusters

Confident with the results obtained in sec.5.2 and sec.5.3 of Chap.5, we conducted in the same chapter a geometric scaling analysis to assess the effect of geometry changes on the Villani-H self-field MPD thruster (Villani, 1982) by varying the power parameter $\frac{I^2}{\dot{m}}$. The purpose here is to understand the physic of thrust

production and energy dissipation, obtain the operating conditions for which the code is stable and propose the first statement of MPD thrusters designing. The concerned geometric parameters are the cathode length and the anode radius. To do so, three different configurations are deducted from the original Villani-H thruster geometry. For each configuration, 10 variants depending of the integer aspect ratio $\frac{l_a}{r_a}$ ranging from 1 to 5 and the cathode length are created yielding 30 cylindrical thruster geometries. For each singular geometry, thrust components, plasma voltage, specific impulse and efficiency are approximated with the main of the developed density-based MHD code. At the end of Chap.5, a stability table of all thruster configurations is established.

1.5.4 Extension of the density-based code to the simulation of applied-field MPD thrusters

It is already established by previous studies that the self-field MPD thruster performance parameters are strongly dependent upon the input power. In Chap.5, thrust, specific impulse and efficiency increase with the discharge current and some discrepancies are observe around the critical current I_c called the onset instability which forces the thruster to perform at lower efficiency. Practicaly, increasing the discharge current above the critical current value conducts to the damage of the cathode. This limitation of the self-field MPD thruster performances by the power parameter $\frac{I^2}{\dot{m}}$ conducts us in Chap.6 to investigate the applied magnetic MPD thrusters as well. The last chapter of this thesis is then dedicated to the extension and application of the developed code to the simulation of applied magnetic field MPD thrusters. The governing equations of classical resistive MHD of Chap.2 are modified so that it can take into account the applied magnetic field, the additional acceleration mechanisms and their corresponding energy contributions. The applied magnetic field from permanent magnet is calculated with a steady-state electromagnetic solver by solving the Poisson's equation for magnetic scalar potential. The applied-field MHD code is validated by calculating the plasma flow inside of the applied-field NASA Lewis Research Center's (NASALeRC) MPD thruster (Krülle, Auweter-Kurtz, and Sasoh, 1998; Mikellides, Turchi, and Roderick, 2000). The effect of the applied magnetic field inside and outside the discharge chamber are further investigated function of the discharge current and the applied magnetic field strength for constant mass flow rate to test the ability of the applied-field MHD code to reproduce the plasma behaviour and the main issues already reported in the literature such as the plasma depletion on anode surface and the limitation of the rotational speed of the plasma inside the discharge chamber.

Finally, A summary of the important findings of this work and the future research possibilities are discussed in Chap.7.

Chapter 2

Governing equations

MHD is the mechanical domain which studies the interaction of an electrical conducting fluids with one or more magnetic fields. Thus, the MHD equations derive from the coupling of Navier-Stokes equations with the Maxwell equations of electrodynamics. In this chapter, before presenting the derivation of MHD equations it is important to discuss briefly the characteristic of plasma and some criteria for its definition. First, the plasma is treated in this work as continuous medium so that all macroscopic quantities are continuous functions of position and time. This assumption of continuity presupposes that we will be interested only in phenomena which vary on a hydrodynamic length scale much greater than the average inter-particle distance. The information of this Chapter is based on (Jahn, 1968; Ferziger and Peric, 2002; Boyd and Sanderson, 2003; Bittencourt, 2004; Goedbloed and Poedts, 2004; Spitzer, 2006; Goebel and Katz, 2008; Hosking and Dewar, 2016)

2.1 Plasma as continuous medium

A plasma can de defined as a quasi neutral gas composed of charged (ions and electrons) and neutral particles which manifests collective behaviour. As the charged particles move, they generate local concentrations of positive or negative charge which give rise to electric fields ($\mathbf{E}$). In the same time, the motion of charges also generates currents and thus magnetic fields ($\mathbf{B}$). These generated fields affect the motion of other particles far away by the mean of the electromagnetic Lorentz force. Indeed, in the presence of the electric and the induced magnetic fields, the motion of an arbitrary particle i inside the plasma of charge q_i and mass m_i, moving with the velocity $\mathbf{U}_i$ can be written as follows (Bittencourt, 2004)

$$\frac{d\mathbf{p}_i}{dt} = q(\mathbf{E} + \mathbf{U}_i \times \mathbf{B}) \tag{2.1}$$

where $\mathbf{p}_i = m_i\mathbf{U}_i$ is the particle momentum. Therefore, treating the plasma as a collection of particles is the most general and understandable way of studying the plasma system and also the most complex (Jahn, 1968). The plasma is then described kinetically by modelling the individual particle dynamics. Thus, a density ρ, a mean velocity $\mathbf{U}$ and a scalar pressure p is assigned to each of the plasma components. The transfer of streamwise momentum from electrons to the bulk of the plasma is accomplished through collisions. All this make the kinetic approach more accurate and realistic than the fluid theory concerning plasma description. Nevertheless, for conditions of interest of plasma thrusters, with electron and ion densities of $\mathcal{O}(10^{21})\ m^{-3}$, mass averaged velocities of $\mathcal{O}(10^{4})\ m/s$, temperatures

of about 2 eV, thermodynamic pressures of $\mathcal{O}(10^{-1}-1)\ Torr$, and magnetic pressures of $\mathcal{O}(1-10)\ Torr$ ($1Torr = 133.322pa$), particle simulations with the kinetic plasma theory are not presently practical, even when following only representative or macro particles (Goebel and Katz, 2008). Furthermore, in order to explain and predict the macroscopic behaviour of the laboratory plasma, it is not of interest to know the detailed individual motion of each particle, since the observable macroscopic properties of a whole plasma are due to the average collective behaviour of its large number of particles. Under these conditions, the most useful approach to understand the nature of electromagnetic plasma acceleration is that of fluid theory (MHD), in which the ionized gas is treated as a continuum fluid. For this reason, the ionized gas physical properties are then described by a set of bulk parameters whose dynamical behaviour is represented in this thesis by a set of conservation relations. Before presenting the set of MHD conservation laws, it is useful first to explain some criteria for the definition of a plasma.

2.1.1 Macroscopic neutrality of the plasma and the Debye shielding

Generally, a plasma remain macroscopically neutral without any external perturbation. This means that under equilibrium conditions with no external forces present and considering the concept of a fluid element i.e in a volume of fluid (plasma), small enough that any macroscopic quantity such as density and temperature have a negligible variation across its dimension but large enough to contain a large number of particles and so to be insensitive to particle fluctuations, the net resulting electric charge is zero (Bittencourt, 2004).

$$n_e = \sum_i n_i = Z n_i \tag{2.2}$$

where, n_e, n_i and Z are the electron and ions density and the ions particle charge number inside the plasma element respectively. Thus, in a plasma consisting of electrons with charge $Q_e = -e$ and one species of ion with a charge number Z and charge $Q_i = Ze$, the current density is then given by:

$$\mathbf{J} = e(Z n_i \mathbf{U}_i - n_e \mathbf{U}_e) = e n_e (\mathbf{U}_i - \mathbf{U}_e) \tag{2.3}$$

In the interior of the plasma the microscopic space charge fields cancel each other and no net space charge exists over a macroscopic region so that there is no macroscopic charge separation. The macroscopic electrical neutrality of the plasma is maintained only over distance in which a balance between the thermal particle energy, which trends to disturb the electrical neutrality, and the electrostatic potential energy resulting from any charge separation, which trends to restore the electrical neutrality, is obtained. This distance is of the order of the a characteristic length parameter of the plasma, called the Debye shielding length (λ_D) (Bittencourt, 2004) which is directly proportional to the square root of the temperature (T) and inversely proportional to the square root of the electron number density according to:

$$\lambda_D = \left(\frac{\epsilon_0 k_B T}{n_e e^2}\right)^{1/2} \tag{2.4}$$

where k_B, ϵ_0 and e are the Boltzmann constant, the permittivity of vacuum and the fundamental electric charge respectively. With $k_B = 1.381 \times 10^{-23}\ m^2kgs^{-2}K^{-1}$, $\epsilon_0 = 8.854 \times 10^{-12}\ m^{-3}kg^{-1}s^4A^2$ and $|e| = 1.602 \times 10^{-19}\ C$ as specified in the Appendix C of (Bittencourt, 2004).

The lower limit in space for the occurrence of quasi-neutrality is given by the Debye sphere, with Debye length λ_D as radius. Thus quasi-neutrality is only given in areas greater than this sphere and appeared therefore as a good assumption for studying plasma phenomena with a scale length L, being longer than the Debye length.

$$\lambda_D \ll L \tag{2.5}$$

In view of the typical plasma properties of interest in MPD thrusters mentioned in sec.2.1, the Debye length is much smaller than the characteristic length, thus the plasma can be regarded as electrically neutral.

2.1.2 Collective behaviour of the plasma

A plasma is an ionized gas but any ionized gas can not be called a plasma. The difference is that, in a neutral gas molecules, there is no net electromagnetic force on it. The neutral gas particles interact only when collisions occur and these collisions control the particle motion. This is quite different in plasma which has charged particles. For plasma the important motions are collective (many particle moving together). The effects of close encounters such as collisions between slightly charged regions of plasma (A and B) separated by a distance r (See Fig.2.1) are of less interest than long range interaction such as the electrostatic forces which decays only slowly as r^2 when the short-range Van der Waals force decays as r^6 (Kubota and Funaki, 2009). Therefore, plasmas show a simultaneous response of many particles (A) to an external stimulus (from B) inside a volume increasing as r^3. A and B exert a force on one another even at large distances. As result of this, the long-range electromagnetic force are so much larger than the force due to ordinary local collisions that the plasma can be good approximated as collisionless and its motion is quasi totally controlled by the state of the plasma in its faraway regions. In this sense, plasmas exhibit collective behaviour, which means that the macroscopic result to an external stimulus is the cooperative response of many plasma particles. One example of the collective behaviour of the plasma is the mutual shielding of plasma particles.

2.1.3 Electrodynamic equations for plasma fluid

Before jumping into the derivation of the governing equations describing the single fluid plasma, it is appropriate to first present the electrodynamic equations which describe the generation of electric field ($\mathbf{E}$) and magnetic field ($\mathbf{B}$) by charges, currents, and change of each other. These equations are presented in the following subsections.

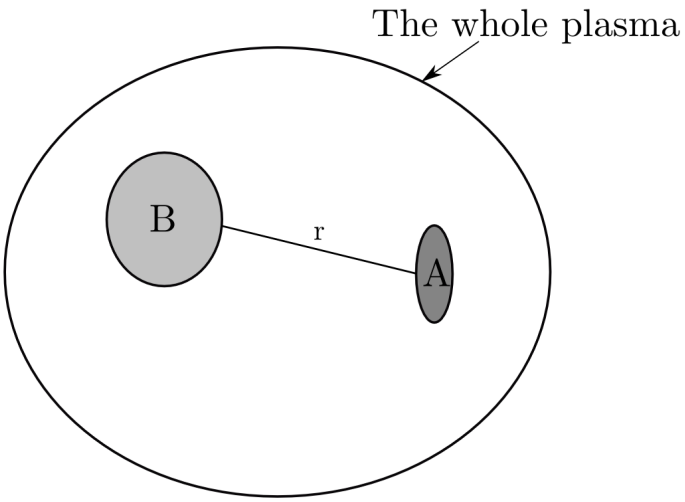

FIGURE 2.1: Diagram illustrating the long range of electromagnetic force in plasma as in (Kubota and Funaki, 2009)

Maxwell's Equations

The electric and magnetic fields that exist in electric propulsion plasmas obey Maxwell's equations formulated in a vacuum that contains charges and currents (Bittencourt, 2004; Goebel and Katz, 2008). Maxwell's equations for these conditions are:

$$\nabla \times \mathbf{B} = \mu_0(\mathbf{J} + \epsilon_0 \frac{\partial \mathbf{E}}{\partial t}) \qquad \textbf{(Ampère's law)} \tag{2.6}$$

$$\nabla \times \mathbf{E} = -\frac{\partial \mathbf{B}}{\partial t} \qquad \textbf{(Faraday's law)} \tag{2.7}$$

$$\nabla \cdot \mathbf{B} = 0 \qquad \textbf{(Gauss's law for magnetism)} \tag{2.8}$$

$$\nabla \cdot \mathbf{E} = \frac{\varrho}{\epsilon_0} \qquad \textbf{(Gauss's law)} \tag{2.9}$$

Here ϱ is the charge density in the plasma and $\mu_0 = 4\pi \times 10^{-7}\ H/m$ is the magnetic permeability of free space. $\epsilon_0 \frac{\partial \mathbf{E}}{\partial t}$ is the displacement current that is neglected because the electric field intensity E is considered as stationary. It is important to note that ϱ and $\mathbf{J}$ comprise all the charges and currents for all the particle species that are present in the plasma, including charged ions. The charge density is then,

$$\varrho = \sum_s q_s n_s = e(Zn_i - n_e) \tag{2.10}$$

Where q_s is the charge state of species s. Since the plasma is assumed macroscopically neutral (see sec.2.1.1), ϱ is taken equal zero.

The induction equation

To obtain the expression of the rate of change of the magnetic field, which is known as the induction equation, we start from another constitutive relation namely the generalised Ohm's law (Hosking and Dewar, 2016). In a neutral plasma containing an equal number density of ions and electrons ($n_i = n_e = n$, the index i and e standing for ions and electrons respectively), the generalised Ohm's law can be written as

$$\mathbf{E} + \mathbf{U} \times \mathbf{B} = \frac{\mathbf{J}}{\sigma} + \frac{\mathbf{J} \times \mathbf{B}}{n_e} - \frac{\nabla p_e}{n_e} \tag{2.11}$$

where σ is the electrical conductivity, inversely related to the resistivity coefficient $\eta = \frac{1}{\sigma}$ and will be discuss in more details in sec.2.3.1. The terms on the left-hand side of Eq.2.11 are often referred to as ideal, as they remain in the limit of zero resistivity, when σ is infinite. The second term represent the back emf (electromotive force) contribution to plasma voltage. The first, the second and the third term on the right-hand side of Eq.2.11 are the resistive drop term, the Hall effect term and the electron pressure term respectively.
By using Ampère's law (Eq.2.6) and Faraday's law (Eq.2.7) to eliminate the current density $\mathbf{J}$ and the electric field $\mathbf{E}$ appearing in Eq.2.11 reproduces

$$\frac{\partial \mathbf{B}}{\partial t} = \nabla \times (\mathbf{U} \times \mathbf{B}) - \nabla \times (\eta \nabla \times \mathbf{B}) - \nabla \times (\frac{1}{\mu_0 n_e} (\nabla \times \mathbf{B}) \times \mathbf{B}) + \nabla \times (\frac{1}{n_e} \nabla p_e) \tag{2.12}$$

The second, the third and the last term in the right hand of Eq.2.12 represents the resistive diffusion of magnetic flux, Hall effect and pressure respectively. In this work, the Hall effect term and the pressure term are neglected. Finally, the resulted convective-diffusive induction equation which will be used in this thesis is

$$\frac{\partial \mathbf{B}}{\partial t} = \nabla \times (\mathbf{U} \times \mathbf{B}) - \frac{1}{\mu_0 \sigma} \Delta \mathbf{B} \tag{2.13}$$

with the magnetic field subjected to Gauss law (no magnetic monopole),

$$\nabla \cdot \mathbf{B} = 0 \tag{2.14}$$

2.1.4 Conservation principle and resistive MHD equations

As we considered in the previous section the plasma as a continuous medium with charges, its macroscopic transport equations are described in the present section by neglecting the identity of its individual particles (ions, electrons and, in the case of a partially ionized plasma, neutral particles). Only the fluid elements are taking into account. Therefore, the starting point is the conservation principle of fluid mechanics for which the general technique for obtaining the conservation laws governing fluid motion is to consider a given quantity of fluid or control mass and its extensive properties such as mass, momentum and energy. The conservation law for an extensive property relates the rate of change of the amount of that property in a given control mass to externally determined effects. The fundamental variables will be intensive rather than extensive properties, for the former are

independent of the amount of matter considered. Examples are density ρ (mass per unit volume) and velocity $\mathbf{U}$ (momentum per unit mass). The following evaluations are done based on the information in (Ferziger and Peric, 2002; Bittencourt, 2004; Goedbloed and Poedts, 2004; Hosking and Dewar, 2016).
If ϕ is any conserved intensive property (for mass conservation, $\phi = 1$; for momentum conservation, $\phi = \mathbf{U}$; for a scalar, ϕ represents the conserved property per unit mass), then the corresponding extensive property Φ can be expressed as:

$$\Phi = \int_{\Omega_{CM}} \rho\phi d\Omega \tag{2.15}$$

Where Ω_{CM} stands for volume occupied by the control mass (CM) of fluid. Thus, the conservation law of all intensive variables can be written in the form:

$$\frac{d}{dt}\Phi = \sum f \tag{2.16}$$

where t is time and f, the forces acting on the CM. For mass, which is neither created nor destroyed, f is zero. Using this definition, the left hand side of each conservation equation for a fixed control volume (CV) can be written as:

$$\frac{d}{dt}\int_{\Omega_{CM}} \rho\phi d\Omega = \frac{d}{dt}\int_{\Omega_{CV}} \rho\phi d\Omega + \int_{S_{CV}} \rho\phi \mathbf{U}\cdot\mathbf{n} dS \tag{2.17}$$

Where Ω_{CV} is the control volume, S_{CV} is the surface enclosing CV, $\mathbf{n}$ is the unit vector orthogonal to S_{CV} and directed outwards dS and $\mathbf{U}$ is the fluid velocity as presented in Fig.2.2. The equations of resistive magnetohydrodynamics, which describe the dynamic of conducting plasma under the influence of a magnetic field, will be presented in the next section. For convenience, V and S represent the control volume and its surface respectively.

Conservation of mass

Accordingly with our physical model, the continuity equation does not have any source or sink terms because this model assumes complete ionization and no recombination. Thus, the integral form of the global continuity equation follows directly from the Eq.2.17, by setting $\phi = 1$:

$$\frac{\partial}{\partial t}\int_V \rho dV + \int_S \rho\mathbf{U}\cdot\mathbf{n} dS = 0 \tag{2.18}$$

Using the Gauss divergence theorem (Spurk and Aksel, 2007), the surface integral may be replaced by a volume integral. Then Eq.2.18 becomes:

$$\int_V [\frac{\partial\rho}{\partial t} + \nabla\cdot(\rho\mathbf{U})] dV = 0 \tag{2.19}$$

Since Eq.2.19 is valid for any size of V, it implies that

$$\frac{\partial\rho}{\partial t} + \nabla\cdot(\rho\mathbf{U}) = 0 \tag{2.20}$$

which is the mass conservation or continuity equation. where ρ is the average density of all species and $\mathbf{U}$ the velocity vector.

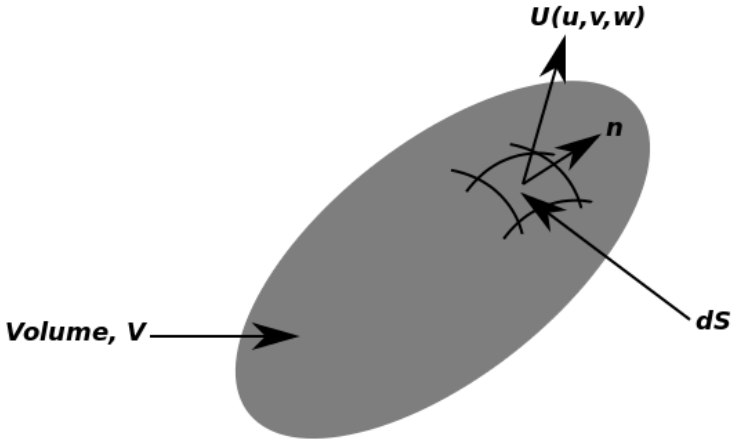

FIGURE 2.2: Closed surface S surrounding the arbitrary volume V inside the fluid and the element of area $\mathbf{dS} = \mathbf{n}dS$ pointing outwards according to (Ferziger and Peric, 2002)

Conservation of momentum

The relation of conservation of momentum of the plasma is analogous to the Navier-Stokes momentum equation, with external body force acting on the fluid as represented in Fig.2.3. By setting $\phi = \mathbf{U}$ in the CV equation (Eq.2.17), we obtain the momentum conservation equation.

$$\frac{\partial}{\partial t}\int_V \rho \mathbf{U} dV + \int_S \rho \mathbf{U}\mathbf{U} \cdot \mathbf{n} dS = \sum f \tag{2.21}$$

To express the right-hand side (RHS) in terms of intensive properties, one has to consider the forces which may act on the fluid in a CV. These forces are: surface forces (pressures, normal and shear stress, surface tension) and body forces (gravity, centrifugal and Coriolis forces, electromagnetic forces).

The surface forces due to pressure and stresses are, from the molecular point of view, the microscopic momentum fluxes across a surface. If these fluxes cannot be written in terms of the properties whose conservation the equation govern (in this case velocity), the system of equations is not closed; that is there are more dependent variables than equations and solution is not possible. This possibility can be avoided by making certain assumptions. The simplest assumption is that the fluid is Newtonian. For Newtonian fluids, the stress tensor $\mathbf{T}$, which is the molecular rate of transport of momentum, can be written:

$$\mathbf{T} = -p\mathbf{I} + \tau_{visc} \tag{2.22}$$

where p is the static pressure and τ_{visc} is the viscous stress tensor for compressible Newtonian flow given by:

$$\tau_{visc} = -(\frac{2}{3}\mu\nabla \cdot \mathbf{U})\mathbf{I} + [\nabla\mathbf{U} + (\nabla\mathbf{U})^T] \tag{2.23}$$

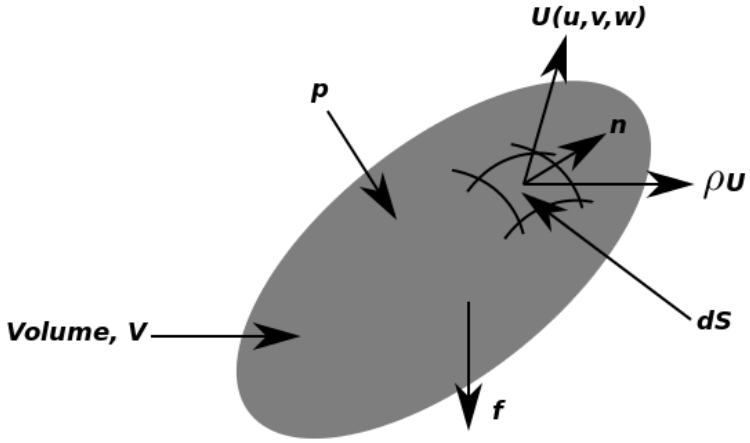

FIGURE 2.3: Closed surface S surrounding the arbitrary volume V inside the fluid and the element of area $\mathbf{dS} = \mathbf{n}dS$ pointing outwards as seen in (Ferziger and Peric, 2002)

where $\mathbf{I}$ is the unit tensor. With the body forces (per unit mass) being represented by $\mathbf{b}$, the integral form of the momentum conservation equation becomes:

$$\frac{\partial}{\partial t}\int_V \rho\mathbf{U}dV + \int_S \rho\mathbf{U}\mathbf{U}\cdot\mathbf{n}dS = \int_S \mathbf{T}\cdot\mathbf{n}dS + \int_V \rho\mathbf{b}dV \tag{2.24}$$

By applying the Guass divergence theorem to the convective and diffusive flux terms, a coordinate free vector form of the momentum conservation equation is obtained:

$$\frac{\partial\rho\mathbf{U}}{\partial t} + \nabla\cdot(\rho\mathbf{U}\mathbf{U} + p\mathbf{I}) = \nabla\cdot\tau_{visc} + \rho\mathbf{b} \tag{2.25}$$

For the case under consideration, the external body force is only the Lorentz force, $\rho\mathbf{b} = \mathbf{J}\times\mathbf{B}$, per volume of the plasma. Where, $\mathbf{J}$ and $\mathbf{B}$ are the current density vector and the magnetic flux vector respectively. The gravitational force ρg could be added in the RHS of Eq.2.25 but in laboratory plasmas, that force is neglected in comparison to the pressure gradient and the Lorentz force. Now, Using the vector identities and the Maxwell equations of sec.2.1.3, we can replace the Lorentz force as defined above by a set of stresses (See Appendix.A)

$$\mathbf{J}\times\mathbf{B} = \nabla\cdot(\frac{\mathbf{B}\mathbf{B}}{\mu_0} - \frac{B^2}{2\mu_0}\mathbf{I}) \tag{2.26}$$

The conservation of momentum is then written as:

$$\frac{\partial\rho\mathbf{U}}{\partial t} + \nabla\cdot[\rho\mathbf{U}\mathbf{U} + (p + \frac{B^2}{2\mu_0})\mathbf{I} - \frac{\mathbf{B}\mathbf{B}}{\mu_0}] = \nabla\cdot\tau_{visc} \tag{2.27}$$

The overall pressure is given by $P_{over} = p + \frac{B^2}{2\mu_0}$, in which the second contribution corresponds to the magnetic pressure. The latter acts like pressure gradient in the direction perpendicular to the magnetic field. Hence, the magnetic field resists to compressibility just like the fluid pressure. The term $(\frac{\mathbf{B}\mathbf{B}}{\mu_0})$ is called hoop stress and acts like a tension along the lines of magnetic force, bearing some similarity

with the viscous stresses. It represents the tension along the magnetic flux lines as if they were elastic cords (Bittencourt, 2004).

To closed the equation system formed by Eq.2.13, Eq.2.20 and Eq.2.27, it is necessary to know the pressure. This may be achived by considering a conservation equation for energy and a thermodynamic equation relating internal energy and transport coefficients to the state variables such as pressure p, density ρ and temperature T. Thus the MHD equations will be closed by the energy equation and the equation of state because of the presence of state variables in the equations.

Conservation of energy

Assuming a quasi-static equilibrium isolated fluid system, the firts law of thermodynamics states that the change in the internal energy per unit mass e between two equilibrium states is equal to the increase in heat energy (Q) per unit mass and the work done (W) per unit mass on the fluid system as formulated in (Boyd and Sanderson, 2003),

$$de = dQ + dW \tag{2.28}$$

where e is a state variable which only depends of the initial and final states regardless the path of the process. While Q and W are path depending variables resulting in an infinity values of dQ and dW for any internal energy change de. Considering the fluid system moving with the velocity $\mathbf{U}$, we have to distinguished the work that contributes to the change of the kinetic energy of the flow and the one which increases the internal energy. That is done by first identifiying the work involving in the change of kinetic energy. The former is obtained by taking the scalar product of $\mathbf{U}$ with the momentum equation (Eq.2.25) and we get:

$$\frac{D(\mathbf{U}^2/2)}{Dt} = \frac{\mathbf{U}}{\rho} \cdot [-(\nabla \cdot p\mathbf{I}) + (\nabla \cdot \tau_{visc})] + \mathbf{U} \cdot (\mathbf{J} \times \mathbf{B}) \tag{2.29}$$

By using the stress tensor $\mathbf{T}$ of Eq.2.22, we have:

$$\frac{D(\mathbf{U}^2/2)}{Dt} = \mathbf{U} \cdot (\mathbf{J} \times \mathbf{B}) + \frac{\mathbf{U}}{\rho} \cdot \mathbf{T} \tag{2.30}$$

More generally, the work done on a fluid element by the body force, which is in the case of this work the Lorentz force, is $\int_{\partial V} \mathbf{U} \cdot (\mathbf{J} \times \mathbf{B}) dV$ and $\int_{\partial S} \mathbf{U} \cdot (\mathbf{T} \cdot \mathbf{n}) dS = \int_{\partial V} \nabla \cdot (\mathbf{U} \cdot \mathbf{T}) dV$ the work due to the surface forces. Hence, the rate of work per unit mass is:

$$\mathbf{U} \cdot (\mathbf{J} \times \mathbf{B}) + \frac{1}{\rho} \nabla \cdot (\mathbf{U} \cdot \mathbf{T}) = \mathbf{U} \cdot (\mathbf{J} \times \mathbf{B}) + \frac{\mathbf{U}}{\rho} \nabla \cdot (\mathbf{T}) + \frac{\mathbf{T}}{\rho} \nabla \cdot (\mathbf{U}) \tag{2.31}$$

comparing Eq.2.30 with Eq.2.31 yields that the rate of work which increases the internal energy per unit mass is just the last term in Eq.2.31 so that:

$$\frac{DW}{Dt} = \frac{\mathbf{T}}{\rho} \nabla \cdot (\mathbf{U}) \tag{2.32}$$

Now concerning the heat energy, two sources are involved. The joule heating $\int_{\partial V}(\frac{|\mathbf{J}|^2}{\sigma})dV$, where $\mathbf{J}$ is the current density and σ the electrical conductivity, and the heat conduction through the boundary surface of the fluid element given by: $\int_{\partial S}\nabla\cdot(k_{th}\nabla T)dS$ where k_{th} is the coefficient of heat conduction. Thus, the rate of change of heat per unit mass is:

$$\frac{DQ}{Dt}=\frac{|\mathbf{J}|^2}{\rho\sigma}+\frac{1}{\rho}\cdot\nabla\cdot(k_{th}\nabla T) \tag{2.33}$$

Now by adding Eq.2.32 with Eq.2.33, Eq.2.28 is rewritten as follows:

$$\frac{De}{Dt}=\frac{|\mathbf{J}|^2}{\rho\sigma}+\frac{1}{\rho}\nabla\cdot(k_{th}\nabla T)+\frac{\mathbf{T}}{\rho}\nabla\cdot\mathbf{U} \tag{2.34}$$

Substitution of Eq.2.22 in Eq.2.34 gives after some manipulations using Eq.2.20,

$$\frac{\partial\rho e}{\partial t}+\mathbf{U}\cdot\nabla(\rho e)+p(\nabla\cdot\mathbf{U})=\tau_{visc}:(\nabla\cdot\mathbf{U})+\eta|\mathbf{J}|^2+\nabla\cdot(k_{th}\nabla T) \tag{2.35}$$

The first term in the left-hand side (LHS) of Eq.2.35 represents the time rate of change of the internal energy in a CV of plasma. This rate of change is sustained by the second term through thermal energy transferred to the CV as a consequence of particle motion. The third term is simply the work done on the CV by the pressures forces. The term in the RHS of Eq.2.35 is the work done by the viscous forces and the electric field on the CV including the heat flux. By multiplying Eq.2.35 with $(\gamma-1)$ and using the perfect gas equation $\rho e=\frac{p}{(\gamma-1)}$ that will be presented in the next subsection, the internal energy equation in term of pressure is deducted,

$$\frac{\partial p}{\partial t}+\gamma p\nabla\cdot\mathbf{U}+\mathbf{U}\cdot\nabla p=(1-\gamma)(\tau_{visc}:(\nabla\mathbf{U})+\eta|\mathbf{J}|^2+\nabla\cdot(k_{th}\nabla T)) \tag{2.36}$$

To obtain the conservation equation of total energy, we have to add expressions for the internal energy, kinetic energy and magnetic energy by following the same conservation principle described above. For the equation of the kinetic energy we take dot product of the momentum conservation equation (Eq. 2.27) with $\mathbf{U}$,

$$\mathbf{U}\cdot[\frac{\partial\rho\mathbf{U}}{\partial t}+\nabla\cdot[\rho\mathbf{U}\mathbf{U}+(p+\frac{B^2}{2\mu_0})\mathbf{I}-\frac{\mathbf{B}\mathbf{B}}{\mu_0}]]=\mathbf{U}\cdot(\nabla\cdot\tau_{visc}) \tag{2.37}$$

Using Eq. 2.20, we have

$$\frac{\partial}{\partial t}(\frac{1}{2}\rho\mathbf{U}^2)-\nabla\cdot(\frac{1}{2}\rho|\mathbf{U}|^2\mathbf{U})+\mathbf{U}\cdot[(p+\frac{B^2}{2\mu_0})\mathbf{I}-\frac{\mathbf{B}\mathbf{B}}{\mu_0}]=\mathbf{U}\cdot(\nabla\cdot\tau_{visc}) \tag{2.38}$$

The magnetic energy equation is derived by multiplying Eq. 2.13 with $\mathbf{B}$.

$$\mathbf{B}\cdot\frac{\partial\mathbf{B}}{\partial t}+\mathbf{B}\cdot\nabla\cdot(\mathbf{U}\mathbf{B}-\mathbf{B}\mathbf{U})=-\mathbf{B}\cdot\frac{1}{\mu_0\sigma}\Delta\mathbf{B} \tag{2.39}$$

which leads to the final expression of the magnetic energy equation,

$$\frac{\partial}{\partial t}(\frac{1}{2}|\mathbf{B}|^2)+\nabla\cdot(\mathbf{B}\cdot\mathbf{B}\mathbf{U}-\mathbf{U}\cdot\mathbf{B}\mathbf{B})+\mathbf{U}\cdot(\mathbf{J}\times\mathbf{B})+\nabla\cdot(\eta\mathbf{J}\times\mathbf{B})+\eta|\mathbf{J}|^2=0 \quad (2.40)$$

This magnetic energy equation can also been found by using the Poynting theorem (See Appendix.A).

The transport equation of total energy (internal energy, kinetic energy and energy density in magnetic field) is finally obtained by adding Eqs. 2.35, 2.38 and 2.40,

$$\frac{\partial\rho E}{\partial t}+\nabla\cdot[(\rho E+p+\frac{\mathbf{B}^2}{2\mu_0})\mathbf{U}-\mathbf{U}\cdot\frac{\mathbf{B}\mathbf{B}}{\mu_0}]=\nabla\cdot[k_{th}\nabla T-(\frac{\eta\mathbf{J}\times\mathbf{B}}{\mu_0})] \quad (2.41)$$

where $\rho E=\frac{p}{\gamma-1}+\frac{1}{2}\rho|\mathbf{U}|^2+\frac{|\mathbf{B}|^2}{2\mu_0}$ is the total energy density of the plasma. The first term represents the internal energy, the second term the kinetic energy and the third term the energy produce by the magnetic field.

Equation of state

The description of MHD fluid, like ordinary fluid, requires an appropriate thermodynamical state equation that relates the variables ρ, p and T. The information of this section is based on (White, 1991; Groll, 2015). Normal practice is to assumed that the fluid is an ideal gas that undergoing a reversible polytropic process which can be either adiabatic (Eq.2.42) or isothermal (Eq.2.43),

$$pV^\gamma=constant \quad (2.42)$$

$$pV=constant \quad (2.43)$$

Here $\gamma=\frac{c_p}{c_v}$ is the ratio of specific heats at constant pressure (c_p) and volume (c_v) which can be defined as $\frac{\partial h}{\partial T}|_p$ and $\frac{\partial e}{\partial T}|_v$ respectively. With h and e respectively the enthalpy and the internal energy per unit mass of the gas. Most generally, these relations can be resumed in one simple equation named the ideal gas equation:

$$pV=nR_0T \quad (2.44)$$

where n is the amount of substance of the gas (in moles) contained in a volume V and R_0 is the so-called the universal gas constant with

$$R_0=8.3144621\frac{J}{Kmol} \quad (2.45)$$

Alternatively, this ideal gas equation can be written in term of the gas constant R and the gas density ρ

$$p=\rho RT \quad (2.46)$$

where $R=\frac{R_0}{M}$ with M the gas molar mass. From Eq.5.1, many useful relations arise. For instance by considering a thermally perfect gas, the specific heats are

constrained to be only temperature dependent, $c_p = c_p(T)$ and $c_v = c_v(T)$. Hence: $de = c_v dT$ and $dh = c_p dT$. Further it follows that γ is a function of temperature only and

$$c_p = c_v + R = \frac{\gamma(T)R}{\gamma(T) - 1} \tag{2.47}$$

$$c_v = \frac{R}{\gamma(T) - 1} \tag{2.48}$$

Finally, by using the calorically perfect gas approximation (c_p and c_v constant), the ideal equation of state can also been written as follows

$$\rho e = \frac{p}{\gamma - 1} \tag{2.49}$$

and the temperature can be obtained from the equations of state by substituting the internal energy in Eq.2.49 and by using Eq.5.1. Thus, the temperature is calculated as follows:

$$T = \frac{1}{c_v}[E - \frac{1}{2}(U^2 + \frac{B^2}{\rho\mu_0})] \tag{2.50}$$

Finally, the closed and suitable system of resistive MHD equations that will be solved in this work can be summarized as follows:

$$\frac{\partial \rho}{\partial t} + \nabla \cdot (\rho \mathbf{U}) = 0 \tag{2.51}$$

$$\frac{\partial \rho \mathbf{U}}{\partial t} + \nabla \cdot [\rho \mathbf{U}\mathbf{U} + (p + \frac{B^2}{2\mu_0})\mathbf{I} - \frac{\mathbf{B}\mathbf{B}}{\mu_0}] = \nabla \cdot \tau_{visc} \tag{2.52}$$

$$\frac{\partial \mathbf{B}}{\partial t} + \nabla \cdot (\mathbf{U}\mathbf{B} - \mathbf{B}\mathbf{U}) = -\frac{1}{\mu_0 \sigma}\Delta \mathbf{B} \tag{2.53}$$

$$\frac{\partial \rho E}{\partial t} + \nabla \cdot [(\rho E + p + \frac{B^2}{2\mu_0})\mathbf{U} - \mathbf{U} \cdot \frac{\mathbf{B}\mathbf{B}}{\mu_0}] = \nabla \cdot [k_{th}\nabla T - (\frac{\eta \mathbf{J} \times \mathbf{B}}{\mu_0})] \tag{2.54}$$

2.2 Ideal MHD equations

The second term in the left hand side of Eq.2.52 is the magnetic convection term, while the second member term expresses magnetic diffusion. Comparing the magnetic diffusion term with the convective term, we obtained the ratio below:

$$\frac{|\nabla \times (\eta \nabla \times \mathbf{B})|}{|\nabla \times \mathbf{U} \times \mathbf{B}|} \approx \frac{\eta B}{L^2}\frac{L}{UB} = \frac{\eta}{UL} = \frac{1}{Re_m} \tag{2.55}$$

Where η is the magnetic diffusivity, L being the physical scale for spatial variations and Re_m, the magnetic Reynolds number. The latter is large when the magnetic diffusivity η is small, or equivalently, when the electric conductivity σ is large. For astrophysical plasmas for example, Re_m is in general a very large number due to large spatial scales of the system. Dissipative effects only become important when the gradients in the magnetic field become large like, for example, in current sheath. When $Re_m \gg 1$, the convective term in Eq.2.52 dominates over the diffusion term and the terms containing σ or η can be dropped from Eq.2.13. Going

one step further and neglecting all dissipation terms in Eq.2.51 and Eq.2.53 leads to ideal MHD which is also referred to as the infinite conductivity limite. Thus, by neglecting the displacement current, the resistivity, the diffusivity and the heat conduction, the equations for ideal MHD can be written as follows

$$\frac{\partial \rho}{\partial t} + \nabla \cdot (\rho \mathbf{U}) = 0 \tag{2.56}$$

$$\frac{\partial \rho \mathbf{U}}{\partial t} + \nabla \cdot [\rho \mathbf{U}\mathbf{U} + (p + \frac{B^2}{2\mu_0})\mathbf{I} - \frac{\mathbf{B}\mathbf{B}}{\mu_0}] = 0 \tag{2.57}$$

$$\frac{\partial \mathbf{B}}{\partial t} + \nabla \cdot (\mathbf{U}\mathbf{B} - \mathbf{B}\mathbf{U}) = 0 \tag{2.58}$$

$$\frac{\partial \rho E}{\partial t} + \nabla \cdot [(\rho E + p + \frac{B^2}{2\mu_0})\mathbf{U} - \mathbf{U} \cdot \frac{\mathbf{B}\mathbf{B}}{\mu_0}] = 0 \tag{2.59}$$

2.3 Transport properties

2.3.1 Electrical conductivity

To determine a quantity of current flowing in fully ionized plasma, it is necessary to evaluate it's conductivity. To do that, we have to look at the plasma fluid microscopically. Let us consider the Lorentz force $Q(\mathbf{E} + \mathbf{U} \times \mathbf{B})$, the force ρg due to gravitation and by adopting the macroscopic neutrality of the plasma from sec.2.1.1, the equations of fluid motion of electron and ions fluids can be written as follows (Woods, 2007):

$$\rho_e \frac{d\mathbf{U}_e}{dt} + \nabla \cdot p_e + e n_e (\mathbf{E} + \mathbf{U} \times \mathbf{B}) + \mathbf{R}_e + \rho_e g = 0 \tag{2.60}$$

$$\rho_i \frac{d\mathbf{U}_i}{dt} + \nabla \cdot p_i - e n_e (\mathbf{E} + \mathbf{U} \times \mathbf{B}) - \mathbf{R}_e + \rho_i g = 0 \tag{2.61}$$

where n_e is the electron number density, $\mathbf{R}_e$ and $-\mathbf{R}_e$ are the force density acting on the electron fluid due to collisions with ions and its corresponding on the ions fluid according to Newton's third law. The index e and i denote electron and ion species. Woods (Woods, 2007) defined the collisional time τ_{ei} as the time it take to an electron to be slow down by a sequence of collisions with ions until the ratio of its velocity to the average velocity of the ions is reduced to zero. In a fully ionized plasma, The average density force R_e due to collisions with ions of an electron is given by:

$$\mathbf{R}_e = \frac{n_e m_e}{\tau_e}(\mathbf{U}_e - \mathbf{U}_i) = n_e m_e \nu_e (\mathbf{U}_e - \mathbf{U}_i) \tag{2.62}$$

where τ_e is the resultant collisional time including electron-electron collision and $\nu_e = \frac{1}{\tau_e}$ its corresponding frequency.

By using Eq. 2.3 and divided the two members of Eq.2.62 by en_e, we obtain:

$$\mathbf{J} = (\frac{e^2 n_e}{m_e \nu_e})\frac{\mathbf{R}_e}{e n_e} \tag{2.63}$$

In the absence of magnetic field, the current density is proportional to the electric field represented in Eq.2.63 by $\frac{\mathbf{R}_e}{en_e}$ and the proportional factor is the electrical conductivity σ

$$\sigma = \frac{1}{\eta} = \frac{e^2 n_e}{m_e \nu_e} \tag{2.64}$$

In the case where electrons only collide with charged particles, each of which has a charged state Z, Spitzer (Spitzer and Härm, 1953) proposed:

$$\sigma = \frac{51.6\epsilon_0^2}{e^2 Z}(\frac{\pi}{m_e})^{1/2}\frac{(k_B T)^{3/2}}{ln\Lambda} \tag{2.65}$$

where

$$ln\Lambda = ln[\frac{12\sqrt{2}\pi(k_B\epsilon_0 T)^{\frac{3}{2}}}{q^3 n^{\frac{1}{2}}}] \tag{2.66}$$

is the Coulomb logarithm. In Eq. 2.66 k_B is the Boltzmann constant, q is related to the electron particle charge, and n is the particle density expressed in particles per cubic meter of plasma. In the present work, concerning the calculation of the electrical conductivity of our single fluid and fully ionized plasma, the Spitzer-Härm approximation is used through Eq.2.65 and Eq.2.66 instead of the more general approach illustrated by Eq.2.64.

2.3.2 Dynamic viscosity and thermal conductivity

Fluid properties can be separated in four types, kinematic properties, e.g. velocity, strain rate, acceleration, transport properties, e.g. viscosity, thermal conductivity or mass diffusivity, thermodynamic properties, e.g. pressure, density and temperature, and other miscellaneous properties, e.g. surface tension, vapour pressure or eddy diffusion coefficients (see (White, 1991)). Most of these properties were described in the previous sections. Now a special focus lies on the dynamic viscosity μ in ideal gases due to the fact that in this thesis, the used gas Argon is supposed to be ideal. The dynamic viscosity varies with pressure and temperature, because of its connection to molecular interactions. Most typical gas problems are considered at a low reduced pressure. For these problems it is common to ignore the pressure dependence and model only the temperature dependence. The viscosity increases with temperature in such gases. In the simulations of this thesis, a temperature dependent dynamic viscosity is supposed at an almost atmospheric pressure condition. Besides, the specific heat capacity is assumed to be constant $c_p = const.$ The numerical model is based on the calculation of the specific enthalpy h. The temperature dependence on μ is described by the model of Sutherland as stated in (Sutherland, 1893) which uses an idealised intermolecular-force potential. For ideal gases it yields a relation between the dynamic viscosity μ and the absolute temperature T by:

$$\mu = \mu_{ref}(\frac{T}{T_{ref}})^{3/2}(\frac{T_{ref} + T_s}{T + T_s}) \tag{2.67}$$

with a reference dynamic viscosity μ_{ref} at a related reference temperature T_{ref} and the so-called Sutherland temperature T_s which is dependent on the observed gas. Eq.2.67 is sometimes used in a simplified form:

$$\mu = \frac{C_1 T^{3/2}}{T + T_s} \tag{2.68}$$

with

$$C_1 = \frac{\mu_{ref}}{T_{ref}^{3/2}}(T_{ref} + T_s) \tag{2.69}$$

where C_1 is the so-called Sutherland coefficient which depends also on the gas.

From the dynamic viscosity, the thermal conductivity is calculated from the relation (White, 1991) below:

$$k_{th} = \frac{\mu c_p}{P_r} \tag{2.70}$$

where P_r is the Prandtl number which is a measure for relatives rates diffusion due to viscosity and thermal conductivity and set in this work to 2/3.

2.4 Compressible MHD waves and shocks

For compressible flows, fluid properties are not only transported by the flow, but also by propagation of longitudinal sound waves. It has be shown that for these waves the variations in pressure and in density, associated with the fluid compressions and rarefactions are described by the isentropic equation (Groll, 2015) of thermodynamics:

$$p\rho^{-\gamma} = constant \tag{2.71}$$

By differentiating Eq.2.71, we obtain:

$$dp = \underbrace{\frac{\gamma p}{\rho}}_{a^2} d\rho = 0 \tag{2.72}$$

thus,

$$a = (\frac{\gamma p}{\rho})^{1/2} = (\frac{\gamma kT}{m})^{1/2} \tag{2.73}$$

a is the sound speed where k_B is the Boltzmann's constant.

In a presence of a magnetic field, the situation is most complicated with the introduction of three new waves: The fast, the Alfvén and the slow waves (See (Sterck, Low, and Poedts, 1998; Goebel and Katz, 2008) and references therein for more details). In this section, these three types of waves are described based on the information in (Bittencourt, 2004; Goebel and Katz, 2008). From a equilibrium position, whenever the conducting fluid is slightly disturbed, the magnetic field lines will perform transverse vibrations. The speed of propagation of these transverse vibrations is expected to be given by:

$$v_A = \frac{B_0}{(\mu_0 \rho_0)^{1/2}} \tag{2.74}$$

v_A is known as the Alfvén speed. Here B_0, ρ_0 and μ_0 are the constant magnetic field intensity, the constant fluid density and the magnetic permeability of vacuum respectively under equilibrium conditions. The Alfvén wave is a purely magnetic wave driven by the magnetic tension force that does not propagate perpendicular to the magnetic field lines.
Beside this transversal vibration, there is also a longitudinal wave motion perpendicular to the magnetic field. In addition to the kinetic fluid pressure p, as we shown before in sec.2.1.4 there is also the magnetic pressure $B^2/2\mu_0$· Hence, the overall pressure is $p + B^2/2\mu_0$. Consequently, the speed (v_m) of the magnetosonic waves satisfies the following relation analogous to Eq.2.72,

$$d(p + B^2/2\mu_0) = v_m^2 d\rho \tag{2.75}$$

By using Eq.2.72 and the fact that the magnetic flux and the mass flux are both conserved during the wave motion, we can write

$$v_m^2 = \frac{d}{d\rho}(p + B^2/2\mu_0)_{\rho_0} = a^2 + v_A^2 = \frac{\gamma p}{\rho} + \frac{B_0^2}{\mu_0 \rho_0} \tag{2.76}$$

Considering small-amplitude perturbations of magnetic field, density and velocity, we can deduce the dispersion relation from the equations (2.20,2.27,2.13 and 3.47) (see (Bittencourt, 2004) for more details). The purpose is to obtain the three independent solutions of the dispersion relation corresponding to the three type of waves that can propagate through a fluid flow immersed in a magnetic field: the pure Alfvén wave, the fast and slow MHD waves. Then, the two other waves are the fast and the slow MHD waves and can be expressed as:

$$c_\pm = (\frac{1}{2}[a^2 + v_A^2 \pm \sqrt{(a^2 + v_A^2)^2 - 4a^2 v_A^2 cos\theta^2}])^{\frac{1}{2}} \tag{2.77}$$

where the plus (or minus) sign stands for a fast (or slow) magnetosonic wave and θ the angle between the wave propagation vector and the magnetic field vector. In contrast to the Alfvén wave the associated displacement vector for these waves has a component parallel with the magnetic field line. The all three wave speeds satisfy the following relation (Sterck, Low, and Poedts, 1998),

$$c_- \leq v_A \leq c_+ \tag{2.78}$$

When a finite amplitude disturbance is applied on the steady state undisturbed fluid, MHD discontinuities are to be expected and can lead to the enhancement of the non linear term of the ideal single fluid MHD equation if the disturbance wave amplitude is large enough. Thus, MHD discontinuities can be defined as regions of gas flow where very strong gradient of pressure, temperature and velocity exist. To describe all the MHD discontinuities involved in this process, the Rankine-Hugoniot relations is introduced to rely jumps across the discontinuity with the propagation speed of the discontinuity. In the frame of the moving discontinuity, it derived from the integral of the ideal single fluid MHD equation presented in sec.2.2 including the divergence free constraint (Goedbloed and Lifschitz, 1997; Goedbloed, 2008). According to (Sterck, Low, and Poedts, 1998), we distinguished three categories of MHD discontinuities: Shocks which require mass flow across of

TABLE 2.1: Observed flow regimes in a perturbed MHD flow

Regime	Mathematical expression	Description
1	$c_+ < U$	superfast, super-Alfvénic, and superslow flow
2	$v_A < U < c_+$	subfast but super-Alfvénic and superslow flow
3	$c_- < U < c_+$	subfast and sub-Alfvénic but superslow flow
4	$U < c_-$	subfast, sub-Alfvénic, and subslow flow

the discontinuity and an increase of the entropy scaling as $c_v ln(p/\rho^\gamma)$ (Laney, 1998) where c_v, p, ρ and γ are the specific heat at constant volume, pressure, density and the ratio of specific heats. Contact and tangential discontinuities which require an entropy jump without mass flow through the discontinuity surface and lastly, the rotational discontinuities which allow a mass flow through the discontinuity by conserving the entropy.

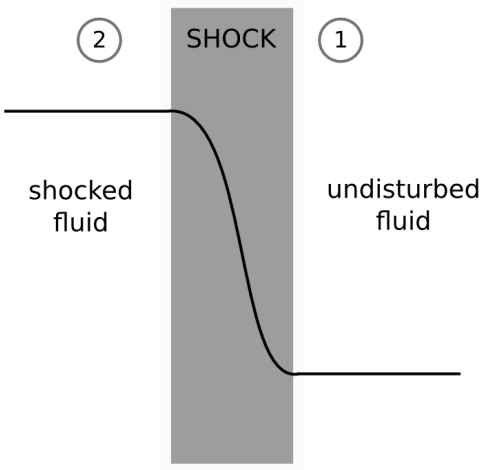

FIGURE 2.4: Shock in an arbitrary continuous medium

Contrary to the classic hydrodynamic case where the only wave speed considered is the speed of sound, the presence of the magnetic field results in a much more complex shock topology. In order of decreasing normal flow velocity U with respect to the various MHD wave speeds (c_+, c_- and v_A), four different flow regimes can occur with the possibility that a pair of those regimes can be connected by a shock. Considering the frame moving with the shock and by assuming the existence of two different regions, the undisturbed fluid region (region 1) and the shocked fluid region (region 2) (see Fig.2.4). As a shock disturbed a stationary fluid in region 1, three MHD shock types can be distinguish (See Tab.2.1). The fast mode shocks in which a discontinuity connects flow in regime 1 with flow in regime 2, the slow mode shocks occurs when the flow switches from regime 3 to regime 4 and all the other possibilities yield a change from a super-Alfvénic to a sub-Alfvénic state and are named intermediate mode shocks. Each type of MHD shocks correspond to

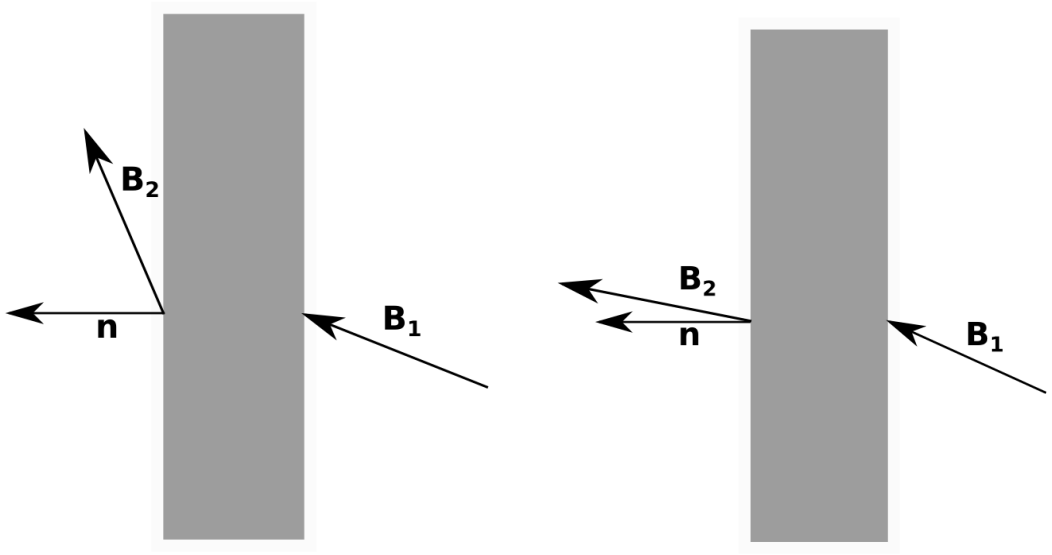

(a) fast shock and fluid rarefaction (b) slow shock and fluid compression

FIGURE 2.5: MHD shock modes

a specific comportment of the magnetic field in the shocked fluid region behind the shock with respect of the shock normal vector. The fast shocks increase the tangential component of the magnetic field (the magnetic field is refracted away from the shock normal vector and the total magnetic field strength increases). There is fluid rarefaction with the lowest density. The slow shocks decrease the tangential component of the magnetic field (the magnetic field is refracted toward the shock normal and the total magnetic field strength decreases). There is fluid compression or densification (see Fig.2.5).

2.5 Summary

In conclusion, the physical model and the corresponding governing equations that describe the plasma flow were discussed in this chapter. The plasma is treated as a neutral single fully ionized gas with macroscopic MHD equations. Hall effect and turbulence effect are neglected. The set of MHD equations, comprising the conservation laws relations for mass, momentum, energy and magnetic field were described. A brief introduction of the MHD characteristic waves and shocks was given in this chapter because of their importance in the simulations results of Chap.4. The techniques for obtaining a numerical solution of these governing equations will be presented in the following chapter.

Chapter 3

Proposed density-based numerical method for MHD flow

From the computational efforts mentioned in sec.1.4, several MHD codes had been developed but most of them remained complex black boxes or are commercialized. Our main purpose in this work is to proposed an alternative to these solvers by making in the present thesis the first statement of the development of an accurate, robust and also easier to use MHD code. MHD code is all about coupling the gas dynamic equations and the Maxwell equations. For that we used the same coupling philosophy as the modified AUSM-MHD scheme of Xisto (Xisto, Pascoa, and Oliviera, 2014), but here we decided to make use of the central-upwind schemes of Kurganov (Kurganov, Noelle, and Petrova, 2001; Kurganov and Tadmor, 2000), which are density based methods. The contribution of this work is essentially the consideration of the magnetic effects in the algorithm proposed by Greenshields (Greenshields et al., 2010). Particularly, we propose a multidimensional consistent treatment algorithm of the Navier-Stokes and Maxwell equations in the conservative formulation. We make use of the *OpenFOAM*® package (*OpenFOAM version 2.3.0*) as a developer tool for the new MHD code. The proposed density-based method will be described in the present chapter. First, we introduced some fundamental concepts regarding the finite volume method. Then the central-upwind method for the solution of flux transport of the MHD equations will be described. After that, the divergence cleaning method we used to overcome the non-zero $\nabla \cdot \mathbf{B}$ is introduced following by the used discretization schemas of gradient and laplacian terms. This section is ended by a short review of the the CFL (Courant-Friedrichs-Lewy) condition.

3.1 Finite volume method

The following explanation are based on (Ferziger and Peric, 2002; Moukalled, Mangani, and Darwish, 2016). Usually, equations in physics are written as a set of partial differential equations (PDE) such as the Maxwell equations to describe the electromagnetic field or the hydrodynamic equations to describe the flow of a fluid (see equations 2.20, 2.27, 2.13 and 2.41 in Chap.2). They are a complicated system of non-linear equations. Only in some cases, analytical solutions can be found, and therefore, another approach has to be used to find a solution of the problem. Computational Magneto-Fluid dynamics (CMFD) unifies the methods and the techniques for obtaining an approximation of the solution of the MHD equations in a numerical manner. The solution can only be an approximation of

the real solution, since it only depends on a finite number of parameters, while the true solution depends on an infinite number of parameters, namely the function value at every point in space. In the case of the present work, solutions of PDEs containing shocks take a central place, and so it is appropriate to work with the conservative form of the equations. As presented in Chap.2, the conservation equation for a general scalar variable ϕ can be express as:

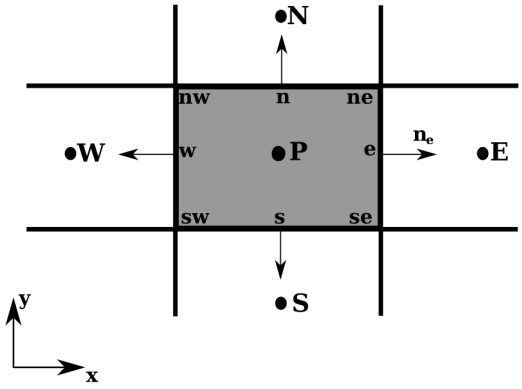

(a) 2D

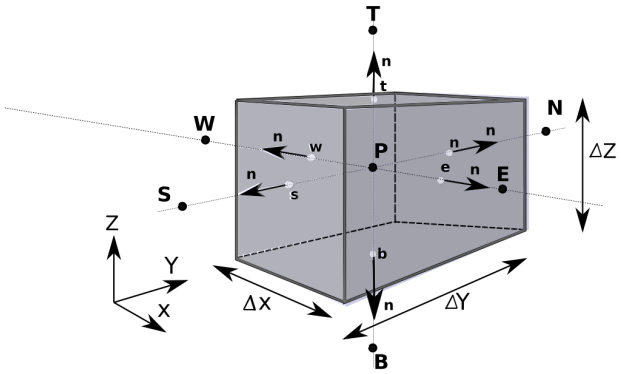

(b) 3D

FIGURE 3.1: Control volume (CV) schema in 2D (a) and 3D (b) in accordance with (Ferziger and Peric, 2002)

$$\underbrace{\frac{\partial(\rho\phi)}{\partial t}}_{\text{transient term}} + \underbrace{\nabla\cdot(\rho\mathbf{U}\phi)}_{\text{convective term}} = \underbrace{\nabla\cdot(\Gamma^{\phi}\nabla\phi)}_{\text{diffusion term}} + \underbrace{Q^{\phi}}_{\text{source term}} \tag{3.1}$$

With ρ the density, $\mathbf{U}$ the velocity, Q the source or sink term and Γ^{ϕ} the term of diffusivity. By tacking the steady-state form of the above equation, we obtain:

$$\nabla\cdot(\rho\mathbf{U}\phi) = \nabla\cdot(\Gamma^{\phi}\nabla\phi) + Q^{\phi} \tag{3.2}$$

An conservative discretization of the governing equations is obtained naturally from a Finite-Volume (FV) formulation. Contrary to finite difference methods where one directly discretizes the differential operations of the PDE, integral approximation is used. This integral form has the advantage to take into account

both continuous and discontinuous solutions, ensures the conservation of physical properties such as mass, momentum or energy, which are called conservative variables and constitutes the starting point of a FV method. In a FV approach, the method of flux balances is used to obtain information about the average flow variables in each control volumes which cover the domain of interest. Thus, by integrating the above equation over the volume control (CV) of Fig.3.1, we can rewrite Eq.3.2 as follows

$$\int_{V_c} \nabla \cdot (\rho \mathbf{U} \phi) dV = \int_{V_c} \nabla \cdot (\Gamma^{\phi} \nabla \phi) dV + \int_{V_c} Q^{\phi} dV \tag{3.3}$$

By using the divergence theorem, the volume integrals of convection and diffusion terms are replaced by the surface integrals. Eq.3.3 becomes

$$\int_{\partial V_c} (\rho \mathbf{U} \phi) d\mathbf{S} = \int_{\partial V_c} (\Gamma^{\phi} \nabla \phi) d\mathbf{S} + \int_{V_c} Q^{\phi} dV \tag{3.4}$$

where **bold** letters indicate vectors, $(\cdot)$ is the dot product, Q^{ϕ} represents the source term, $\mathbf{S}$ the surface vector, $\mathbf{U}$ the velocity vector, ϕ the conserved quantity, and $\int_{\partial V_c}$ the surface integral over the volume V_c.

By assuming a continuously distribution of the variables over the surfaces, Eq.3.4 is transformed as the sum of particular flows through each face S_f

$$\sum_f (\rho \phi_f) \cdot (\mathbf{U}_f \cdot \mathbf{S}_f) = \sum_f ((\Gamma_f)^{\phi} \cdot (\nabla \phi)_f \cdot \mathbf{S}_f) + \int_{V_c} Q^{\phi} dV \tag{3.5}$$

where the summand f stands for the number of the individual faces $\mathbf{S}_f$ of the entire boundary surface ∂V_c. In Eq.3.5 the surface fluxes are evaluated at the faces of the CV boundaries rather than integrated within it. Here, P denoted the node in the middle of the CV. N and S denoted the points which are located in the y-axis direction representing the north and the south direction in relation to the CV position. Analogicaly, the point W and E denoted the points which are located in the x-axis direction representing the west and the east direction in relation to the CV position. In three dimensional case, the points T and B located in z-axis direction denoted the top and the bottom of the CV respectively. n , e, s and w are the boundary faces of the CV around P. In two dimensional case, these points would indicate the edges of the particular face. The velocity $\mathbf{U}_f$ is always normal to the surface $\mathbf{S}_f$.

The surface and volume integral can be approximated by interpolation of variable values either in the midpoint P or one or more extra locations at the cell faces. Three methods are very common for this interpolation: the Midpoint rule, the Trapezoid rule and Simpson's rule (See (Ferziger and Peric, 2002) for more details). All methods are based on the same principle, but are of different order, due to the utilised numbers of points in which the surface integral is approximated. At this point only the Midpoint rule is presented for a two dimensional example. The Midpoint rule is defined by

$$F_e = \sum_{S_e} f dS \approx f_e S_e \tag{3.6}$$

The integral is approximated by the value of f at the cell face's centre and the entire cell face area. This method is an interpolation of second order and needs the

value of the integrand f at the position e. Furthermore, an interpolation for the volume integral has be found. To approximate the volume integral in the easiest way, one takes the product of the mean value and CV volume

$$Q_p = \int_V q dV = \bar{q}\Delta V \approx q_p \Delta V \tag{3.7}$$

where q_p is the value at the centre. This method is of second order and no interpolation is needed, because in the CV's centre point P all variables are known. For an interpolation of a higher order, the values of q are required at more positions as solely in the centre. Therefore, nodal values have to be interpolated. Some appropriate interpolation methods will be presented in the following section. Another method for the approximation of the volume integral is the Gaussian integration, which uses besides the estimated values at the grid nodes also the so-called weight coefficients. For the interval $[-1, 1]$, the integral is formulated in (Liu and Quek, 2013) by

$$F = \int_{-1}^{1} f(\xi) d\xi = \sum_{j=1}^{m} \omega_j f(\xi_j) \tag{3.8}$$

The interval $[-1, 1]$ can be transformed to any arbitrary one with help of a linear transformation. The node ξ_j and the weight coefficient ω_j should be chosen in a way, that Eq.3.8 produces an exact result of a possible high order polynomial. Note that a higher number of nodes does not assure a higher accuracy of the obtained results in any case. But a higher number of nodes will increase the computational effort in any case. The exact number of nodes is dependent on the integrand. An overview of different possible nodes and weight coefficient as well as further information is given in (Moukalled, Mangani, and Darwish, 2016).

3.1.1 Interpolation schemes

As mentioned in the previous section, the approximation of the surface and volume integrals of the CV requires the variable values at locations other than the cell midpoint P. Therefore, these values have to be interpolated by known nodal values. In this section, diverse possibilities for such an interpolation scheme are demonstrated. The listed schemes are explained with help of cell face e for a value ϕ and its derivatives. This values are needed to estimate the convective $F_c = \rho\phi\mathbf{U} \cdot \mathbf{S}$ and diffusive flux $F_d = \Gamma\nabla\phi \cdot \mathbf{S}$ through the CV's surface. Here, the used interpolation method is obligated to be of the same order as the chosen integral approximation to receive the same accuracy. The following explanation are based on the information in (Ferziger and Peric, 2002; Schaefer, 2006).

Central Differencing Scheme (CDS)

For the central diferencing schemes (CDS), ϕ_e is interpolated as the weighted average of both nearest nodes E and P according to Fig.3.2

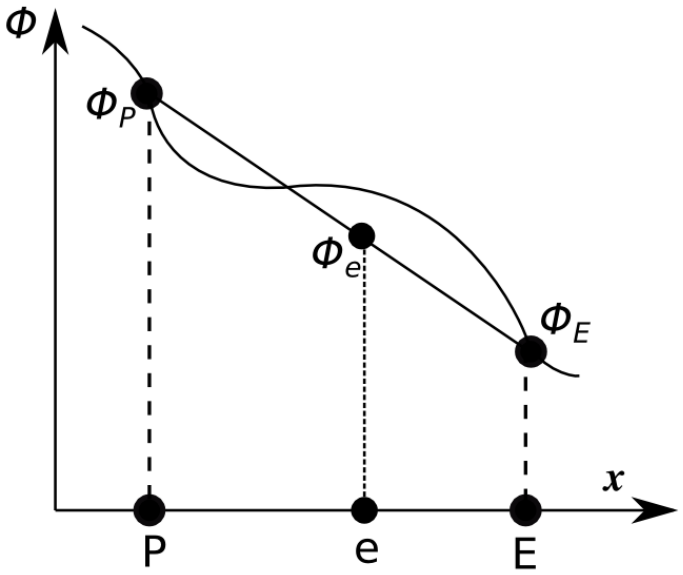

FIGURE 3.2: Approximation of ϕ_e with CDS method according to (Schaefer, 2006)

$$\phi_e = \lambda_e \phi_E + (1 - \lambda_e)\phi_P \tag{3.9}$$

where λ_e is the linear interpolation factor which represents the distance between the neighboured points by

$$\lambda_e = \frac{x_e - x_P}{x_E - x_P} \tag{3.10}$$

A Taylor series expansion of ϕ_e around P shows that the scheme is of second order

$$\phi_e = \lambda_e \phi_E + (1 - \lambda_e)\phi_P - \frac{(x_e - x_P)(x_E - x_P)}{2}(\nabla^2 \phi)_P + \mathcal{O}(h^3) \tag{3.11}$$

By considering a linear approximation between the nodes P and E, the gradient is approximated by

$$(\nabla \phi)_e \approx \frac{\phi_E - \phi_P}{x_E - x_P} \tag{3.12}$$

By using Taylor series expansion around ϕ_e, the truncation error leads to the following relation

$$\epsilon_\tau = \frac{(x_e - x_P)^2 - (x_E - x_e)^2}{2(x_E - x_P)}(\nabla^2 \phi)_e - \frac{(x_e - x_P)^3 - (x_E - x_e)^3}{6(x_E - x_P)}(\nabla^3 \phi)_e + \mathcal{O}(h^3) \tag{3.13}$$

Which shows that the leading error term depend quadratically on the grid spacing. In fact, the second order of the method is obtained when e is located in the middle of the interval $[P, E]$ which make the leading error term be proportionnal to

$(\Delta x)^2$. For a irregular grid spacing, the leading error term become proportionnal to (Δx) and a potential grid expansion. The use of central differencing approximations may conduct to unphysical oscillations which affect the solution. Most particularly by coupling this interpolation technique with staggered grid scheme leads to not accurate resolution when small time steps are enforced by stability requirements (Kurganov, Noelle, and Petrova, 2001). Therefore, to overcome this issue, one often uses the so-called upwind approximations, which are not or less sensitive to this problem. The basic principle of these methods is to make the interpolation dependent of the direction of the velocity vector by taking advantage of the transport property of convection processes. The following subsection present the upwind techniques.

Upwind Differencing Scheme (UDS)

Beside the CDS, there is another approximation for the value at CV face centre e namely the upwind interpolation. This interpolation method is formulated according to Fig.3.3.

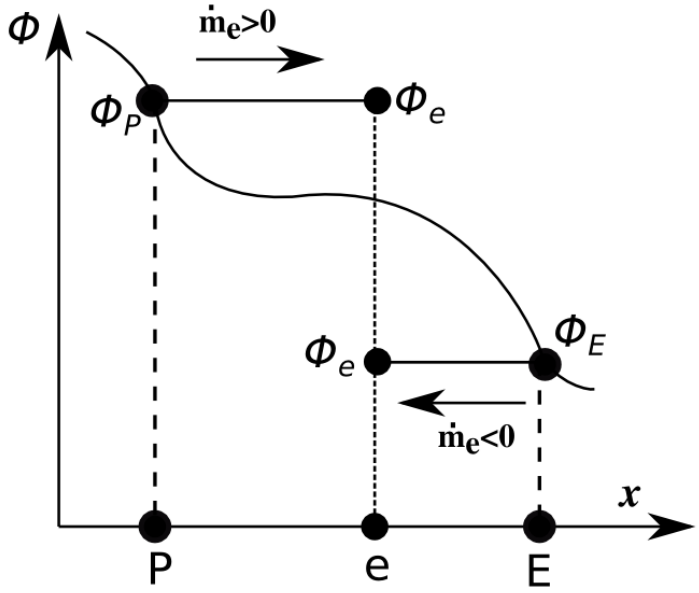

FIGURE 3.3: Mass flux dependent approximation of ϕ_e with UDS method according to (Schaefer, 2006)

The value of ϕ_e is interpolated between two nodes P and E at the boarder of face e depending on the direction of the mass flux. ϕ_e is assumed as the value of the point which is located upstream or upwind to the boarder e. This interpolation equals the backward differencing scheme (BDS), respectively forward differencing scheme (FDS), in Finite difference methods (Ferziger and Peric, 2002; Moukalled,

Mangani, and Darwish, 2016), as illustrated in Fig.3.3. Hence, the direction of the flux is essential for the definition of ϕ_e

$$\phi_e = \begin{cases} \phi_P & \text{if } \dot{m}_e > 0, \\ \phi_E & \text{if } \dot{m}_e < 0. \end{cases} \tag{3.14}$$

The Taylor series expansion around P is given as follows:

$$\phi_e = \phi_P + (x_e - x_P)(\nabla\phi)_P + \frac{(x_e - x_P)^2}{2}(\nabla^2\phi)_P + \mathcal{O}(h^3) \tag{3.15}$$

The UDS approximation retains only the first term on the right-hand side of Eq.3.15, so it is a first-order scheme. The arising truncation error is then

$$f_e^{diff} = \Gamma_e(\nabla\phi)_e \tag{3.16}$$

This error term produces a false diffusive flux in the direction normal to the flow. This flux can influence the numerical results in this way that peaks or rapid variations in the variables will be smooth out. It can be expressed by

$$\Gamma = \Gamma_e^{real} + \Gamma_e^{num} \tag{3.17}$$

where, $\Gamma_e^{num} = (\rho\phi)_e\Delta x/2$. This produced numerical diffusion can be even intensified in multidimensional problems. If the transport direction is nearly perpendicular to the CV face, one obtains a relatively good approximation of the convective fluxes with the UDS method ($(\frac{\partial\phi}{\partial x})_P \sim 0$). Otherwise the approximation can be quite inaccurate and for large velocities (large fluxes) and as the scheme is only of first order, a very fine grid resolution ($(x_e - x_P) \sim 0$) are required to reach a high accurate solutions.

Others interpolation schemes

Beside these aforementioned interpolation schemes, there are other schemes with at less the same accuracy than CDS and UDS. An upwind approximation frequently employed is the quadratic upwind interpolation, which is well known as the QUICK method (Quadratic Upwind Interpolation for Convective Kinematics). In contrary with the UDS, QUICK estimates the border value ϕ_e by constructing a parabola through ϕ_P, ϕ_E and at a third nodal point ϕ_W or ϕ_{EE} that is located upstream (W or EE) depending of the flow direction. If a uniform grid is used, the evaluation of ϕ_e conduct to

$$\phi_e = \begin{cases} \frac{6}{8}\phi_P + \frac{3}{8}\phi_E - \frac{1}{8}\phi_W & \text{if } \dot{m}_e > 0, \\ \frac{3}{8}\phi_P + \frac{6}{8}\phi_E - \frac{1}{8}\phi_{EE} & \text{if } \dot{m}_e < 0. \end{cases} \tag{3.18}$$

In this case, the QUICK method possesses an interpolation error of third order. It is somewhat more accurate than the CDS but also computational more expensive. In the other hand, the UDS can be expanded to a second order method by considering two upstream data points. The resulting linear upwind differencing scheme (LUDS) corrects the UDS estimation of ϕ_P (for $\dot{m}_e > 0$) with an upwind biased gradient $\frac{\phi_P - \phi_W}{x_P - x_W}$ multiplied by $x_e - x_P$, the distance between the node P and the

east face. Thus, for a equidistant grids $x_P - x_W = \Delta x$ and $x_e - x_P = \frac{1}{2}\Delta x$, the LUDS technique conducts to

$$\phi_e = \begin{cases} \phi_P + \frac{1}{2}(\phi_P - \phi_W) & \text{if } \dot{m}_e > 0, \\ \phi_E + \frac{1}{2}(\phi_E - \phi_{EE}) & \text{if } \dot{m}_e < 0. \end{cases} \tag{3.19}$$

It is also possible to mix different approximations for the convective flux. In the purpose to combine the advantages of an accurate approximation of a higher order scheme with the better robustness and boundedness properties of a lower order schemes (mostly the UDS method). For example, one could use CDS, but switch to UDS in the case where CDS would produce an oscillatory solution. One could also use hybrid schemes to reduce computational cost by moving to higher order schemes only when required.
Such schemes, classified as linear schemes (Waterson and Deconinck, 2007) are stable but remain weak whenever unphysical spatial oscillations occur. In fact, the Godunov's theorem (Roe, 1986) predicted this limitation by stating that, all these schemes are constrained to remain spatially first-order schemes to preserve their monotonicity. The solution of this issue was found to be the use of non linear approximation schemes. These non-linear schemes can be constructed by using flux limiters which are functions that define the convection scheme based on a ratio of local gradients in the solution. The concept is to limit the flux of conserved variable into a CV to a level that will not produce a local maximun or minimun of the profile of that variable in the correspondant CV.

3.1.2 Flux limiter functions

For the seek of accurate solution, it is important to have a stable scheme that does not produce oscillatory solutions in regions with strong gradients. This can be achieved by using a scheme that guarantees bounded behaviour of the solution, like monotonicity preserving schemes. Such kind of schemes assure that a monotone mesh function at time step n will be kept monotone at time level $n+1$. In a monotonicity preserving scheme, the values of local maxima are non-increasing in time, while the values of local minima are non-decreasing. In that case the scheme is monotone, it is also monotonicity preserving. However, this condition of monotonicity might be too strong since monotone schemes can only be first order accurate. Harten (Schaefer, 2006) introduced the concept of Total Variation Diminishing (TVD) schemes which can be defined for a mesh function u as

$$TV(u^n) = \sum_{-\infty}^{\infty} |u_{i+1}^n - u_i^n| \tag{3.20}$$

In the case that for all mesh functions u of bounded TV, we have:

$$TV(u^{n+1}) \leq TV(u^n) \tag{3.21}$$

the scheme is called TVD. Harten (Schaefer, 2006) proved that any monotone scheme for a one-dimensional scalar conservation law is TVD, and that a TVD scheme is monotonicity preserving. Hence, when we consider the Godunov's theorem (Roe, 1986), only non-linear schemes can be higher-order and TVD. Thus, by expressing the higher-order correction of the interpolation schemes listed below

as a general weighted average of the centred and upwind gradients in the solution (Waterson and Deconinck, 2007), we have:

$$\phi_e = \phi_P + \frac{(x_e - x_u)}{2} B[(\frac{\partial \phi}{\partial x})_f, (\frac{\partial \phi}{\partial x})_u] \tag{3.22}$$

with $(\frac{\partial \phi}{\partial x})_f = \frac{\phi_E - \phi_P}{x_E - x_P}$ and $(\frac{\partial \phi}{\partial x})_u = \frac{\phi_P - \phi_W}{x_P - x_W}$. $B(p,q)$ is a non-linear averaging function that yields to higher-order accuracy where required while retaining the boundedness of the scheme. $B(p,q)$ is a homogeneous function and then Eq.3.22 can be reformulated as:

$$\phi_e = \phi_P + \frac{(x_e - x_u)}{2} \beta(r)(\frac{\partial \phi}{\partial x})_u) \tag{3.23}$$

where $\beta(r) = B(r,1)$ is a limiter function and r, the gradient ratio defined as:

$$r = \frac{(\frac{\partial \phi}{\partial x})_f}{(\frac{\partial \phi}{\partial x})_u} \tag{3.24}$$

In a case of uniform grid, r can be rewritten as follows:

$$r = \frac{\phi_E - \phi_P}{x_E - x_P} \tag{3.25}$$

A limiter function $\beta(r) = r$ returns a second-order central scheme, while $\beta(r) = 1$ represents a second-order linear-upwind interpolation scheme (LUDS). In order to ensure boundedness, the limiter function has to satisfy certain properties which are (Waterson and Deconinck, 2007):

$$\begin{cases} \beta(r) \geq 0 & \text{for all r,} \\ \beta(r) = 0 & \text{if } r \leq 0, \end{cases} \tag{3.26}$$

The conditions listed above guarantee that the limiter function achieve fully bounded behaviour in the solution without comprimising the accuracy by the best linear schemes. A review of the best and the most used limiter functions can be found in Chapter 13 of (Toro, 2009) and also in (Waterson and Deconinck, 2007). The limiter functions used in this work are presented in the next section.

3.2 Discretization of convective terms: The central and central-Upwind schemes

Concerning the approximation of the surface and volume integrals, as we mentioned in Sec.1.5.1 of Chapter.1, in this thesis we make used of the central-upwind schemes which have central schemes properties because the evolution step over time employs intergration over Riemann fans and does not require a Riemann solver and a characteristic decomposition. They have also an upwind nature, because the width of the Riemann fans are estimated by using one side information (See Kurganov (Kurganov, Noelle, and Petrova, 2001; Kurganov and Tadmor, 2000)). In the present section, the description of the central-upwind schemes is based on (Greenshields et al., 2010). Thus, considering a three-dimensional flow,

the ideal form of the system of equations (2.20, 2.27, 2.13 and 2.41) can be written in the following conservative form in Cartesian coordinate system:

$$\frac{\partial \mathbf{W}}{\partial t} + \frac{\partial \mathbf{F}_x}{\partial x} + \frac{\partial \mathbf{F}_y}{\partial y} + \frac{\partial \mathbf{F}_z}{\partial z} = 0 \tag{3.27}$$

$$\mathbf{W} = \begin{pmatrix} \rho \\ \rho U_x \\ \rho U_y \\ \rho U_z \\ B_x \\ B_y \\ B_z \\ \rho E \end{pmatrix}, \; F_x = \begin{pmatrix} \rho U_x \\ \rho U_x^2 + P_{over} - \frac{1}{\mu_0} B_x^2 \\ \rho U_x U_y - \frac{1}{\mu_0} B_x B_y \\ \rho U_x U_z - \frac{1}{\mu_0} B_x B_z \\ 0 \\ B_y U_x - B_x U_y \\ B_z U_x - B_x U_z \\ (\rho E + P_G) U_x - B_x (B_x U_x - B_y U_y + B_z U_z) \end{pmatrix}$$

with F_y and F_z obtained by properly permuting indices. The overall pressure and total energy are given by:

$$P_{over} = \; p + \frac{1}{2\mu_0}(B_x^2 + B_y^2 + B_z^2) \tag{3.28}$$

$$E = \frac{1}{2}(U_x^2 + U_y^2 + U_z^2) + c_v T + \frac{1}{2\rho\mu_0}(B_x^2 + B_y^2 + B_z^2) \tag{3.29}$$

The discretisation for convective terms in the equation system (3.27) of a general tensor field $\mathbf{W} = (\rho, \rho\mathbf{U}, \mathbf{B}, \rho E)$ is as follows:

$$\int_V \nabla \cdot [\mathbf{UW}] dV = \int_S \mathbf{dS} \cdot [\mathbf{UW}] \approx \sum_f \mathbf{S}_f \cdot \mathbf{U}_f \mathbf{W}_f = \sum_f \phi_f \mathbf{W}_f \tag{3.30}$$

where Σ_f is a summation over cell faces and $\phi_{f,\pm} = \mathbf{S}_{f,\pm} \cdot \mathbf{U}_{f,\pm}$ the volumetric flux. When the fluxes at boundaries are known, the cell averaged quantities $\bar{W}$ can be updated after applying a time marching method. Since FV methods consist of the set of average cell values, there is no direct information about the values of the flow variables at the cell faces. In order to evaluate the fluxes $\overrightarrow{\mathbf{F}}(W)$, the vector of flow variables $\mathbf{W}$ can be represented in the cell by some piecewise approximation. This is what is called the reconstruction. Each cell has a different piecewise approximation of $\mathbf{W}$. when the reconstructed values of $\mathbf{W}$ are used to evaluate $\overrightarrow{\mathbf{F}}(W)$ at the cell faces, they produce different approximations of the flux at the boundary between two control volumes, thus, the flux is discontinuous at the boundary. Therefore, some interpolation formula, also named numerical flux function, must be used to evaluate the fluxes across the cell faces. There exists different schemes, most of them had been developed for the purpose of solving problems in fluid dynamics (see (Leveque, 2002) and references therein for more details). However, it is not evident to extend the numerical schemes used in hydrodynamics to MHD, since the MHD equations are so far more complex. The numerical schemes must be able to capture all different and highly anisotropic MHD wave modes. Another difficulty with CMFD is that Gauss's law for the magnetic field has to be satisfied everywhere at all times. The presence of non-zero $\nabla \cdot \mathbf{B}$ might introduce an erroneous force into the momentum equation, causing

the scheme to converge to an non-physical solution of the equations or even to blow up the computation. Therefore, it is necessary to have a stable and robust scheme including a divergence cleaning method (see sec.3.4). *OpenFOAM*® uses a finite volume discretization scheme that solves the equations in a segregated approach, meaning that for the system of equations governing our problem of interest, separate matrix equations are created for each one, and are solved within an iterative sequence. We assumed that each face has an owner cell and neighbour cell. The face area vector $\mathbf{S}_f$ is a vector normal to the face surface pointing out of the owner cell, whose magnitude is that of the area of the face, as shown in Fig. 3.4.

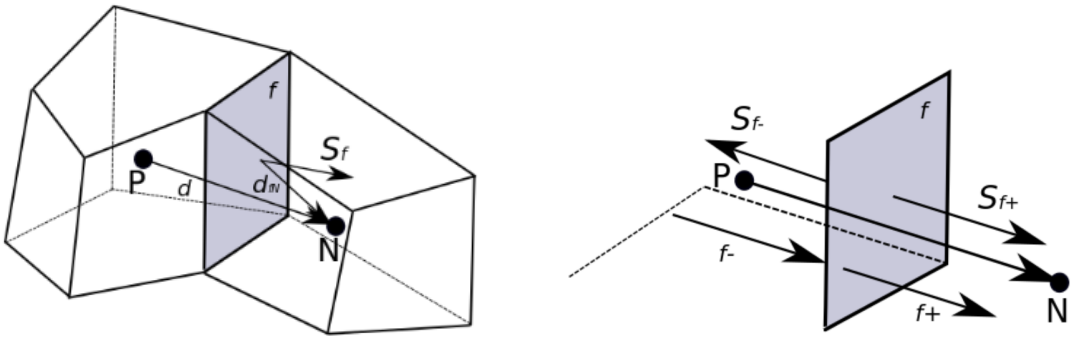

(a) Finite volume discretization schema (b) Greenshields interpolation schema

FIGURE 3.4: Finite volume discretization and the Greenshields interpolation schemas in accordance with (Greenshields et al., 2010)

The linear interpolation of $\mathbf{W}_f$ is evaluated using the weighting coefficient w_f regarding to Fig. 1a:

$$W_f = w_f W_P + (1 - w_f) W_N \tag{3.31}$$

Here, w_f is defined by:

$$w_f = |\mathbf{S}_f \cdot \mathbf{d}_{fN}| / |\mathbf{S}_f \cdot \mathbf{d}| \tag{3.32}$$

Greenshields makes use of the KT (Kurganov and Tadmor) (Kurganov and Tadmor, 2000) and KNP (Kurganov, Noelle and Petrova) methods (Kurganov, Noelle, and Petrova, 2001) in their original form for multidimensional systems using the so-called 'dimension-by-dimension' reconstruction. The interpolation procedure is split in two directions corresponding to flow outward and inward of the face owner cell. Greenshields denote these directions f_+, coinciding with the directions $+S_f$, and f_-, coinciding with $-S_f$ (See Fig. 1b). Thus, the previously discretization (Eq. 3.30) can be written as:

$$\sum_f \phi_f W_f = \sum_f [\alpha(\phi_{f+} W_{f+} + \kappa_{f+}) + (1 - \alpha)(\phi_{f-} W_{f-} + \kappa_{f-}) + \varpi_f (W_{f-} - W_{f+}) + \frac{1}{2}(\Phi_- + \Phi_+)] \tag{3.33}$$

The first two terms on the right-hand side of Eq. 3.33 are flux evaluations in the f_+ and f_- directions, respectively. The third term is only required in cases where the convection term is part of a substantive derivative (2.20, 2.27 and 2.41). This additional diffusion term uses a volumetric flux ϖ_f based on the maximum speed of propagation of any discontinuity that may exist at the face between values interpolated in the f_+ and f_- directions. The fourth term is employed for the treatment of the magnetic stress tensor and for the coupling of the potential scalar variable ψ with the induction equation. This term will be discussed in more details in sec.3.4. All these terms except the fourth term can be presented as follows:

$$\mathbf{W}_f = \begin{pmatrix} \rho \\ \rho U_x \\ \rho U_y \\ \rho U_z \\ B_x \\ B_y \\ B_z \\ \rho E + P_{over} \end{pmatrix}, \kappa_f = \begin{pmatrix} 0 \\ S_x P_{over} \\ S_y P_{over} \\ S_z P_{over} \\ -b_f U_x \\ -b_f U_y \\ -b_f U_z \\ -b_f(\mathbf{U} \cdot \mathbf{B}) \end{pmatrix}, \varpi_f = \begin{pmatrix} 0 \\ \omega_f \\ \omega_f \\ \omega_f \\ 0 \\ 0 \\ 0 \\ \omega_f \end{pmatrix}$$

where $b_f = \frac{(B_{f-}+B_{f+})}{2}$ with $B_f = S_x B_x + S_y B_y + S_z B_z$, with S_x, S_y and S_z being the cell face area components.
Regarding the evaluation of α and ϖ_f, the f_+ and f_- contributions are weighted equally so that the weighting coefficient is $\alpha = 0.5$ (Central scheme) for the KT method. The KNP method calculated α based on the one-sided local speeds of propagation (Central upwind). The volumetric fluxes associated with the local speeds of propagation can be calculated as follows:

$$\Psi_{f+} = max(c_f|S_f| + \phi_{f+}, c_f|S_f| + \phi_{f-}, 0) \tag{3.34}$$

$$\Psi_{f-} = min(c_f|S_f| - \phi_{f+}, c_f|S_f| - \phi_{f-}, 0) \tag{3.35}$$

The convective fluxes are then calculated using the appropriate characteristic speed $u \pm c$. Xisto et al.(Xisto, Pascoa, and Oliviera, 2013) employed the common fast magnetosonic speed at a control volume face which is given by:

$$c_f = min(c_+, c_-) \tag{3.36}$$

where $c_\pm$ is obtained from Eq.2.77 by using Eq.2.74,

$$c_\pm = (\frac{1}{2}[a_\pm^2 + \frac{B_\pm^2}{\mu_0 \rho_\pm} + \sqrt{(a_\pm^2 + \frac{B_\pm^2}{\mu_0 \rho_\pm})^2 - 4a_\pm^2 \frac{B_{n,\pm}^2}{\mu_0 \rho_\pm}}])^{\frac{1}{2}} \tag{3.37}$$

where $a_\pm$ are the outward and the inward states for the speed of sound and $B_n = S_f \cdot B$ is the component of magnetic field normal to the cell face.
The weighting factor is:

$$\alpha = \begin{cases} \frac{1}{2} & \text{for the KT method} \\ \frac{\Psi_{f+}}{\Psi_{f+}+\Psi_{f-}} & \text{for the KNP method} \end{cases} \tag{3.38}$$

TABLE 3.1: Limiter definition

Limiter	Limiter functions
Minmod	$max[0, min(1, r)]$
Van Leer	$\frac{r+\|\mathbf{r}\|}{1+r}$
Van Albada	$\frac{r+\|\mathbf{r}^2\|}{1+r}$
MUSCL	$max[0, min(2r, \frac{r+1}{2}, 2)]$
SuperBee	$max[0, min(2r, 1), min(r, 2)]$

the diffusive volumetric flux is calculated according to:

$$\omega_f = \begin{cases} \alpha max(\Psi_{f+}, \Psi_{f-}) & \text{for the KT method} \\ \alpha(1-\alpha)(\Psi_{f+} + \Psi_{f-}) & \text{for the KNP method} \end{cases} \tag{3.39}$$

In this work, we use limiters that are available in *OpenFOAM*®, such as Minmod, VanLeer, Vanalbada that are total variation diminishing (TVD) in order to switch between low and higher-order schemes (See (Greenshields et al., 2010) and the references therein for more details). The time derivative terms are discretized by a simple Euler scheme. The above extended flux calculation schemes are renamed as KNP-MHD and KT-MHD (Greenshields et al., 2010; Kurganov, Noelle, and Petrova, 2001) as they are now able to deal with ideal magnetohydrodynamics equations. For switching between the low and high-order schemes, a flux limiter function $\beta(r)$ is introduced in the interpolation procedure where r represents the ratio of successive gradients of the interpolated variable that is constrained to $r \geq 0$. Greenshields (Greenshields et al., 2010) defines r on polyhedral mesh for the f_+ direction as follows:

$$r = 2\frac{\mathbf{d} \cdot (\nabla \mathbf{W})_P}{(\nabla_d \mathbf{W})_f} - 1 \tag{3.40}$$

where $\mathbf{W}$ is a scalar field, $(\nabla \mathbf{W})_p$, the full gradient determined at the owner cell P by linear interpolation and $(\nabla_d \mathbf{W})_f = \mathbf{W}_N - \mathbf{W}_P$ is the gradient component normal to the face, scaled by $|\mathbf{d}|$. Some of the limiter functions are given on the Table.3.1. Then, the f_+ interpolation of $\mathbf{W}$, for example, is simply evaluated as

$$\mathbf{W}_{f+} = (1 - g_{f+})\mathbf{W}_P - g_{f+}\mathbf{W}_N \tag{3.41}$$

where $g_{f+} = \beta(1 - w_f)$ and w_f is the weighting coefficient of Eq.3.32.

3.3 Discretization of gradient and laplacian terms

All the gradient terms of the governing equation which also including ∇p are integrated over the CV and discretized as follows:

$$\int_V \nabla \mathbf{W} dV = \int_S d\mathbf{S}\mathbf{W} \approx \sum_f \mathbf{S}_f \mathbf{W}_f \tag{3.42}$$

The Kurganov schemes (Kurganov and Tadmor, 2000; Kurganov, Noelle, and Petrova, 2001) separate the interpolation procedure into f_+ and f_- directions according to:

$$\sum_f \mathbf{S}_f \mathbf{W}_f = \sum_f [\alpha \mathbf{S}_f \mathbf{W}_{f+} + (1-\alpha)\mathbf{S}_f \mathbf{W}_{f-}] \tag{3.43}$$

There are also usage of same limiter as mentioned in the Table.3.1 for f_+ and f_- interpolation. Laplacian terms are discretized initially with the diffusion coefficient Γ for the polyhedral meshes as follows:

$$\int_V \nabla \cdot (\Gamma \nabla \mathbf{W}) dV = \int_S d\mathbf{S}(\Gamma \mathbf{W}) \approx \sum_f \Gamma_f \mathbf{S}_f \cdot (\nabla \mathbf{W}_f) \tag{3.44}$$

Diffusion coefficient Γ_f in the face f is determined by linear interpolation from the value of the cell centroid. When vector $\mathbf{S}_f$ and vector $\mathbf{b}$ (see Fig.3.4.a) are not parallel to each other and the face f is an orthogonal face. In case of a non-orthogonal face the term $\mathbf{S}_f \cdot (\nabla \mathbf{W}_f)$ is resolved into an orthogonal component represented in terms of $\mathbf{W}$ at the cell centroids (N and P) and a non-orthogonal component represented by a full gradient of $\mathbf{W}$ at the face. The equation is as follows:

$$\mathbf{S}_f \cdot (\nabla \mathbf{W}_f) = A(\mathbf{W}_N - \mathbf{W}_P) + \mathbf{a} \cdot (\nabla \mathbf{W})_f \tag{3.45}$$

Where $A = |\mathbf{S}_f|^2/(\mathbf{S}_f \cdot \mathbf{b})$ and $\mathbf{a} = \mathbf{S}_f - A\mathbf{b}$.

3.4 The Divergence cleaning method

In computational MHD, failure to enforce and maintain the solenoidal property of the magnetic field which requires $\nabla \cdot \mathbf{B}$ result in non linear numerical instabilities and discretization errors increasing over time. These issues manifest themselves mainly by wrong propagation speed of discontinuities, appearance of unphysical effects such as plasmas transport orthogonal to the magnetic field and negative values of thermodynamic variables such as pressure. Several methods have been developed to overcome this issue, including Brackbill and Barnes projection method (Brackbill and Barnes, 1980), Evans and Hawley's constrained transport (Evans and Hawley, 1988) and the Powell's eight wave approach (Powell, 1994; Powell et al., 1999). In this work, to ensure that $\nabla \cdot \mathbf{B} = 0$ both physically and numerically, the hyperbolic divergence cleaning method of Dedner (Dedner et al., 2002) is used. The divergence free constraint can be coupled with the induction equation through the introduction of a new potential scalar variable, ψ (see (Dedner et al., 2002) and references therein for more details). The equation describing the evolution of the magnetic field , Eq. 2.13 is then replaced with the following equation:

$$\frac{\partial \mathbf{B}}{\partial t} + \nabla \cdot (\mathbf{U}\mathbf{B} - \mathbf{B}\mathbf{U}) + \nabla \psi = 0 \tag{3.46}$$

An additional equation needs to be solved for ψ

$$\frac{\partial \psi}{\partial t} + c_h^2 \nabla \cdot \mathbf{B} = -\frac{c_h^2}{c_d^2}\psi \tag{3.47}$$

Where c_h which acts like a velocity and the dissipation coefficient c_d are determined by:

$$c_h = \frac{CFL}{\Delta t \times max(\frac{1}{h})} \tag{3.48}$$

$$c_d = \sqrt{-\Delta t \frac{c_h^2}{ln(C_r)}} \tag{3.49}$$

Where h is the cell size, CFL is the Courant–Friedrichs–Lewy number and $0 < C_r < 1$. In this work $C_r = 0.9$ (Dedner et al., 2002). This cleaning method ensures that any artificial source of $\nabla \cdot \mathbf{B}$ is convected out of the domain with the speed c_h and is damped by the dissipation coefficient c_d. Now the governing MHD equations can be updated as:

$$\frac{\partial}{\partial t}\begin{pmatrix}\rho\\ \rho\mathbf{U}\\ \mathbf{B}\\ \rho E\\ \psi\end{pmatrix} + \nabla\cdot\begin{pmatrix}\rho\mathbf{U}\\ \rho\mathbf{U}\mathbf{U} + \mathbf{P}_{over}\mathbf{I} - \frac{\mathbf{B}\mathbf{B}}{\mu_0}\\ \mathbf{U}\mathbf{B} - \mathbf{B}\mathbf{U} + \nabla\psi\\ (E + \mathbf{P}_{over})\mathbf{U} - \frac{\mathbf{B}\mathbf{B}}{\mu_0}\cdot\mathbf{U}\\ c_h^2\mathbf{B}\end{pmatrix} = \nabla\cdot\begin{pmatrix}\mathbf{0}\\ \tau_{visc}\\ -\frac{1}{\mu_0\sigma}\Delta\mathbf{B}\\ k_{th}\nabla T - (\frac{\eta\mathbf{J}\times\mathbf{B}}{\mu_0})\\ -\frac{c_h^2}{c_d^2}\psi\end{pmatrix} \tag{3.50}$$

and all the terms of Eq.3.33 are updated as follow including the divergence cleaning terms:

$$\mathbf{W}_f = \begin{pmatrix}\rho\\ \rho U_x\\ \rho U_y\\ \rho U_z\\ B_x\\ B_y\\ B_z\\ \rho E + P_{over}\\ \psi\end{pmatrix},\ \kappa_f = \begin{pmatrix}0\\ S_x P_{over}\\ S_y P_{over}\\ S_z P_{over}\\ -b_f U_x\\ -b_f U_y\\ -b_f U_z\\ -b_f(\mathbf{U}\cdot\mathbf{B})\\ 0\end{pmatrix},\ \varpi_f = \begin{pmatrix}0\\ \omega_f\\ \omega_f\\ \omega_f\\ 0\\ 0\\ 0\\ \omega_f\\ 0\end{pmatrix},\ \Phi_f = \begin{pmatrix}0\\ -B_x b_f\\ -B_y b_f\\ -B_z b_f\\ S_x\psi\\ S_y\psi\\ S_z\psi\\ 0\\ c_h^2 b_f\end{pmatrix}$$

3.5 Stability condition

The aim in CFD is to compute the solution for the largest local time step possible in order to save computational time and make a study for long term evolution. The physical restriction is to control the propagation of information brought by waves or advected with fluid. Now, let us consider the maximum speed of propagation $c_{max} = |\mathbf{U}| + c_{fast}$ and a typical width Δx of a cell. A time interval for the time-marching method can be estimated based on some different characteristic time scales such as: the time scale of dissipative effects of viscosity, thermal conduction and magnetic diffusion. In the case of ideal MHD, one has only to take into account the time scale of convection:

$$\Delta t_{conv} \leq \frac{\Delta x}{c_{max}} \tag{3.51}$$

Where $c_{fast} = c_+$ is the fast magnetosonic speed of Eq.2.77 of sec.2.4 and $\mathbf{U}$ the fluid flow velocity.

Even though the convection of propellant is of primary importance to propulsion, the characteristic time scale of the dissipative effects is normally shorter than Δt_{conv}, because it is proportional to Δx^2 (Kubota, 2009). Among the dissipative phenomena, one of the severest phenomena is the magnetic diffusion whose time scale is:

$$\Delta t_{magdiff} \leq \mu_0 \sigma \Delta x^2 \simeq O(10^{-10} - 10^{-11})\ s \tag{3.52}$$

Basically the time interval of every step is determined to satisfy this restriction. For a steady state solution, local time step technique, by which a time interval is locally determined for each cell, is employed in the restriction above to accelerate the convergence.

3.6 Performance of the density-based central-upwind methods for ideal MHD

In this section, the robustness and the accuracy of the central-upwind schemes of the new density-based numerical algorithm is tested on a series of benchmark numerical simulations which are: The MHD schock tube, the Orszag-Tang vortex and the cloud-shock interaction. The MHD schock tube test demonstrates the ability of the proposed scheme to capture the MHD waves propagation as well as shock discontinuities. The Orszag-Tang vortex problem tests the accuracy of the schemes for dominantly smooth problems with strong interactions between several shock waves and the cloud-shock interaction is used to test the schemes on highly super fast flows which involves the interaction between a MHD shock and a denser cloud. Some important applications of the above mentioned tests can be find in geophysics (earthquake) and in astrophysics (Sunspots, the interaction between solar wind and the magnetosphere, the interaction of supernova rests with a inhomogeneous interplanetary and interstellar medium). Before we present our simulations, let us introduce some definitions. We define downstream as the direction in which the incident shock is moving, and upstream the opposite one.

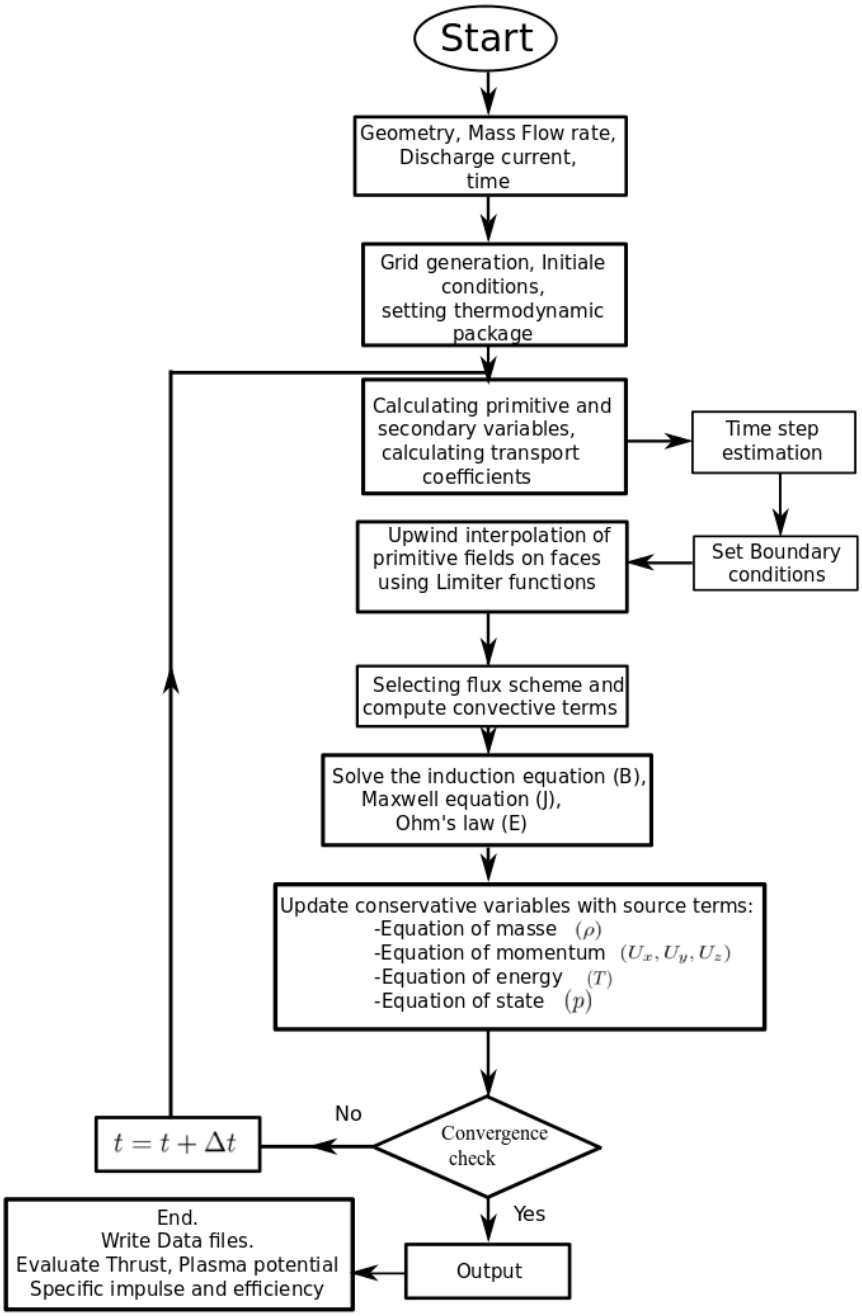

FIGURE 3.5: Algorithm describing the density-based code

In MHD, A Alfvèn Mach number is the ratio of shock velocity in the upstream medium to the Alfvèn speed, $M_A = \frac{|\mathbf{U}|}{v_A}$, where $v_A = \frac{|\mathbf{B}|}{\sqrt{\rho}}$ is the Alfvèn speed (See sec.2.4 of Chap.2). It's the analogue of the hydrodynamic Mach number defined as $M = \frac{|\mathbf{U}|}{a}$ where a is the speed of sound. The plasma beta is the ratio of the kinetic pressure at a point inside the plasma to the confining magnetic pressure at the plasma boundary $\beta = \frac{2p}{B^2}$. It is also known as the measure of the relative magnitudes of the kinetic and the magnetic pressure. The shock strength parameter of two distinct flow regions $\chi = \frac{\rho_2}{\rho_1}$, where ρ_2 and ρ_2 are the density respectively downstream and upstream. The magnetic reconnection

(Picone and Dahlburg, 1990) is when magnetic field connect and disconnect and can concentrate mechanical or magnetic energy in both space and time. In the following subsections we have choose unit for $\mathbf{B}$ such that $\mu_0 = 1\ H/m$. The results are presented and discussed in the following subsection.

3.6.1 The MHD shock tube problem

The MHD shock tube problem is one of the applications of the hydrodynamic shock tube problem of Sod (Sod, 1978) and one of the best numerics examples for testing the ability of a MHD code to capture the MHD discontinuities (shocks, rarefactions, contact discontinuities and compound waves). The computational domain and the initial states are those of Brio-Wu shock tube (Brio and Wu, 1988). The initial conditions and the set-up of the Brio-Wu tube problem are presented in Fig. 3.6.

$$(\rho, u_x, u_y, u_z, B_x, B_y, B_z, p) = \begin{cases} (1, 0, 0, 0, \frac{3}{4}, 1, 0, 1) & \text{if } x < 0.5 \\ (\frac{1}{8}, 0, 0, 0, \frac{3}{4}, -1, 0, \frac{1}{10}) & \text{if } x \geq 0.5 \end{cases} \tag{3.53}$$

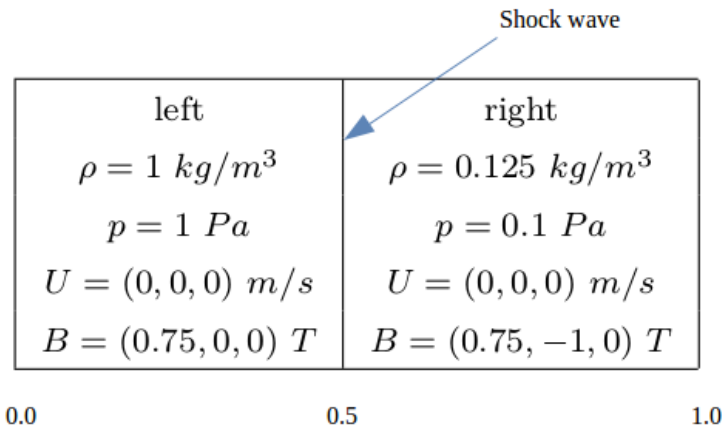

FIGURE 3.6: Initial conditions and geometry of the Brio-Wu shock tube problem

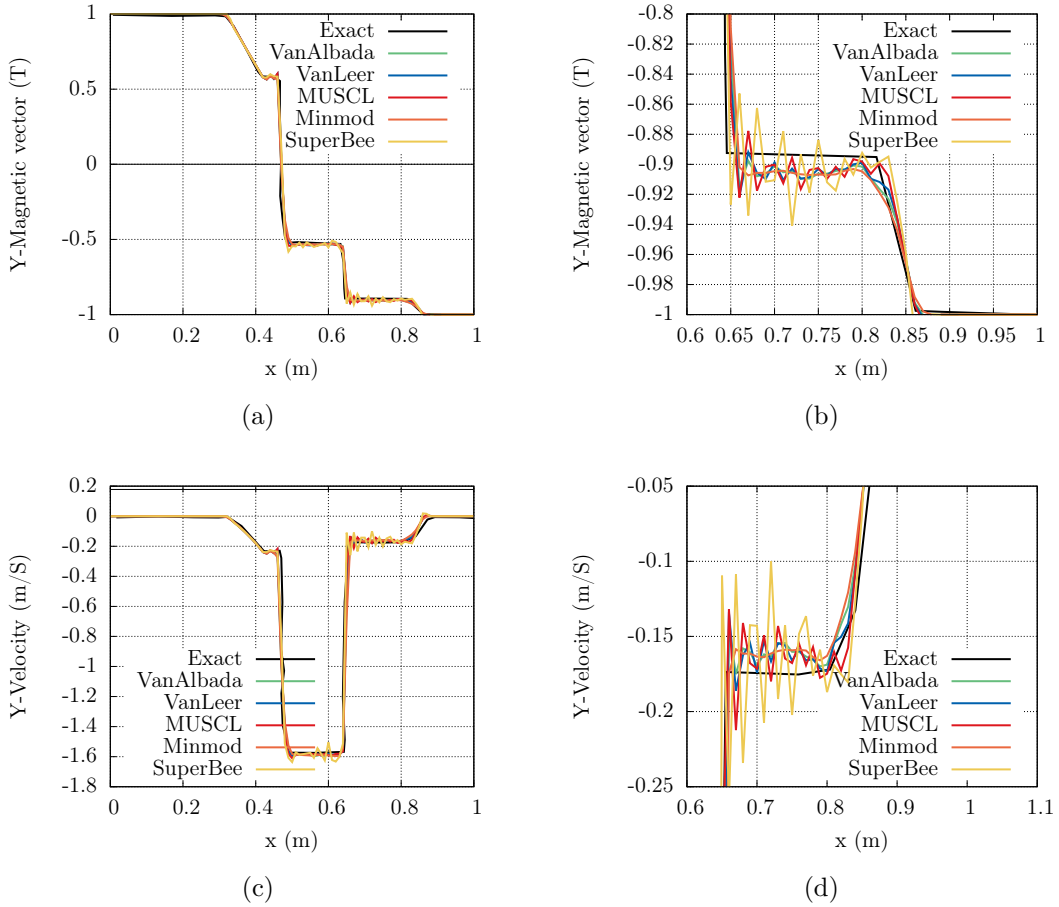

FIGURE 3.7: Performance of the different function limiters of Tab.3.1 with the KNP-MHD schemes on the Brio-Wu shock tube problem against the exact solution for y-component of magnetic field (a-b) and y-component of velocity (b-c) at $t = 0.1\ s$ on a 2D grid with 400×40 mesh

As mentioned in sec.3.1.2, to ensure the boundedness of the schemes and avoid oscillatory solutions, we used flux limiter functions. To know which limiter functions can be appropriate for our code, an analyse is conducted on the Brio-Wu shock tube problem by coupling our KNP-MHD flux scheme with the flux limiter functions presented in Tab.3.1. It appears that the numerical solution is very sensitive to the choice of the flux limiter function. The results obtained are presented in Fig.3.7 and it can be clearly seen that except the VanAlbada and the Minmod flux limiter functions, the others exhibit very strong oscillatory solutions at the front of the shock wave even with the KT-MHD flux scheme. Consequently, if not specified, the Minmod function has been chosen as limiter functions for all simulations performed in this work.

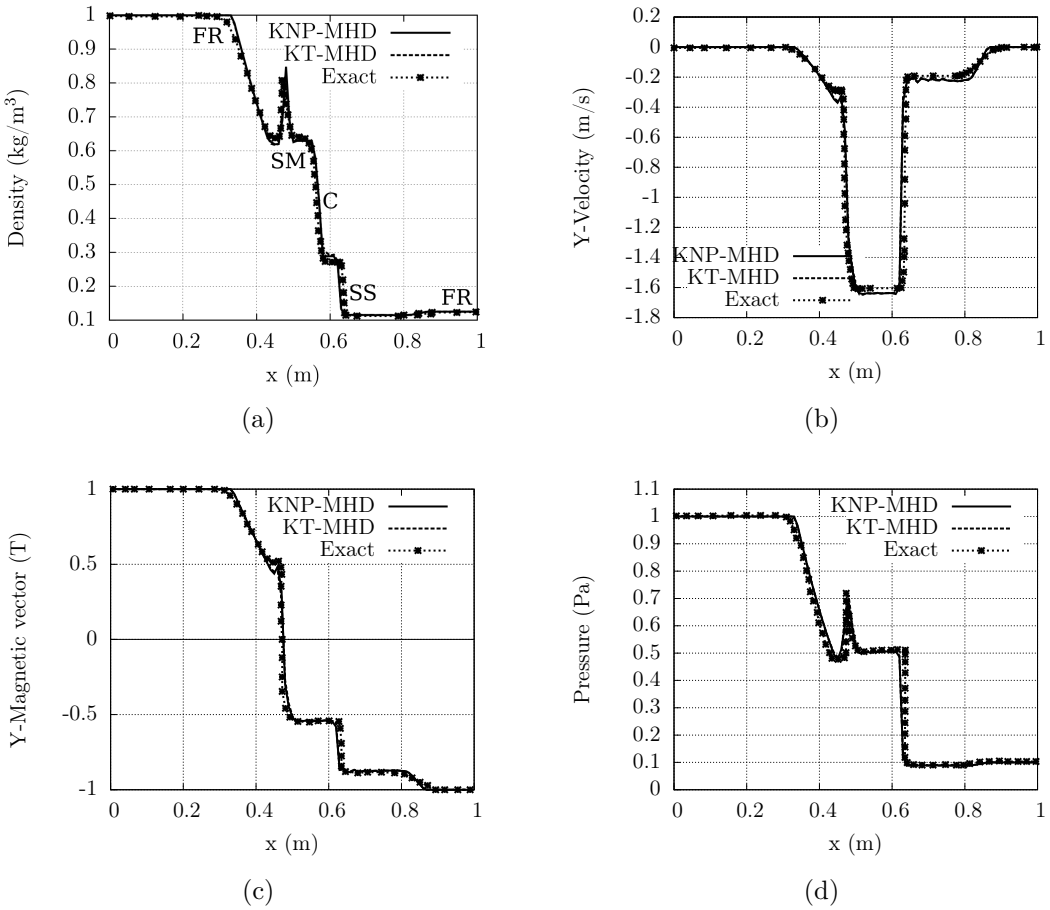

FIGURE 3.8: Comparison of exact density (a), y-component of velocity (b), y-component of magnetic field (c) and pressure (d) profiles with numerical simulation results at $t = 0.1\ s$ on a 2D grid with 800×80 mesh

Fig. 3.8 shows the comparison of analytical y-component of magnetic field, y-component of velocity, density and pressure profiles with numerical simulation results of our ideal MHD code with both flux schemes KNP-MHD and KT-MHD at $t = 0.1\ s$. In the density and pressure profiles of Fig. 3.8a and Fig. 3.8d, we can distinguish from left to right, a fast rarefaction wave (formed to the high pressure and high density side) denoted by FR in the figure, followed by a slow compound wave (formed behind the contact discontinuity) denoted in the figure by SM, moving to left, a contact discontinuity (C), slow shock (formed in the front of the contact discontinuity), denoted by SS in the figure and a fast rarefaction wave (corresponding to the low pressure and low density side) moving to the right. The middle two jumps in the profile for B_y (see Fig. 3.8c) are two slow waves: one shock and one rarefaction. Fig. 3.8b shows the profile of U_y formed by two fast shocks to the left and right both separated in the middle by one fast rarefaction. All These observations prove that, our solver is able to resolve all the MHD characteristic waves, shocks and discontinuities.

We now consider a one-dimensional Riemann problem given by the same hydrodynamic data as the Sod's Riemann problem (Sod, 1978):

$$(\rho, u_x, u_y, u_z, B_x, B_y, B_z, p) = \begin{cases} (1, 0, 0, 0, \frac{3}{4}, 1, 0, 1) & \text{if } x < 0 \\ (\frac{1}{8}, 0, 0, 0, \frac{3}{4}, -1, 0, \frac{1}{10}) & \text{if } x \geq 0 \end{cases} \tag{3.54}$$

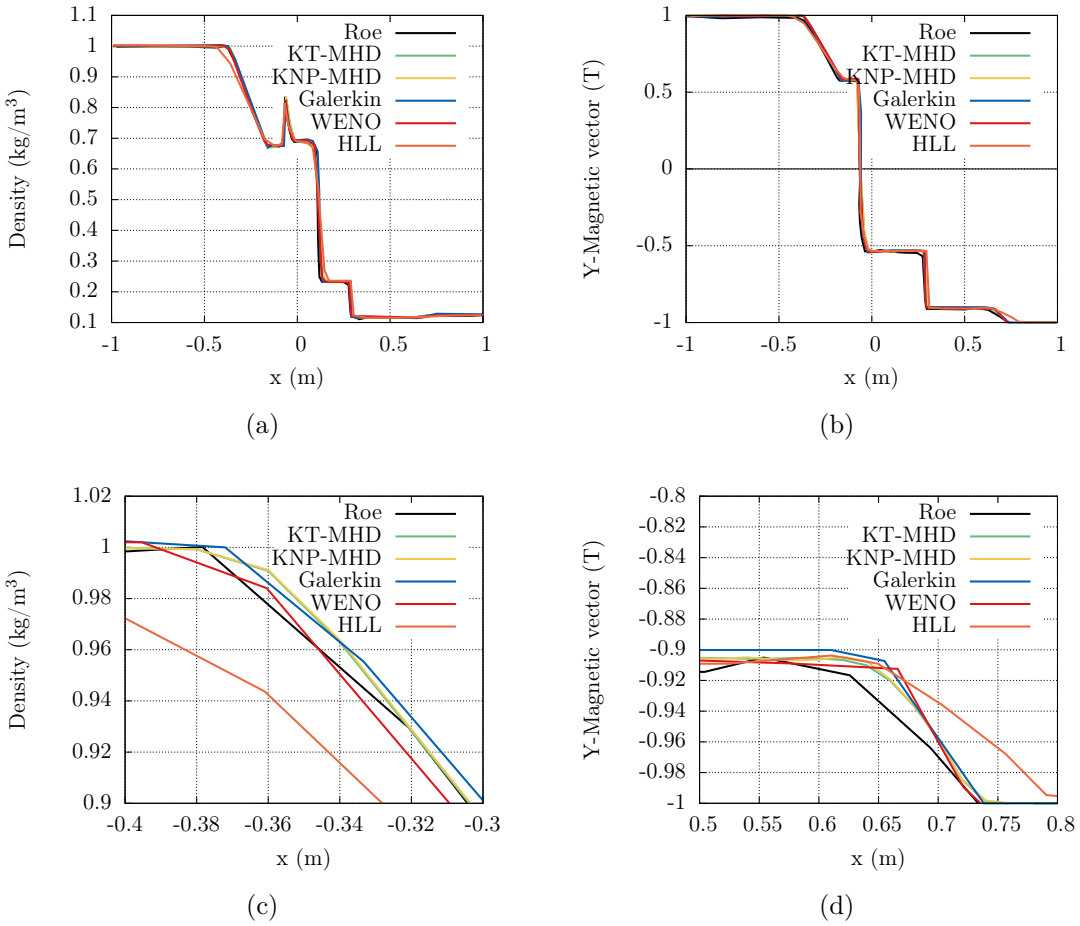

FIGURE 3.9: Comparison of our simulation results on a 1D Riemann problem with 800 points with a 1D grid Roe type second order upwind scheme (Brio and Wu, 1988), a discontinuous Galerkin method (Li, Xu, and Yakovlev, 2011), a WENO scheme (Shen, Zha, and Huerta, 2012) and a HLL approximation (Gurski, 2004) for density (a) and y-component of magnetic field (b) at $t = 0.2\ s$

The computational domain is taken to be $[-1, 1]$ with 800 grid points and $\gamma = 2$. The solution at $t = 0.2\ s$ is shown in Fig.3.10 which presents the comparison of the numerical results of our flux schemes both using the Minmod flux limiter with two Riemann solvers namely the second order upwind Roe scheme (Brio and Wu, 1988), considering here as the reference and a Harten-Lax-van Leer (HLL) approximation (Gurski, 2004) and also with two more modern schemes, a high order weighted essentially non-oscillatory (WENO) scheme (Shen, Zha, and Huerta, 2012) and a central discontinuous Galerkin method (Li, Xu, and Yakovlev, 2011). Fig.3.10.c

and Fig.3.10.d show the solutions around the fast rarefaction and the slow shock in greater detail. It appears that our KNP-MHD and KT-MHD are both less dissipative than the HLL approximation relatively to Roe scheme after the fast rarefaction wave and lie closest to the Roe solution around the slow shock. These results illustrate the robustness and the accuracy of our flux schemes to deal with MHD shocks.

3.6.2 The Orszag-Tang vortex problem

Now, we test our ideal MHD code by simulating the formation of the compressible two dimensional Orszag-Tang vortex problem (1979). This test is useful in describing local supersonic regions in a turbulent, compressible, dissipative conducting fluid. The simulations involve complex interactions of multiple shock waves along the diagonals with the inhomogeneous density distribution to produce turbulence. The Orszag-Tang system is doubly periodic and the initial condition consists of single-mode solenoidal velocity and magnetic field. The initial mass density and presure are flat. For the purpose to compare our results with other previous work, we choose similar initial states as those of Baldas and Tadmor (Baldás and Tadmor, 2005) on the computational domain $[0, 2\pi] \times [0, 2\pi]$ with periodic boundary conditions. The initial conditions for velocity and magnetic field are presented in Fig. 3.10.

$$(\rho, u_x, u_y, u_z, B_x, B_y, B_z, p) = (\gamma^2, -sin(y), sin(x), 0.0, -sin(y), sin(2x), 0.0, \gamma) \tag{3.55}$$

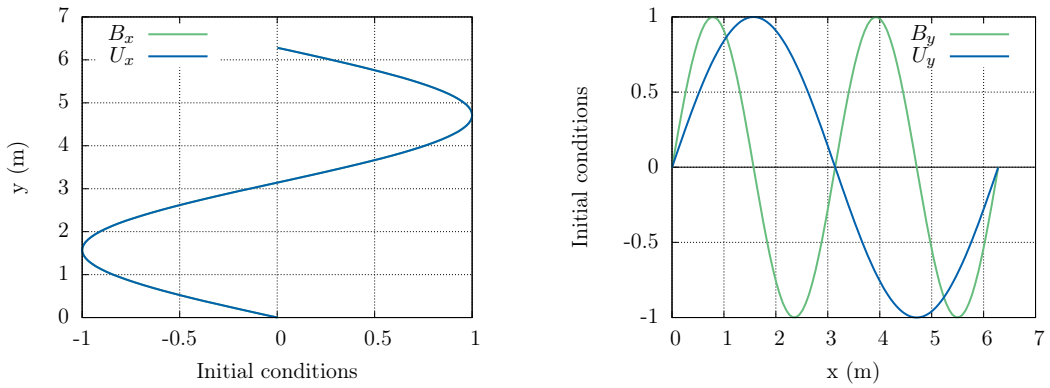

(a) (b)

FIGURE 3.10: Initial conditions for velocity and magnetic field of the Orszag-Tang vortex in y direction (a) and x direction (b) at $x = \pi$ and $y = \pi$ sections respectively

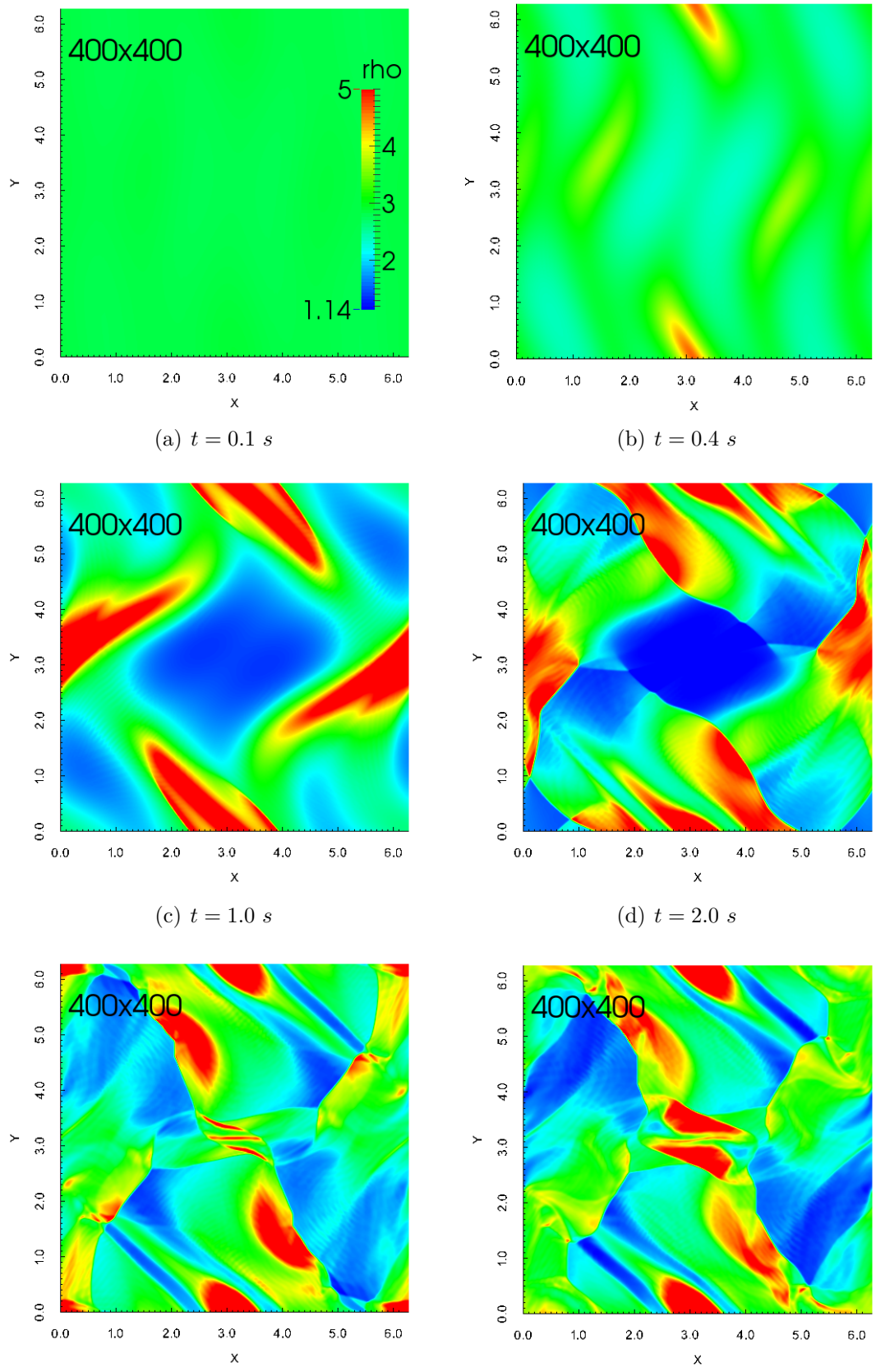

(a) $t = 0.1\ s$ (b) $t = 0.4\ s$

(c) $t = 1.0\ s$ (d) $t = 2.0\ s$

(e) $t = 2.8\ s$ (f) $t = 3.14\ s$

FIGURE 3.11: Temporal progression of the density contour simulations of the Orszag-Tang problem for $0.1\ s \leq t \leq 3.14\ s$ on the $N = 400 \times 400$ grid. Density in (kg/m^3)

where $\gamma = 5/3$.

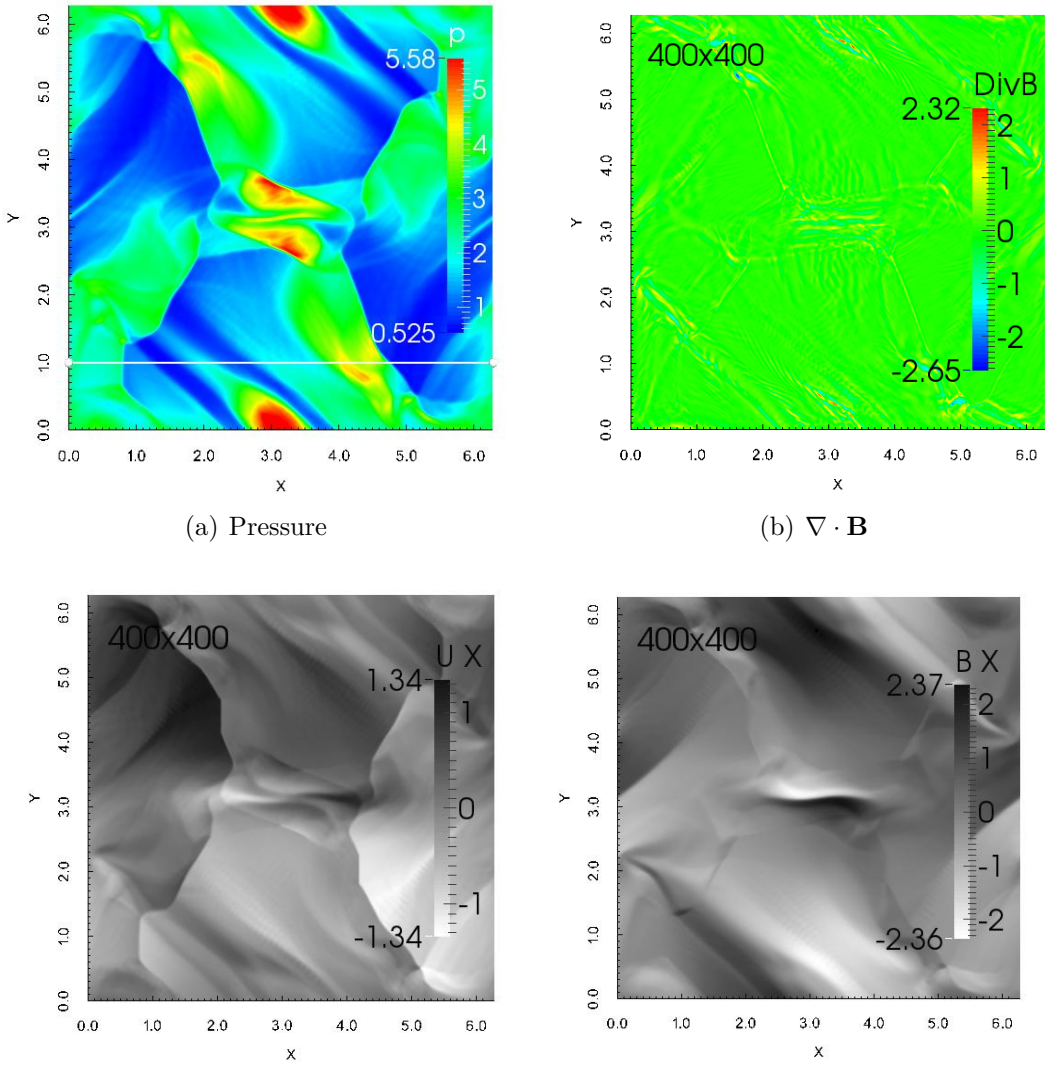

(a) Pressure

(b) $\nabla \cdot \mathbf{B}$

(c) X-Velocity

(d) X-Magnetic vector

FIGURE 3.12: Pressure (a), $\nabla \cdot \mathbf{B}$ (b), x-component of velocity (c), x-component of magnetic field (d) and of the Orszag-Tang vortex computed at $t = \pi s$ on the 400×400 mesh with the KT-MHD scheme

With the initial average Alfvèn Mach number $M_A = \gamma = 1.67$ and the average plasma beta $\beta = \frac{10}{3}$, numerical simulations are conducted on a $N \times N$ grid with $N = 50, 100, 200, 300, 512$. Because of the symmetry and periodicity of this test, the shocks can interact multiple times each other and with the varying mass density field. Thus, from smooth initial condition, the flow becomes gradually very complex as expected to the transition towards MHD turbulence. The temporal evolution of density plotted in Fig. 3.11 shows that the flow in the Orszag-Tang vortex initially rarefy the plasma in the central region, permitting magnetic reconnection there (Fig. 3.11c). Fig. 3.12 displays pressure, $\nabla \cdot \mathbf{B}$, x-component of velocity and magnetic field for $t = \pi s$ when discontinuities have formed and interacted. Here, we noticed the similarity of the different contours involving strong

gradient toward the two diagonals, which underlined the high level of correlation between the global physical properties of this test case.

The contour of $\nabla \cdot \mathbf{B}$ plotted in Fig. 3.12b show that numerical errors are important only on the regions of discontinuity. For more quantitative comparisons between our schemes and previous schemes (Shen, Zha, and Huerta, 2012), we plot in Fig. 3.13, the value of pressure in horizontal slice along $y = 1.0$ (See Fig. 3.12a) at time 3 s. The results are shown for a 512×512 grid and compared with those of Shen et al.(Shen, Zha, and Huerta, 2012). Except the deviation observed around $x = 1.5\pi$, the simulations agree well in general.

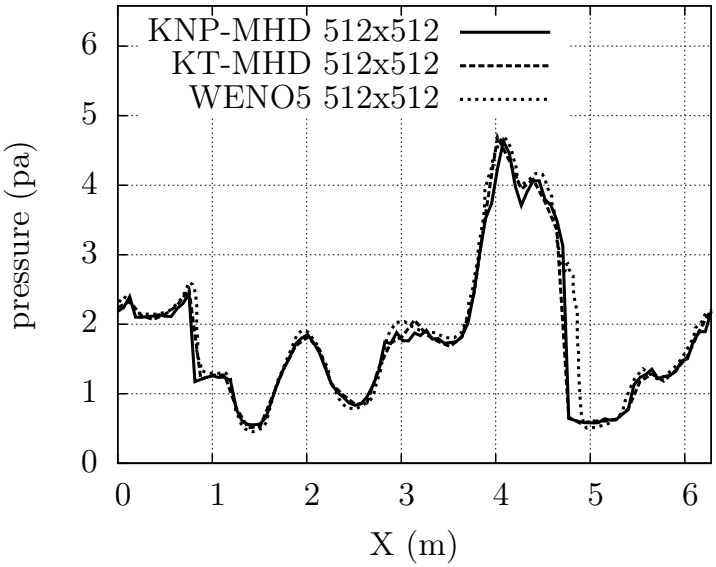

FIGURE 3.13: comparison of the WENO-5 scheme of Shen et al.(Shen, Zha, and Huerta, 2012) with the KNP-MHD and KT-MHD flux scheme of the present solver for the pressure profile at $t = 3\ s$ along the line $y = 1\ m$

By integrating Eq. 3.27, we determined the relative conservation errors for momentum and total energy which is the difference between the right and the left side of Eq. 3.27. Profiles on Fig. 3.14 notice that at some times the conservatives laws are not fulfilled. That is probably due to the magnetic reconnection (Picone and Dahlburg, 1990) which occurs at these times e.g $t \sim 1.0\ s$ and $t \sim 2.8\ s$.
We considered a high resolution run with uniform grid N=512 as a reference solution and we evaluated the solution at time $t = 3.14\ s$. The relative numerical errors of any fluid variable W is deducted from (Fogang et al., 2015):

$$\delta_N(W) = \frac{\sum_{j=1}^{N}\sum_{k=1}^{N}|W_{j,k}^{N} - W_{j,k}^{high}|}{\sum_{j=1}^{N}\sum_{k=1}^{N}|W_{j,k}^{high}|} \tag{3.56}$$

and it's average over all variables considered, the average numerical errors, is given by:

$$\delta_N = \frac{1}{4}(\delta_N(v_x) + \delta_N(v_y) + \delta_N(B_x) + \delta_N(B_y)) \tag{3.57}$$

TABLE 3.2: Relative numerical errors (δ_N) and convergence order (R_N) for Orszag-Tang vortex problem using KT and KNP flux schemes at $t = 3.14\ s$

N	KNP-MHD		KT-MHD	
	δ_N	R_N	δ_N	R_N
50	0.28974		0.30370	
100	0.15937	0.86	0.16383	0.89
200	0.08266	0.95	0.08065	1.02
300	0.04714	1.38	0.04604	1.38
400	0.04236	0.96	0.02875	1.49

The corresponding convergence order is evaluated by: $R_N = \frac{log(\frac{\delta_{N_2}}{\delta_{N_1}})}{log(\frac{N_2}{N_1})}$. Where δ_{N_1} and δ_{N_2} are the average numerical errors obtained with the coarser grid N_1 and the finer grid N_2 respectively.

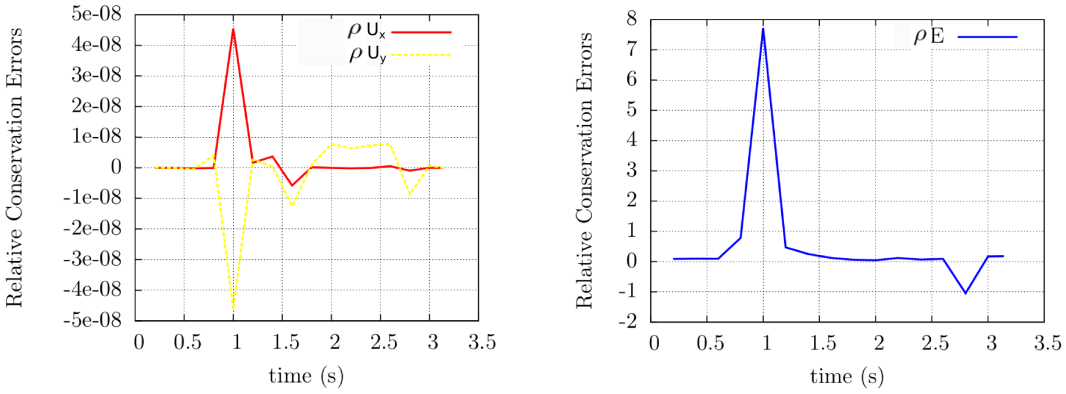

(a) Momentum (b) Total Energy

FIGURE 3.14: Time histories of the two components of momentum $\rho U_X, \rho U_Y$ and total energy ρE for $0.1\ s \leq t \leq 3.14\ s$ on the $N = 400 \times 400$ grid

The convergence rate for the two schemes are between the first and the second order (see Tab.3.2). Here, the third order accuracy expected for the completely smooth flow is not achieved by both the KNP-MHD and the KT-MHD because of the use of flux limiters which, in presence of strong shocks and discontinuities, tend to attenuate the solution gradient.

3.6.3 Cloud-shock interaction

This process is common in the interstellar medium where shocks produced by supernova explosions interact with the surrounding multi-phase medium (Aluzas, 2014). The cloud-shock interaction test presented by Xisto et al (Xisto, Pascoa, and Oliviera, 2014) is used to test the ability of the present solver to simulate the interaction between a MHD shock and a high density cloud. The computational

domain is $(x, y)\epsilon[0, 1]$ and described by an uniform $N \times N$ grid. The initial conditions contain a discontinuity parallel to the y axis at $x = 0.6\ m$ with the left (post-shock) and right (pre-shock) states

$$(\rho, u_x, u_y, u_z, p, B_x, B_y, B_z) = \begin{cases} (3.86, 0, 0, 0, 167.34, 0, 2.18, -2.18) & \text{if } x < 0.6 \\ (1, -11.25, 0, 0, 1, 0, 0.56, -0.56) & \text{if } x \geq 0.6 \end{cases} \tag{3.58}$$

with the adiabatic index $\gamma = 5/3$.

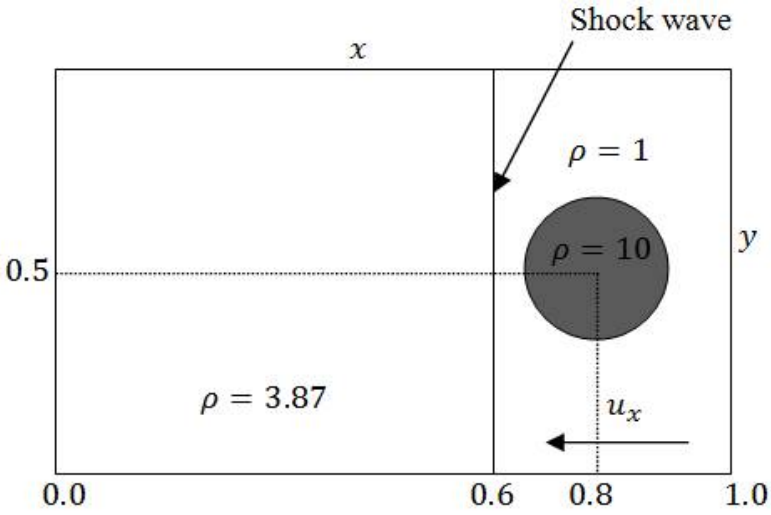

FIGURE 3.15: Initial conditions for density and the geometry used for the cloud-shock interaction test case

A circular density cloud with radius 0.15 m has $\rho_c = 10\ kg/m^3$ and is located at $(x, y) = (0.8, 0.5)$. Thus, the cloud is denser compared to its surrounding with a shock strength parameter $\chi = \frac{\rho_c}{\rho} = 10$. Where ρ_c and ρ are the density of the cloud and the density of its surrounding respectively. The value of pressure inside and outside the cloud is $p = 1\ Pa$, giving a sound speed in the ambient gas of $a = \sqrt{5/3}\ \frac{m}{s}$ and a initial pre-shock Mach number of 8.7. The strength of the magnetic field can be given through the initial calculated plasma beta parameter in the pre-shock region which is 2.5 which corresponds to a Alfvèn Mach number of 4.2 (super-Alfvénic pre-shock flow).

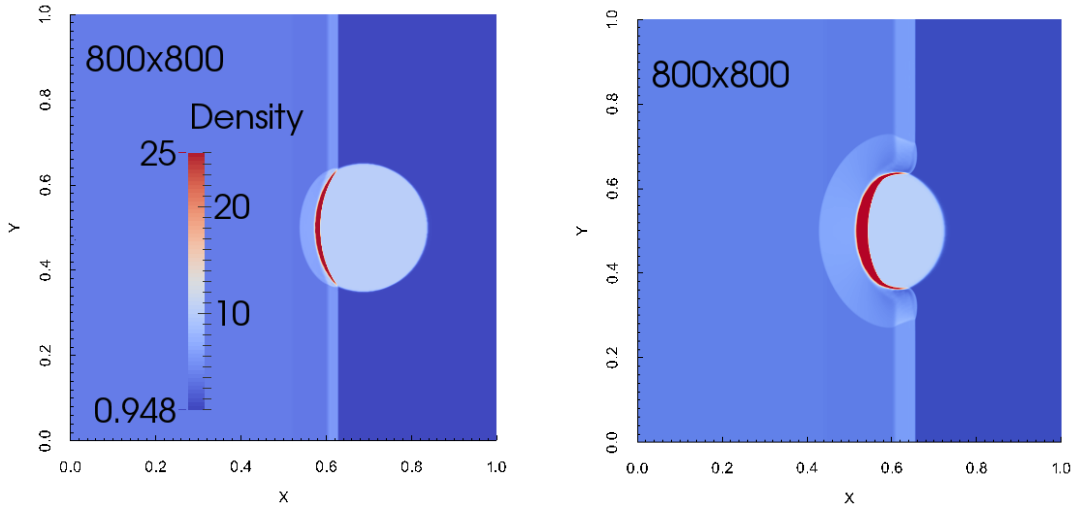

(a) $t = 0.01\ s$ (b) $t = 0.02\ s$

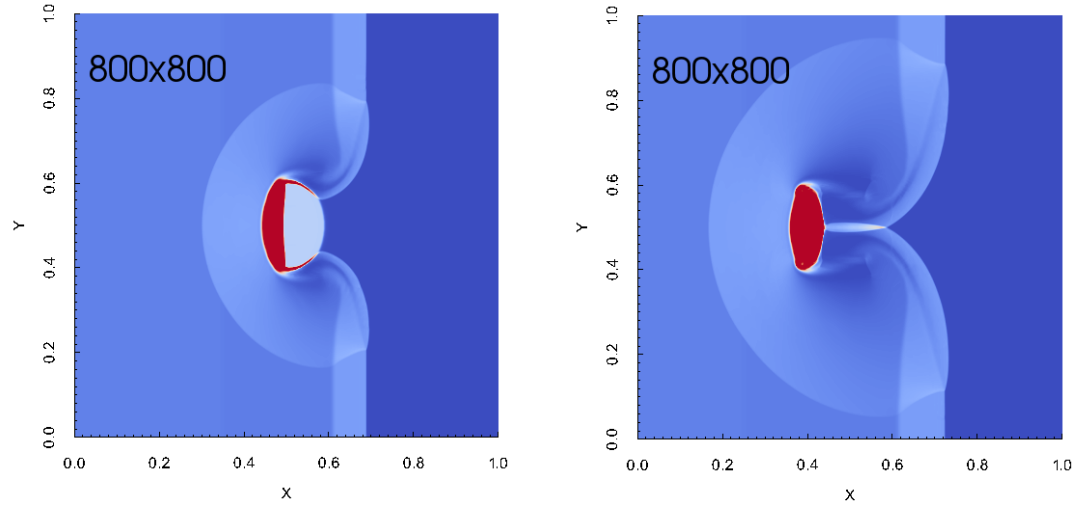

(c) $t = 0.03\ s$ (d) $t = 0.04\ s$

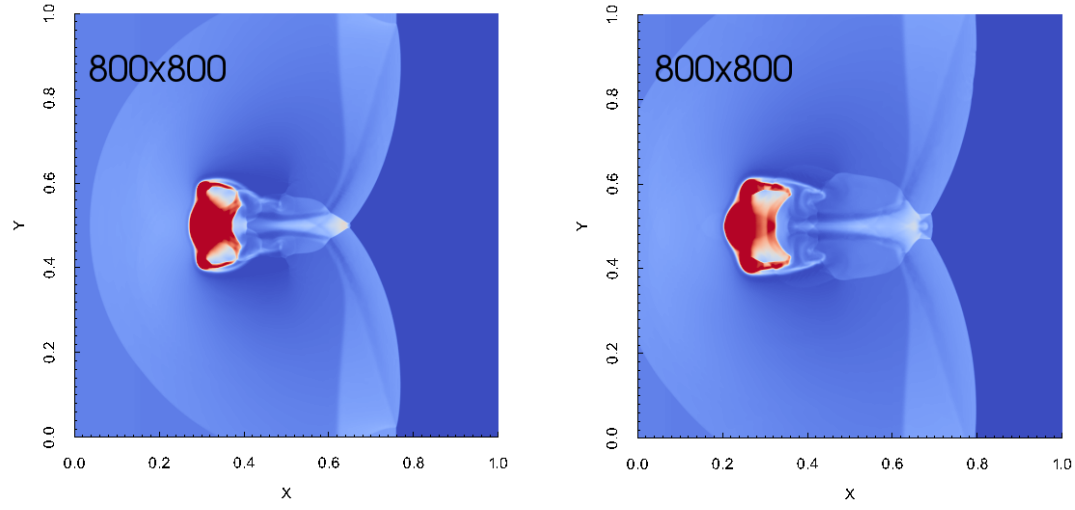

(e) $t = 0.05\ s$ (f) $t = 0.06\ s$

FIGURE 3.16: Temporal progression of the density contour simulations for the cloud-shock interaction for $0.01 \leq t \leq 0.06$ on the $N = 800 \times 800$ grid

The geometry and initial conditions for density used in our simulation are shown in Fig. 3.15. The simulations are carried out on $N = 200, 400, 600, 800$ grids using only the KT-MHD, since there are no differences between our two schemes according to the previous tests. Fig. 3.16 shows the temporal evolution of density in the time range of $0.01\ s \leq t \leq 0.06\ s$ with the highest grid resolution $N = 800$. The cloud-shock interaction simulated here can be divided into three main phases. Firstly, we have the *expansion phase* or the phase before the collision where the cloud and the fast plane shock are moving against one another. After the *expansion phase*, we have what we called the *collision phase* where the plane shock front moving from left crushes the cloud and strongly compressed it. Two fast shock are then created. A stronger fast shock which transmits into the cloud and a reflected fast shock propagating upstream into the shocked gas (See Fig. 3.16 from $t = 0.01\ s$ to $t = 0.03\ s$). The last phase is the *re-expansion phase* which takes place when the reflected fast shock generated in the previous phase completely covers the cloud and the formation of a Mach disk downstream into the pre-shock region is observed since the transmitted shock is strongly supersonic ($M \gg 1$)(See Fig. 3.16 from $t = 0.04\ s$ to $t = 0.06\ s$).

Between the two fast shocks, we can clearly distinguish in the temporal contours of density (Fig. 3.16) one contact discontinuity which move with the front side of the cloud and where the density has its highest value. As the cloud moves to left, it creates a bow shock in its front, where the pressure is maximal. The cloud motion also generates a low pressure region at its rear, where the magnetic pressures dominates the gas pressure giving a very weak plasma beta ($\beta \ll 1$) and consequently an important Lorentz force (See Fig. 3.17.a, Fig. 3.17.b and Fig. 3.17.c). Furthermore, the transverse magnetic field patterns are deformed by the moving cloud by adhering to its contouring in which a very complex features are taking place. These discontinuities in the rear of the cloud are described with a good resolution even with the coarser grid. The results presented in Fig. 3.18 are obtained at $t = 0.06\ s$ after the strong collision between the shock and cloud has taken place. The contact discontinuities and shock waves are very well simulated. The results are in accordance with those obtained by the AUSM scheme presented by Xisto et al.(Xisto, Pascoa, and Oliviera, 2013).

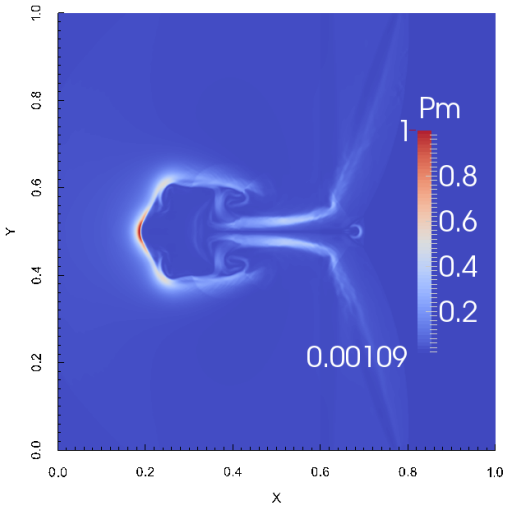

(a) Normalized Magnetic pressure

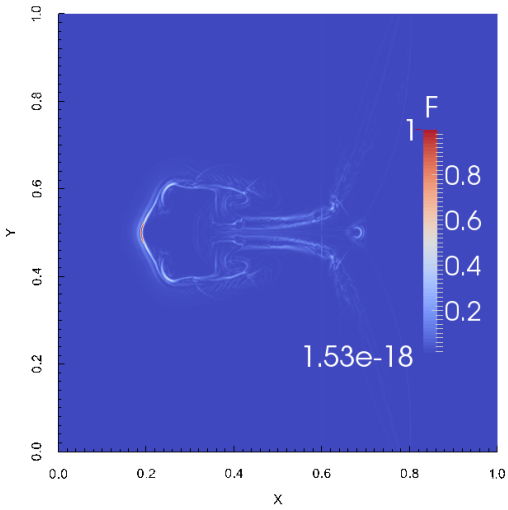

(b) Normalized Lorentz force

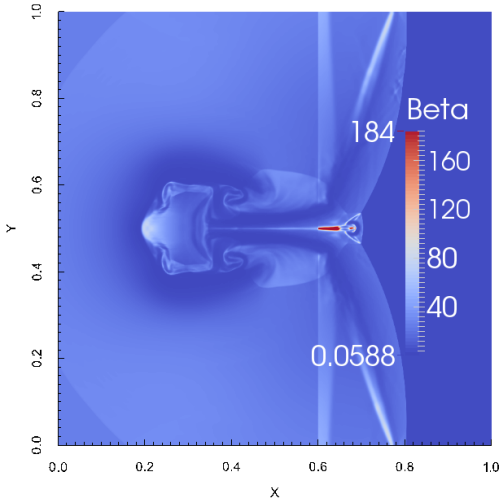

(c) Plasma Beta

FIGURE 3.17: Normalized magnetic pressure, Pm (a), Lorentz force density, F (b) and the plasma Beta distributions of the cloud-shock interaction at $t = 0.06$ on the $N = 800 \times 800$ grid. Magnetic pressure in Pa and Lorentz force density in N/m^3

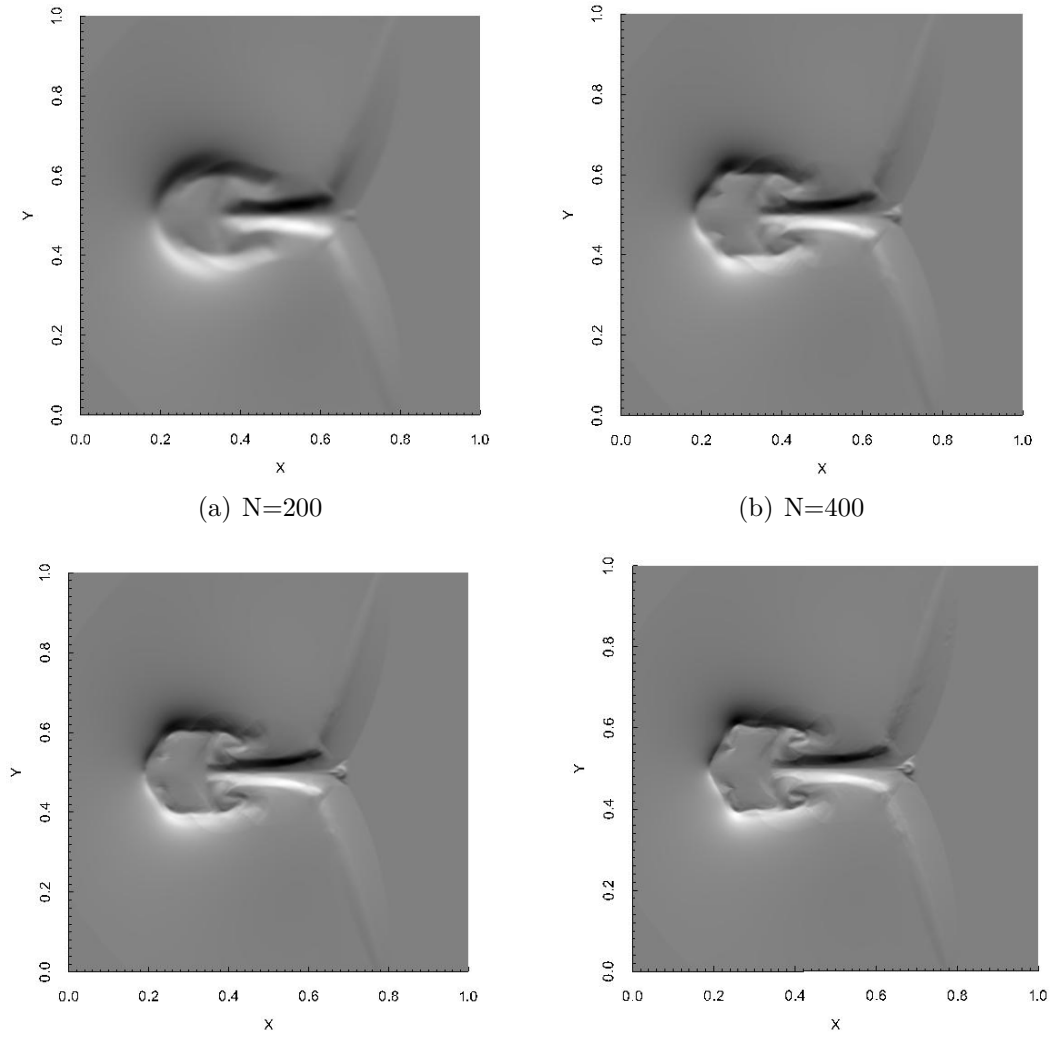

(a) N=200 (b) N=400

(c) N=600 (d) N=800

FIGURE 3.18: Magnetic fields for the 4 grids N=200 (a), N=400, N=600 (b) and N=800 (c) for $t = 0.06\ s$

3.7 Summary

The fundamental concepts of the central-upwind flux calculation had been presented in this chapter in the light of the finite volume method. The extension of the semi-discrete central-upwind schemes of Greenshields for Euler equations to MHD equations including the magnetic divergence free constraint were described. The proposed MHD solver is formulated in the integral form of conservation laws, does not require eigen-decomposition and allows the possibility to switch between the KT-MHD method (central scheme) and the KNP-MHD (upwind scheme) if necessary. The stability control parameter (CFL) had been reviewed as well as the discretization method of the gradient and laplacian term. A description of how the developed solver works is presented in Fig.3.5. The corresponding conservations

laws given by Eqs.(2.20, 2.27, 2.13, 2.41), can be expressed concisely as follow:

$$\frac{\partial}{\partial t}\begin{pmatrix}\rho\\ \rho\mathbf{U}\\ \mathbf{B}\\ \rho E\\ \psi\end{pmatrix}+\nabla\cdot\begin{pmatrix}\rho\mathbf{U}\\ \rho\mathbf{U}\mathbf{U}+\mathbf{P}_{over}\mathbf{I}-\frac{\mathbf{B}\mathbf{B}}{\mu_0}\\ \mathbf{U}\mathbf{B}-\mathbf{B}\mathbf{U}+\nabla\psi\\ (E+\mathbf{P}_{over})\mathbf{U}-\frac{\mathbf{B}\mathbf{B}}{\mu_0}\cdot\mathbf{U}\\ c_h^2\mathbf{B}\end{pmatrix}=\nabla\cdot\begin{pmatrix}\mathbf{0}\\ \tau_{visc}\\ -\frac{1}{\mu_0\sigma}\Delta\mathbf{B}\\ k_{th}\nabla T-(\frac{\eta\mathbf{J}\times\mathbf{B}}{\mu_0})\\ -\frac{c_h^2}{c_d^2}\psi\end{pmatrix} \tag{3.59}$$

By setting the parabolic term $\begin{pmatrix}\tau_{visc}\\ -\frac{1}{\mu_0\sigma}\Delta\mathbf{B}\\ k_{th}\nabla T-(\frac{\eta\mathbf{J}\times\mathbf{B}}{\mu_0})\end{pmatrix}=\begin{pmatrix}\mathbf{0}\\ \mathbf{0}\\ \mathbf{0}\end{pmatrix}$, we obtain the ideal MHD equations of sec.2.55.

The ideal form of the present density-based method is validated against some benchmark MHD problems. In Brio-Wu shock tube test, the schemes provide high-resolution results by capturing strong and slow shock, fast and slow rarefaction and do not produce oscillations behaviour. For the Orszag-Tang vortex and the cloud shock interaction, the schemes work well and avoid some issues such as the non positivity of pressure. According to the obtained numerical results, the schemes are considered efficient, robust and also simple to implement. In conjunction with the standard techniques for the numerical solution of the dissipative terms of the resistive MHD equations, in the next chapters these schemes will be applied to plasma flow simulations in MPD thrusters.

Chapter 4

Magneto-plasma dynamic (MPD) thrusters

Despite the advances in combustion research, the highest exhaust velocity of a functional chemical propulsion system, 3.600 to 4.500 m/s from sea level to high altitude, is still inadequate for most deep-space missions of interest. The present situation of space exploration calls for missions beyond the moon and for such missions, chemical propulsion is not a viable option, except for the case of launch vehicles where high thrust is required. Functionally, the inability of chemical propulsion systems to achieve higher exhaust velocities is due to limitation in the maximum tolerable temperature in the combustion chamber and to avoid excessive heat transfer to the walls. Both these limitations can be overcome by use of electric propulsion, which can be defined as the acceleration of gases for propulsion by electrical heating and/or by electric and magnetic volume forces. In sec.1.2 of Chap.1, we introduced the three categories of electric propulsion thrusters. This section is dedicated to the MPD thrusters, their principle and the different physical processes involved. Jahn (Jahn, 1968) defined the MPD thrusters as the devices in which the acceleration of the ionized gas is ruled by the Lorentz body force which results from the interaction of currents driven through the gas with magnetic field. The magnetic field can be self-induced by the discharge current applied between the electrodes (Self-field MPD thruster) or can be external, i.e, supplied by permanent magnets or coils (Applied-field MPD thruster). The magnetoplasmadynamic (MPD) thrusters have the unique capability, among all other developed electric propulsion systems, of processing megawatt power levels in a simple, small and robust device, producing thrust densities as high as $10^5\ N/\ m^2$ (Jahn, 1968) and capability to operate with high power ranging from 100 kW to $\sim 1MW$ for self-field MPD thrusters (SFMPDT) and from 10 kW to $\sim 100\ kW$ for applied-field MPD thrusters (AFMPDT) (see Fig.1.4 of Chap.1). These features render them the good candidates for high energy deep-space missions.
In this chapter, we illustrate briefly the designs, the basic principles of MPD thrusters and the physical phenomenon encountered in the self-field as well as in the applied-field MPD thrusters.

4.1 Principle of the MPD thrusters

The MPD thrusters as electric propulsion system propel the space engine by using the same basic principle as chemical rockets. The mass is accelerated and ejected from the vehicle. In its most elementary form, a MPD thruster consists of

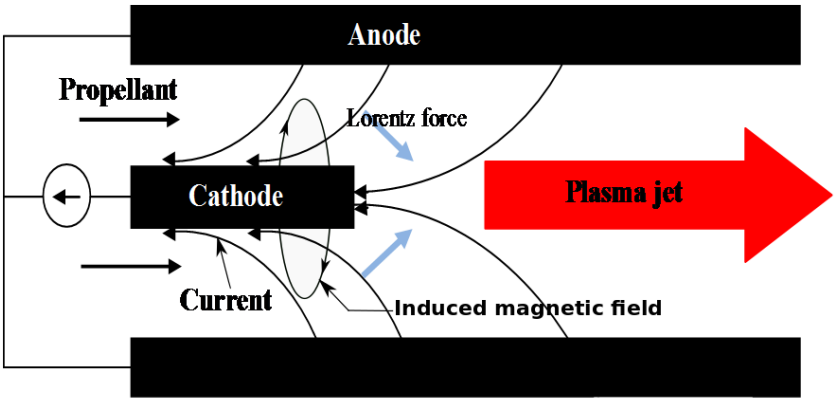

FIGURE 4.1: Principe design of a self-field MPD thruster

a cylindrical cathode surrounded by a concentric anode (Fig.4.1). An electric arc applied between the electrodes heats up and ionizes the gaseous propellant creating a quasi-neutral plasma within the discharge chamber. The resulted discharge current carried by the plasma flow to the electrodes interacts with the magnetic field causing a Lorentz force to accelerate the plasma. In fact, when a flow of ionized gas with a scalar conductivity σ is subjected to an electric field $\mathbf{E}$ and a magnetic field $\mathbf{B}$, perpendicular to each other and to the gas velocity $\mathbf{U}$, a current density $\mathbf{J} = \sigma(\mathbf{E} + \mathbf{U} \times \mathbf{B})$ will flow through it, parallel to $\mathbf{E}$ and will interact with the magnetic field $\mathbf{B}$ to provide a body force density $\mathbf{J} \times \mathbf{B}$ which will accelerate the plasma.

4.1.1 Self-field MPD thrusters

In the case of SFMPDT, the produced Lorentz force, consists of a "blowing force", its axial component which accelerates the plasma and a "pumping force", its radial component, which is responsible of the increase of the gas dynamic pressure force (generated as the propellant is heated by the discharge) around the cathode tip and then contribute to thrust. The evaluation of these two acceleration mechanisms was well illustrated by Jahn (Jahn, 1968) who isolated the two processes in idealized self-field MPD thruster models with display the blowing and the pumping interaction separately. From both, a more realistic model is deducted where both mechanisms act simultaneously for the purpose to evaluate the total electromagnetic thrust which is considered to be the sum of the blowing and the pumping contributions derived separately. Indeed, By considering an infinite cylindrical column of conducting fluid with an uniform current beam normal to the cathode end surface such as $\mathbf{J} = j_x(r)\vec{x}$, the electromagnetic pumping contribution which force the plasma to contract radially (Pinch effect) (Bittencourt, 2004), can be illustrated in an idealized self-field MPD thruster model (see Fig.4.2.b) in cylindrical coordinate system (r, θ, x). The resulted Lorentz density body force is therefore radial and in equilibrium must be balanced by a radial gas pressure gradient (equilibrium pinch):

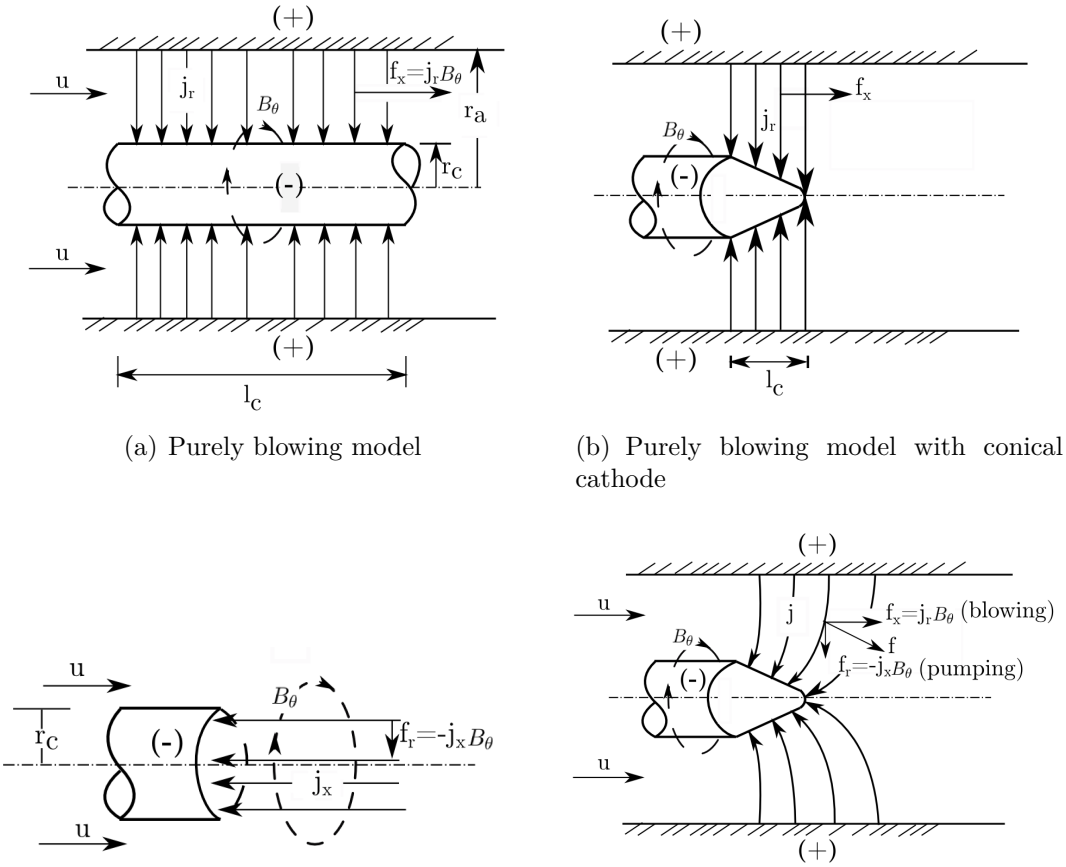

(a) Purely blowing model

(b) Purely blowing model with conical cathode

(c) Purely pumping model

(d) Hybrid model

FIGURE 4.2: Idealized models of a self-field thruster with an uniform radial current (a), radial current into conical cathode (b), uniform axial current (c) and the hybrid model (c) considering the cylindrical coordinate system and according to (Jahn, 1968): l_c is the cathode length, r_c and r_a are the cathode and the anode radius respectively

$$f_r = -j_x(r)B_\theta(r) = \frac{dp(r)}{dr} \tag{4.1}$$

From the Maxwell-Ampère's law (see Eq.2.9), we have in cylindrical coordinate

$$\frac{1}{r}\frac{d}{dr}(rB_\theta(r)) = \mu_0 j_x(r) \tag{4.2}$$

from which we get

$$j_x(r) = \frac{1}{\mu_0}\frac{dB_\theta(r)}{dr} + \frac{1}{\mu_0}\frac{B_\theta(r)}{r} \tag{4.3}$$

By replacing the above expression of $j_x(r)$ in Eq.4.1, we obtain

$$\frac{dp(r)}{dr} = -\frac{1}{2\mu_0 r^2}\frac{d}{dr}(r^2 B_\theta^2(r)) \tag{4.4}$$

By integrating this equation from $r = 0$ to a general radius $r > 0$,

$$p(r) - p(0) = -\frac{1}{2\mu_0}\int_0^r \frac{1}{r^2}\frac{d}{dr}(r^2 B_\theta^2(r)) \tag{4.5}$$

At the same time it is important to mention that inside a cylinder of general radius r, the total enclosed current $I_x(r)$ is

$$I_x(r) = \int_0^r j_x(r) 2\pi r dr \tag{4.6}$$

This total enclosed current is related to $B_\theta(r)$ by the Maxwell-Ampère's law in its integral form

$$B_\theta(r) = \frac{\mu_0}{2\pi r} I_x(r) = \frac{\mu_0}{r}\int_0^r j_x(r) r dr \tag{4.7}$$

From Eq.4.7, Eq.4.6 and Eq.4.5 knowing $j_x(r)$ we can deduce the radial distribution for $B_\theta(r)$, $I_x(r)$ and $p(r)$. Indeed, by considering the case in which the conducting fluid lies almost entirely inside $r = r_c$ with a constant current density $j_x(r)$,

$$j_x = \frac{I_0}{\pi r_c^2} \tag{4.8}$$

By substitution of Eq.4.8 in Eq.4.7, we have

$$B_\theta(r) = \frac{\mu_0}{r}\int_0^r j_x r dr = \begin{cases} \frac{\mu_0 I_0}{2\pi r_c^2} r & \text{if r} < r_c \\ \frac{\mu_0 I_0}{2\pi r} & \text{if } r \geq r_c, \end{cases} \tag{4.9}$$

Substituting this result into Eq.4.5 in the case in which $r < r_c$, since $p(r) = 0$ for $r \geq r_c$, we obtain a parabolic dependence for the pressure versus radius,

$$p(r) = -\frac{1}{2\mu_0}\int_0^r \frac{\mu_0^2 I_0^2 r^4}{4\pi^2 r_c^4} dr = \frac{\mu_0 I_0^2}{4\pi^2 r_c^2}(1 - \frac{r^2}{r_c^2}) \tag{4.10}$$

Since this pressure on the cathode is not balanced at the anode end of the discharge chamber, the integral of $p(r)$ over the cathode surface contributes to thrust with:

$$F_{pumping} = 2\pi\int_0^R p(r) r dr = \frac{\mu_0 I^2}{8\pi} \tag{4.11}$$

Now, the blowing mechanism is evaluated in a idealized self-field model that allows only radial current flow which is azimuthally and axially uniform between the co-cylindrical anode and cathode (see Fig.4.2.a). Analogous to the previous purely pumping self-field, the purely azimuthal self-induced field is deduced from the Maxwell-Ampère's law (see Eq.2.9). The obtained induced magnetic field is then linear in x and inversely proportional to r between the electrodes:

$$B_\theta(r, x) = \frac{\mu_0 I_0}{2\pi r}(1 - \frac{x}{l_c}) \tag{4.12}$$

Where $I_0 = 2\pi r l_c j_r$ is the total current and l_c the cathode length. The body Lorentz force density is thus purely axial and proportional to $\frac{x}{r^2}$:

$$f_x(r, x) = j_r B_\theta = \frac{\mu_0 I_0^2}{4\pi^2 r^2 l_c^2}(l_c - x) \tag{4.13}$$

By integrating Eq.4.13 over the gap volume, the total axial force applied to the gas stream is obtained:

$$F_{blowing} = \frac{\mu_0 I_0^2}{4\pi^2 r^2 l_c^2} \int_0^{l_c} \int_0^{2\pi} \int_{r_c}^{r_a} \frac{l_c - x}{r^2} r dr d\theta dx = \frac{\mu_0 I_0^2}{4\pi} ln \frac{r_a}{r_c} \tag{4.14}$$

In the case in which a conical-tip cathode is used, the above purely blowing electromagnetic thrust is modified to

$$F_{blowing} = \frac{\mu_0 I_0^2}{4\pi} (ln \frac{r_a}{r_c} + \frac{1}{4}) \tag{4.15}$$

The second term representing the blowing contribution within r_c.

Now, the total electromagnetic acceleration is computed as the sum of the above contributions from an idealized hybrid model involving the pumping and the blowing acceleration mechanisms discussed sperately above (see Fig.4.2.c).

$$F = F_{pumping} + F_{blowing} = \frac{\mu_0 I_0^2}{4\pi} (ln \frac{r_a}{r_c} + \frac{3}{4}) \tag{4.16}$$

This result show that the total electromagnetic thrust depend of the total discharge current and the thruster geometry through the ratio of anode to cathode radius and the cathode end surface (Fig4.2.b). In the other hand, it is independent of the mass flow rate and of the current distribution between anode and cathode, and more appropriate to the curved diffuse arc patterns actually observed in the MPD arcs (see Fig.4.2.d).

4.1.2 Applied-field MPD thrusters

In SFMPDT, the main acceleration mechanism is represented by the interaction between the discharge current and the self-induced magnetic field. That means, high thrust level (high specific impulse required for deep space missions) can only be obtained for high discharge current (5-100 kA) and consequently for high power (MWs). Contrary to SFMPDT, the AFMPDT, introduce new acceleration mechanisms that do not directly depend on the discharge current and thus can allow the thruster to effectively operate at lower powers and achieved high specific impulse (Krülle, Auweter-Kurtz, and Sasoh, 1998). Indeed, an external magnetic field is applied, having components in the axial and radial directions. Thus, an electromagnetic "swirling force" and a "Hall force" are generated. At all, four acceleration mechanisms have been identified. The relative importance of each depends upon thruster design and operating conditions (current, mass flow rate, applied field strength). The four mechanisms, as shown in Fig.6.1, are (Choueiri, 1998): The *gas dynamic acceleration* which contains the joule heating and the expansion of the plasma through physical and/or magnetic nozzle. The *self-field acceleration* take place as the discharge current arc interacts with the self-induced magnetic field leading to axial and radial acceleration of plasma. From the interaction of the discharge current with the applied magnetic field, substantial plasma rotation is produced. This is the *swirl acceleration* mechanism. The produced rotation kinetic energy can be partly converted via expansion in a magnetic nozzle into

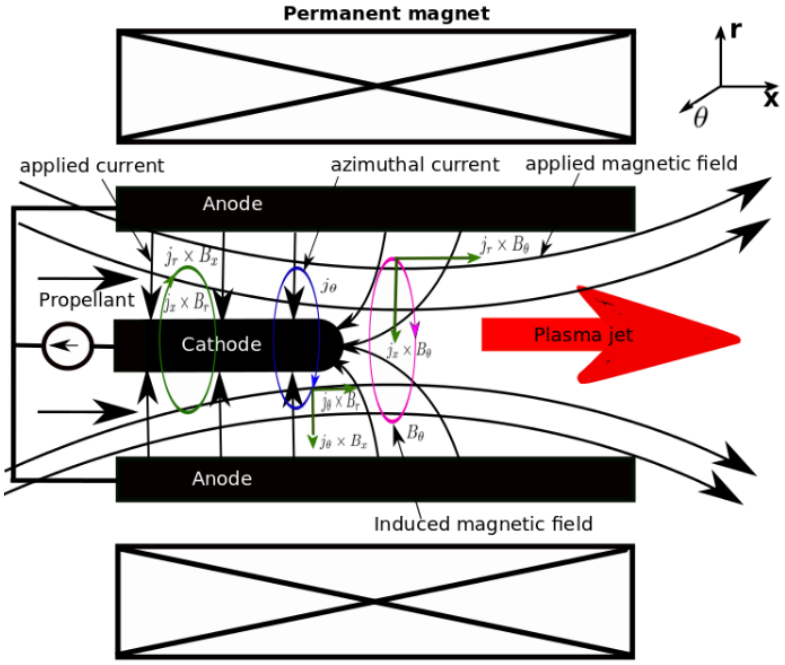

FIGURE 4.3: Principe design of an applied-field MPD thruster with coaxial applied magnetic field

axially directed thrust energy. And lastly, we have the *Hall acceleration* mechanism which is produced from the interaction of the induced azimuthal current (Hall current) with the applied magnetic field and produces an axial Lorentz force which increase thrust in axial direction and a radial Lorentz forces which confine the plasma by increasing the pumping force.

Other advantages in adopting an AFMPDT is the extension of a significant fraction of the current downstream of the thruster geometry particularly on the tip of the cathode. However, the complex acceleration processes of AFMPDT which depends on the distribution of interacting plasma parameters are not well understood yet and remain one of the main challenge in the field of MPD thrusters design and simulation.

4.1.3 Thrust evaluation

At typical operating condition of self-field MPD thrusters, the thermal contribution is proved to be much smaller than the electromagnetic contribution (Burton, Clark, and Jahn, 1983; Albertoni, Paganucci, and Andrenucci, 2015) so that the electromagnetic thrust can be assimilated to the total thrust F_{total}. For that condition, from Eq.4.16, Maecker (Maecker, 1955) introduced its well-known relation for continuum plasma and ideal approximation:

$$F_{Maecker} = \frac{\mu_0}{4\pi} I^2 (ln\frac{r_a}{r_c} + A) \tag{4.17}$$

where I is the total discharge current and A is a dimensionless constant between 0 and 1 (Sankaran, Choueiri, and Jardin, 2005). In this study, we considered $A = 0$ accordingly to the cathode tip form adopted in the present work (see sec.4.1.1).

r_a and r_c are the radii of anode and cathode, respectively. Maecker's model is known to predict the electromagnetic thrust with acceptable accuracy because of its capacity to provide good prediction of the magnetic pressure acting on the boundaries. Considering now that an external magnetic field is applied to create a field with axial lines of force with $B_r/B_x \ll 1$ and $B_{ap} \simeq B_x$ where B_r corresponds to the radial component of the applied magnetic field in a cylindrical coordinate system. The predominant acceleration mechanism in thrust production depends on the selection of operating parameters and thruster geometry. For moderate applied magnetic fields, the hall contribution can be neglected beside of the swirl, the electromagnetic and the thermal acceleration. As a consequence, it is possible to express the overall thrust produced by an applied-field MPD device as the sum of the axial directed self-field force, the thermal thrust and the swirl electromagnetic force which puts the plasma in rotation before being converted in useful axial thrust (Fradkin and Blackstock, 1970; Krülle, Auweter-Kurtz, and Sasoh, 1998; Albertoni, Paganucci, and Andrenucci, 2015)

$$F_{total} = T_{th} + T_{Self} + T_{Swirl} + T_{Hall} \simeq T_{Self} + T_{th} + T_{Swirl} \tag{4.18}$$

In Eq.4.18, T_{Swirl} represents an upper limit for the azimuthal acceleration force since viscous forces (highly collisional plasma) and diamagnetic effects (high ion temperatures) (Kagaya and Tahara, 2005) tend to reduce its converted fraction into useful thrust. Thus, the useful part of the azimuthal acceleration thrust contribution can be compute as

$$T_{Swirl} = \chi \int_V (\mathbf{J}_{dis} \times \mathbf{B}_{ap}) dV \tag{4.19}$$

where χ is the conversion factor which can be chosen between 0.2 and 0.5. The overall thrust of the applied field MPD thruster can be expressed as in (Kagaya and Tahara, 2005):

$$F_{total} = T_{Self} + T_{th} + \chi \int_V (\mathbf{J}_{dis} \times \mathbf{B}_{ap}) dV \tag{4.20}$$

where T_{Self}, the electromagnetic component of the total thrust is calculated with the volume integral of the axial component of the Lorentz force,

$$T_{Self} = \int_V (\mathbf{J}_{dis} \times \mathbf{B}_i)_x dV \tag{4.21}$$

And the thermal component can easily be deduced by subtracting the self and the swirl contribution from the total thrust as follows:

$$T_{th} = F_{total} - T_{Self} - T_{Swirl} \tag{4.22}$$

In an AFMPDT as in SFMPDT, the self Lorentz force consists mainly of the gradient of the magnetic pressure $B_i^2/(2\mu_0)$ where B_i is the induced magnetic field from the applied discharge current I. This magnetic pressure is exerted primarily on the back plate of the discharge chamber. Since $B_i \sim I$, at low discharge current the MPD thruster acts as an electrothermal device with a total thrust, F_{total} given by

$$F_{total} = \dot{m} a_0 + p_C A_C \tag{4.23}$$

Where $\dot{m}$ is the mass flow rate, a_0 is the plasma sound speed and p_C is the pressure at the cathode exit section, A_C.

4.2 Phenomenological description of the MPD thrusters

4.2.1 The magnetic pressure and the plasma confinement

The magnetic pressure is the radially oriented force per unit surface that a magnetic field exerts on a fluid column (plasma in the case of interest). In the steady-state condition, the MHD equation of Chap.2 are simplified as follows:

$$\nabla p = \mathbf{J} \times \mathbf{B} \tag{4.24}$$
$$\nabla \times \mathbf{B} = \mu_0 \mathbf{J} \tag{4.25}$$
$$\nabla \cdot \mathbf{B} = 0 \tag{4.26}$$

Substituting $\mathbf{J}$ in the above equations gives:

$$\nabla \cdot \mathbf{B} = 0 \tag{4.27}$$
$$\nabla p = \mu_0 (\nabla \times \mathbf{B}) \times \mathbf{B} \tag{4.28}$$

The Lorentz force in the RHS of Eq.4.28 can be written as the divergence of the magnetic part of the electromagnetic stress tensor $\overline{\overline{\tau}}^m$ (see Appendix.A),

$$\mathbf{J} \times \mathbf{B} = \frac{1}{\mu_0}(\nabla \times \mathbf{B}) \times \mathbf{B}$$
$$= \nabla \cdot (\overline{\overline{\tau}}^m) = \nabla \cdot [\frac{1}{\mu_0} \begin{pmatrix} (B_x^2 - B^2/2) & B_x B_y & B_x B_z \\ B_y B_x & (B_y^2 - B^2/2) & B_y B_z \\ B_z B_x & B_z B_y & (B_z^2 - B^2/2) \end{pmatrix}] \tag{4.29}$$

Then from Eq.4.28 we have:

$$\nabla p = \nabla \cdot (\overline{\overline{\tau}}^m) \qquad or \qquad \nabla \cdot (p\mathbf{I} - \overline{\overline{\tau}}^m) = 0 \tag{4.30}$$

In the case of an axial magnetic field $\mathbf{B} = B\vec{e_z}$, Eq.4.30 can be rewritten as follows:

$$\nabla \cdot \begin{pmatrix} (p + B^2/2\mu_0) & 0 & 0 \\ 0 & (p + B^2/2\mu_0) & 0 \\ 0 & 0 & (p - B^2/2\mu_0) \end{pmatrix} = \begin{pmatrix} 0 \\ 0 \\ 0 \end{pmatrix} \tag{4.31}$$

Thus,

$$\begin{cases} \frac{\partial}{\partial x}(p + B^2/2\mu_0) &= 0 \\ \frac{\partial}{\partial y}(p + B^2/2\mu_0) &= 0 \\ \frac{\partial}{\partial z}(p - B^2/2\mu_0) &= 0 \end{cases} \tag{4.32}$$

and with the Gauss's law $\frac{\partial B}{\partial z} = 0$ we have:

$$(p + B^2/2\mu_0) = constante \tag{4.33}$$

Thus, when an externally magnetic field is applied on a bounded plasma, the thermodynamic pressure radially decreases from the axis outward, while the magnetic pressure increases in the same direction such a way that, $p + B^2/2\mu_0$ remains constant at each point of the plasma according to Eq.4.33. And when the applied magnetic field is strong enough, the thermodynamic pressure vanishes on the outer boundary surface of the plasma with the consequence of the confinement of the plasma inside that outer surface by the magnetic field. Thus,

$$(p + B^2/2\mu_0)_{inside\ the\ plasma} = (p_0 + B_0^2/2\mu_0)_{outer\ surface} = constant \tag{4.34}$$

where p_0 and B_0 are the thermodynamic pressure and the magnetic field at the outer surface of the plasma. Since $p_0 = 0$, the constant can be evaluated and Eq.4.34 rewritten as:

$$(p + B^2/2\mu_0)_{inside\ the\ plasma} = (p_0 + B_0^2/2\mu_0)_{outer\ surface} = p_{max} \tag{4.35}$$

$p_{max} = B_0^2/2\mu_0$ is the maximum plasma pressure that can be contained for a given magnetic field intensity B_0. Thus, the magnetic pressure concept appear then clearly as the confinement mechanism in various MHD technological applications such that thermonuclear fusion devices and MPD thrusters where the hot plasma has to be confined away from material surfaces.

To measured the relative importance of the thermodynamic pressure over the magnetic pressure, a dimensionless plasma beta parameter is defined as:

$$\beta = \frac{p}{B^2/2\mu_0} \tag{4.36}$$

In a confined plasma, β range between 0 and 1 since the pressure inside the plasma is always less than $B_0^2/2\mu_0$ the magnetic pressure at the outer surface. Of course, in the region of no confinement, β can be more than unity. In the case of the MPD thrusters modelling, the plasma beta helps to understand the plasma depletion near the anode (Kubota, 2009) and contributes to provide a more stable and suitable pressure initial condition (Sankaran, 2005).

4.2.2 The critical current and the onset of instabilities

Several experiment and theoretical investigations shown that the overall efficiency and the exhaust velocity increase with the current. Thus, the specific impulse and the efficiency of the MPD thruster, which are the most important MPD thruster performance characteristics, also increase with the current. Regrettably, it has been found that for each geometrical arrangement, a critical current I_c exists beyond which the MPD thruster operation leads to strong numerical instabilities (Lapointe, 1992; Sankaran, 2005), which makes the solvers unstable and undermines their value. From this point, the flow becomes highly unstable with important oscillations of the arc voltage and in the same time the erosion rate of

the electrodes increases by orders of magnitude. More generally for a particular propellant, these instabilities were related to what we call in this thesis the power parameter $I^2/\dot{\mathbf{m}}$ (Burton, Clark, and Jahn, 1983). High value of power parameter correspond to predominantly electromagnetic acceleration, and provide higher values of specific impulse. Low values of power parameter correspond to predominantly electrothermal acceleration, and lower values of specific impulse.

To predict the electromagnetic force of an idealized self-field MPD thruster, including both axial and radial component of Lorentz force, Maecker (Maecker, 1955) proposed a continuum based model. The Maecker model express thrust as a function of geometry and discharge current:

$$F_{Maecker} = \frac{\mu_0}{4\pi}(ln\frac{r_a}{r_c} + A)I^2 = bI^2 \tag{4.37}$$

where r_a and r_c are the radii of the anode and the cathode, respectively, and A is a dimensionless constant between 0 and 1. This formula indicates that the electromagnetic thrust caused by the self-field MPD thrusters is proportional to I^2 and the proportionality factor b only depends on geometry of the thruster. The model of Maecker provides good thrust approximation most particularly by higher current and will be very helpful in this thesis in the understanding of thrust scaling trends. In the other hand, several experimental activities have shown that, ionization and acceleration are so far the most important energy sinks in MPD thrusters beside electrode heating, erosion of cathode, excitation of neutral atom and plasma thermal losses (Sankaran, 2005) and both share the same source, namely the current power. At the nominal regime (see (Choueiri, 1998) and references therein), there is an equipartition of energy sinks between both ionization and the useful acceleration of the ionized propellant. So, in terms of power, one can write:

$$\frac{1}{2}Fv_{ex} = \dot{m}(\frac{\phi_i}{M_a}) \tag{4.38}$$

where v_{ex} is the plasma exhaust velocity, ϕ_i and M_a are the first ionization potential and the atomic weight of the propellant, $\dot{m}$ the mass flow rate of the gas propellant and F the thrust with which the ionized plasma is pushed outside the thruster. By using Eq.4.38, the nominal regime equation (Eq.4.37) can be rewritten as follows:

$$\frac{\mu_0}{4\pi}(ln\frac{r_a}{r_c} + A)I^2u_{ex} = 2\dot{m}(\frac{\phi_i}{M_a}) = \dot{m}u_{ci}^2 \tag{4.39}$$

where u_{ci} is the critical ionization velocity defined as

$$u_{ci} = (\frac{2\phi_i}{M_a})^{1/2} \tag{4.40}$$

Thus the nominal operation correspond to the operating condition of MPD thrusters for that $v_{ex} = u_{ci}$ for the current value I_c named Alfvén critical ionization current. This current can be obtained by substitution in Eq.4.39.

$$I_c = [\frac{\dot{m}\sqrt{2\phi_i/M_a}}{\frac{\mu_0}{4\pi}(ln\frac{r_a}{r_c} + A)}]^{1/2} \tag{4.41}$$

This characteristic current is used to nondimensionalize the thruster current and this conducts to the dimensionless parameter ξ defined as

$$\xi = \frac{I}{I_c} = [\frac{\frac{\mu_0}{4\pi} I^2 (ln\frac{r_a}{r_c} + A)}{\dot{m}\sqrt{2\phi_i/M_a}}]^{1/2} \tag{4.42}$$

Choueiri (Choueiri, 1998) shown that the nominal operation is achieved at $\xi = 1$ and many experimental and theoretical research are being done to push it to as high values (≥ 1) as possible. In this thesis, to analyse the MPD thrusters, ξ will be used instead of the power parameter $I^2/\dot{\mathbf{m}}$ since the propellant (Argon) remains the same for all our simulations and it provides more informations concerning the thrusters operating conditions than the power parameter. Indeed, we use it more particularly in Chap.5 by changing the configurations of the thruster with the purpose to identified the most stable and efficient thruster geometries.

4.2.3 The Tank pressure

With the increase of the computational resources, several researchers make use of CFD to investigate the MPD thrusters. To obtain realistic solution, appropriate boundary conditions are required. Therefore, there is a large range of boundary conditions types which permit the flow to enter and exit the solution domain. In the case of the MPD thrusters supposed to operate encountered in outer space it is very important to reproduce the low pressure vacuum environment and thus to be able to reproduce the true performance of the thrusters in vacuum. Several previous studies mentioned the fact that the thrust and the efficiency were often overestimated in ground experimental tests because the tank outside the thruster could not reach the low pressure likely to be in space. Indeed, using spectroscopic methods, connolly et al.(Connolly, Sovie, and Seikel, 1970) measured the species axial velocity in the plasma plume in a series of experiments at NASA's Lewis Research Center on a water cooled applied-field MPD thruster. They observed that the performance varied with the background pressure and the plasma is significantly accelerated 10 *cm* downstream of the thruster exit. This observation point out the fact that, there is an important amount of magnetic field and currents downstream of the exit plane which are responsible of the Lorentz accelerator force applied on the plasma plume at that point. Another suggestion is that, the boundary conditions outside of the thruster are of huge importance in their analysis. In CFD, to avoid the effect of the outer environment to affect the results, the computational domain is generally assumed to be large enough such that there are no normal gradients in any of the flow properties at the free stream boundaries. This solution is practical but also computational expensive. In the present thesis to overcome this issue a special attention will be given to the pressure boundary condition at the tank's boundaries considering a considerably large tank volume.

4.2.4 Current distribution and the magnetic Reynolds number

In the general case of a nonstationary fluid with a finite electrical conductivity, the magnetic induction will change as a result of convection with the fluid and diffusion

through the fluid. These two mechanisms are represented respectively by the two terms on the right hand side of Eq.2.13 of sec.2.1.3 of Chap.2. By considering the subscript *ref* as the characteristic value of any quantity, the ratio of the convection to diffusion effects is characterized by the dimensionless parameter named the magnetic Reynolds number in analogy with the ordinary Reynolds number of fluid mechanics (Ferziger and Peric, 2002).

$$Re_m = \mu_0 L_{ref} \sigma_{ref} U_{ref} \tag{4.43}$$

Where U_{ref} and L_{ref} are the reference velocity and the characteristic distance for variation of B_{ind} namely in this case, the thruster length. For flows with $Re_m \ll 1$, the magnetic field diffusion governed by the the resistive term $\frac{1}{\mu_0 \sigma}\Delta\mathbf{B}$ in Eq.2.13 is relatively large compared to the convective term $\nabla \times (\mathbf{U} \times \mathbf{B})$ so that the convection of $\mathbf{B}$ lines by the fluid is negligible, and the magnetic induction produced by the currents in the fluid can be neglected. When $Re_m \gg 1$, the convective term is dominant and the diffusion of the magnetic field through the fluid become insignificant and the diffusion term in Eq.2.13 can be neglected.

At the same time it is also possible to define a scale length Λ_m for which the diffusive and convective effects are of the same order. This scale length will be called the magnetic interaction length (Chanty, 1992) and is defined by the following expression:

$$\Lambda_m = \frac{1}{\mu_0 \sigma_{ref} U_{ref}} = \frac{L_{ref}}{Re_m} \tag{4.44}$$

With this definition the magnetic Reynolds number becomes:

$$Re_m = \frac{L_{ref}}{\Lambda_m} \tag{4.45}$$

As the magnetic Reynolds number increases, the current concentration at the ends of the thruster channel becomes more pronounced. Three regions are then distinguished: The inlet current concentration where there is a strong dissipation, the core of the channel where there is little current and little dissipation, and the exit current concentration regions, again with strong dissipation. The current concentration regions at the ends of the channel scale as the magnetic interaction length. As the magnetic Reynolds number decreases, both the inlet and exit current concentration regions joined each other and a homogeneous discharge current repartition over the whole length of the channel is created.

In the AFMPDT, the induced $\mathbf{B}_{ind}$ and the applied $\mathbf{B}_{ap}$ magnetic fields coexist. The conductive plasma is surrounded by a solenoid such that its current density is deducted from the simplified Ohm's law of sec.2.1.3 by neglecting the Hall effect term and the electron pressure term:

$$\mathbf{J} = \sigma(\mathbf{E} + \mathbf{U} \times \mathbf{B}) \tag{4.46}$$

where $\mathbf{B} = \mathbf{B}_{ap} + \mathbf{B}_{ind}$ is the total magnetic field vector. By short-circuiting the the electrodes, the plasma currents are due to the plasma flow with velocity $\mathbf{U}$ in total magnetic field $\mathbf{B}$, so that $\mathbf{E} = \vec{0}$ in the laboratory frame. Then, the

electric field in another frame, moving at **U** relative to the laboratory frame, is obtained as:

$$\mathbf{E}^{'} = \mathbf{E} + \mathbf{U} \times \mathbf{B} = \mathbf{U} \times \mathbf{B} \tag{4.47}$$

Thus, $J \sim \sigma E^{'} \sim \sigma U B$ in order of magnitude and by applying the Ampere's law on both the induced and the external fields, we obtain:

$$\begin{cases} \nabla \times \mathbf{B}_{ind} &= \mu_0 \mathbf{J} \\ \nabla \times \mathbf{B}_{ap} &= 0 \qquad \text{(inside the plasma)} \end{cases} \tag{4.48}$$

By integrating the first equation of the above system and by substituting J, we have

$$(B_{ind})_{ref} = \mu_0 L_{ref} J_{ref} = \mu_0 L_{ref} \sigma_{ref} U_{ref} B_{ref} \tag{4.49}$$

Since $\mathbf{B} = \mathbf{B}_{ap} + \mathbf{B}_{ind}$, then we have:

$$\frac{(B_{ind})_{ref}}{(B_{ap})_{ref} + (B_{ind})_{ref}} = \mu_0 L_{ref} \sigma_{ref} U_{ref} \equiv Re_m \tag{4.50}$$

Where the applied field B_{ap} is taken at the cathode tip and the induced field B_{ind} at the cathode surface direct at the front of inlet. Re_m is the Reynolds magnetic number and can be interpreted as the measure of the ratio of induced to total magnetic field. Eq.4.50 indicates that, for $Re_m = 1$, the induced and the external fields are of equal importance. If $Re_m \gg 1$, the induced field dominates the problem and if $Re_m \ll 1$, it can be reasonably neglected.

Additionally to its definition as the measure of the effect of the flow on **B**, by using Eq.2.25, the dimensionless magnetic interaction parameter (Kruger and Mitchner, 1973) may also be defined more generally as the measure of the ratio of the Lorentz force $\mathbf{J} \times \mathbf{B}$ to the inertia force.

$$S = \frac{L_{ref} \sigma_{ref} B_{ref}^2}{\rho_{ref} U_{ref}} \tag{4.51}$$

It is then possible to define several other dimensionless parameters all dependent to Re_m and S. They are:

The Hartmann number, which is a measure of the ratio of the $\mathbf{J} \times \mathbf{B}$ force to the viscous force in incompressible MHD flow,

$$H = L_{ref} B_{ref} (\frac{\sigma_{ref}}{\mu_{ref}})^{1/2} = (SRe)^{1/2} \tag{4.52}$$

where Re and μ_{ref} are the Reynolds number of fluid mechanics and the dynamic viscosity of the fluid respectively.

The Alfvèn Mach number:

$$M_A = \frac{U_{ref}}{(v_A)_{ref}} = (Re_m / S)^{1/2} \tag{4.53}$$

where $(v_A)_{ref}$ is the characteristic Alfvèn speed of Eq.2.74 in sec.2.4.

The Lundquist number which is the value of the magnetic Reynolds number at the Alfvèn speed.

$$L = L_{ref}\sigma_{ref}B_{ref}(\frac{\mu_0}{\rho_{ref}})^{1/2} = (SRe_m)^{1/2} \tag{4.54}$$

4.2.5 Plasma sheath and the anode potential fall

In the present work, the plasma is treated as quasineutral fluid. However, at the interface of the plasma and the boundary surface, there is a plasma sheath region where the quasineutrality of the plasma fails i.e where the number densities of ions and electrons are different. Bittencourt (Bittencourt, 2004) defined the plasma sheath as the boundary layer in the region near the wall of any body surface of a solid material when the latter is immersed in a plasma. The body gain a negative charge and consequently a negative potential with respect to the plasma potential. Concerning MPD thrusters, the existence of the plasma sheath region at the anode is one of the principal MPD thruster's performance limiter. Since it is designated by several studies (Myers and Soulas, 1992; Niewood, 1993; Lev and Choueiri, 2012) to be a great contributor to SFMPDTs and AFMPDTs energy dissipation. For instance, Myers et al.(Myers and Soulas, 1992) highlighted the linear positive correlation of the anode sheath voltage fall with discharge current and applied magnetic field. This correlation, according to Myers works, is not due to direct impact of the applied magnetic field on the anode voltage fall but to the indirect effect of applied magnetic field through the pumping radial Lorentz force. Lev et al.(Lev and Choueiri, 2012) explains that the increase of the applied magnetic field leads to an increase of the radial pinching Lorentz force which in turn decreases the plasma density in the near anode region. This diminution of the plasma density at the edge of the anode reduces the electrons density and to kept a constant density current on the anode, a larger sheath potential fall for attracting electrons through the sheath is required. The larger is the applied magnetic field, the larger is the anode plasma depletion and consequently larger is the anode potential fall through the sheath. The plasma sheath is not included in the present code and its mathematical description will not be presented here. However, the dependence of the applied magnetic field on plasma density reduction at the anode surface due to the pumping radial Lorentz force will be presented.

4.3 Preceding computational efforts of the MPD thrusters

4.3.1 Self-field MPD thrusters

Since the beginning of the designing and investigation of self-field MPD thrusters at the end of the sixties with the works of Morozov (Brushlinskii, Gerlakh, and Morozov, 1968), many efforts have been made by researchers to understand the physics of discharge and to develop appropriate code. In contrast with the hardware simplicity of the MPD thruster devices (see Fig.4.1), their problem can not be solve easily because of the extreme complexity of the physics involve. The

few problem areas are physical and numerical. As physical problem we have real gas effect which includes the process of ionization and recombination, the thermal non-equilibrium of the formed plasma ($T_e \neq T_i \neq T_h$, T_e, T_i and T_h are the electrons, ions and heavy particles temperature respectively), the problem of friction (low density and high temperature environment), the Hall effect, the strong gas dynamic expansion, the effect of anomalous transport (electrical conductivity) and difficulty to separate flow and discharge by high magnetic Reynolds number. In the other hand, we have numerical issues. The necessary coupling of partial differential equations involving the Maxwell equation which are elliptical with the Navier-Stokes equations which are hyperbolic including non linearities and step gradients. All these listed problems make a realistic description of the acceleration process analytically inaccurate. Additionally to these issues, we have the high cost of high-power thruster experimental facilities. To overcome all these difficulties, numerical research appears as the best option to investigate self-field MPD thrusters helped by the improved availability of computational power. Recently, notable numerical studies focussing on the simulation of the plasma flow inside a self-field MPD thruster have been carry out. Niewood (Niewood, 1989) proposed a finite difference, one dimensional unsteady method dedicated to the self-field MPD thrusters plasma flow investigation. For the calculation of the convective fluxes of continuity and momentum equations the Rusanov's method is used while the MacCormack's method is used to deal with the magnetic field and the electron temperature equations. The electron continuity and the ion temperature were computed by the Donor cell method. Chanty (Chanty, 1992) employed the Galerkin finite difference method coupled with a perturbations theory on a subdivided domain to study various aspect of the MPD thruster's flow field. Niewood (Niewood, 1993) developed a axisymmetric method to solve the MHD equations using the finite difference method. The axial component of the convective flux vector is computed using the Steger-Warming scheme while the radial component is evaluated with the Rusanov's method. Lapointe (Lapointe, 1991) used a two dimensional, thermal equilibrium, single fluid MHD code which incorporates classical plasma transport coefficients and Hall effect to predict steady-state self-field MPD thrusters performance. The code assumes the perfect gas equation of state, a fully ionized Argon plasma and does not include electrode sheath effects. Moreover, to refined the calculations of classical plasma transport coefficients, the separate electron and ions temperatures is included (Lapointe, 1992) and provide more accuracy concerning the plasma voltage drop, viscous flow loses and thruster efficiency. Caldo proposed an unsteady two dimensional two temperature numerical model to investigate the effects of anomalous transport on the fluid flow and thrusters efficiency. A modified finite difference MacCormack's method is used for fluid flow simulation, while steady magnetic field equation was computed with a modified Jacobi method. At the Institute of Space System (IRS) of the university of Stuttgart, in order to assess the performance range and achieve a better understanding of the self-field MPD thrusters, numerical MPD codes have been developed and applied. Indeed, Sleziona (Sleziona, Auweter-Kurtz, and Schrade, 1992; Sleziona, Auweter-Kurtz, and Schrade, 1993) proposed a finite volume two dimensional and thermal nonequilibrium code which allow the determination of the current. Their code used a Godunov upwind flux interpolations for the non linear hyperbolic partial

differential equations for the flow field while a modified Gauss-Seidel algorithm is used to solve the elliptical electromagnetic discharge equation and the electron energy equation for the steady phase. To improve the conformity with the physical phenomena of the plasma flow in the region of high specific impulses, the code includes a higher ionization mode and real gas effects for Argon. Winter (Winter et al., 1997) developed an Osher method to calculate the inviscid flux vector while the parabolic fluxes are computed with a finite difference method. Heiermann (Heiermann, 2002) employed a finite volume method to solve a turbulent axisymmetric Argon plasma flow using unstructured and adaptive meshes. A flux vector splitting scheme is used to calculate the inviscid fluxes and the approximate solution at the cell faces are linearly reconstructed by using a weighted essentially non-oscillatory (WENO) scheme. Hall effect, thermal nonequilibrium and reactions are considered. Mikellides (Mikellides, 2004) utilized the multiblock arbitrary-coordinate hydromagnetic (MACH2) code to investigate the operation and performance of a megawatt-class, quasi-steady, self-field MPD thruster. Sankaran (Sankaran, 2005) used a characteristics-splitting scheme coupled with an anti-diffusion technique for the simulation of ideal MHD equations solving flow and magnetic field equations in a self-consistent manner and extended it to the plasma flow simulation of the princeton's Argon-fed full-scale benchmark thruster and the lithium force accelerator. His numerical scheme includes a detailed model of classical transport, real gas equation of state, multi-level ionization models, anomalous transport and multi-temperature effects for Argon and lithium plasmas. Kubota (Kubota, 2009) proposed an unsteady two dimensional model for MPD thrusters investigation. The TVD Lax-Friedrich scheme is used and coupled with a minmod limiter to deal with convective flux vector and the MUSCL (Monotonic upstream schemes for conservation laws) schemes to maintain a second order spatial accuracy. This Algorithm incorporates a nonequilibrium single level ionization and recombination process, two temperatures model with the effects of viscosity and a collisional radiative model for Argon ion. More recently, Ahangar (Ahangar, Ebrahimi, and Shams, 2014) used a most completed two dimensional axisymmetric code to simulate the plasma flow field in a self-field MPD thruster. They make used of the Roe's scheme in combination with Powell's eigensystem technique for the convective flux vector evaluation. To obtain more stability and accuracy the code is coupled with a modified MUSCL technique called OMUSCL2. To accurately capture the physics of plasma phenomena, different physical-chemical sub-models including multi level non-equilibrium ionization model, generalized Ohm's law for partially ionized plasma, micro-instabilities effects, two temperature model and a real gas equation of state are considered.

Despite the important progress realized so far by the aforementioned computational efforts, there still remains something to do for the improvement of the MPD thrusters modelisation. The areas of improvement can be classified in three categories: The equations formulation, the physical models and the numerical schemes used to solve the equations. In fact, formulate the equations in non conservative form can lead to numerical instabilities at high value of power parameter $I^2/\dot{\mathbf{m}}$. Indeed, the thruster acceleration mode switches from predominantly electrothermal mode to predominantly electromagnetic mode as the power parameter increases at constant mass flow rate. This causes the total energy to be dominated by the

magnetic and the kinetic energy due to the strong expansion of the plasma at the exit of the thruster in a low density environment. Wrong estimation of one of them conducts to a negative internal energy or pressure. Niewood faces the same issue in (Niewood, 1989) where the fluid flow equations and the discharge equation are not solved in self-consistent manner. Therefore, the fluid flow and the magnetic equations have to be formulated conservatively and solved self-consistently (Sankaran, 2005).

4.3.2 Applied-field MPD thrusters

Concerning the AFMPDT, research over the last decades has mainly been experimental than theoritical because of the insufficient comprehension of the acceleration and power loss mechanism involved in the AFMPDT. Nevertheless, beside the huge research activities concerning the self-field MPD thrusters, several theoretical analyses have also been made to better understand the complex physical process involved in the AFMPDT and to propose designing guidelines for such devices. Krülle (Krülle, 1972) used simple set of flow equations with an assumed applied-field distribution to study acceleration mechanisms at low current densities and mass-flow rates. The model used assumed that the plasma is fully ionized and the self-induced fields are negligible when compared to the applied magnetic field. Thus, the acceleration effects of self-induced magnetic field even the Joule heating are not taken into account. However, In his analysis, a considerable part of the local thrust was caused by pressure forces balancing the radial confinement by the pumping component of the Hall electromagnetic body force $j_\theta B_x$. Substantial azimuthal Hall currents were also calculated well downstream of the thruster's exit. The magnitude of these currents and their persistence downstream of the exhaust plane increased with applied magnetic field strength. Tankara and Kimura (Tankara and Kimura, 1988) with their finite element, particularly the Galerkin weighted residual method, predicted the current distribution and plasma acceleration mechanisms in MPD arcjets with applied magnetic fields. Their code is based on two-dimensional set of induction equation and quasi-one dimensional gas dynamic equations resolved with a Runge-Kutta method. They come to the conclusion that, the higher current concentration on the cathode base can be relaxed by increasing the strength of applied magnetic field, although in the case of strong applied magnetic field there exits the possibility of the occurrence of a current vortex in the downstream region. The axial and azimuthal body forces increase with the applied magnetic field strength and when the discharge current decreased, the azimuthal body force caused by the applied magnetic field can be more important than the axial self-field body force. Mikellides (Mikellides, Turchi, and Roderick, 2000) used the finite volume based code MACH2 to study plasma acceleration and thrust performance on the NASA Lewis Research Center $100 - kW$, steady-state, AFMPDT for a wide range of applied magnetic field strengths $0.034 - 0.102\ T$ at cathode tip, discharge current $750 - 1250\ A$ with a constant Argon mass-flow rate $\dot{m} = 0.1\ g/s$. They captured the expected linear increase of thrust with both applied magnetic field strength and discharge current. Plasma voltage prediction captured both the magnitude and the linear increase with increasing applied

magnetic field strength. Most importantly, They also found that the electromagnetic azimuthal force applied to the plasma is opposed by viscous forces that limit the maximum attainable rotational speed to magnitude much smaller than values expected only from inertia. The finite volume based code for Argon plasma including thermal and chemical non-equilibrium models, SAMSA (Self and Applied field MPD thrusters Simulation Algorithm), previously developed at the university of Stuttgart (Sleziona, Auweter-Kurtz, and Schrade, 1992; Sleziona, Auweter-Kurtz, and Schrade, 1993) is extended to the study of AFMPDT with the purpose to enhance their performance by optimizing the geometry (M. Auweter-Kurtz, Fertig, and Kurtz, 2005). Recent results with AFMPDT have shown that the ratio of the input power to the anode power fraction increased with increasing the axial magnetic field strength and the anode radius. Kubota et al.(Kubota and Funaki, 2009) investigated the acceleration mechanism of a plasma flow within an AFMPDT with a two dimensional numerical code whose physical model includes the ion-rich sheath effect and a heat transfer model concerning the electron energy on the anode. The maximum magnetic field inside the thrusters range from 0.008 T to 0.25 T with a constant mass flow rate of 0.1 g/s and a constant discharge current of 1000 A. He concludes that most of the azimuthal kinetic energy and the specific enthalpy is lost as the thermal conduction to the electrodes and as consequence, an operation with low swirl motion and with high azimuthal current is preferable.

Despite the fact that basic properties of flow fields inside the AFMPDT have been identified and illustrated in several numerical studies, research on AFMPDT remain principally experimental because of its very complex mechanisms of thrust production and energy conversion. The few numerical studies present in the litterature are either based on simple set of equations with one or two dimensional geometries or used a complex numerical schemes involving Riemann solvers or characteristic decompositions and Jacobian evaluation making them not easier to implement.

4.4 Summary

In the present chapter, the MPD thrusters are presented and the physic of thrust production is explain for each type involved in this work, namely the SFMPDT and the AFMPDT. Furthermore, some challenging phenomena encountered in MPD thrusters investigation are presented. They are, the onset phenomenon, the vacuum chamber pressure, the effect of magnetic field strength on the plasma current distribution within the thruster through the magnetic Reynold number and the plasma sheath. At the end of this Chapter, previous numerical studies of MPD thrusters are listed. As the main purpose of this work is to propose a new reliable numerical technique to deal with plasma flow inside MPD thrusters, experimental and previous numerical simulation results are used in the next chapter to demonstrate the ability of the present code to capture the simulated thruster behaviour. Once the verification of the developed resistive MHD solver is accomplished, a parameter study is done to get insight of the improvement of the SFMPDT acceleration performance.

Chapter 5

Resistive MHD results: Self-field MPD thruster simulations

Confident with the results obtained in Chap.3 with the developed density-based code and its physical and numerical models, we are going now in the present chapter, through comparisons of our calculated results with experimental data and simulations of previous works, to validate the resistive version of the code. The purpose to do so is to be able to make predictions on less investigated self-field MPD thrusters and obtain fundamental plasma properties concerning thrust production and energy repartition. The chosen geometries for the simulations are the Princeton's Full Scale Benchmark Thruster (PFSBT) and Extended Anode Thruster (PEAT) and the Villani-H MPD thruster. First, general properties and previous studies of self-field MPD thrusters are shown.

5.1 Physical modelling

The model we present in this work is dedicated to the description of an electrically conducting but electrically neutral fluid. We assumed that the propellant gas (Argon) is injected into the discharge chamber as a fully-ionized fluid in a state of thermal equilibrium ($T = T_e = T_i$, where the indices e and i refer to electron and ion, respectively). Electrical sheath, Hall effect and radiation processes are neglected. We did not deal with turbulence because of his negligible contribution to the studied cases of interest. In the other hand, for higher discharge current, it is well known that the ideal equation of state fails for prediction of thermodynamic variables of the plasma flow inside MPD thrusters simulation since it involved insufficient energy sinks (Sankaran, 2005). However, in this thesis to reduce the harmful effect of using ideal equation of state, we implement the real gas ratio of specific heats as a function of temperature according to (Sankaran, 2005; Xisto, Pascoa, and Oliviera, 2015).

$$\gamma(T) = K_3 + K_4 e^{(T-K_5)/K_6)^2} \tag{5.1}$$

where K_3, K_4, K_5 and K_6 are coefficients that were approximated to fit a particular function and can be found in Tab.5.1. This particular $\gamma(T)$ function can be switch on in our code before starting simulation if required.

In the next sections, we used the above described numerical approach to simulate two of the Princeton's self-field MPD thrusters. The physical model, initial and boundary conditions are given. Results are presented and discussed by using

TABLE 5.1: Coefficients of the calculation of γ according to (Xisto, Pascoa, and Oliviera, 2015)

Range of T $[K]$	K_3	K_4	K_5	K_6
$8000 < T \leq 13000$	1.112166	0.529956	8050.606514	1318.851134
$13000 < T \leq 40000$	1.105401	0.025267	15142.82094	2394.061632

the dimensionless parameter ξ defined by Eq.4.42 in Chap.4 rather than the discharge current. The performance parameters, specific impulse and efficiency are evaluated by using the Eq.1.11 and Eq.1.12 of Chap.1.

5.2 The Princeton's Full Scale Benchmark Thruster

The Princeton's full scale benchmark thruster (PFSBT) presented in Fig.5.1, studied numerically by Sankaran (Sankaran, Choueiri, and Jardin, 2005) and widely experimentally investigated at the department of mechanical aerospace sciences of the same university (Boyle, 1974; Burton, Clark, and Jahn, 1983), is chosen to test the validity of the resistive version of the proposed density-based algorithm. The PFSBT device consists of a coaxial 0.95 *cm* thoriated tungsten cathode radius with 20 *cm* length surrounded by an anode, which is an annular aluminium disk of 10.2 *cm* of diameter with a 20.4 *cm* diameter orifice. The solution is computed iteratively from an initial condition to steady (quasi) state. Thus appropriate boundary conditions are needed for the computational domain illustrated in Fig.5.1.

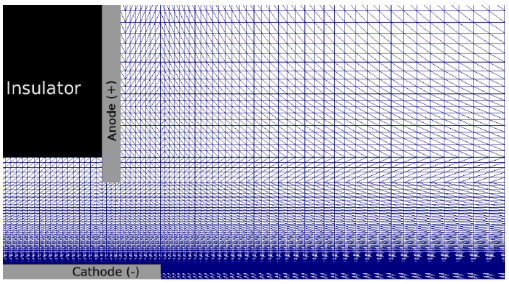

FIGURE 5.1: PFSBT Computational domain

Experimentally, Argon propellant is injected through an insulating boron nitride backplate, with either all the propellant injected near the anode radius, or with half of the propellant injected through an annulus near the cathode base and half through a ring of 12 evenly spaced ports located 3.8 *cm* radially from the thruster axis (50 : 50).

5.2.1 Boundary and initial conditions

The partial differential equations of sec.2.1.4 in Chap.2 are hyperbolic (Kurganov, Noelle, and Petrova, 2001). Thus, they must be calculated from an initial state to

a steady state by a time-marching algorithm with suitable boundary conditions. For the simulations conducted in this chapter, the inputs of the code consist of the thruster discharge current, the propellant mass flow rate and a specified plasma temperature. The computational domain is chosen to be large enough to enclose all the current within the domain.

Hydrodynamic conditions

At inlet, the propellant with a specified mass flow rate (6 g/s) is assumed to be injected with a velocity normal and uniformly to the inlet patch, which correspond most closely to the 50 : 50 propellant split used in the experiments (Boyle, 1974; Burton, Clark, and Jahn, 1983). Consequently, a no gradient boundary condition is adopted for pressure at inlet which is calculated from the equation of state in response to the computational domain solution. Practically, the propellant at room temperature cross the inlet as neutral gas and it is supposed to be heated and fully ionized by the joule heating few millimeters downstream of the thruster inlet. This process can not be captured by the fluid theory used in this thesis, thus the temperature of the propellant at inlet is considered to be high enough (around 1 eV) so that the plasma flow can be considered as fully ionized.

On the anode, a sheath region (King and Callas, 1988) (consequently an electric field) which can be defined as the boundary process sets by anode in response to the presence of a potential difference formed between anode and plasma, is observed. The existence of a sheath region exhibits a non neutral charge density near the wall which makes the plasma to be non fully ionized. Consequently the assumptions of quasi-neutrality, single fluid and fully ionized plasma adopted in this work failed. Therefore, for this work, sheaths are ignored. At all solid boundaries, a no slip condition is imposed for the velocity field and all convective fluxes as presented in Eq.3.59 of Chap.3 are zero since:

$$\mathbf{n} \cdot \mathbf{U} = 0 \tag{5.2}$$

where $\mathbf{n}$ is the normal unit vector of the considered wall boundary surface. To the wall, the temperature is considered slightly less than the plasma flow temperature because thermal conduction into the wall is not currently taking into account in the code. At the outlet, the normal gradients in any of the flow properties are set to zero and a wave transmissive boundary condition is applied for pressure to create a tendency towards the specified outlet value while setting the instantaneous computational value to be something as consistent as possible with the outgoing characteristics. This is done by solving the equation (*OpenFOAM version 2.3.0*):

$$\frac{D}{Dt}(\psi, \mathbf{U}_w) = 0 \tag{5.3}$$

with $\psi = \frac{1}{RT} = \frac{\rho}{p}$ the compressibility, $\mathbf{U}_w$ the wave velocity at outlet and $\frac{D}{Dt}$ the Lagrangian time-derivative moving with plasma. The initial value of pressure in the computational domain is chosen in such a way that $\beta = \frac{p}{B^2/2\mu_0} > 10^{-2}$ (Sankaran, 2005) to ensure the conservation of the energy equation since the thermodynamic pressure is deducted from the total energy density as follows:

$$\frac{p}{\gamma - 1} = \rho E - \frac{1}{2}\rho|\mathbf{U}|^2 - \frac{|\mathbf{B}|^2}{2\mu_0} \tag{5.4}$$

Boundary conditions for electromagnetic fields

To be able to integrate the induction equation over time, boundary conditions for magnetic field have to be specified. As described in sec.4.1.1 of Chap.4, the initial induced azimuthal magnetic field $B_{\theta,0}$ is generated at inlet by the discharge current within a coaxial thruster can be determined from the Maxwell-Ampère's law with the expression:

$$B_{\theta,0} = \frac{\mu_0 I}{2\pi r} \tag{5.5}$$

where I is the total discharge current and $r_{cathode} \leq r \leq r_{anode}$. During our simulation campaign, for high current, it become clear that if we instantly applied the full discharge current at the inlet, the magnetic contribution in Eq.2.27 and Eq. 2.41 of sec.2.1.4 of Chap.2 will rapidly increase and caused reverse flow and negative values of pressure direct near the inlet. To overcome this problem we applied the discharge current gradually through an appropriate induced magnetic field function depending on time (see Fig.5.4).

$$B_{inlet} = \begin{cases} 0, & \text{if } t < t_1. \\ B_{\theta,0}\frac{t-t_1}{t_2-t_1}, & \text{if } t_1 < t < t_2. \\ B_{\theta,0}, & \text{if } t > t_2 \end{cases} \tag{5.6}$$

At the electrodes, the boundary condition of the tangential component of magnetic field flux intensity $\mathbf{B}_t$ is derived from the Ampère's law of sec.2.1.3 and by using the Stoke's theorem as in (Jackson, 1998).

$$\oint_C \mathbf{B} \cdot \mathbf{dl} = \mu_0 \iint_S (\mathbf{J} + \frac{\partial \mathbf{D}}{\partial t}) \cdot \mathbf{n} dS \tag{5.7}$$

By integrating Eq.5.7 around an elongated rectangular contour C with an infinitesimal area S at the interface plasma-conductor yields:

$$\oint_C \mathbf{B} \cdot \mathbf{dl} = \mu_0 \iint_S (\mathbf{J} \cdot \mathbf{n}) dS = \mu_0 \mathbf{J}_{S_c} \tag{5.8}$$

since the integral of $\frac{\partial D}{\partial t}$ approaches zero but not the surface current $\mathbf{J}_{S_c}$ (see (Griffiths, 1999) for more details). Thus

$$\mathbf{n} \times (\mathbf{B}_t - \mathbf{B}_{t_c}) = \mu_0 \mathbf{J}_{S_c} \tag{5.9}$$

where $\mathbf{n}$ is the normal vector of the electrode surface pointing from the electrode into plasma, $\mathbf{B}_{t_c}$ is the magnetic field flux intensity and $\mathbf{J}_{S_c}$ is the current density at the electrode surface. For insulated walls, $\mathbf{J}_{S_c} = 0$. Consequently, all the current flows at the surface and the tangential component of $\mathbf{E}$ is zero making the

electrode surfaces equipotential. Likewise by using the Gauss's law of sec.2.1.3, the normal component of the magnetic field flux intensity $\mathbf{B}_n$ is continuous across the electrode surface

$$\mathbf{n} \cdot (\mathbf{B}_n - \mathbf{B}_{n_c}) = 0 \tag{5.10}$$

where $\mathbf{B}_{n_c}$ is the normal component of the magnetic field flux intensity at the electrode surface.

At the exit boundaries, the magnetic field is set to zero. But this has to be compatible with the size of the simulation domain to avoid non physical values of pressure. In fact, pressure is evaluated by subtracting the contribution of magnetic and kinetic energy from the internal energy. At the exit boundaries if the magnetic field is set to zero and the computation domain too small, then the simulations results will be unrealistic. Thus, the computational domain is chosen to be large enough to suit with this assumption.

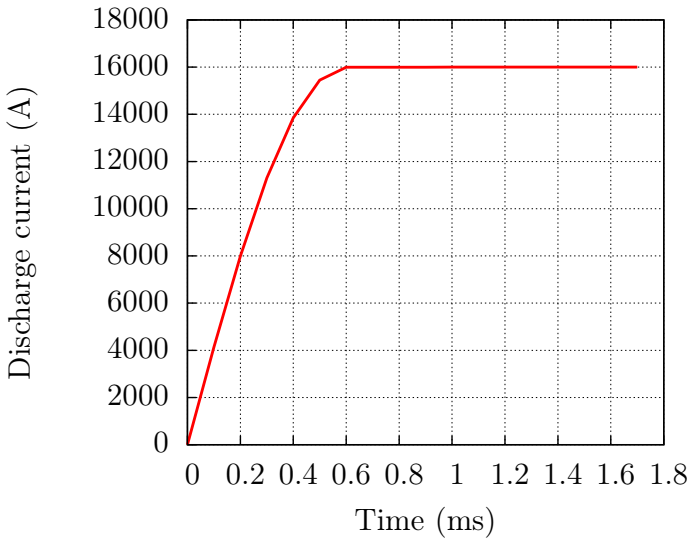

FIGURE 5.2: The time evolution of the discharge current at the inlet of the PFSBT for the case with $I = 16\ kA$

5.2.2 Computational results

During our simulation campaign, for high current, it become clear that if we instantly applied the full discharge current at the inlet, the magnetic contribution in Eq.2.13 and Eq. 2.41 will rapidly grow up and caused reverse flow and negative values of pressure direct near the inlet. To overcome this problem we applied the discharge current gradually through an appropriate function depending of time (see Fig.5.4(a)). Fig.5.3(b) shows the magnitude of magnetic field and the discharge charge in percentage distribution. For the nominal case (Sankaran, Choueiri, and Jardin, 2005) with $I = 16\ kA$ ($\xi \sim 1$) and $\dot{m} = 6\ g/s$ of Argon, we obtained the following results: As expected the magnetic field decreases radially from cathode surface to insulator where the non conducting boundary condition is imposed. The same trend is observed also for discharge current distribution, which diffuse

inside the discharge chamber from inlet ($\sim$ 97 %) to cathode tip ($\sim$ 20 %). Fig. 5.4(b) presents simulated and experimental x-velocity measurements. The present model predicts the similar behaviour and velocity values fairly accurately, but diverge from experimental values several inlet channel diameters downstream of the discharge chamber.

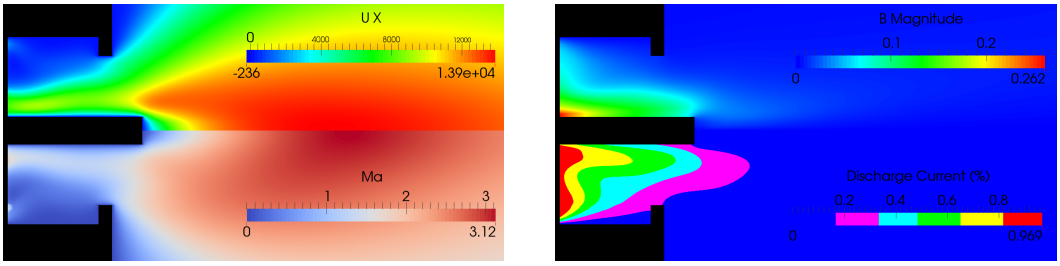

(a) X-Velocity and Mach number (b) Magnitude of B field and current

FIGURE 5.3: Distribution of the x-component of velocity and Mach number (a) and the magnitude of B field and discharge current in percentage (b)

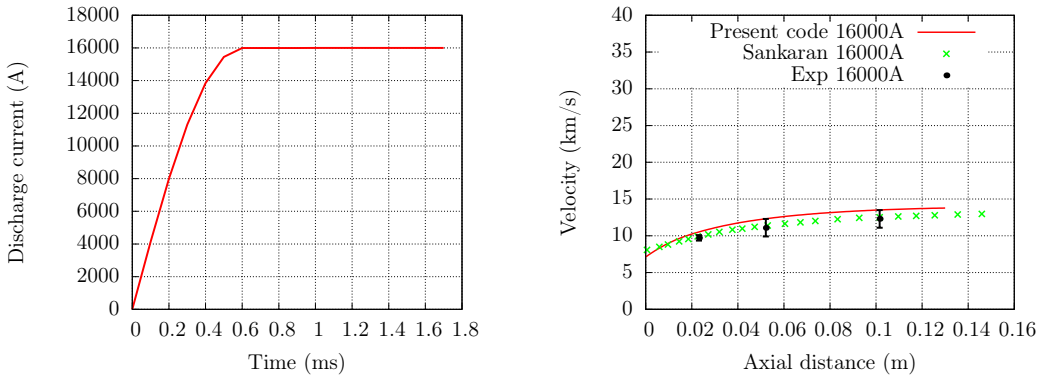

(a) Discharge (b) Velocity

FIGURE 5.4: The time evolution of the discharge current at the inlet of the PFSBT for the case of interest with $I = 16\ kA$ (a) and Comparison of the x-component of plasma velocity with the two temperatures and multi-level ionization code of Sankaran (Sankaran, Choueiri, and Jardin, 2005) and the experimental data of Boyle (Boyle, 1974) for $\dot{m} = 6\ g/s$ (Ar) and $I = 16\ kA$ (b)

The plasma flow leave the thruster with the velocity around 9 km/s (see Fig.5.3(a)). This value have been observed experimentally by Boyle (Boyle, Clark, and Jahn, 1976) with his *time-of-time flight probe technique*. The exhaust plasma flow continues to increase for several anode orifice diameters downstream of the cathode tip achieving a speed of 13.9 km/s with a Mach number of 3.12 for the present code, 13 km/s for the two temperature and multi-level ionization code of Sankaran (Sankaran, Choueiri, and Jardin, 2005) and 12.5 km/s for the experiment (Boyle, 1974; Boyle, Clark, and Jahn, 1976). These differences link to

the fact that the physic of plasma ionization is not yet implemented in our model which caused a low consumption of the thermal energy produced through the gas heating by the current arc (joule heating process). An important part of this energy is converted to kinetic energy which accelerate the plasma flow as we can see in Fig.5.5(d). For each axial velocity profile, the maximum value is observed near the cathode and the minimun value on the electrode surfaces. That is due to the dominance of the magnetic fied (consequently the Lorentz force) on the cathode surface and the non slip boundary condition on the electrodes respectively. Inside the discharge chamber, the pressure increases with the rise of temperature till its highest value at the cathode surface near the inlet where the current is stronger. Fig.5.5(b) shows the axial evolution of the pressure in the discharge chamber function of the applied current. As the plasma rapidly flows outside of the thruster, a extremely low pressure (wake) region (about 32 pa for the case with $I = 20\ kA$ or $\xi \sim 1.4$) direct after the cathode tip involving recirculating flow due to viscosity (Kármán, 1963) is created. After the wake region, the pressure increases once again downstream and decreases rapidly to match the fixed simulation domain outlet pressure (see Fig.5.5(c)). For a good comparison with the previous study, the total thrust is evaluated in the same way as in (Sankaran, Choueiri, and Jardin, 2005), where the total thrust is calculated from the momentum flux at all the thruster boundaries,

$$F_{total} = \int_A U_x(\rho \mathbf{U} \cdot dA) \tag{5.11}$$

Fig. 5.6 presents the calculated values of thrust, which are compared to the experimental data of Boyle (Boyle, 1974), the Maecker analytic approximation and the simulation results of Sankaran (Sankaran, Choueiri, and Jardin, 2005). The thrust increases almost linearly as the discharge current increases from 38.6 N to 73.5 N. The code overestimates the thrust for lower value of ξ (< 1) with the highest difference at $\xi = 0.8$ (23 % for experiment, 38 % for Maecker and 14.11 % for Sankaran results). At the nominal case, the present code trends to agree very well with experiment and the simulation of Sankaran (the difference is about 3.88 % for experiment, 6.1 % for Maecker and 2.26 % for Sankaran). For Higher values of current, the present code underestimates the thrust with the highest difference at $\xi = 1.34$ (11.04 % for experiment, 3.6 % for Maecker and 4.45 % for Sankaran results).

5.3 The Princeton's Extended Anode Thruster

The Princeton's extended anode thruster (PEAT) presented in Fig.5.7, studied numerically by Lapointe (Lapointe, 1991; Lapointe, 1992) and widely experimentally investigated at the Princeton University is chosen to test the validity of the proposed density-based algorithm.

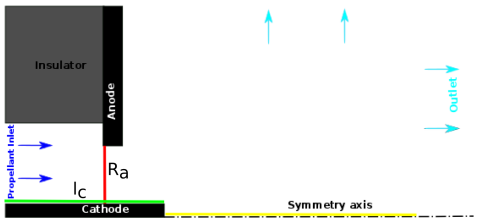

(a) Thruster geometry and plotting lines

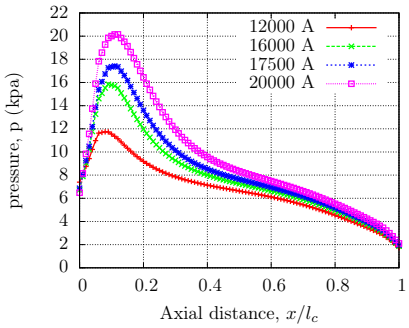

(b) Pressure in the discharge chamber

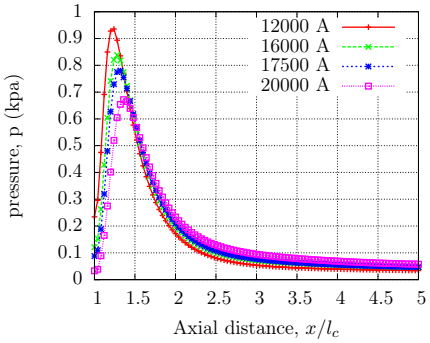

(c) Pressure downstream of the cathode

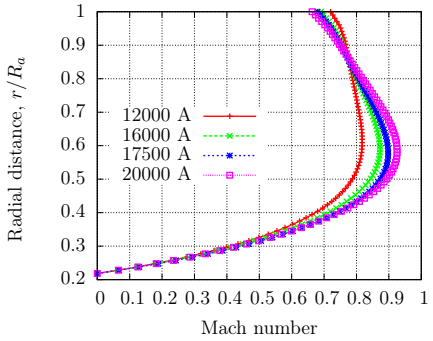

(d) Mach number

FIGURE 5.5: Effect of the discharge current on plasma dynamic pressure in the discharge chamber from the inlet boundary to anode tip (green line) (b) and downstream from the cathode tip along the symmetry axis (yellow line) (c) and the Mach number profile over the radial line between anode and cathode (red line) (d) for $\dot{m} = 6\ g/s$ of Argon: $l_c = 0.1\ m$ is the cathode length and $R_a = 0.0435\ m$ is the anode internal radius

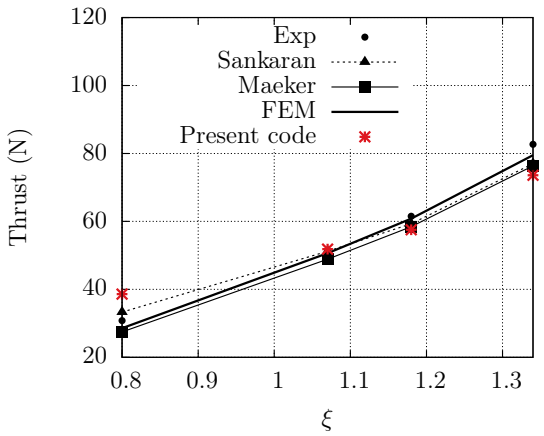

FIGURE 5.6: Comparison of the thrust characteristics for $\dot{m} = 6\ g/s$ (Ar) with experimental data (Boyle, 1974; Boyle, Clark, and Jahn, 1976) and the simulation of Sankaran (Sankaran, Choueiri, and Jardin, 2005). FEM: Electromagnetic thrust

5.3.1 Boundary and initial conditions

This device consists of a coaxial 0.95 cm thoriated tungsten cathode radius with 20 cm length surrounded by a 3.2 cm radius copper anode with 21.6 cm length. Experimentally, Argon propellant is injected through an insulating boron nitride backplate, with either all the propellant injected near the anode radius, or with half of the propellant injected through an annulus near the cathode base and half through a ring of 12 evenly spaced ports located 2 cm radially from the thruster axis (50 : 50). For our simulations, the propellant is assumed to be injected uniformly through the inlet surface, which correspond most closely to the 50 : 50 propellant split used in the experiments. The inputs of the code consist of the thruster discharge current, the propellant mass flow rate (6 g/s) and a specified temperature. Here, the starting values and boundary conditions are almost the same as in the PFSBT. Except the fact that here, the temperature on the electrodes is set at 3000 K (Lapointe, 1991) providing a smoother temperature transition between the electrode surface and the hot plasma.

5.3.2 Computational results

Thrust is calculated by integrating Eq.1.8 at thruster exit. While the integration of Eq.1.13 over a line between the cathode and the anode gives the plasma potential. The current flow patterns are plotted in Fig.5.8 and highlighted the influence of the plasma flow on the current distribution, which are driven out of the discharge chamber downstream as the magnetic field increases. This strong influence is due to the resistive diffusive term in the induction equation which is related to the electrical conductivity. In the case of $I = 20\ kA$, a current vortex is observed in the downstream region and point out the beginning of the instabilities. The distribution of temperature and the corresponding real gas ratio of specific heats γ are shown in Fig.5.8.c and Fig.5.8.d respectively. As the plasma temperature increases, γ deviates from the ideal value of 5/3 for Argon and ranges between 1.1 for higher temperature values $> 11.0\ kK$ and 1.13 for lower temperature values $\leq 11.0\ kK$ which is in accordance with the results of Sankaran (Sankaran, 2005) and allows a better prediction of thermodynamic variables.

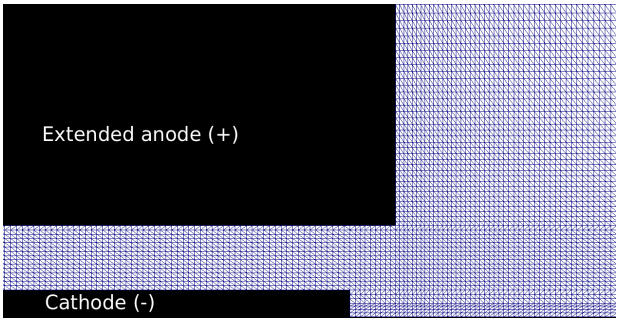

FIGURE 5.7: PEAT Computational domain

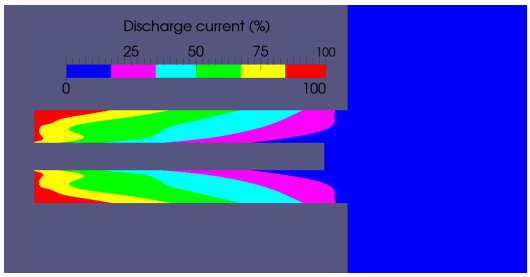

(a) $I = 16\ kA$

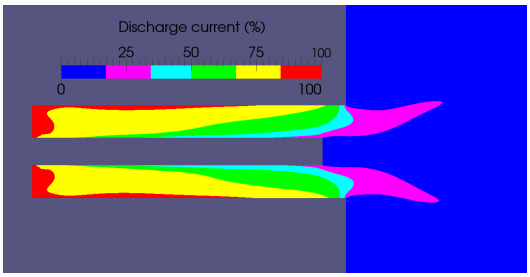

(b) $I = 20\ kA$

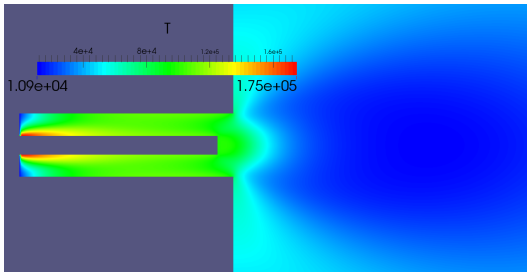

(c) Temperature

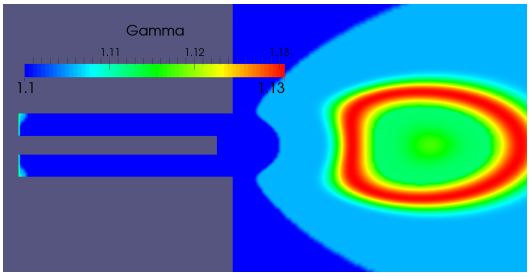

(d) Real gas ratio of specific heats

FIGURE 5.8: The current distribution as percentage of its maximum on the PEAT discharge chamber with $I = 16\ kA$ (a) and $I = 20\ kA$ (b), temperature (c) and real gas ratio of specific heats (d) distribution with $I = 15\ kA$

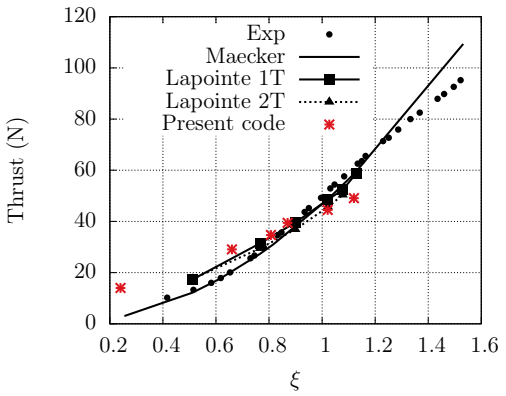

(a) Thrust (F_{total})

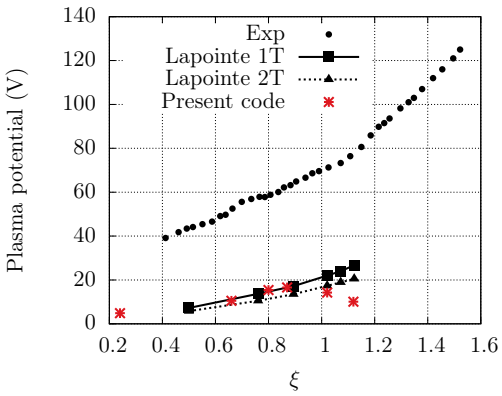

(b) Voltage

FIGURE 5.9: Comparison of the thrust caracteristics for $\dot{m} = 6\ g/s$ (Ar) with the 1-T single temperature code, the 2-T two-temperature code of Lapointe and experimental data (Lapointe, 1991; Lapointe, 1992) (a) and comparison of plasma voltage with the 1-T single temperature code, the 2-T two-temperature code and total voltage experimental data (b)

As expected, thrust increases almost linearly as the discharge current increases from 14 N at $\xi = 0.24$ to 49.11 N at $\xi = 1.12$ with the best performance recorded around $\xi = 0.9$ where the predicted thrust is 39.47 N corresponding to 0.17 % and 1.11 % difference with Lapointe 1-T code and Lapointe 2-T code respectively.

While the agreement is within 0.83 % in comparison with experimental data. Fig. 5.9 shows the comparison between the present model with the numerical predictions of Lapointe and the experimental measurements. The present code predicts the thrust fairly accurately but diverge from experimental data for current values less than 10 kA (predominantly thermal acceleration regime) (see Fig. 5.9(a)). The present density-based method performs better as the current values approaching 15 kA (predominantly electromagnetic acceleration regime). The present code was able to provide steady state results until current values of 22 kA ($\xi = 1.12$). But some oscillations of thrust and plasma voltage were observed as the discharge current approaching 21 kA which corresponds to the critical current ($\xi = 1$ in Fig.5.9.a and Fig.5.9.b) and affected the solver accuracy. This issue was already reported by Lapointe (Lapointe, 1992). The present code overestimate the electrical conductivity which strongly depends of the plasma temperature (See Eq.2.65 in Chapter.2). As the discharge current increases, the electrical conductivity increases with $T^{3/2}$ which lowers the plasma potential according to the Ohm's law equation (Eq.2.11) and consequently also the electrical input power of the thruster and conducts to higher values of efficiencies. Measured total voltage-current (plasma voltage and electrode fall potential) and predicted plasma voltage-current characteristics are shown in Fig. 5.9(b). The present model correctly reproduce the trend of the experimental data, but are consistently lower by approximatively 40 V, just as the two models of Lapointe. This huge difference is due to the lack of electrode fall calculation in the present model and also in the two models (1-T and 2-T code) of Lapointe (Lapointe, 1991; Lapointe, 1992).

5.4 Geometric scaling analysis on the Villani-H self-field MPD thruster

Galvanised by the results of sec.5.2 and sec.5.3, we attempt in this section to determine the performance trend of a self-field MPD thruster, the operating conditions for which the solver is stable and of course propose the first statement of efficient MPD thrusters designing. The geometry chosen for the geometric scaling analysis is one of the series of constant area coaxial thrusters used by Villani (1982) (Sankaran, 2005). It appear as the best choice to do this investigation because of the simplicity of its geometry (see Fig.5.10). To ensure that, the conclusion deducted in this subsection are in line with the reality, we first simulated the Villani-H thruster configuration already numerically investigated by Sankaran (Sankaran, 2005) and more recently by Ahangar (Ahangar, Ebrahimi, and Shams, 2014) who obtained good agreement with experiments. Fig.5.10 shows the computational domain. The cathode and the anode radii were $r_c = 0.0095\ m$ and $r_a = 0.051\ m$ respectively while their length were maintained to $l_c = 0.264\ m$ for cathode and $l_a = 0.2\ m$ for anode which corresponds to the aspect ratio $l_a/r_a \sim 4$. In the experiment case, the cold gas propellant (Argon) is not injected uniformly at the inlet surface but through 12 holes as represented in Fig.5.10 and is ionized few millimeters downstream of the inlet. In our simulation, the inlet temperature is considered to high enough (1 eV) such that we can assume the gas as fully ionized. The computational domain is taken large enough such that there are no

normal gradients in any of the flow properties at the the free stream boundaries. At inlet, the magnetic field is calculated once again as a function of the total discharge current with the expression:

$$B_0 = \frac{\mu_0 I}{2\pi r} \tag{5.12}$$

where I is the total discharge current and $r_{cathode} \leq r \leq r_{anode}$.

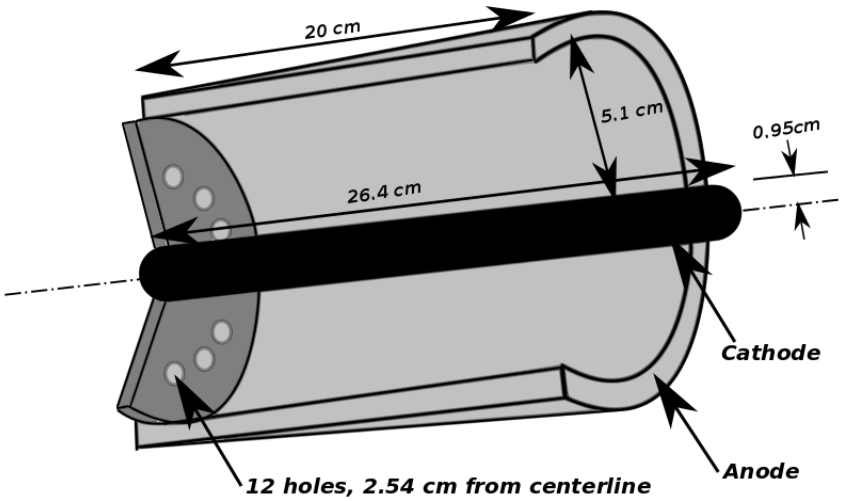

FIGURE 5.10: Villani-H MPD thruster geometry

On the electrode walls a no slip condition is imposed for the velocity field, the temperature is considered slightly less than the plasma flow temperature and a perfectly electrical conducting wall is specified for the magnetic field. At the exit boundaries, the normal gradients in any of the flow properties are set to zero and the magnetic field is fixed as zero. At the initial time, the domain is filled with a background pressure of 10 pa at a temperature of 300 K. The mass flow rate of 0.006 kg/s is imposed at inlet. As already mentioned in sec.5.2.2, the discharge current is made to increase gradually to the required value. The equation are then solved in a time-dependent manner until steady state. To check the convergence, we plotted the time evolution of the flow variables at the exit of the thruster. The numerical solution is considered converged when the lines representing the changes of the variables over time become parallel to the time axis. In this subsection, our results are compared with those of Ahangar (Ahangar, Ebrahimi, and Shams, 2014) and Sankaran (Sankaran, 2005).

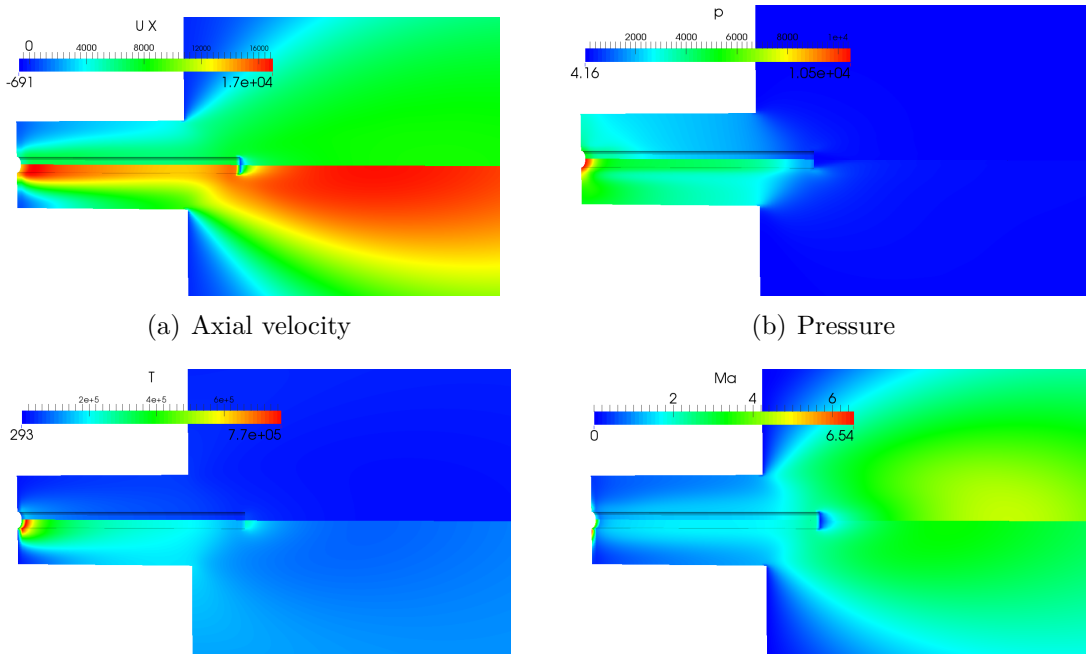

(a) Axial velocity (b) Pressure

(c) Temperature (d) Mach number

FIGURE 5.11: Axial velocity (a), pressure (b), temperature (c) and Mach number (d) distributions with $\xi = 0.47$ and $\xi = 1$ respectively in top and bottom of each capture

Fig.5.11 shows the calculated distribution of axial velocity, pressure, temperature and Mach number with the discharge current 8 kA (top) and 15 kA (bottom) both cases corresponding to the dimensionless current $\xi = 0.47$ and $\xi = 1$ (the nominal case). The plasma leaves the thruster with the axial velocity around 6 km/s and increases up to 8 km/s downstream of the cathode tip for $\xi = 0.47$. For $\xi = 1$, the axial velocity ranges from 8 km/s to 15 km/s at the thruster exit. The maximum velocity increases to a maximum of 8 km/s for $\xi = 0.47$ and 17 km/s for $\xi = 1$ downstream of the cathode tip. The velocity increases as $\frac{1}{r}$ with r the radius of any points of the plasma flow inside the thruster, because of the similar trend of Lorentz force. These results were also observed by Sankaran for $\xi = 1$. The temperature inside the discharge chamber increases from 300 K to 1.5×10^5 K for $\xi = 0.47$ and 7.7×10^5 K for $\xi = 1$ at the intersection of inlet and cathode surface. That is due to the joule heating which increases with reduction of radius. Fig.5.12 presents the spatial distribution of magnetic field in term of the percentage of its maximal value at inlet. The magnetic field diffuses and it is convected downstream by the plasma flow with a maximal value observed (0.14 T for $\xi = 0.47$ and 0.26 T for $\xi = 1$) at the intersection of inlet and cathode. The tendency of the magnetic field and the current to propagate downstream is significant as the velocity of the plasma increases making the convection term of Eq.2.13 important. But this propagation in the simulation is always less important than in experiment and Sankaran (Sankaran, 2005) explained this observation by stating that the current in the experiment is allowed to attach on the outer surface of the anode, while it is not possible in simulation. In Fig.5.13, the magnetic Reynolds number, calculated according to Eq.4.43, is used to highlight the behavior of the

current density when the convection term of Eq.2.13 become important than the diffusion term. As mentioned before in sec.4.2.4 of Chapter.4, the current concentration at the ends of the thruster channel becomes more pronounced when the magnetic Reynolds number increases. In Fig.5.13.d, with $Re_m = 400$, the expected three regions are clearly distinguished. The inlet current concentration region, the core of the channel with little concentration and the exit current concentration. As the magnetic Reynolds number decreases, these three regions vanish and a homogeneous current density distribution takes place.

Now, concerning the evaluation of the plasma potential between any two points (A and B) in the simulation domain, the relation below is used:

$$V_A - V_B = -\int_A^B \mathbf{E} \cdot \mathbf{dr} \tag{5.13}$$

where **dr** is the change in position. By considering the cathode as the potential reference (0 V), we computed the plasma potential between the cathode surface and the inner anode surface. The present code predicts a plasma potential drop of 25.27 V for $\xi = 0.47$ and 35.32 V for $\xi = 1$. These results could not be compared with experimental results because they did not take into account the anode drop potential. But, they agree well with the simulation results of Ahangar which predict a plasma voltage drop of 24.67 V for $\xi = 0.47$ while the value obtained by Sankaran is 30.83 V with $\xi = 1$. The thrust is computed by using Eq.5.11. For $\xi = 0.47$, the present code predicts a thrust of 18.8 N and this result compares very well with those of Villani (Villani, 1982) (15.6 N) and Ahangar (Ahangar, Ebrahimi, and Shams, 2014) who obtained thrust of 16.34 N and 17.81 N by using the MUSCL technique of Lax-Friedrichs Method, including Saha's equilibrium ionization model named LFME algorithm. In the case with $\xi = 1$, we obtained a thrust of 41.3 N while Sankaran predicts 42.9 N and the analytical formula of Maecker predicts a thrust of 41.2 N.

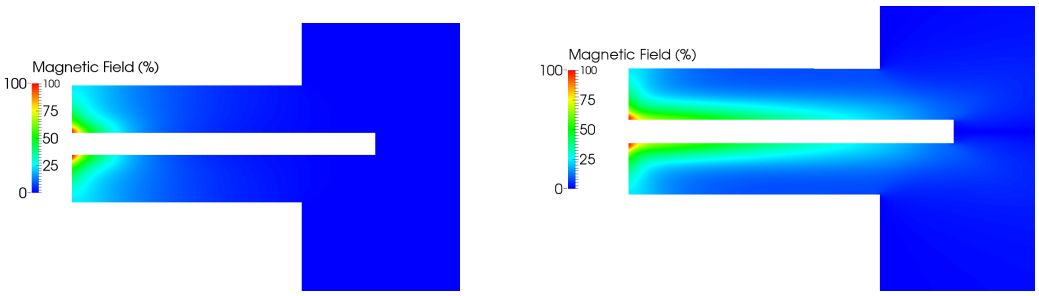

(a) $\xi = 0.47$ (b) $\xi = 1$

FIGURE 5.12: Distribution of magnetic field in percentage of the maximum value for $\dot{m} = 6\ g/s$ of Argon

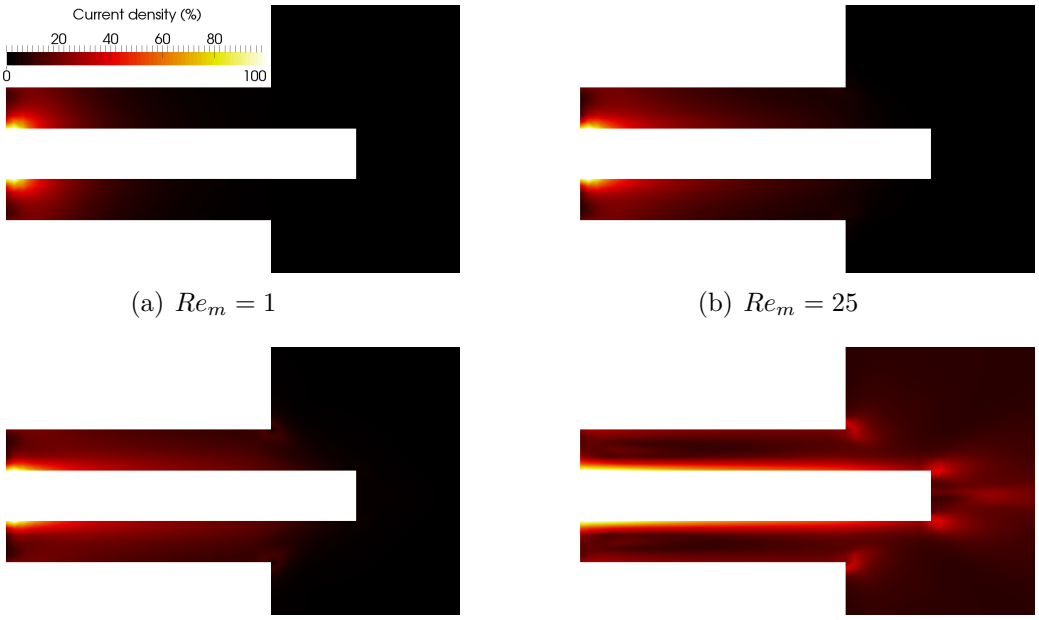

(a) $Re_m = 1$ (b) $Re_m = 25$

(c) $Re_m = 125$ (d) $Re_m = 400$

FIGURE 5.13: Variation of the current density with the magnetic Reynolds number on the Villani-H thruster with cathode length $l_c = 13.2\ cm$ and aspect ratio $l_a/r_a = 4$ for $\dot{m} = 6\ g/s$ of Argon (see Tab.5.2)

Now, from the original geometry of Villani (Villani, 1982) investigated above, we deducted three different configurations and for each of them, variants are created depending on the cathode length and on the aspect ratio which is actually the ratio of the anode length to its radius. The first main geometry case (MPDT01) consists of a cathode with 0.95 cm radius, surrounded by an anode with 2.5 cm radius. The second set (MPDT02) kept the cathode radius of MPDT01 but increase anode radius to 5.1 cm. The last case (MPDT03) has the same anode radius as MPDT02 but doubled the cathode radius to 1.81 cm. For each geometry, the full three dimensional computational domain is subdivided in about 1,500,000 cells, the aspect ratio thrusters l_a/r_a are scaled from 1 to 5 and the cathode length can take two distinct values $l_c = 13.2\ cm$ and $l_c = 26.4\ cm$ yielding 30 cylindrical thruster geometries. The argon propellant mass flow rate is kept constant at 6.0 g/s, and is assumed to be totally ionized for all cases. ξ values, ranging from 0.2 to 1.12 are evaluated for each geometry (see Tab.5.2).

5.4.1 MPDT01

MPDT01 geometry set has a cathode radius of 0.0095 m with a anode radius of 0.025 m. The calculated critical current from Eq.4.41 is $I_c = 21.630\ kA$. The code was not able to converge for $l_a/r_a = 1$ with both cathode length. Convergence was obtained only with the shorter cathode for all the ξ values with $l_a/r_a = 4$ and $l_a/r_a = 5$. Fig. 5.14.a presents the behaviour of the different components of thrust including the analytic thrust of Maecker for the aspect ratio $l_a/r_a = 4$. The

TABLE 5.2: MPDT geometries, $\frac{I^2}{\dot{\mathbf{m}}}$ and corresponding dimensionless current ξ values for the numerical parameter study on the HLRN. r_a, l_a and l_c denote anode radius, anode length and cathode length respectively.

Case geometry	$\frac{l_a}{r_a}$	$\frac{I^2}{\dot{\mathbf{m}}}[10^9 \cdot \frac{A^2 s}{kg}]$	ξ	$l_c[m]$
$MPDT01$	1	5.72	0.27	0.132
$r_c = 0.0095[m]$	2	11.2	0.38	0.264
$r_a = 0.025[m]$	3	18.4	0.5	
	4	25.6	0.58	
	5	48.4	0.8	
		60.2	0.89	
		73.5	0.97	
		85.88	1.05	
		96.8	1.114	
$MPDT02$	1	5.72	0.342	0.132
$r_c = 0.0095[m]$	2	11.2	0.5	0.264
$r_a = 0.051[m]$	3	18.4	0.63	
	4	25.6	0.73	
	5	48.4	1.0	
		60.2	1.12	
$MPDT03$	1	5.72	0.275	0.132
$r_c = 0.0181[m]$	2	11.2	0.388	0.264
$r_a = 0.051[m]$	3	18.4	0.5	
	4	25.6	0.585	
	5	48.4	0.8	
	4	60.2	0.89	
	5	70.0	0.97	
		83.62	1.06	

total thrust and plasma potential (Fig. 5.14.b) increased with increasing ξ and we can clearly distinguish the different plasma acceleration mode. For small values of ξ, the thermal acceleration is the most responsible of plasma acceleration. The transition from thermal acceleration mode to electromagnetic acceleration mode occur at ξ around 0.45 which correspond to a discharge current value of about 10 kA. The effect of this transition on the MPDT01 thruster performance is well illustrated on efficiency profile (see Fig.5.14.b) which decreases by the thermal acceleration mode and starts to increase as the electromagnetic thrust becomes dominant till a value of 18.75 % at $\xi = 0.89$ which correspond to the highest value of total thrust (41.28 N), plasma potential of 40 V and specific impulse of 702 s. Before the critical current, $I_c = 21.6\ kA$ ($\xi = 1$), discrepancies for all the performance variables investigated are observed (Onset of thruster instability). For $l_a/r_a = 5$ (Fig. 5.15), the trend is almost the same. The maximum calculated thrust (39.86 N) is obtained at $\xi = 0.9$, corresponding to a plasma potential of 40 V, a specific impulse of 677 s and a efficiency of roughly 17.2 %. According to these results, we can conclude that, for stability and efficiency, shorter cathode with large aspect ratio configuration are recommended over all operating conditions. For the present case, the maximum efficiency 18.75 % is obtained with $l_a/r_a = 4$.

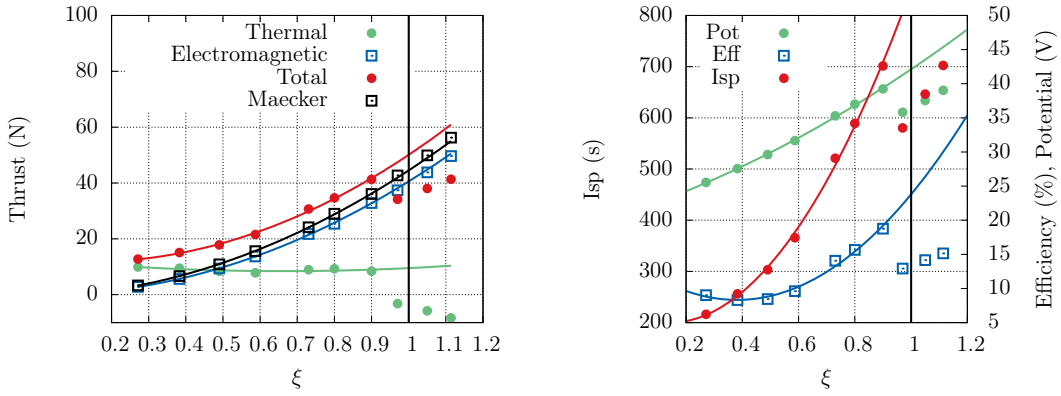

(a) Thrust

(b) Specific impulse, efficiency and plasma voltage

FIGURE 5.14: MPDT01 performance with shorter cathode and aspect ratio $l_a/r_a = 4$

5.4.2 MPDT02

MPDT02 geometry set has a cathode radius of 0.0095 m with a anode radius of 0.051 m. The critical current is $I_c = 16.9\ kA$. The solver was not able to converge for $l_a/r_a = 1$ with both cathode length. For the shorter cathode ($l_c = 13.2\ cm$) configuration, convergence was obtained for all the ξ values with $l_a/r_a > 1$. While steady state solutions were achieved with the longer cathode ($l_c = 26.4\ cm$) thrusters only for $l_a/r_a \geq 4$ which shows again the stability of the thrusters with short cathode comparing to the long cathode thrusters. Thrust, specific impulse, plasma current voltage and efficiency increase with increasing the dimensionless current ξ.

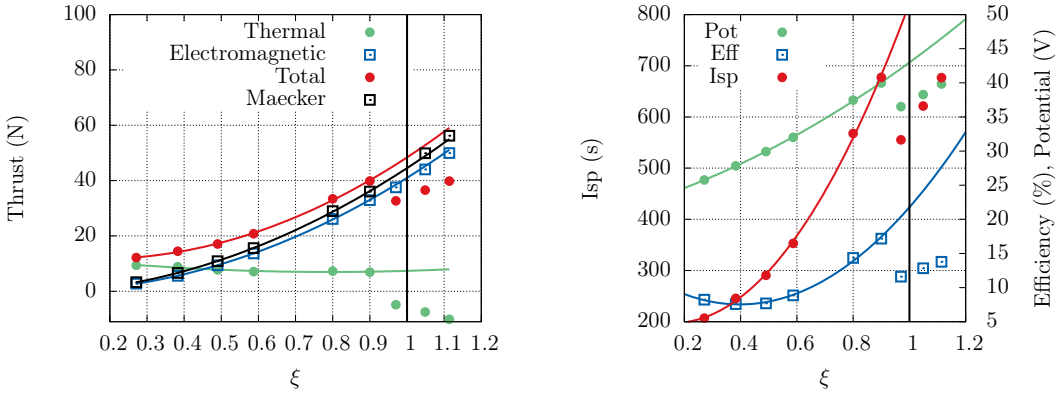

(a) Thrust

(b) Specific impulse, efficiency and plasma voltage

FIGURE 5.15: MPDT01 performance with shorter cathode and aspect ratio $l_a/r_a = 5$

Except for short cathode thruster with $l_a/r_a = 2$ where the efficiency decreases from 38 % at $\xi = 0.34$ to 26.69 % at $\xi = 0.74$ and start to increase after that with a value of 27 % at the critical current $\xi = 1$ (see Fig.5.16.b). This is due to the fact that, when the aspect ratio of the thruster is small, the expansion of plasma at the thruster exit and the useful energy loss in thermal form are huge. In Fig.5.16.a, this behaviour is well illustrated by the dominance of thermal thrust in a large range of ξ values.

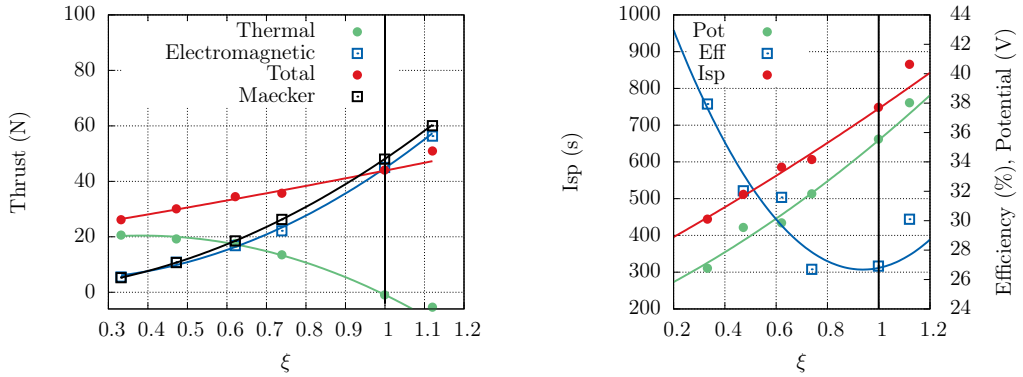

(a) Thrust

(b) Specific impulse, efficiency and plasma voltage

FIGURE 5.16: MPDT02 performance with short cathode and aspect ratio $l_a/r_a = 2$

The transition to the predominantly electromagnetic acceleration regime occurred at $\xi = 0.62$. Nevertheless, a maximal thrust of 44 N with a positive quasi non existent thermal component, a specific impulse of 750 s and a plasma potential of 35.55 V are achieved at critical current. Overall, in regard to the results obtained in this subsection, MPDT02 provides more stable operating conditions than MPDT01 with a maximum specific impulse of about 1000 s, corresponding

to a thrust value of 58 N, a plasma potential of 35.7 V and an efficiency of 46.36 % at critical current for $l_a/r_a = 5$ with long cathode (see Fig.5.19.d).

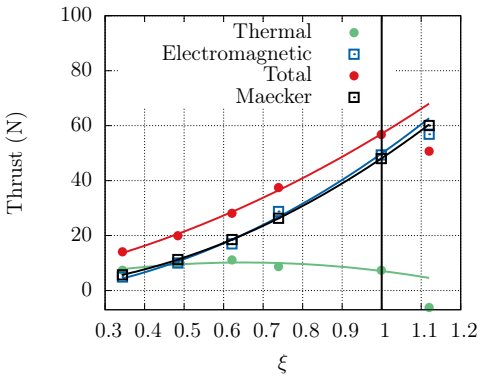

(a) Thrust

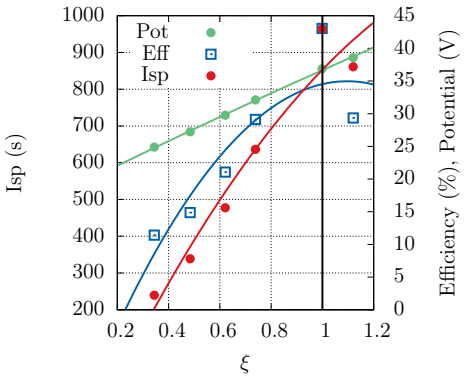

(b) Specific impulse, efficiency and plasma voltage

FIGURE 5.17: MPDT02 performance with short cathode and aspect ratio $l_a/r_a = 3$

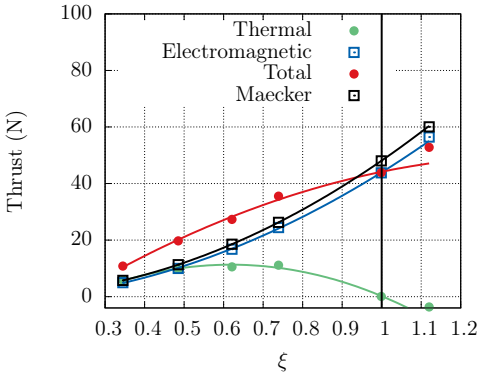

(a) $l_c = 0.132\ m$

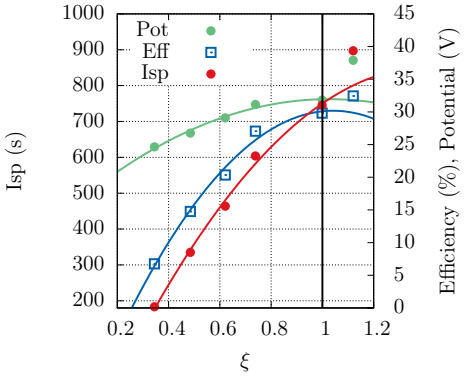

(b) $l_c = 0.132\ m$

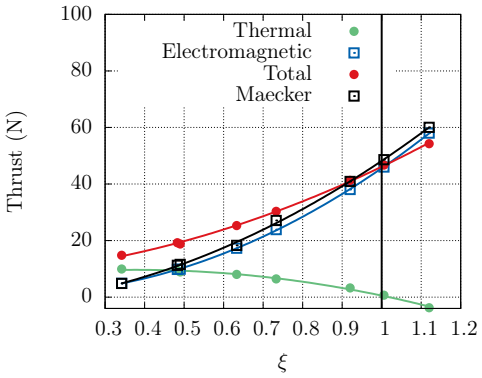

(c) $l_c = 0.264\ m$

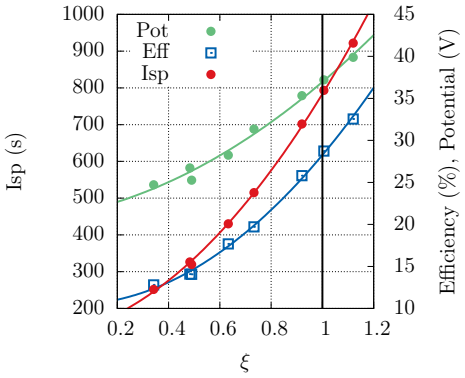

(d) $l_c = 0.264\ m$

FIGURE 5.18: MPDT02 performance with aspect ratio $l_a/r_a = 4$

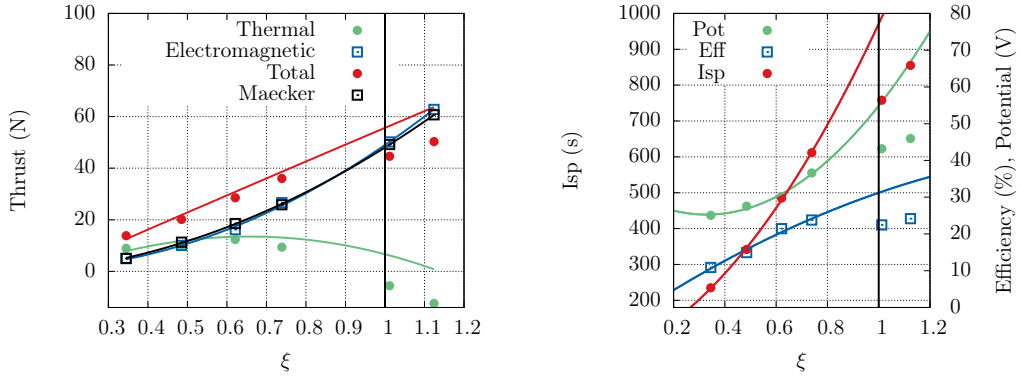

(a) $l_c = 0.132\ m$ (b) $l_c = 0.132\ m$

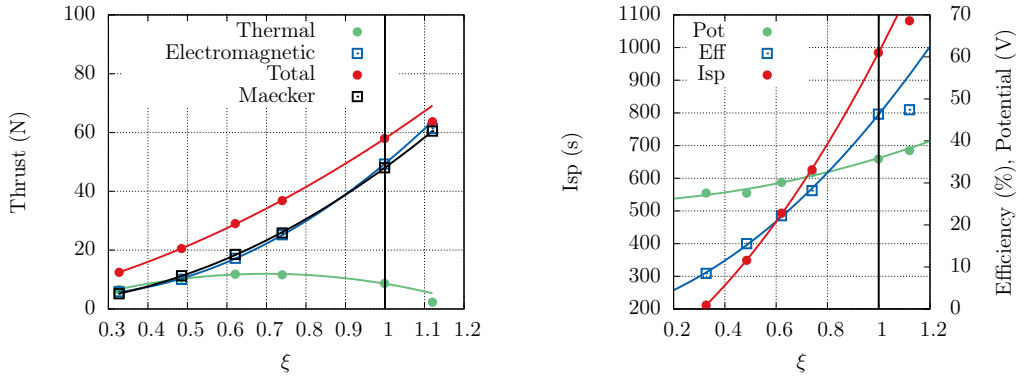

(c) $l_c = 0.264\ m$ (d) $l_c = 0.264\ m$

FIGURE 5.19: MPDT02 performance with aspect ratio $l_a/r_a = 5$

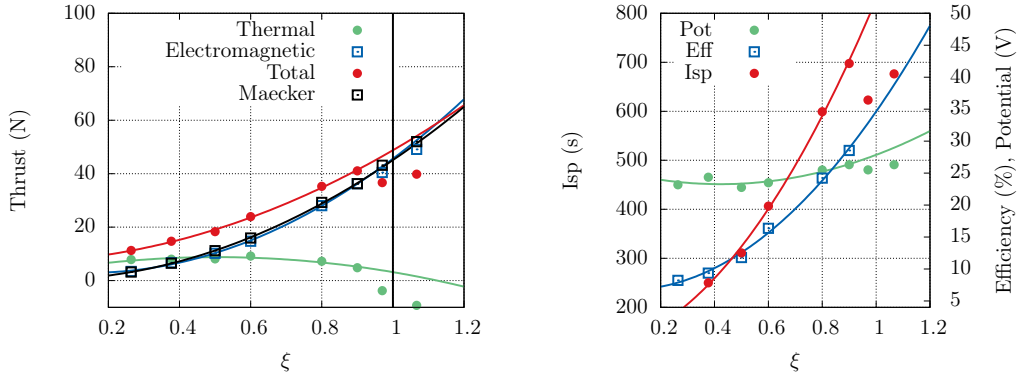

(a) Thrust (b) Specific impulse, efficiency and plasma voltage

FIGURE 5.20: MPDT03 performance with short cathode and aspect ratio $l_a/r_a = 2$

5.4.3 MPDT03

The last geometry set is MPDT03 which retained the same anode radius of 0.051 m as MPDT02 but doubled the cathode radius from 0.0095 m to 0.018 m. The critical

current for this configuration is $I_c = 21.0\ kA$. Calculated thrust, voltage, specific impulse and efficiencies versus ξ are plotted from Fig.5.20 to Fig.5.25. The solver was not able to converge for $l_a/r_a = 1$ with both cathode length and for all ξ values. For the shorter cathode configuration, convergence was obtained for all the ξ values with $l_a/r_a > 1$. While steady state solutions were achieved with the longer cathode ($l_c = 26.4\ cm$) thrusters only for $l_a/r_a \geq 4$, proving that the thruster stability can be obtained for a wide range of operating conditions with short cathode length. For each aspect ratio, thrust, specific impulse and plasma current voltage increase with increasing the dimensionless current ξ. For some configurations, the efficiency first decreases and then increases as the thruster access the predominantly electromagnetic acceleration mode. That effect is more important for shorter cathode configuration with aspect ratio $l_a/r_a \geq 3$ (see Fig.5.21.b and Fig.5.25.b). The highest efficiency of 30 % is obtained with the longer cathode and $l_a/r_a = 4$ (Fig. 5.23.d) corresponding to a thrust of 42.04 N, potential of 26.425 V and specific impulse of 714.2 s at $\xi = 0.9$. The potential appears to be almost constant for all configurations with a pic value of 27.82 V for $l_a/r_a = 5$ with shorter cathode corresponding to an efficiency of 27.82 %, the highest values of specific impulse around 729 s and thrust of 43 N at $\xi = 0.9$ (Fig.5.25.a, b). Overall, in regard to the results obtained in this subsection, MPDT03 provides more stable operating conditions than MPDT01 with a maximun specific impulse of 1000 s at critical current for $l_a/r_a = 5$ with long cathode (see Fig.5.19.d). The MPDT03 offered stable operating conditions just as much as MPDT02 but by increasing the discharge current, it exhibits the onset instability earlier ($\xi = 0.8$) than the previous MPD thruster geometries and its maximum specific impulse of 729 s obtained with the short cathode and $l_a/r_a = 5$ is less than 1000 s highest specific impulse obtained with MPDT02.

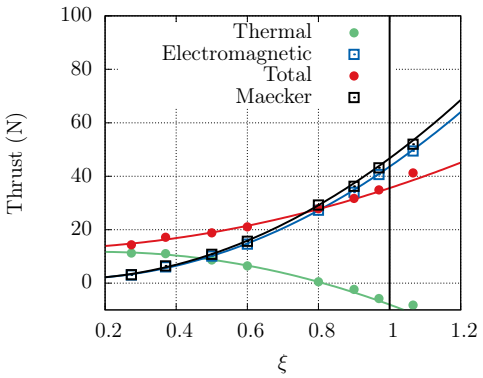

(a) Thrust

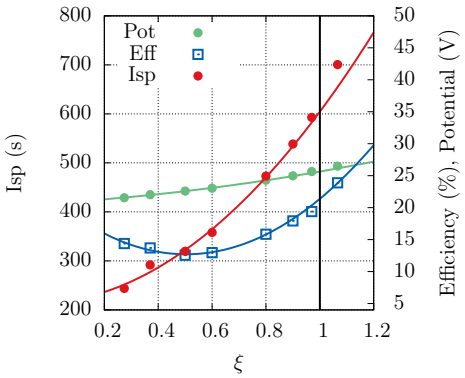

(b) Specific impulse, efficiency and plasma voltage

FIGURE 5.21: MPDT03 performance with short cathode and aspect ratio $l_a/r_a = 3$

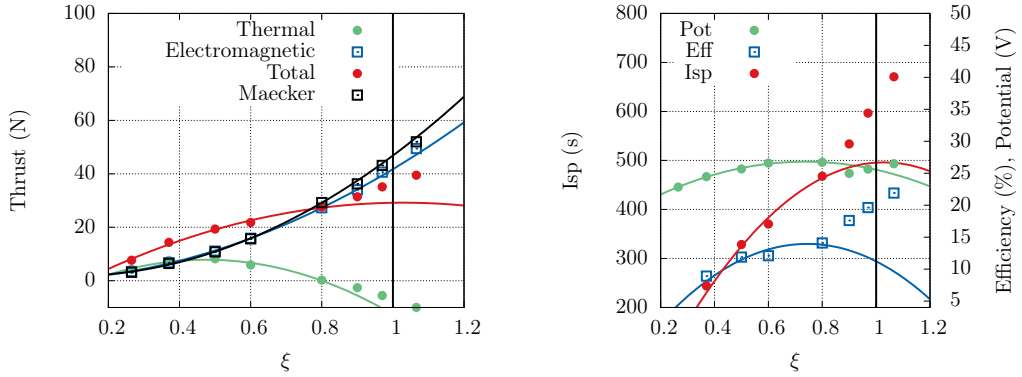

(a) $l_c = 0.132\ m$ (b) $l_c = 0.132\ m$

FIGURE 5.22: MPDT03 performance with short cathode and aspect ratio $l_a/r_a = 4$

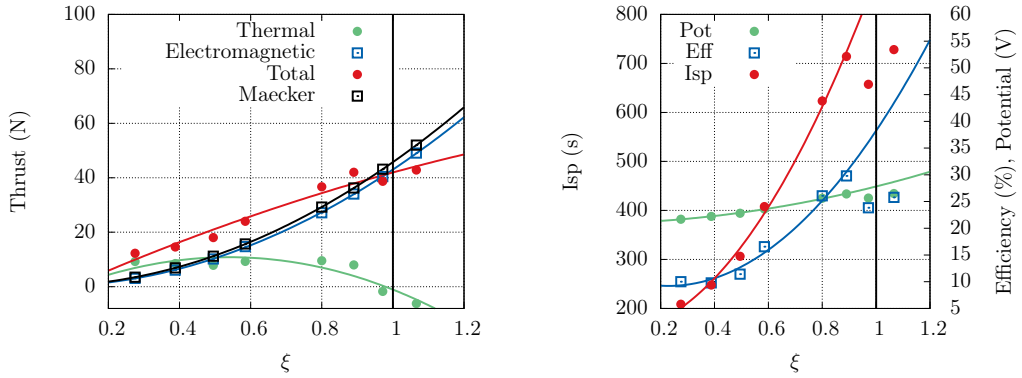

(a) $l_c = 0.264\ m$ (b) $l_c = 0.264\ m$

FIGURE 5.23: MPDT03 performance with long cathode and aspect ratio $l_a/r_a = 4$

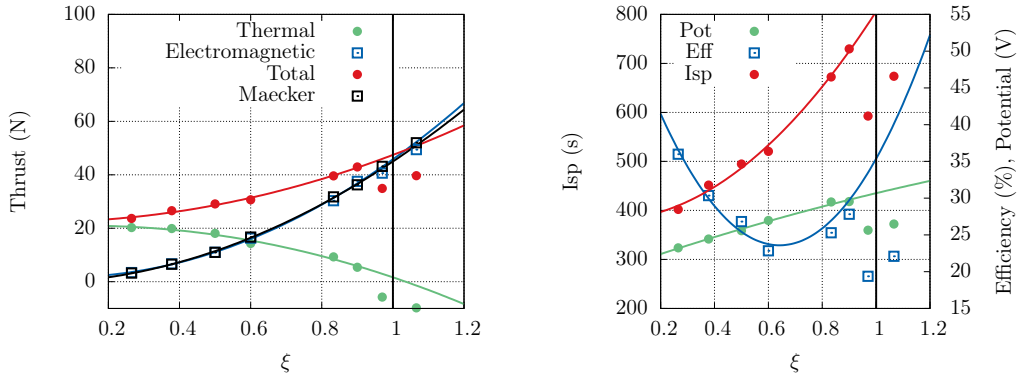

(a) $l_c = 0.132\ m$ (b) $l_c = 0.132\ m$

FIGURE 5.24: MPDT03 performance with short cathode and aspect ratio $l_a/r_a = 5$

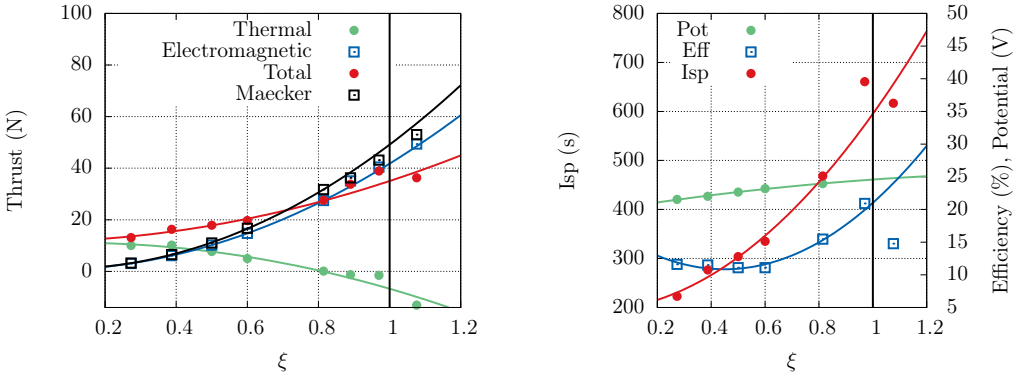

(a) $l_c = 0.264\ m$ (b) $l_c = 0.264\ m$

FIGURE 5.25: MPDT03 performance with long cathode and aspect ratio $l_a/r_a = 5$

5.5 Summary

The main goal of the present chapter was to underline the ability of the density-based method to deal with the physical process of plasma flow acceleration in the self-field MPD thrusters. According to the single fluid approximation of plasma, the physical model implemented in the present code is maintained as simple as possible. Nevertheless, the application of the developed numerical algorithm for the simulations of the self-field MPD thrusters demonstrates that the present method is robust and able to reproduce the main flow characteristics as well as the performance parameters. The PFSBT have been simulated and the results shows good agreement with the experimental values (Boyle, 1974) and numerical simulation results of Sankaran (Sankaran, Choueiri, and Jardin, 2005), with the best performance at the nominal operating condition (3.8 % and 2.2 % difference under the measured thrust value and the results of Sankaran respectively). Good performance have been obtained also by the prediction of thrust and plasma voltage of the PEAT. The difference between the simulation results and experiment is over 10 % for $0.2 < \xi < 0.8$. The code perform better as the discharge current increases till $\xi \leq 0.9$ and just before the beginning of the onset instability with the best performance around $\xi = 0.9$. We reported at that point, 0.17 %, 1.11 % and 0.83 % thrust difference between our computational results and Lapointe 1-T, 2-T codes and experimental data respectively. For $\xi \geq 1$, the results became worst due to the onset voltage instability. The simulation conducted on the Villani thruster produce satisfactory results and allows us to conduct a first attempt to MPD thruster designing. Regarding the results obtained in the geometric analysis, a short cathode is recommended for a stable operating conditions and long cathode allows higher values of efficiency and specific impulse to be achieved. In both configuration, higher aspect ratio l_a/r_a is recommended over all operating conditions (See Tab.5.3 and Tab.5.4). Overall we can conclude that, the present density-based code overestimated the thrust for $\xi < 1$ and underestimated it for $\xi \geq 1$. That is mainly due to the fact that we ignored several complicated physical processes such as ionization, particle collisions by considering the plasma as a singly fully ionized

TABLE 5.3: MPDT geometries with $l_c = 0.132\ m$ and ξ values for the numerical parameter study on the HLRN. "S" and "U" denote steady-state solution and lack of steady-state code convergence respectively.

Case geometry		ξ								
		0.27	0.38	0.5	0.58	0.8	0.89	0.97	1.05	1.114
$MPDT01$	$\frac{l_a}{r_a}$									
$r_c = 0.0095[m]$	1	U	U	U	U	U	U	U	U	U
$r_a = 0.025[m]$	2	U	U	U	U	U	U	U	U	U
	3	U	U	U	U	U	U	U	U	U
	4	S	S	S	S	S	S	S	S	S
	5	S	S	S	S	S	S	S	S	S
$MPDT02$	$\frac{l_a}{r_a}$									
$r_c = 0.0095[m]$	1	U	U	U	U	U	U	U	U	U
$r_a = 0.051[m]$	2	S	S	S	S	S	S	S	S	S
	3	S	S	S	S	S	S	S	S	S
	4	S	S	S	S	S	S	S	S	S
	5	S	S	S	S	S	S	S	S	S
$MPDT03$	$\frac{l_a}{r_a}$									
$r_c = 0.0181[m]$	1	U	U	U	U	U	U	U	U	U
$r_a = 0.051[m]$	2	S	S	S	S	S	S	S	S	S
	3	S	S	S	S	S	S	S	S	S
	4	S	S	S	S	S	S	S	S	S
	5	S	S	S	S	S	S	S	S	S

fluid. Indeed, the input power of the thruster is divided between three dominant processes namely joule heating, ionization and acceleration of the propellant gas. Considering the physical model used here, That's means that, for $\xi < 1$, we have less energy sinks and consequently, thrust is overestimated. For $\xi = 1$, the nominal operating condition occurred and there is an equipartition of the input power between acceleration and ionization. The difference of the calculated thrust with the experimental thrust is then minimized. For $\xi \geq 1$, the acceleration is dominant more particularly by the electromagnetic acceleration and it is well known that the momentum of the neutral particles is not affected by the electromagnetic forces but only by collisions with ions. Thus, the difference between calculated thrust and experimental thrust increases again and the thrust is underestimated. To overcome this difficulty in the near future work, the improvement of the physical model must be investigated. Nevertheless, the code is robust and stable by high values of discharge current or ξ. For several geometric configurations the code achieved the steady-state and the onset instability is also observed. Concerning the designing effort of the MPD thruster with the present code, a right compromise has to be found between efficiency (long cathode) and the thruster stability (short cathode) and both with high thruster aspect ratio l_a/r_a.

TABLE 5.4: MPDT geometries with $l_c = 0.264\ m$ and ξ values for the numerical parameter study on the HLRN. "S" and "U" denote steady-state solution and lack of steady-state code convergence respectively.

Case geometry		ξ								
		0.27	0.38	0.5	0.58	0.8	0.89	0.97	1.05	1.114
$MPDT01$	$\frac{l_a}{r_a}$									
$r_c = 0.0095[m]$	1	U	U	U	U	U	U	U	U	U
$r_a = 0.025[m]$	2	U	U	U	U	U	U	U	U	U
	3	U	U	U	U	U	U	U	U	U
	4	U	U	U	U	U	U	U	U	U
	5	U	U	U	U	U	U	U	U	U
$MPDT02$	$\frac{l_a}{r_a}$									
$r_c = 0.0095[m]$	1	U	U	U	U	U	U	U	U	U
$r_a = 0.051[m]$	2	U	U	U	U	U	U	U	U	U
	3	U	U	U	U	U	U	U	U	U
	4	S	S	S	S	S	S	S	S	S
	5	S	S	S	S	S	S	S	S	S
$MPDT03$	$\frac{l_a}{r_a}$									
$r_c = 0.0181[m]$	1	U	U	U	U	U	U	U	U	U
$r_a = 0.051[m]$	2	U	U	U	U	U	U	U	U	U
	3	U	U	U	U	U	U	U	U	U
	4	S	S	S	S	S	S	S	S	S
	5	S	S	S	S	S	S	S	S	S

Chapter 6

Applied-field MPD thruster simulations: NASA-ReLC MPD thruster

Regarding the results obtained in the previous chapter, it become clear that the strong correlation of thruster performance parameters (thrust, efficiency and specific impulse) with the discharge current could be the major weakness for the self-field MPD thruster more particularly when a very high thrust value is required (long deep space mission). Indeed, in SFMPDT, the main acceleration mechanism is represented by the interaction between the discharge current and the self-induced magnetic field. That means, high thrust level can be obtained only for high discharge current (5-100 kA) and consequently for high power (MWs). That was well proved in the previous chapter. By operating around the critical current the onset instability appears as the main issue of the SFMPDT. To avoid that difficulty, the alternative of AFMPDT is investigated and constitutes a huge area of research activities in spatial exploration (Myers, 1990; Myers and Soulas, 1992; Mikellides, Turchi, and Roderick, 2000; Mikellides and Tu, 2000; Kodys and Choueiri, 2005; Kubota and Funaki, 2009; Albertoni, Paganucci, and Andrenucci, 2015). In the case of the AFMPDT, an external magnetic field is applied to enhance acceleration and plasma confinement. A lower plasma current is required to produce the same propulsive power than the SFMPDT. The AFMPDT introduces new acceleration mechanisms that do not directly depend on the discharge current and thus can allow the thruster to effectively operate at lower powers and achieved high specific impulse (Krülle, Auweter-Kurtz, and Sasoh, 1998). In sec.4.1.2 of Chap.4 we mentioned that when a external magnetic field is applied to an MPD thruster, additional acceleration mechanisms are added to the SFMPDT acceleration as presented in Fig.4.3. The thruster consists of a central cathode and a coaxial anode ring. Both are surrounded by a magnetic coil or permanent magnet producing an applied magnetic field whose field forms a magnetic nozzle diverging downstream of the thruster exit. In the present section the flow fields of the NASA Lewis Research Center $100 - kW$ are simulated and the influence of the magnetic field strength and the discharge current on the thrust performance is investigated for a wide range of applied magnetic field strengths $0.034 - 0.12\ T$ at cathode tip, discharge current $750 - 2000\ A$ with a constant Argon mass-flow rate $\dot{m} = 0.1\ g/s$.

6.1 Plasma fluid model for applied-field MPD thrusters and thrust evaluation

6.1.1 Plasma fluid model

Once again, for the calculation of the plasma flow inside an applied-field MPD thruster, the model used in this chapter assumes an electrically conducting but electrically neutral fluid immersed in a non-uniform magnetic field. The propellant gas (Argon) is injected into the discharge chamber as a fully-ionized fluid in a state of thermal equilibrium ($T = T_e = T_i$, where the index e and i refers to electrons and ions, respectively). Likewise to Chap.5, electrical sheath, Hall effect and radiation processes are neglected. We did not deal with turbulence because of his negligible contribution to the studied cases of interest. In presence of external applied magnetic field $B_{ap} = (B_r, 0, B_x)$, B_{ap} have to be distinguished from $B_i = (0, B_\theta, 0)$, the self induced magnetic field both expressed in the cylindrical coordinate system (r, θ, x) more suitable for axisymmetric problem. The total magnetic field variable $B = B_{ap} + B_i$ is introduced in the basic MHD equations of Chap.2. The components of the total current density $\mathbf{J}$ are computed as follows:

$$\mathbf{J} = \begin{pmatrix} j_r \\ j_\theta \\ j_x \end{pmatrix} = \begin{cases} \mathbf{J}_{dis} = \begin{pmatrix} j_r \\ 0 \\ j_x \end{pmatrix} = \frac{1}{\mu_0} \nabla \times \mathbf{B}_i \\ \\ \mathbf{J}_{ind} = \begin{pmatrix} 0 \\ j_\theta \\ 0 \end{pmatrix} = \sigma(\mathbf{U} \times \mathbf{B}_{ap}) \end{cases} \tag{6.1}$$

From the generalised Ohm's law (Eq.6.2) without the Hall effect and the electron pressure term derived from Eq.2.11 of sec.2.1.3 and the corresponding energy equation (Eq.6.3) above,

$$\mathbf{J} = \sigma(\mathbf{E} + \mathbf{U} \times \mathbf{B} \tag{6.2}$$

$$\mathbf{E} \cdot \mathbf{J} = \frac{|\mathbf{J}|^2}{\sigma} + (\mathbf{J} \times \mathbf{B}) \cdot \mathbf{U} \tag{6.3}$$

the acceleration and energy production mechanisms for a single fluid and fully ionized plasma are deducted. Indeed, considering all the acceleration mechanisms present when an applied magnetic field is used, the MHD equations of sec.2.1.4 in Chap.2 have to be altered since the hall and swirl Lorentz force and the corresponding energy production terms have to be included in the conservative equations of momentum and total energy respectively. As mentioned in sec.4.1.2 of Chap.4, theses additive electromagnetic forces are the Hall Lorentz force (F_{Hall}) and the Swirl Lorentz force (F_{Swirl}). The Hall Lorentz force results from the interaction of the azimuthal component of the total current density of Eq.6.1 namely the induced current density with the applied magnetic field. While the swirl Lorentz

force results from the interaction of the discharge current density with the applied magnetic field. Both can be defined as follows:

$$T_{Hall} = \int_V (\mathbf{J}_{ind} \times \mathbf{B}_{ap}) dV \tag{6.4}$$

$$T_{swirl} = \int_V (\mathbf{J}_{dis} \times \mathbf{B}_{ap}) dV \tag{6.5}$$

Finally, the equations which are resolved in the present chapter are derived from the MHD equations of Chap.2 (Eq.2.50, Eq.2.51, Eq.2.52, Eq.2.53) by including the work done by the swirl and the Hall Lorentz forces on the plasma take as a whole are defined as:

$$\frac{\partial \rho}{\partial t} + \nabla \cdot (\rho \mathbf{U}) = 0 \tag{6.6}$$

$$\frac{\partial \rho \mathbf{U}}{\partial t} + \nabla \cdot [\rho \mathbf{U}\mathbf{U} + (p + \frac{B^2}{2\mu_0})\mathbf{I} - \frac{\mathbf{B}\mathbf{B}}{\mu_0}] = \nabla \cdot \tau_{visc} \tag{6.7}$$

$$\frac{\partial \mathbf{B}_i}{\partial t} + \nabla \cdot (\mathbf{U}\mathbf{B}_i - \mathbf{B}_i\mathbf{U}) = -\frac{1}{\mu_0 \sigma} \Delta \mathbf{B}_i \tag{6.8}$$

$$\frac{\partial \rho E}{\partial t} + \nabla \cdot [(\rho E + p + \frac{B_i^2}{2\mu_0})\mathbf{U} - \mathbf{U} \cdot \frac{\mathbf{B}_i \mathbf{B}_i}{\mu_0}] = \nabla \cdot [k_{th} \nabla T - (\frac{\eta \mathbf{J}_{dis} \times \mathbf{B}_i}{\mu_0})] + \frac{|\mathbf{J}_{ind}|^2}{\sigma} + (\mathbf{J} \times \mathbf{B}_{ap}) \cdot \mathbf{U} \tag{6.9}$$

6.2 Code validation and numerical results

The developed density-based solver is used in this section to simulate the plasma flow inside the applied field NASA Lewis Research Center's (NASALeRC) MPD thruster (Krülle, Auweter-Kurtz, and Sasoh, 1998) because of its wide range of experimental data bank. It consisted of a cathode with 1.27 *cm* radius, surrounded by an anode with 5.1 *cm* radius both are 7.6 *cm* long. The magnet coil that provides the applied magnetic field is 15.3 *cm* long with a 10.15 *cm* radius. Practically, to avoid the creation in the discharge chamber of two magnetic forces pointing in opposite direction and to reduce the heat transfer from the thruster plume to the electrodes (Myers, 1990), the magnet is placed with one end coinciding with the exit plane of the thruster. The mass flow rate of Argon is maintained constant to 0.1 g/s at inlet, the discharge current strength is scaled from 750 A to 2000 A. The five values of the applied magnetic field strength, as measured at the cathode tip, range from 0.012 T to 0.1 T. The most challenging results of the numerical simulations are presented below.

6.2.1 Boundary and initiale conditions

The inputs of the code consist of the thruster discharge current, the propellant mass flow rate and a specified temperature. At inlet, the magnetic field is calculated as

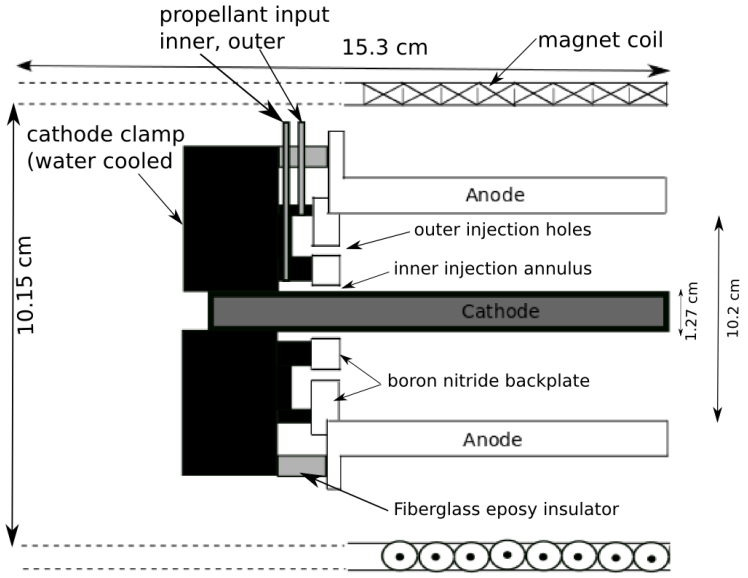

FIGURE 6.1: Geometry of the applied field NASA Lewis Research Center's MPD Thruster (Krülle, Auweter-Kurtz, and Sasoh, 1998) that is used for the present project

a function of the total discharge current with the expression:

$$B_0 = \frac{\mu_0 I}{2\pi r} \tag{6.10}$$

where I is the total discharge current and $r_{cathode} \leq r \leq r_{anode}$.
As, we considered the plasma flow as fully-ionized, the temperature at inlet is considered to be high enough (1 eV). On the electrode walls a slip condition is imposed for the velocity field while a no slip condition is used for insulated walls. The temperature is considered slightly less than the plasma flow temperature and a perfectly electrical conducting wall is specified for the induced magnetic field. At the exit boundaries, the normal gradients in any of the flow properties are set to zero and the induced magnetic field is fixed as zero. The computational domain is chosen to be large enough to enclose all the current within the domain and the induced magnetic field is fixed as zero at all exit boundaries. The axial and radial components of magnetic field, which represent the contribution of the applied magnetic field generated by the permanent magnet, are additionally added through a steady-state electromagnetic solver. In fact, the applied magnetic field is compute from the magnetic scalar potential ψ_m by solving the magneto static equations as in (Jackson, 1998; Vanderlinde, 2005) for a hard ferromagnet with a given magnetization $\mathbf{M}(r)$, function of coordinates and largely independent of the magnetic field:

$$\nabla \cdot \mathbf{B}_{ap} = \nabla \cdot \mu_0(\mathbf{H} + \mathbf{M}) = 0 \tag{6.11}$$

$$\nabla \times \mathbf{H} = \mathbf{J} \tag{6.12}$$

where $\mathbf{H}$ and $\mathbf{M}$ are the magnetic field and the magnetization produced by a permanent magnet. If there is no current density $\mathbf{J}$ (no free currents), Eq.6.12 reduces to $\nabla \times \mathbf{H} = 0$. Since the vector field is curl free, the magnetic scalar potential ψ_m is introduced just as $\mathbf{E} = -\nabla V$ (see Eq.1.13) in the electrostatics:

$$\mathbf{H} = -\nabla \psi_m \tag{6.13}$$

Assuming that the medium is linear and the magnetic permeability is constant, Eq.6.11 and Eq.6.13 are combined to the Laplace equation

$$\Delta \psi_m = 0 \tag{6.14}$$

Thus, once the magnetic scalar potential is evaluated through resolution of the differential equation Eq.6.14, the magnetic fields $\mathbf{H}$ and its flux density $\mathbf{B}$ can be calculated. Eq.6.11 yields to:

$$\nabla \cdot \mathbf{H} = -\nabla \cdot \mathbf{M} \tag{6.15}$$

Together with Eq.6.13 this leads to the magnetostatic Poisson equation

$$\Delta \psi_m = -\rho_m \tag{6.16}$$

where $\rho_m = -\nabla \cdot \mathbf{M}$ is the magnetic charge density. Thus, the magnetic scalar potential $\psi_m(r)$ produced at position $P(r)$ by a hard ferromagnet (source) of volume $V^{'}$ and surface $S^{'}$ with a magnetization $\mathbf{M}(r^{'})$ at position $r^{'}$ (see Fig.6.2) is given by the following integral:

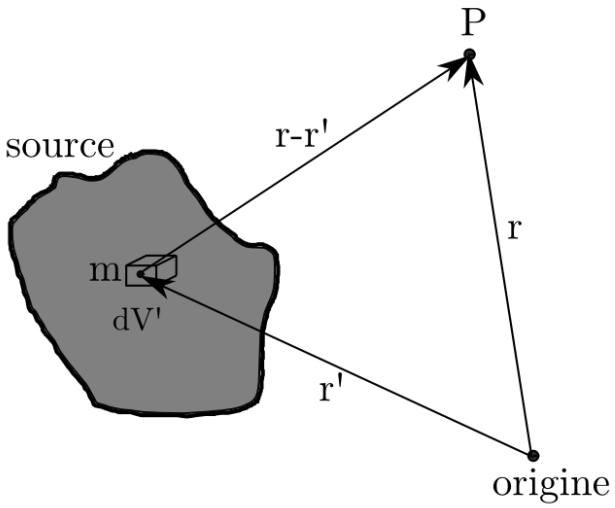

FIGURE 6.2: The magnetized object (source) and the target point (P) in the related frame

$$\psi_m(r) = -\frac{1}{4\pi}\int_V \frac{\rho_m(r')}{|r-r'|}d^3r' = -\frac{1}{4\pi}\int_V \frac{\nabla'\cdot\mathbf{M}(r')}{|r-r'|}d^3r' \tag{6.17}$$

In Fig.6.2, m is the dipole moment produced by a single volume dV'. By using integration by parts (See sec.A.2.3 of Appendix.A) and the divergence theorem may yield to:

$$\psi_m(r) = -\frac{1}{4\pi}\{\int_V \nabla'\cdot[\frac{\mathbf{M}(r')}{|r-r'|}]d^3r' - \int_V \mathbf{M}(r')\cdot\nabla'\frac{1}{|r-r'|}d^3r'\} = \\ -\frac{1}{4\pi}\int_S \frac{\mathbf{M}(r')}{|r-r'|}dS' + \frac{1}{4\pi}\int_V \mathbf{M}(r')\frac{1}{|r-r'|}d^3r' \tag{6.18}$$

The basic solution of the magnetic scalar potential equation at position r is then:

$$\psi_m(r) = -\frac{1}{4\pi}\int_V \frac{\nabla'\times\mathbf{M}(r')}{|r-r'|}d^3r' + \frac{1}{4\pi}\int_S \frac{\mathbf{n}'\times\mathbf{M}(r')}{|r-r'|}dS' \tag{6.19}$$

Since the magnetization vanishes at infinity, the first integral drops to zero at the surface when the divergence theorem is used. Where $\mathbf{n}'$ is the normal unit vector of the surface boundary S' of the ferromagnet. Fig.6.3 shows the contour plot of the magnetic scalar ψ_m and the vector plot of obtained magnetic flux density B_{ap} for a magnetization value $M = 860\ kA/m$ and magnet length of $L = 20\ mm$ with radius $R = 10\ mm$

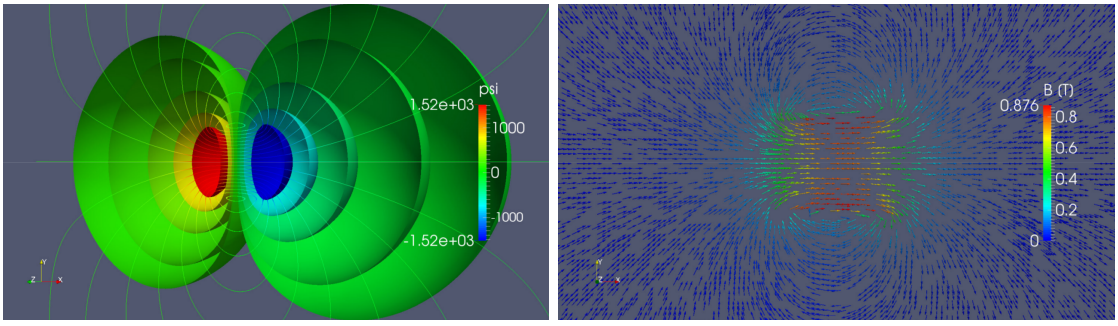

FIGURE 6.3: Contour plot (isosurfaces) and field lines of the magnetic scalar potential ψ_m (left) and Vector plot of the applied magnetic flux density B (right)

6.2.2 Results and discussion

The main effect of the application of an external magnetic field is to axially improve the plasma exhaust velocity and in the same time the thrust performance of the thruster. To do so, two physical processes are combined: Inside the discharge chamber, the plasma is put into rotation by the swirl component of the Lorentz force and outside the thruster, the expansion of the plasma plume downstream of

the anode face is contained in an effective divergence angle by the formed magnetic nozzle to axially accelerate the plasma. In the following subsections the quantitative effect of these two processes will be presented and discussed. For all simulations, steady-state was achieved at computational time value around 2 ms and numerically confirmed by a quasi horizontal progression over time of the axial velocity, temperature and pressure at the thruster exit in Fig.6.5.

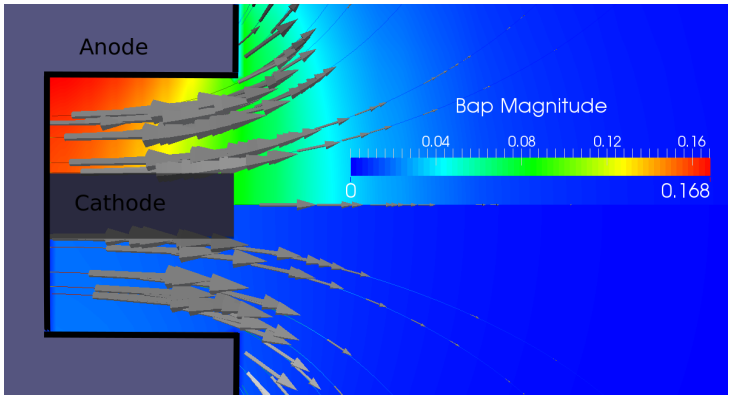

FIGURE 6.4: The applied magnetic field flux density distribution for $\mathbf{B}_{ap} = 100mT$ (top) and $\mathbf{B}_{ap} = 12mT$ (bottom) on the NASALeRC MPD thruster at the cathode tip

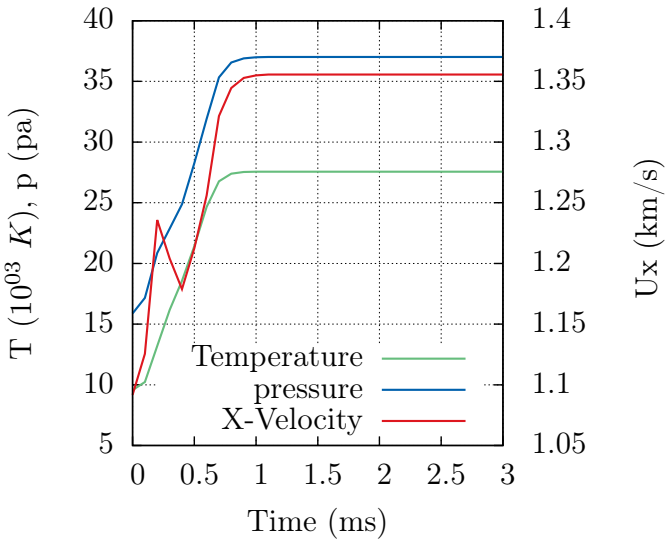

FIGURE 6.5: Simulation convergence test on the NASALeRC MPD thruster with $\dot{m} = 0.1\ g/s$, discharge current of $I = 1000\ A$ and $B_{ap} = 34\ mT$ at cathode tip

Effect of the applied magnetic field inside the NASALeRC MPD thruster

As the plasma flows outside of the thruster, the rotational energy as well as the thermal energy are converted to kinetic energy of axial motion. And both the

rotational and the thermal energy increase by increasing the applied magnetic field flux density strength B_{ap}. This physical process is illustrated by the helicoidal form of the velocity field lines in the axial direction of the thruster in Fig.6.7. The absolute value of the azimuthal component of velocity is maximal in discharge chamber near the anode surface and direct at the front of inlet near the cathode because of the presence of high values in these regions of both the applied magnetic flux density and the discharge current. It decreases from the discharge channel outward to the thruster exit and it is almost zero in the plume region as illustrated in Fig.6.7 for $B_{ap} = 34\ mT$ with $I = 1000\ A$ and $\dot{m} = 0.1\ g/s$ where the highest value of azimuthal velocity is about 3 km/s in the discharge chamber and around 1 km/s at the thruster exit. A direct consequence of this is the creation of a stagnation zone (Mikellides and Tu, 2000) where the axial component of plasma velocity is minimal and for cases with high applied magnetic field strength B_{ap}, negative values are observed exhibiting the existence of a force pointing in the opposite direction than the plasma flow.

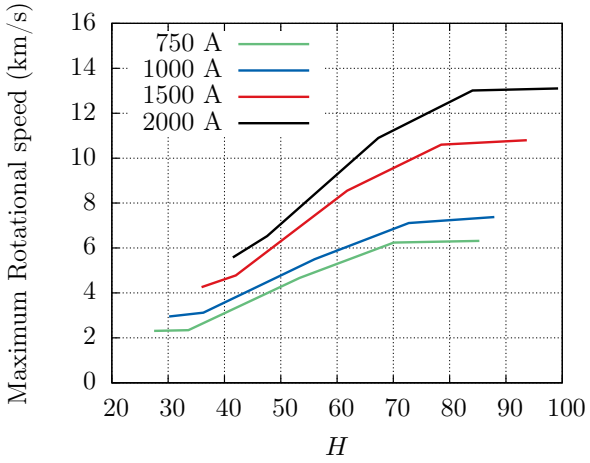

FIGURE 6.6: The maximum rotational speed in the discharge chamber function of H the Hartmann number with $\dot{m} = 0.1\ g/s$

By plotting the maximal rotational speed function of the Hartmann number H in Fig.6.6 for constant mass flow rate and for different values of discharge current ranging from 750 A to 2000 A, the correlation of the viscous force on the azimuthal speed is observed. The Hartmann number, which is the ratio of electromagnetic forces to the viscous forces, for all case investigated is always of two orders of magnitude greater than 1 which illustrate the importance of the viscous force compared to the magnetic forces. Thus, as the swirl Lorentz force increase with the applied magnetic field strength, the rotational speed increases and reaches a maximum value rather than continuously increases and then trends to be constant after that. This insights the existence of a critical rotational speed function of viscosity and magnetic forces namely discharge current and total magnetic field. According to the momentum equation (Eq.2.27 of Chap.2) the author of this limiting effect on azimuthal speed can only be the viscous drag. This behaviour was already observed in some previous work (Mikellides, Turchi, and Roderick, 2000) and illustrated the importance of viscous forces when compared to the electromagnetic forces. For $B_{ap} = 102\ mT$ with $I = 1000\ A$ corresponding in this study to the

Hartmann number $H = 88$, the present code predicts a maximal azimuthal speed of 7.38 km/s while the theory and the MACH2 code of Mikellides (Mikellides, Turchi, and Roderick, 2000) predict 30 km/s and 11 km/s respectively. These results point out the weakness of the physical model implemented in the present code. More particularly the viscosity coefficient which is evaluated in this work by the Sutherland model, did not include the two temperatures effect and appeared to be not suitable for plasma modelling because of high temperature encountered.

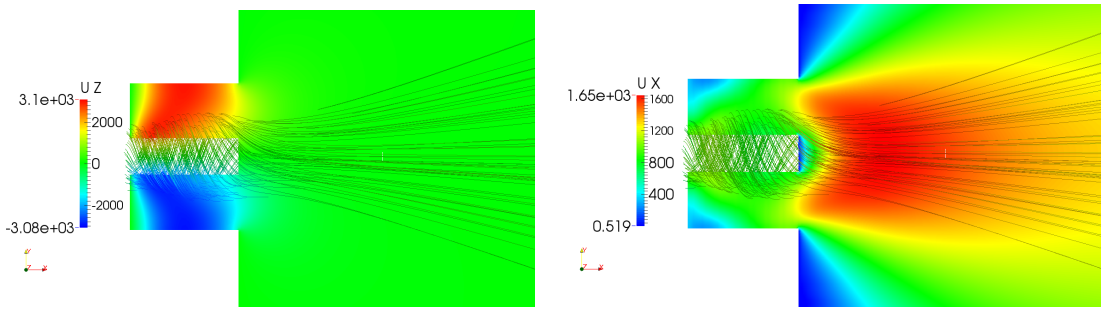

FIGURE 6.7: The swirl (left) and axial (right) component of velocity including velocity field lines in the discharge chamber with $\dot{m} = 0.1\ g/s$, discharge current of $I = 1000\ A$ and $B_{ap} = 34\ mT$

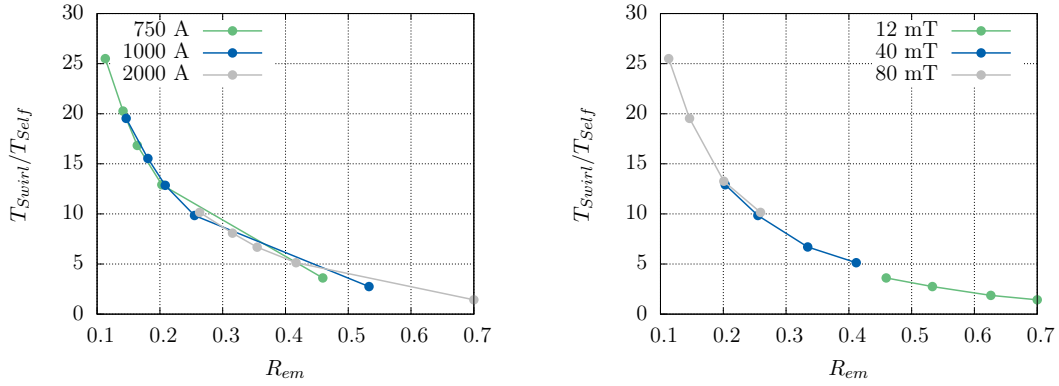

(a) Thrust ratio Vs Re_m (b) Thrust ratio Vs Re_m

FIGURE 6.8: Ratio of swirl over self component of thrust function of current (a), the ratio of the swirl over the self component of thrust (b) function of Re_m the magnetic Reynolds number with $\dot{m} = 0.1\ g/s$

Since the magnetic Reynolds number scales as the ratio of the induced magnetic field to the total magnetic field as mentioned with Eq.4.50 in sec.4.2.4 of Chap.4, it decreases by increasing the applied magnetic field and consequently has its values in the interval $[0, 1]$. The profile of the ratio of swirl to self thrust reveals that for a constant value of discharge current (induced magnetic field strength), the swirl to self thrust ratio increases by increasing the applied magnetic strength which corresponds to the decreasing of the magnetic Reynolds number (see Fig.6.8.a). The swirl to self thrust ratio is then inversely proportional to the magnetic Reynolds

number. This behaviour is the same by increasing the current at constant applied magnetic field strength (see Fig.6.8.b) because the self thrust increases as the discharge current increases. But the ratio remains greater than 1 for all cases considered. That is due to the fact that the swirl thrust depends of both the discharge current and the applied magnetic field. While the self thrust only depend of the discharge current. Thus, it appeared that the swirl component of thrust is dominant than the self thrust and it is mostly responsible with the thermal thrust of the acceleration of the plasma out of the thruster. In addition the fact that the magnetic Reynolds number remains in the order of $\mathcal{O}(10^{-1})$ shows the relative importance of the applied magnetic field in comparison to the induced magnetic field and moreover the effect of the former on plasma flow can not be neglected in all case considered in the present work. The above results are then used to derived an analytic expression for swirl and self thrust ratio since the swirl and the self thrust ratio scales in the same interval value and follows almost the same parabolic function of magnetic Reynolds number regarding the results of Fig.6.8. This parabolic function expressing the inverse proportionality of thrust ratio with magnetic Reynolds number can be defined as:

$$\frac{T_{Swirl}}{T_{Self}} = f(Re_m) = \frac{A}{Re_m^2} + \frac{B}{Re_m} + C \tag{6.20}$$

where A, B et C are constants. By taking $A = 0.0007$, $B = 3.0$ and $C = -5/2$ the ratio of swirl Lorentz force to self Lorentz force using Eq.6.20 is compared to the prediction of the present density-based solver in Fig.6.9. This insights much better the negative correlation of thrust ratio with the magnetic Reynolds number. Is then preferable to operate with lower magnetic Reynolds number that means lower discharge current and higher applied magnetic field to obtain high swirl thrust and consequently high total thrust with high specific impulse.

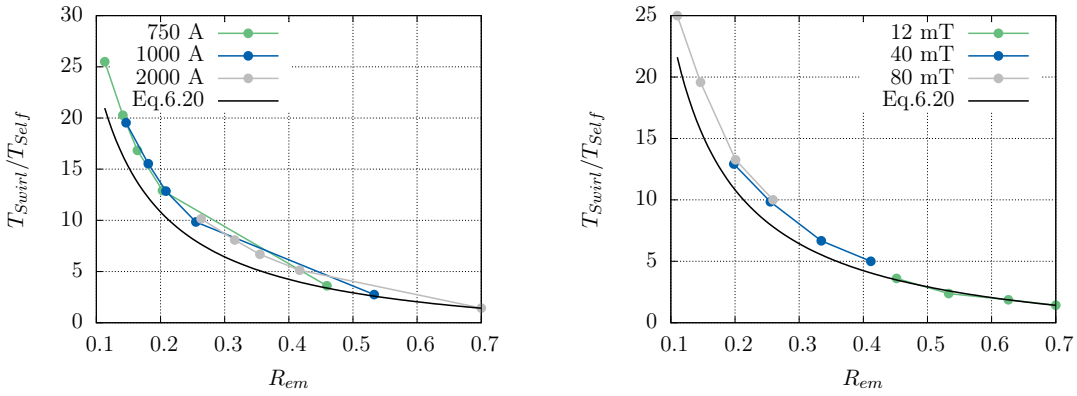

(a) Thrust Vs R_{em} (b) Thrust Vs R_{em}

FIGURE 6.9: Thrust function of applied magnetic field (a) and thrust function of current (b) with $\dot{m} = 0.1\ g/s$, $A = 0.0007$, $B = 3.0$ and $C = -5/2$

In Fig.6.10, the effect of the increase of applied magnetic field on the plasma density is illustrated with constant discharge current (1000 A in the present case).

There is a notable decrease of plasma density at the anode as well as at the cathode surfaces when the magnetic field increases. For all cases, the highest plasma density is at inlet near the anode surface. At the anode this starvation of plasma density can be explain by the increase of the pinching effect of the radial Lorentz force $(\mathbf{J} \times \mathbf{B})_r = j_\theta B_x - j_x B_\theta$ with the increase of applied magnetic field, where $\mathbf{J}$ and $\mathbf{B}$ are the total density current and the total magnetic field as presented in sec.6.1. This pinching effect of the Lorentz force on the depletion of the plasma density at the anode surface has been used by several numerical and experimental studies to explain the increase of the anode potential fall at the anode (Kubota, 2009; Lev, 2012). At the cathode the decreasing of the plasma density by increasing the applied magnetic field is mainly due to the swirl Lorentz force $(\mathbf{J} \times \mathbf{B})_\theta = j_x B_r - j_r B_x$ acting to rotate the plasma analogically to the mechanical torque of a hollow cylinder and creating an inertial force which pushes the plasma radially from the center of the rotation circle (cathode) outward.

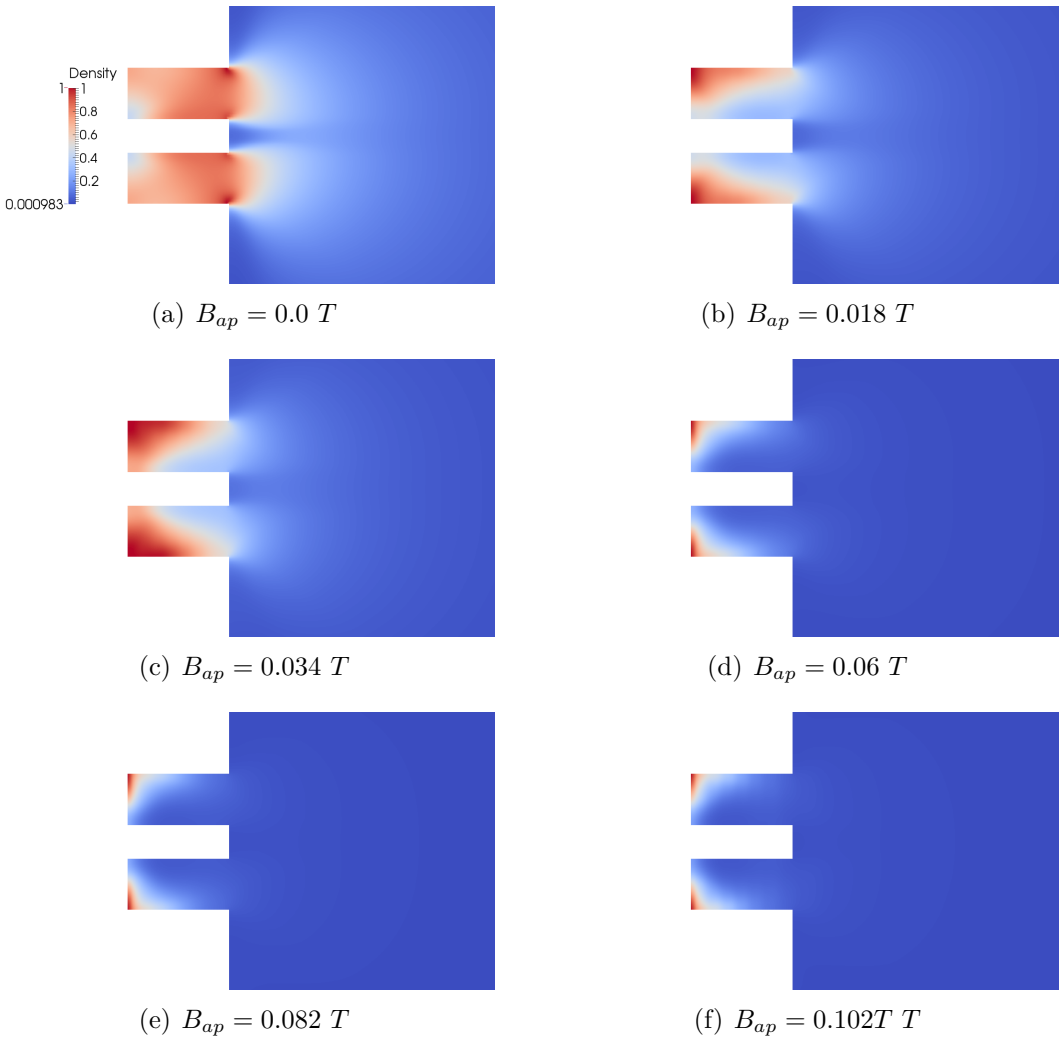

(a) $B_{ap} = 0.0\ T$ (b) $B_{ap} = 0.018\ T$

(c) $B_{ap} = 0.034\ T$ (d) $B_{ap} = 0.06\ T$

(e) $B_{ap} = 0.082\ T$ (f) $B_{ap} = 0.102T\ T$

FIGURE 6.10: Steady-state distribution of the plasma density inside the discharge chamber with $\dot{m} = 0.1\ g/s$ and discharge current of $I = 1000\ A$ for various B_{ap} values ranging from $0.0\ T$ to $0.102\ T$

The inertial force created increases which the azimuthal speed which increases with

the applied magnetic field. The quantification of this inertial force is not investigated in the present work but could be an interesting topic for further research.

Effect of the applied magnetic field outside the NASALeRC MPD thruster

Outside the MPD thruster, the acceleration in the plume region of the thruster is based on the conversion of the above mentioned rotational energy via expansion in a magnetic nozzle which is formed by the diverge magnetic field lines. The induced azimuthal currents interact with the applied magnetic field to produce a radially confining electromagnetic force as shown in Fig.6.11. In Fig.6.12, the present results are compared with those of (Mikellides, Turchi, and Roderick, 2000) and experimental data (Myers, 1990). With the initial temperature value of 1 eV, since the plasma is supposed to be fully ionized, the thrust variation function of the applied magnetic field and discharge current is underestimate by the present code. The differences observed with experiment values (Myers, 1990) is due to the simplified physical model employed in this work concerning the viscous force acting on plasma which seems to be over evaluated and also to the energy losses at the anode surface in the sheath layer which is not took into account in the present model. Nevertheless, the code reproduced the increase of thrust as predicted by some previous modelling and analytic works (Myers, 1990; Tang et al., 2012; Albertoni, Paganucci, and Andrenucci, 2015) and demonstrated the capability of the present code to predict plasma acceleration process in the AFMPDT. By supplying more energy through the plasma temperature ($T_{init} = 3\ eV$), the results of the density-based code exhibits a good agreement with experimental data (see Fig. 6.12(a) and Fig. 6.12(b)). In light of these encouraging results concerning the predictive capabilities of the theory, we proceed to a parameter study with the purpose to identify the effect of applied magnetic field strength and discharge current in thrust performance of the NASALeRC MPD thruster. Fig. 6.13 shows the evolution of thrust depending of applied magnetic field strength and discharge current. For each value of discharge current, the linear increase of thrust with increasing applied magnetic field strength is maintained and the higher is the discharge current, the higher is the maximal of the produced thrust (See Fig.6.13(a)). The same trend is observed in Fig.6.13(b) by interchanging the applied magnetic field strength with the discharge current but with a weaker slope showing that with this configuration, thrust is more sensible to the applied magnetic field than the discharge current.

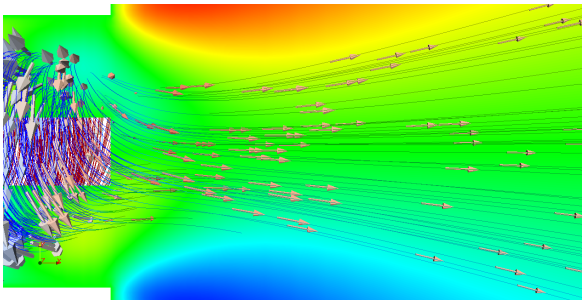

FIGURE 6.11: Distribution of the Y-Component of velocity including velocity field lines and vectors on the NASALeRC MPD thruster at the cathode tip with $\dot{m} = 0.1\ g/s$, $\mathbf{B}_{ap} = 60mT$ and discharge current of $I = 1000\ A$

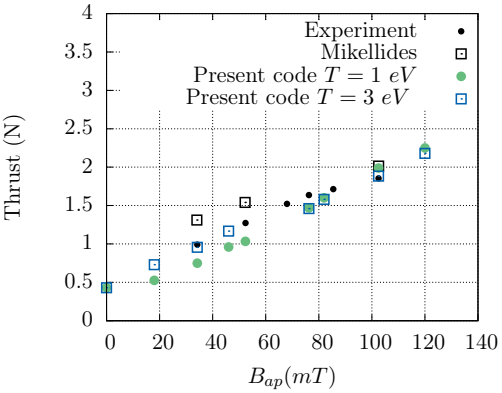

(a) Thrust Vs Applied magnetic field

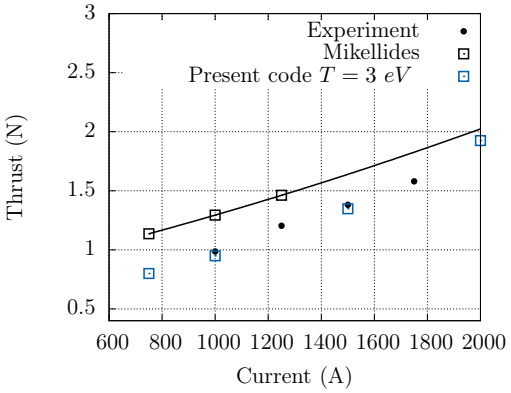

(b) Thrust Vs Discharge current

FIGURE 6.12: Thrust vs applied magnetic field strength (at the cathode tip) with $\dot{m} = 0.1\ g/s$ and discharge current of $I = 1000\ A$ (a) and thrust vs discharge current with $\dot{m} = 0.1\ g/s$ and $B_{ap} = 0.034\ T$

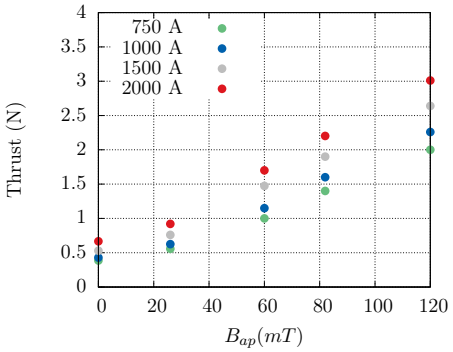

(a) Thrust Vs Applied magnetic field

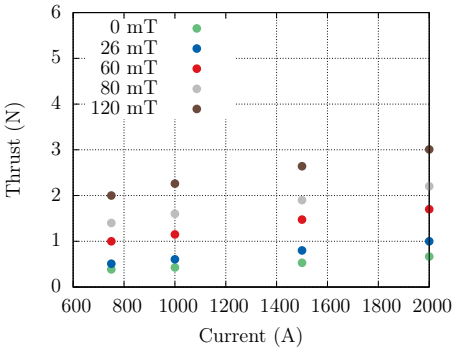

(b) Thrust Vs Discharge current

FIGURE 6.13: Thrust function of applied magnetic field (a) and thrust function of current (b) with $\dot{m} = 0.1\ g/s$

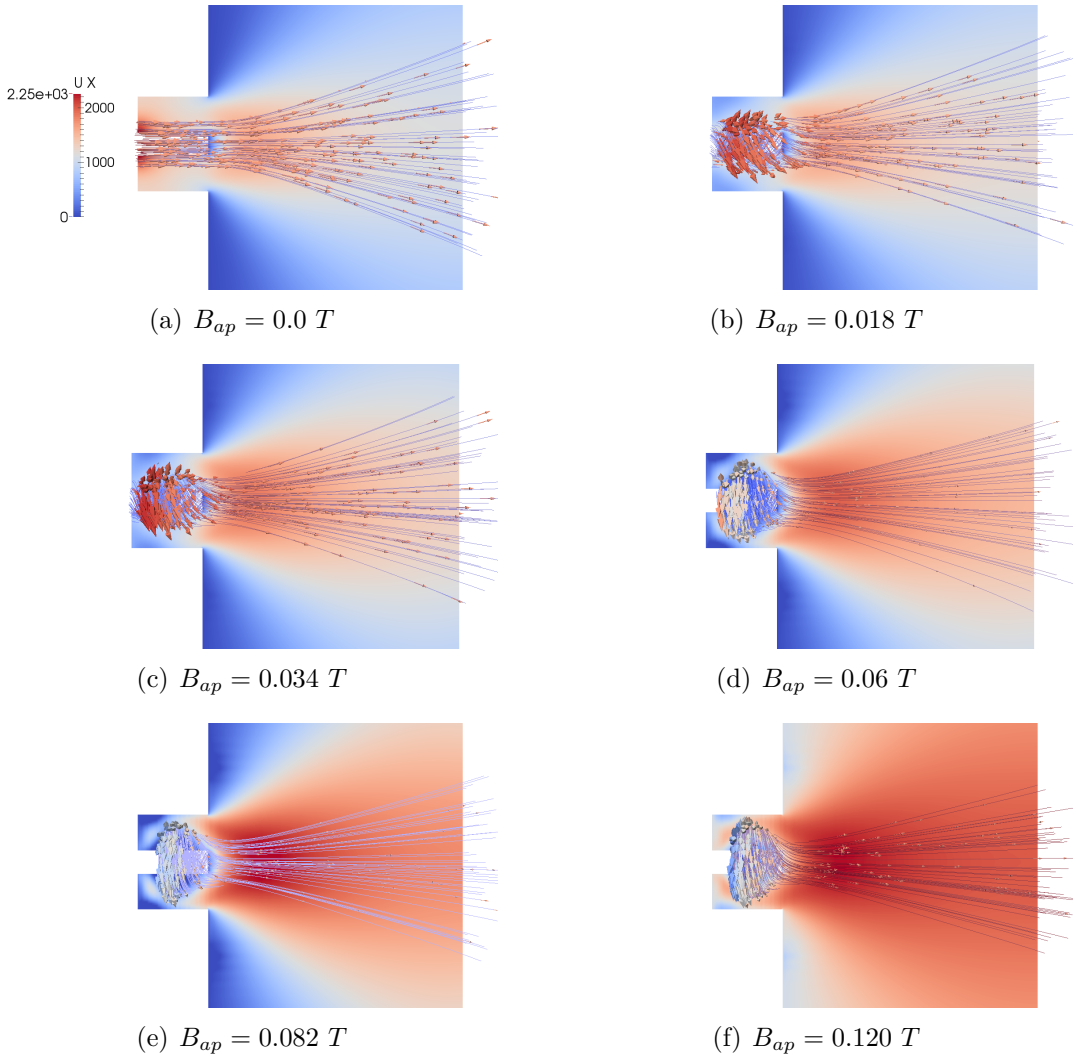

(a) $B_{ap} = 0.0\ T$ (b) $B_{ap} = 0.018\ T$

(c) $B_{ap} = 0.034\ T$ (d) $B_{ap} = 0.06\ T$

(e) $B_{ap} = 0.082\ T$ (f) $B_{ap} = 0.120\ T$

FIGURE 6.14: Steady state contour of the X-component of velocity including velocity field lines and vectors with $\dot{m} = 0.1\ g/s$ and discharge current of $I = 1000\ A$ for various B_{ap} values ranging from $0.0\ T$ to $0.12\ T$

The increase of thrust with the applied magnetic field is more highlighted in Fig.6.14. In the plume region the plasma is accelerated by the expansion through the magnetic nozzle and also by the conversion of the azimuthal kinetic energy to the axial useful kinetic energy. With no magnet corresponding to the Reynolds magnetic number $Re_m = 1$, the plasma velocity lines in the discharge chamber are almost parallel to the thruster centreline and diverge from it as the plasma expands downstream. The maximal axial velocity value is located at the inlet near the cathode surface because of the presence there of the highest value of discharge current. The plasma acceleration is then completely produced by the self Lorentz force $\mathbf{J}_{dis} \times \mathbf{B}_{ind}$ and by the joule heating. When an external magnet comes into the system, the plasma starts to rotate in response to the swirl Lorentz force $\mathbf{J}_{dis} \times \mathbf{B}_{ap}$ and a helicoidal plasma flow is produced in the discharge chamber. As the applied magnetic field increase, the plasma is accelerated downstream in the plume region and due to the increasingly plasma density starvation in the discharge chamber,

the rotational spectrum moves to the cathode tip and its radius increases. As the applied magnetic field increases, from 0.018 T to 0.12 T, the magnetic Reynolds number decreases from 0.43 to 0.1 showing the increase of the dominance of the applied magnetic field over the self-induced magnetic field. Thus, the acceleration of the plasma outside the thruster is now mainly conducted by the swirl Lorentz force, assisted by the self Lorentz force and the joule heating.

6.3 Summary

In the present Chapter, the developed density-based method has been extended and apply to the numerical modelling of the applied-field NASALeRC MPD thruster. The resistive MHD equations have been modified by introducing the additional Lorentz force and their energy contributions. The applied magnetic field is compute by a steady state electromagnetic solver and imported. As the main goal of this chapter was to underline the ability of the density-based method to deal with the physical process of plasma flow acceleration in the applied-field MPD thrusters according to single fluid approximation of plasma, the physical model implemented is maintained as simple as possible. Thus, the perfect gas equation of state, the non generalized Ohm's law i.e without electron pressure and Hall effects and the spitzer-Harm formulation for electrical conductivity have been considered. The application of the developed numerical algorithm for the simulations of the applied-field NASALeRC MPD thruster with the applied magnetic field values ranging from 0.018 T to 0.12 T, discharge current values ranging from 750 A to 2000 A and constant mass flow rate of $\dot{m} = 0.1\ g/s$ demonstrates that the method presented can reproduce the theory of thrust production and plasma acceleration. Indeed, the quasi linear increase of the total thrust with the applied magnetic field and with the discharge current are reproduced. The limitation of the rotational speed of plasma in the discharge chamber as well as the depletion of the plasma density on the anode surface as the applied magnetic field increases are also described by the present code. And more importantly, it has been found that the ratio of swirl to self thrust depends only of the magnetic Reynolds number and can be approximated by an analytic parabolic function. Thus, to obtain a higher thrust is then preferable to operate with lower magnetic Reynolds number which means higher applied magnetic field compares to induced magnetic field. Nevertheless, the code underestimate the experimental thrust values because of the non suitable viscosity model implemented and the presence of some energy sink such as the sheath voltage at the anode surface which are not considered. To overcome these issues in the near future work, the improvement of the physical model and most particularly the transport and thermophysical properties must be investigated.

Chapter 7

Summary and conclusions

In this chapter, the main results of the present work are recapitulated and discussed along with its limitations. Finally, future improvement possibilities of the physical and numerical model used are underlined.

7.1 Contributions of this thesis

The aim of the present work is the development of a density-based method for the numerical modelling of the magnetohydrodynamics equations. For that purpose, the semi-discrete central-upwind schemes of Kurganov (Kurganov, Noelle, and Petrova, 2001; Kurganov and Petrova, 2000) initially developed for Euler equations have been extended to MHD equations including the magnetic divergence free constraint of Dedner at al.(Dedner et al., 2002). The proposed MHD solver satisfies the integral form of conservation laws, does not require eigenvector-decomposition, allows the possibility to switch between the KNP-MHD and the KT-MHD method and also the use of the real gas transport and thermophysical properties such as the ratio of specific heats and the viscosity coefficient if necessary.

First of all, in Chap. 3 the development of the density-based numerical method in the finite volume framework is explain in detail. The variables values needed for the approximation of the surface and volume integrals of the CV have been interpolated by using the central-upwind scheme which allows us to take advantage of the high resolution and the simplicity of the central schemes while retaining the strength of the less dissipative upwind schemes concerning the estimation of the convective fluxes in two direction depending of the vector velocity of the flow. To permit the central-upwind discretization schemes to achieve the higher-order accuracy possible, limiter functions are used. The time integration is performed using a simple Euler implicit scheme.

7.1.1 Ideal MHD

The robustness and the accuracy of the central-upwind schemes of the new density-based numerical algorithm is tested on a series of benchmark numerical simulations. The obtained simulation results in sec.3.6 demonstrate that the method presented is competitive with the existing best methods. For instance, for the MHD shock tube problem, the schemes provide good agreement with the analytical solution and high-resolution results by capturing strong and slow shock, fast and slow rarefaction waves with the one-dimensional Brio-Wu shock tube test. An analysis about several flux limiter functions is conducted and the Minmod function

has been chosen as limiter functions for all simulations performed in this work because of its ability to provide very smooth solutions without producing oscillation behaviours in comparison to other flux limiter functions. With the Sod's Riemann problem MHD adaptation, our KNP-MHD and KT-MHD performed better than the HLL approximation relatively to Roe scheme after the fast rarefaction wave and lie closest to the Roe solution around the slow shock. These results illustrate the robustness and the accuracy of our flux schemes to deal with MHD shocks.

The second test, the Orszag-Tang vortex, reveals the ability of the central-upwind schemes to capture the transition from a smooth initial condition to MHD turbulence state including local supersonic regions of a compressible conducting fluid. The comparison of our schemes with the WENO-5 scheme of Shen (Shen, Zha, and Huerta, 2012) shows satisfactory agreement. The conservation errors for momentum and total energy have been evaluated over time and except at two points where the magnetic reconnection is supposed to occur, the conservative laws are fulfilled. The convergence rate of both schemes KNP-MHD and KT-MHD are between the first and the second order because of the use of flux limiter.

Lastly, the cloud-shock interaction problem is used to test the ability of the present solver to deal with the interaction between MHD shocks and a denser cloud. The KT-MHD works well and avoid some issues such as the non positivity of pressure. The contact discontinuities and shock waves are very well simulated and the main expected phases of the interaction are very well observed. The results are in accordance with those obtained by the AUSM scheme presented by Xisto (Xisto, Pascoa, and Oliviera, 2013).

7.1.2 Self-field MPD thrusters

This thesis represent the first attempt to the development of a central-upwind density-based code dedicated to the simulation of MPD thrusters. That is the raison why the physical model implemented in the present code is maintained as simple as possible. The propellant used is Argon and it is injected into the discharge chamber as fully ionized single fluid in a state of thermal equilibrium. Electrical sheath on electrodes, Hall effect, turbulence and radiation process are neglected. Nevertheless, the application of the developed numerical algorithm for the simulations of the self-field MPD thrusters demonstrates that the present method is able to evaluate the main flow characteristics as well as the performance parameter.

In Chap.5, the first application case, the Princeton's full scale benchmark thruster (PFSBT), have been simulated and the results shows good agreement with the experimental values (Boyle, 1974) and numerical simulation results of Sankaran (Sankaran, Choueiri, and Jardin, 2005). The best performance has been obtain at the nominal operating condition (3.8 % and 2.2 % difference under the measured thrust value and the results of Sankaran respectively).

Good results have been also obtained by the prediction of thrust and plasma voltage of the second application case, the Princeton's extended anode thruster (PEAT). The difference between the simulation results and experiment is over 10 % for $0.2 < \xi < 0.8$. The code perform better as the discharge current increases till $\xi \leq 0.9$ and just before the beginning of the onset instability with the best

performance around $\xi = 0.9$. We reported at that point, 0.17 %, 1.11 % and 0.83 % thrust difference between our computational results and Lapointe 1-T, 2-T codes and experimental data respectively. For $\xi \geq 1$, the results became worst due to the onset voltage instability.

The last self-field MPD thruster application case used in this work concerned the Villani thruster. Simulation produce satisfactory results and allows us to conduct a first MPD thruster designing study. Regarding the results obtained in the geometric analysis, a short cathode is recommended for a stable operating conditions. That is due to the fact that the long channel anode contributes to retain the radial aerodynamic expansion of the plasma at the end of the cathode which consequently prevents plasma depletion (Kubota, 2009) around the anode surface. Long cathode allows higher values of efficiency and specific impulse to be achieved. In both configuration, higher aspect ratio l_a/r_a is recommended over all operating conditions (See Tab.5.3 and Tab.5.4). Concerning the designing effort of the MPD thruster with the present code, a right compromise has to be found between efficiency (long cathode) and the thruster operation stability (short cathode) and both with high thruster aspect ratio l_a/r_a. In conclusion, the code is robust and stable by high values of discharge current or ξ and for several geometric configurations, the steady-state has been achieved and the onset instability observed.

7.1.3 Applied-field MPD thrusters

Due to limitations of the SFMPDT to operate at high currents because of thermal problem and onset instabilities, the present code has been extended in Chap.6 to AFMPDT. The applied magnetic field is compute from a steady-state electromagnetic solver where the Poisson's equation for the magnetic scalar potential, generated by a permanent magnet, is solved. The applied-field NASALeRC MPD thruster is chosen to test the ability of the code to evaluate thruster performance parameters as well as its capacity to reproduce plasma flow behaviours and acceleration mechanisms in the simultaneous presence of self and applied magnetic field. Argon is maintained as propellant and once again it is injected in the discharge chamber with the mass flow rate $\dot{m} = 0.1\ g/s$ as fully ionized single fluid in a state of thermal equilibrium. The values of applied magnetic field considered are ranging from 0.018 T to 0.12 T with discharge current values ranging from 750 A to 2000 A.

At the thruster exit, the quasi linear increase of the total thrust with the applied magnetic field and with the discharge current are reproduced. For both parameter studies, the maximum recorded value of total thrust is around 3 N with an applied field value of 0.12 T and a discharge current of 2000 A. As more energy have been supplying in the system through the plasma initial temperature better agreement with the experimental data has been achieved, pointing the fact that there is several sources and sinks of energy which are not considered.

In the discharge chamber, the expected rotational motion of plasma, generated by the swirl component of the Lorentz force, has been captured by the code. At constant discharge current, the rotational speed of the plasma increases by increasing the strength of the applied magnetic field and a maximum of $\sim 7\ km/s$

is obtained with $I = 1000\ A$ and $B_{ap} = 120\ mT$. This value is 30 % below the value of the maximal rotational speed reported by Mikellides (Mikellides and Tu, 2000) ($\sim 10\ km/s$). The difference is mainly due to the absence of a suitable viscosity model in the physical model considered in this work.

Finally, it appears that, the conversion of the azimuthal kinetic energy to the axial useful kinetic energy is the main responsible of the acceleration of the plasma in the plume region of the thruster and for an efficient operating condition, it is preferable at constant applied magnetic field to reduce the azimuthal speed by increasing the discharge current and at constant discharge current to enhanced the azimuthal speed by increasing the applied magnetic field.

7.2 Improvement possibilities

To improve the present code and make it be more efficient and practical to MHD equations for compressible and conducting fluid, several aspect remain to be investigated:

1. Upgrade the developed computational model by including the relevant physical-chemical processes such as a multi-level non equilibrium ionization model, species transport and energy transfer through collisions and discharge in our density-based central-upwind schemes environment. In fact, the present density-based code overestimated the thrust for $\xi < 1$ and underestimated it for $\xi \geq 1$. That is mainly due to the fact that several complicated physical processes such as those listed above are ignored by considering the plasma as a singly fully ionized fluid. Indeed, the input power of the thruster is divided between three dominant processes namely joule heating, ionization and acceleration of the propellant gas. Considering the physical model used here, That's means that, for $\xi < 1$, we have less energy sinks and consequently, thrust is overestimated. For $\xi = 1$, the nominal operating condition occurred and there is an equipartition of the input power between acceleration and ionization. The difference of the calculated thrust with the experimental thrust is then minimized. For $\xi \geq 1$, the acceleration is dominant because of its huge electromagnetic component and it is well known that the momentum of the neutral particles is not affected by the electromagnetic forces but only by collisions with ions. Thus, the difference between calculated thrust and experimental thrust increases again and the thrust is underestimated. To overcome this difficulty in the near future work, the plasma specie equations (momentum and energy) have to be implemented including a multi-level non equilibrium ionization model and recombination.

2. As reveals in Chap.5, the prediction of discharge voltage remains an important disadvantage of the present code and constitutes the most urgent improvement which have to be done in the near future. Indeed, an accurate evaluation of the discharge voltage including electrode falls will conduct to better efficiency prediction of the thrusters. Previous studies demonstrate that the Hall effect term in Ohm's law is responsible of the plasma depletion near the anode surface which causes anode potential fall and onset instabilities. In the other hand Anode potential fall plays an important role on energy loss mechanism and therefore its contribution has to be taken into account for a correct prediction of thruster performance parameters. To do so, sheath effect has to be included in Ohm's law more specifically

in the magnetic field equation. Moreover, a more suitable boundary condition at the electrodes for the handling of the sheath region has to be implemented.

3. The code provides computations for both planar and cylindrical geometries. It can deal with complex geometry configurations without any code modification. Nevertheless, the code at this stage can only handle Cartesian coordinate system just as all OpenFOAM based solvers. It is well known that the physic of plasma acceleration is well described in a cylindrical coordinate due to the geometry of the thruster first, and more particularly to the huge importance of the azimuthal components of magnetic field and current regarding the swirl movement of the plasma in the discharge chamber. Thus, it will be suitable and more efficient to convert the Cartesian coordinate system to the cylindrical coordinate system to be able to well capture the plasma acceleration in all three dimensions.

7.3 Concluding remarks

The code presented in this thesis used a time-marching algorithm to solve a full three dimensional, single fluid MHD equations. It represents the first simulation of MPD thrusters with a pure density-based central-upwind schemes. Its main purpose was not intended to highlighted all the physical-chemical mechanisms involved in MPD thrusters but to develop from the bottom up a suitable and consistent method to deal with MHD shocks, discontinuities and physic of plasma acceleration. The present method in contrary of several sophisticated code existing in the literature, does not require eigen-decomposition, is simple to implement and to handle. From the ideal benchmark MHD problems to the self and/or applied MPD thrusters, the results obtained are of great quality as they compare well with experiments as well as with numerical simulations of previous studies of literature.

PhD Student contribution

Name: Charles CHELEM MAYIGUE, M. Sc.

In the dissertation the results from the supervision of the following student work are:

Development of the ideal and resistive MHD code *2014 - 2015*

- Implementation of the magnetohydrodynamic (MHD) equations in a compressible density-based solver environment. In fact the challenge was to alter the Navier-Stokes equations in a pre-existing code based on Kurganov and Tadmor flux scheme methods and dedicated to the study of compressible transonic flows, so that the discharge current, the induced magnetic field and their effects on the flow could be taken into account and transported consistently with the standard thermo-fluid dynamic variables such as temperature, pressure, velocity and density.
- Implementation of the electrical conductivity according to Spitzer-Harm formulation for fully ionized and single temperature plasma.
- Implementation of a divergence cleaning method and use of the limiter functions to prevent some numerical issues regarding the purpose of the present work and to improve the quality of the results.

Simulations and validation of the resulted codes *2015 - 2016*

- Validation of the ideal MHD code through numerical simulations of ideal MHD benchmark problems (The Brio-Wu shock tube problem, the cloud-shock interaction and the Orszag-Tang vortex problem) and co-writing the papers titled *Computational magneto-hydrodynamic modeling of hyper-sonic flows with resolved shock wave diffusion* and *"A density-based method with semi-discrete central-upwind schemes for ideal magnetohydrodynamics"*.
- Building up the geometries, definition and implementation of suitable boundary conditions for magneto-plasma dynamic (MPD) thrusters. More particularly for the induced magnetic field and pressure.
- Performing simulations for low-powered Argon plasma thrusters (less than 10000 A) and prediction of the different components of thrust (thermal and electromagnetic) and plasma votage. Comparaison of the predicted thrust with the analytic model of Maecker.
- Co-writing the paper titled *"Magneto-Plasmadynamic Thruster modelling with coaxial induced magnetic field"*.

- Extension of the code to High-powered Argon MPD thrusters (more than 10000 A) by implementing a real gas ratio of specific heats more appropriate for high plasma temperature.
- Performing simulations of the self-field MPD thrusters and comparison with experimental data and previous studies of literature.

Extension of the code to applied-field MPD thrusters *2016 - 2017*

- Development of the applied-field MHD model, modification of the resistive MHD equations to introduce the new source and sink terms related to the existence of a permanent magnet surrounding the anode.
- Building up the geometries and definition of the applied magnetic field boundary condition.
- Performing simulations of the applied-field MPD thrusters and comparison with experimental data and previous studies of literature.
- Co-writing two additional papers related to the self- and applied-field MPD thrusters not yet submitted.

Appendix A

Vectors and manipulations

A.1 Vector identities

A list of the most frequently exploited identities. Here $\mathbf{A}$, $\mathbf{B}$, $\mathbf{C}$ are vectors fields and Φ a scalar field. $\mathbf{I}$ and $\overline{\overline{\tau}}$ are the unit dyad and a tensor respectively.

$$\mathbf{A}\cdot(\mathbf{B}\times\mathbf{C})=\mathbf{C}\cdot(\mathbf{A}\times\mathbf{B})=\mathbf{B}\cdot(\mathbf{C}\times\mathbf{A}), \tag{A.1}$$

$$\mathbf{A}\times(\mathbf{B}\times\mathbf{C})=\mathbf{A}\cdot\mathbf{C}\mathbf{B}-\mathbf{A}\cdot\mathbf{B}\mathbf{C},(\mathbf{A}\times\mathbf{B})\times\mathbf{C}=\mathbf{A}\cdot\mathbf{C}\mathbf{B}-\mathbf{B}\cdot\mathbf{C}\mathbf{A}, \tag{A.2}$$

$$\nabla\times\nabla\Phi=0, \tag{A.3}$$

$$\nabla\cdot(\nabla\times\mathbf{A})=0, \tag{A.4}$$

$$\nabla\times(\nabla\times\mathbf{A})=\nabla\nabla\cdot\mathbf{A}-\nabla^2\mathbf{A}, \tag{A.5}$$

$$\nabla\cdot(\Phi\mathbf{A})=\mathbf{A}\cdot\nabla\Phi+\Phi\nabla\cdot\mathbf{A}, \tag{A.6}$$

$$\nabla\times(\Phi\mathbf{A})=\nabla\Phi\times\mathbf{A}+\Phi\nabla\cdot\mathbf{A}, \tag{A.7}$$

$$\mathbf{A}\times(\nabla\times\mathbf{B})=(\nabla\mathbf{B})\cdot\mathbf{A}-\mathbf{A}\cdot\nabla\mathbf{B}, \tag{A.8}$$

$$(\mathbf{A}\times\nabla)\times\mathbf{B}=(\nabla\mathbf{B})\cdot\mathbf{A}-\mathbf{A}\nabla\cdot\mathbf{B}, \tag{A.9}$$

$$\nabla(\mathbf{A}\cdot\mathbf{B})=(\nabla\mathbf{A})\cdot\mathbf{B}+(\nabla\mathbf{B})\cdot\mathbf{A}=\mathbf{A}\cdot\nabla\mathbf{B}+\mathbf{B}\cdot\nabla\mathbf{A}+\mathbf{A}\times(\nabla\times\mathbf{B})+\mathbf{B}\times(\nabla\times\mathbf{A}), \tag{A.10}$$

$$\nabla\cdot(\mathbf{A}\mathbf{B})=\mathbf{A}\cdot\nabla\mathbf{B}+\mathbf{B}\nabla\cdot\mathbf{A}, \tag{A.11}$$

$$(\nabla\mathbf{B})\cdot\mathbf{B}=\nabla\cdot[\frac{\mathbf{B}\cdot\mathbf{B}}{2}\mathbf{I}], \tag{A.12}$$

$$\nabla\cdot(\mathbf{A}\times\mathbf{B})=\mathbf{B}\cdot\nabla\times\mathbf{A}-\mathbf{A}\cdot\nabla\times\mathbf{B}, \tag{A.13}$$

$$\nabla\times(\mathbf{A}\times\mathbf{B})=\nabla\cdot(\mathbf{B}\mathbf{A}-\mathbf{A}\mathbf{B})=\mathbf{A}\nabla\cdot\mathbf{B}+\mathbf{B}\cdot\nabla\mathbf{A}-\mathbf{B}\nabla\cdot\mathbf{A}-\mathbf{A}\cdot\mathbf{B}, \tag{A.14}$$

A.2 Manipulations

A.2.1 The Lorentz force and the magnetic stress tensor

The mathematical manipulations we used in this thesis concerned mainly the Lorentz force and its energical contributions. The Lorentz force $\mathbf{J} \times \mathbf{B}$ can be written as the divergence of the magnetic part of the electromagnetic stress dyad by using the vector identities:

$$\mathbf{J} \times \mathbf{B} = \frac{1}{\mu_0}(\nabla \times \mathbf{B}) \times \mathbf{B} = \frac{1}{\mu_0}[(\mathbf{B} \cdot \nabla)\mathbf{B} - (\nabla \mathbf{B}) \cdot \mathbf{B}] \tag{A.15}$$

Using Eq.A.12, we have:

$$\mathbf{J} \times \mathbf{B} = \frac{1}{\mu_0}[(\nabla \cdot \mathbf{BB}) - \nabla \cdot (\frac{1}{2}B^2\mathbf{I})] = \nabla \cdot (\overline{\overline{\tau}}^m) \tag{A.16}$$

where $\overline{\overline{\tau}}^m$ is the magnetic stress dyad which can be written in a cartesian coordinate system as follows:

$$\overline{\overline{\tau}}^m = \begin{pmatrix} (B_x^2 - B^2/2) & B_x B_y & B_x B_z \\ B_y B_x & (B_y^2 - B^2/2) & B_y B_z \\ B_z B_x & B_z B_y & (B_z^2 - B^2/2) \end{pmatrix}$$

Now concerning the energical contributions of the Lorenz force, some manipulations have to be done. For instance, by using Eq.A.13, the term in the right hand side of Eq.2.40 is developped to obtain the magnetic energy equation in sec.2.1.4 of Chap.2:

$$\nabla \cdot (\eta \mathbf{J} \times \mathbf{B}) = \mathbf{B} \cdot (\nabla \times \eta \mathbf{J}) - \eta \mathbf{J} \cdot (\nabla \times \mathbf{B}) \tag{A.17}$$

Then, by using $\mathbf{J} = \frac{1}{\mu_0}(\nabla \times \mathbf{B})$, we have:

$$\mathbf{B} \cdot (\nabla \times \eta \mathbf{J}) = \nabla \cdot (\eta \mathbf{J} \times \mathbf{B}) + \mu_0 \eta |\mathbf{J}|^2 \tag{A.18}$$

By using Eq.A.13 and Eq.A.2, the second term of the left hand side of the same Eq.2.40 is developped as follows:

$$\nabla \cdot (\mathbf{B} \times (\mathbf{U} \times \mathbf{B})) = (\mathbf{U} \times \mathbf{B}) \cdot (\nabla \times \mathbf{B}) - \mathbf{B} \cdot (\nabla \times (\mathbf{U} \times \mathbf{B})) \tag{A.19}$$

thus,

$$\mathbf{B} \cdot (\nabla \times (\mathbf{U} \times \mathbf{B})) = (\mathbf{U} \times \mathbf{B}) \cdot (\nabla \times \mathbf{B}) - \nabla \cdot (\mathbf{B} \times (\mathbf{U} \times \mathbf{B})) = \mu_0 \mathbf{U} \cdot (\mathbf{J} \times \mathbf{B}) - \nabla \cdot (\mathbf{B} \cdot \mathbf{BU} - \mathbf{U} \cdot \mathbf{BB}) \tag{A.20}$$

A.2.2 The Poynting theorem and the magnetic energy equation

Let us recall the Maxwell equation we considered in this work:

$$\nabla \times \mathbf{H} = (\mathbf{J} + \frac{\partial \mathbf{D}}{\partial t}) \qquad \textbf{(Ampère's law)} \tag{A.21}$$

$$\nabla \times \mathbf{E} = -\frac{\partial \mathbf{B}}{\partial t} \qquad \textbf{(Faraday's law)} \tag{A.22}$$

$$\nabla \cdot \mathbf{B} = 0 \qquad \textbf{(Gauss's law for magnetism)} \tag{A.23}$$

$$\nabla \cdot \mathbf{D} = \varrho \qquad \textbf{(Gauss's law)} \tag{A.24}$$

where E is the electric field strength, ϱ the free charge density, B the magnetic induction, D the electric displacement and H the magnetic field.

The energy of an assemblage of charges in a closed volume can be written as follows:

$$W = \frac{1}{2} \int \varrho(\vec{r}) \phi(\vec{r}) d^3 r \tag{A.25}$$

where ϕ is the electric scalar potential defined as follows:

$$\mathbf{E} = -\nabla \phi \tag{A.26}$$

Thus, by substituting Eq.A.24 in Eq.A.25, we obtained:

$$W = \frac{1}{2} \int (\nabla \cdot \mathbf{D}) \phi(\vec{r}) d^3 r \tag{A.27}$$

By using the manipulation of Eq.A.6 gives:

$$W = \frac{1}{2} \int [\nabla \cdot (\phi \mathbf{D}) - \mathbf{D} \cdot \nabla \phi(\vec{r})] d^3 r = \frac{1}{2} \int \nabla \cdot (\phi \mathbf{D}) d^3 r - \frac{1}{2} \int \mathbf{D} \cdot \nabla \phi(\vec{r}) d^3 r \tag{A.28}$$

The integral of the RHS first term is then converted to a surface integral by the divergence theorem and remove because here the surface is considered to infinity. Thus,

$$W = -\frac{1}{2} \int \mathbf{D} \cdot \nabla \phi(\vec{r}) d^3 r = \frac{1}{2} \int \mathbf{E} \cdot \mathbf{D} d^3 r = \int u_E d^3 r \tag{A.29}$$

where u_E is electric energy density which can be expressed as:

$$u_E = \frac{\mathbf{E} \cdot \mathbf{D}}{2} \tag{A.30}$$

In the particular case of a linear electric medium with electric permittivity ϵ the electric energy density can be approximated as:

$$u_E = \frac{\epsilon E^2}{2} \tag{A.31}$$

In the same way, the magnetic energy density is given by:

$$u_M = \frac{\mathbf{H} \cdot \mathbf{B}}{2} \tag{A.32}$$

And in a linear magnetic medium with magnetic permeability μ, we have:

$$u_M = \frac{B^2}{2\mu} \tag{A.33}$$

The total energy density in electromagnetic field is thus given by:

$$u_{em} = u_E + u_M = \frac{\mathbf{E}\cdot\mathbf{D}}{2} + \frac{\mathbf{H}\cdot\mathbf{B}}{2} \tag{A.34}$$

In the case of an electromagnetic field confined in a given volume, the electromagnetic energy contained in a given volume changes by the mechanical work done by the electromagnetic field on the currents and by radiative flow of energy across the surface of the volume considered. First, the corresponding mechanical power is given by:

$$P_m = \int (\mathbf{F}\cdot\mathbf{v})d^3r = \int [\rho(\mathbf{E}+\mathbf{v}\times\mathbf{B})\cdot\mathbf{v}]d^3r = \int (\mathbf{E}\cdot\mathbf{J})d^3r \tag{A.35}$$

where $\mathbf{F} = \rho(\mathbf{E}+\mathbf{v}\times\mathbf{B})$ is the electromagnetic force density and $\mathbf{J} = \rho\mathbf{v}$ the current density. The rate of change of the electromagnetic energy in the volume can be deduced as follows for a linear magnetic and linear electric medium:

$$\frac{dW}{dt} = \int \frac{\partial u_{em}}{\partial t} d^3r \tag{A.36}$$

By substituting Eq.A.34 in Eq.A.36, we obtained:

$$\begin{aligned}
\frac{dW}{dt} = \frac{1}{2}\int \frac{\partial}{\partial t}(\epsilon E^2 + \frac{B^2}{\mu})d^3r & \\
&= \int (\epsilon\mathbf{E}\frac{\partial\mathbf{E}}{\partial t} + \mathbf{B}\frac{\partial(\mathbf{B}/\mu)}{\partial t})d^3r \\
&= \int (\mathbf{E}\frac{\partial\mathbf{D}}{\partial t} + \mathbf{H}\frac{\partial\mathbf{B}}{\partial t})d^3r \\
&= \int [\mathbf{E}\cdot(\nabla\times\mathbf{H}-\mathbf{J}) - \mathbf{H}\cdot(\nabla\times\mathbf{E})]d^3r \\
&= \int [-(\mathbf{E}\cdot\mathbf{J}) + \mathbf{E}\cdot(\nabla\times\mathbf{H}) - \mathbf{H}\cdot(\nabla\times\mathbf{E})]d^3r
\end{aligned} \tag{A.37}$$

By using Eq.A.14 for the two last terms in Eq.A.37, we have:

$$\frac{dW}{dt} = -\int \nabla\cdot(\mathbf{E}\times\mathbf{H})d^3r - \int (\mathbf{E}\cdot\mathbf{J})d^3r \tag{A.38}$$

where $\vec{\pi} = \mathbf{E}\times\mathbf{H}$ is the Poynting vector. Thus,

$$\frac{dW}{dt} = \int \frac{\partial u_{em}}{\partial t} d^3r = -\int (\nabla\cdot\vec{\pi})d^3r - \int (\mathbf{E}\cdot\mathbf{J})d^3r \tag{A.39}$$

For an arbitrary volume, we obtained the conservation energy equation of electrodynamics :

$$\frac{\partial u_{em}}{\partial t} + \nabla\cdot\vec{\pi} = -\mathbf{E}\cdot\mathbf{J} \tag{A.40}$$

Thus,

$$-\frac{dW}{dt} = \int (\mathbf{E}\cdot\mathbf{J})d^3r + \int (\vec{\pi}\cdot\mathbf{n})S_f \tag{A.41}$$

Here we can easily identify in the RHS of Eq.A.41 the mechanical work of the electromagnetic field (the joule heating term) and the rate of energy flowing across the boundary surface S_f with normal vector $\mathbf{n}$ pointing outward of the considered volume.

From Eq.A.40 the magnetic field energy equation can be deduced as follows:

$$-\frac{\partial}{\partial t}(\frac{B^2}{2\mu_0} + \frac{\epsilon_0 E^2}{2}) = \mathbf{E}\cdot\mathbf{J} + \nabla\cdot\vec{\pi} \tag{A.42}$$

By using the Ohm's law and Eq.A.14, from Eq.A.42 we have:

$$-\frac{\partial}{\partial t}(\frac{B^2}{2\mu_0}) = \frac{|\mathbf{J}|^2}{\sigma} + \mathbf{U}\cdot(\mathbf{J}\times\mathbf{B}) + \frac{1}{\mu_0\sigma}\nabla\cdot(\mathbf{J}\times\mathbf{B}) + \frac{1}{\mu_0}\nabla\cdot(\mathbf{B}\cdot\mathbf{B}\mathbf{U} - \mathbf{U}\cdot\mathbf{B}\mathbf{B}) \tag{A.43}$$

which is the magnetic energy equation.

A.2.3 The magnetic scalar potential

Considering two functions A and B such that $A = A(x)$ and $dA = A^{'}dx$ while $B = B(x)$ and $dB = B^{'}dx$. The integration by parts of the product of the two function is written as follows:

$$\int (AB)^{'} = \int A\frac{dB}{dx}dx + \int B\frac{dA}{dx}dx \tag{A.44}$$

yielding

$$\int A\frac{dB}{dx}dx = \int (AB)^{'} - \int B\frac{dA}{dx}dx \tag{A.45}$$

Now concerning the magnetic scalar potential, the main used manipulation is the integration by parts defined as follows:

$$\int_V \nabla^{'}\cdot[\frac{\mathbf{M}(r^{'})}{|r-r^{'}|}]d^3r^{'} = \int_V \frac{\nabla^{'}\cdot\mathbf{M}(r^{'})}{|r-r^{'}|} + \int_V \mathbf{M}(r^{'})\cdot\nabla^{'}\frac{1}{|r-r^{'}|}d^3r^{'} \tag{A.46}$$

which gives

$$\int_V \frac{\nabla^{'}\cdot\mathbf{M}(r^{'})}{|r-r^{'}|} = \int_V \nabla^{'}\cdot[\frac{\mathbf{M}(r^{'})}{|r-r^{'}|}]d^3r^{'} - \int_V \mathbf{M}(r^{'})\cdot\nabla^{'}\frac{1}{|r-r^{'}|}d^3r^{'} \tag{A.47}$$

Bibliography

Ahangar, M., R. Ebrahimi, and M. Shams (2014). "Numerical simulation of non-equilibrium plasma flow in a cylindrical MPD thruster using a high-order flux-difference splitting method". In: *Acta Astronautica* 103, pp. 129–141. URL: http://dx.doi.org/10.1016/j.actaastro.2014.07.008.

Albertoni, R., F. Paganucci, and M. Andrenucci (2015). "A phenomenological performance model for applied-field MPD thrusters". In: *Acta Astronautica* 107, pp. 177–186. URL: http://dx.doi.org/10.1016/j.actaastro.2014.11.017.

Aluzas, R. (2014). "Numerical Simulations of Shock-Cloud Interactions". PhD thesis. School of Physics and Astronomy, University of Leeds.

Baldás, J. and E. Tadmor (2005). "A central differencing simulation of the Orszag-Tang vortex system". In: *IEEE Transactions on plasma science* 33.02, pp. 470–471. URL: http://www.csun.edu/~jb715473/papers/balbas-tadmor_ieee.pdf.

— (2006). "Non-oscillatory Central Schemes of one-dimensional MHD Equations: II: Higher-resolution semi-discrete schemes". In: *SIAM J. Sci. Comput.* 28.2, pp. 533–560. URL: http://www.csun.edu/~jb715473/papers/balbas-tadmor.pdf.

Baldás, J., E. Tadmor, and C. Wu (2004). "Non-oscillatory Central Schemes of one-dimensional MHD Equations: I". In: *J. Comput. Phys.* 201.1, pp. 261–285. URL: http://www.sciencedirect.com/science/article/pii/S0021999104002293.

Bittencourt, J. A. (2004). *Fundamentals of Plasma Physics*. Springer Science+Business Media, LCC, pp. 645–673.

Boyd, T.J.M. and J.J. Sanderson (2003). *The Physics of Plasmas*. Cambridge University Press.

Boyle, M. J. (1974). "Acceleration Processes in the Quasi-Steady Magnetoplasmadynamic Discharge". PhD thesis. Princeton University, New Jersey. URL: https://ntrs.nasa.gov/archive/nasa/casi.ntrs.nasa.gov/19750005557.pdf.

Boyle, M. J., K. E. Clark, and R. G. Jahn (1976). "Flow field characteristics and performance limitations of quasi-steady magnetoplasmadynamic accelerators". In: *AIAA* 14, pp. 955–962. URL: http://alfven.princeton.edu/publications/boyle-aiaa-1976.

Brackbill, J.U. and D.C. Barnes (1980). "The Effect of Nonzero $\nabla \cdot \mathbf{B}$ on the numerical solution of the magnetohydrodynamic equations". In: *J. Comput. Phys* 35.3, pp. 426–430. DOI: 10.1016/0021-9991(80)90079-0.

Brio, M. and C. C. Wu (1988). "An upwind differencing scheme for the equations of ideal magnetohydrodynamics". In: *J. Comput. Phys* 75.2, pp. 400–422. URL: http://www.sciencedirect.com/science/article/pii/0021999188901209.

Brushlinski, K. V., N. I. Gerlakh, and A. I. Morozov (1967). "Calculation of two-dimensional unsteady plasma flows of finite conductivity in the presence of the

Hall effect". In: *Magnitnaya Gidrodinamika (Magnetohydrodynamics)* 1. URL: ....

Brushlinski, K. V., N. I. Gerlakh, and A. I. Morozov (1968). "Effect of finite conductivity on stationary self-contracting plasma flows". In: *Soviet Physics-Doklady* 13, pp. 588–590.

Brushlinski, K. V. and A. I. Morozov (1968). "On the evolutionary of equations of magnetohydrodynamics taking the Hall effect into account". In: *PMM Journal of Applied Mathematics and Mechanics* 32, pp. 957–959. URL: ....

Brushlinskii, K.V., N.I. Gerlakh, and A.I. Morozov (1968). "On the Evolutionary of Equations of Magnetohydrodynamics Taking the Hall Effect into Account". In: *PMM Journal of Applied Mathematics and Mechanics* 32.5, pp. 957–959. DOI: 10.1016/0021-8928(68)90021-X.

Burton, R. L., K. E. Clark, and R. G. Jahn (1983). "Measured Performance of a Multimegawatt MPD Thruster". In: *Journal Of Spacecraft* 20, pp. 299–304. DOI: 10.2514/3.25596.

Chanty, J.M.G. (1992). "Analysis of two-dimensional flows in magneto-dynamic plasma accelerators". PhD thesis. Massachusetts Institute of Technology, Cambridge, Massachusetts. URL: http://hdl.handle.net/1721.1/42529.

Choueiri, E. Y. (1998). "Scaling of Thrust in Self-Field Magnetoplasmadynamic Thrusters". In: *Journal of Propulsion and Power* 4.5, pp. 744–753. DOI: 10.2514/2.5337.

Colella, P. and P. Woodward (1984). "The piecewise parabolic method (PPM) for gas-dynamical simulation". In: *J. Comput. Phys* 54.2, pp. 174–201. URL: https://crd.lbl.gov/assets/pubs_presos/AMCS/ANAG/A141984.pdf.

Connolly, D.J., R.J. Sovie, and G.R. Seikel (1970). "Performance and Diagnostics of a Water-Cooled Magnetoplasmadynamic Arc Thruster". In: *NASA TN D-5836*, pp. 1–40. URL: https://ntrs.nasa.gov/archive/nasa/casi.ntrs.nasa.gov/19700018629.pdf.

Constantin, L. A. and A. Kurganov (2006). "Adaptive Central-Upwind Schemes for Hyperbolic Systems of Conservation Laws". In: *Theory, Numerics, Applications* 95, pp. 95–103. URL: http://129.81.170.14/~kurganov/Constantin-Kurganov.pdf.

Dedner, A. et al. (2002). "Hyperbolic Divergence Cleaning for the MHD Equations". In: *J. Comput. Phys* 175.2, pp. 645–673. URL: www.sciencedirect.com/science/article/pii/S002199910196961X.

Evans, C. and J.F. Hawley (1988). "Simulation of magnetohydrodynamic flows". In: *The Astrophysical Journal* 332, 659–677. DOI: 10.1086/166684.

Ferziger, J. H. and M. Peric (2002). *Computational Methods for Fluid Dynamics*. 3rd edition. Berlin, Germany: Springer. DOI: 10.1007/978-3-642-56026-2.

Fogang, F. et al. (2015). "An extension of AUFSR scheme for the ideal magnetohydrodynamics equations". In: *Computers and Fluids* 114, pp. 297–313. URL: http://dx.doi.org/10.1016/j.compfluid.2015.02.003.

Fradkin, D.B. and A.W. Blackstock (1970). "Experiments using a 25-kW hollow cathode lithium vapour MPD arcjet". In: *AIAA J* 8.5, 886–894. DOI: 10.2514/3.5783.

Goebel, D. M. and I. Katz (2008). *Fundamentals of Electric Propulsion*. Hoboken, NJ, USA: John Wiley and Sons, pp. 3–5. URL: http://onlinelibrary.wiley.com/doi/10.1002/9780470436448.index/summary.

Goedbloed, H. and S. Poedts (2004). *Principles of Magnetohydrodynamics*. New York: Cambridge University Press, pp. 162–166.

Goedbloed, J.P. (2008). "Time reversal duality of magnetohydrodynamic shocks". In: *Physics of Plasmas* 15.6, p. 062101. DOI: 10.1063/1.2919795.

Goedbloed, J.P. and A. Lifschitz (1997). "Stationary symmetric magnetohydrodynamic flows". In: *Physics of Plasmas* 4.10, p. 3544. DOI: 10.1063/1.872251.

Greenshields, C. J. et al. (2010). "Implementation of semi-discrete, non-staggered central schemes in a collocated, polyhedral, finite volume framework, for high-speed viscous flows". In: *Int. J. Numer. Meth. Fluids* 63.1, pp. 1–21. URL: onlinelibrary.wiley.com/doi/10.1002/fld.2069/pdf.

Griffiths, D.J. (1999). *Introduction to Electrodynamics*. Ed. by Prentice Hall. Third edition. Upper Saddle River, New Jersey.

Groll, R. (2015). *Diffusionsmodellierung*. Vol. 1. Springer Spektrum, pp. 83–183. DOI: 10.1007/978-3-658-11342-1.

Gurski, K.F. (2004). "An HLLC-Type approximate Riemann solver for ideal magnetohydrodynamics". In: *SIAM J. Sci. Comput.* 25.6, 2165–2187. DOI: 10.1137/S1064827502407962.

Harten, A., P. D. Lax, and B. Van Leer (1983). "On upstreaming differencing and Godunov-type schemes for hyperbolic conservation laws". In: *SIAM Review* 25.1, pp. 35–61. URL: http://epubs.siam.org/doi/abs/10.1137/1025002.

Harten, A. et al. (1997). "Uniformly high order accurate essentially non-oscillatory schemes, III". In: *J. Comput. Phys* 131.2, pp. 3–47. URL: http://www.ece.uvic.ca/~bctill/papers/numacoust/Harten_etal_1987.pdf.

Heiermann, Jörg (2002). "Ein Finite–Volumen–Verfahren zur Lösung magnetoplasmadynamischer Erhaltungsgleichungen". PhD thesis. Institut für Raumfahrtsysteme, Universität Stuttgart.

Hosking, R. J. and R. L. Dewar (2016). *Fundamentals Fluid Mechanics and Magnetohydrodynamics*. Springer Science+Business Media, Singapore, pp. 157–201.

Huazheng, F. and F. Xueshang (2015). "Splitting based scheme for three-dimensional magnetohydrodynamics with dual time stepping". In: *Chin. J. Space Sci.* 35.01, pp. 9–17. URL: http://www.cjss.ac.cn/EN/abstract/abstract2101.shtml#.

Jackson, J.D. (1998). *Classical Electrodynamics*. 3rd Edition. New York: John Wiley & Sons. ISBN: 978-0-471-30932-1.

Jahn, R. G. (1968). *Physics of Electric Propulsion*. New-York, USA: McGraw-Hill.

Jiang, G. S. et al. (1998). "High-Resolution non-oscillatory central schemes with nonstaggered grids for hyperbolic conservation laws". In: *SIAM. J. Numer. Anal.* 35.6, pp. 2147–2168. URL: ftp://ftp.math.ucla.edu/pub/camreport/cam97-7.pdf.

Kagaya, Y. and H. Tahara (2005). "Swirl Acceleration in a Quasi-Steady MPD Thruster by Applied Magnetic Nozzle". In: *IEPC Paper 05-54*.

Kármán, T. von (1963). *Aerodynamics*. New York: McGraw-Hill Paperback, pp. 61–101.

King, D.Q. and J.L. Callas (1988). *MPD thruster erosion research*. Tech. rep. Jet Propulsion Lab, California Inst. of Tech, Pasadena. URL: http://www.dtic.mil/dtic/tr/fulltext/u2/a205644.pdf.

Kodys, A. D. and E. Y. Choueiri (2005). "A critical review of the state-of-the-art in the performance of applied-field magnetoplasmadynamic thrusters". In: *The 41st AIAA/ASME/SAE/ASEE Joint Propulsion Conference and Exhibit, July 10-14, Tucson*, pp. 198–216. DOI: 10.2514/6.2005-4247.

Kruger, C.H. and M. Mitchner (1973). *Partially Ionized Gases*. A Wiley-Interscience Publication, New-York: John Wiley & Sons, pp. 189–198.

Krülle, G. (1972). "theoretical treatment of current, mass flow and related distribution in MPD plumes". In: *9th Electric Propulsion Conference, International Electric Propulsion Conference, AIAA Paper 72-501*. DOI: 10.2514/6.1972-501.

Krülle, G., M. Auweter-Kurtz, and A. Sasoh (1998). "Technology and Application Aspects of Applied Field Magnetoplasmadynamic Propulsion". In: *Journal of Propulsion and Power* 14.5, pp. 754–763. DOI: 10.2514/2.5338.

Kubota, K. (2009). "Numerical Study on plasma flowfield and performance of magnetoplasmadynamic thrusters". PhD thesis. Department of Energy Sciences, Tokyo Institute of Technology. URL: heliospace.isas.jaxa.jp/thesis/200905_Kubota_PhD_Thesis.pdf.

Kubota, K. and I. Funaki (2009). "Numerical Analyses on Plasma Acceleration Processes in Applied-Field Magnetoplasmadynamic Thruster". In: *IEPC Paper 2009-227*, pp. 1–12. URL: http://erps.spacegrant.org/uploads/images/images/iepc_articledownload_1988-2007/2009index/IEPC-2009-227.pdf.

Kurganov, A. and C. T. Lin (2006). "On the reduction of numerical dissipation in Central-Upwind Schemes". In: *Com. Comput. Phys.* 2.1, pp. 141–163. URL: http://www.cscamm.umd.edu/centpack/publications/files/KurganovLinCiCP2006-centpack.pdf.

Kurganov, A., S. Noelle, and G. Petrova (2001). "Semidiscrete Central-Upwind Schemes for Hyperbolic Conservation Laws and Hamilton-Jacobi Equations". In: *SIAM J. SCI. Comput* 23.03, pp. 707–740. URL: 129.81.170.14/~kurganov/Kurganov-Noelle-Petrova.SISC-01.pdf.

Kurganov, A. and G. Petrova (2000). "Central schemes and contact discontinuities". In: *Math. Numer. Anal.* 34.6, pp. 1259–1275. URL: http://www.esaim-m2an.org/articles/m2an/pdf/2000/06/m2an0053.pdf.

Kurganov, A. and E. Tadmor (2000). "New High-Resolution Central Schemes for Nonlinear Conservation Laws and Convection-Diffusion Equations". In: *J. Comput. Phys* 160.03, pp. 241–282. URL: www.cscamm.umd.edu/tadmor/pub/central-schemes/Kurganov-Tadmor.JCP-00I.pdf.

Laney, Culbert B. (1998). *Introduction. In Computational Gasdynamics*. Cambridge: Cambridge University Press. DOI: 10.1017/CBO9780511605604.002.

Lapointe, M. R. (1991). "Numerical simulation of self-field MPD thrusters". In: *AIAA* 91-2341. DOI: 10.2514/6.1991-2341.

— (1992). "Numerical simulation of geometric scale effects in cylindrical self-field MPD thrusters". In: *AIAA* 92-3297. DOI: 10.2514/6.1992-3297.

Lev, D. and E.Y. Choueiri (2012). "Scaling of efficiency with applied magnetic field in magnetoplasmadynamic thrusters". In: *Journal of Propulsion and Power* 28.3, pp. 609–616. DOI: 10.2514/1.B34194.

Lev, Dan (2012). "Investigation of Efficiency in Applied Field MagnetoPlasma-Dynamic Thrusters". PhD thesis. Department of Mechanical and Aerospace Engineering: Princeton University. URL: https://alfven.princeton.edu/publications/thesis/lev-thesis-2012.pdf.

Leveque, R. J. (2002). *Finite Volume Methods for Hyperbolic Problems*. University of Washington, USA: Cambridge University Press.

Li, F., L. Xu, and S. Yakovlev (2011). "Central Discontinuous Galerkin Methods for Ideal MHD Equations with the Exactly Divergence free Magnetic field". In: *J. comput. phys.* 230.12, pp. 4828–4827. URL: http://www.sciencedirect.com/science/article/pii/S0021999111001495.

Li, S. (2008). "High-Order Central Scheme on Overlapping Cells for Magneto-Hydrodynamics Flows with and without Constrained Transport Method". In: *J. comput. phys.* 227.15, pp. 7368–7393. URL: http://www.cscamm.umd.edu/centpack/publications/files/SLiMHDw_outCTJCP2008-centpack.pd.

Liu, G.R. and S.S. Quek (2013). *Finite Element Method-A Practical Course*. first. New York: Butterworth-Heinemann, pp. 129–172. DOI: 10.1016/B978-075065866-9/50008-6.

Liu, Y. et al. (2007). "High-Order Central Scheme on Overlapping Cells for Magneto-Hydrodynamics Flows with and without Constrained Transport Method". In: *Commun. comput. phys.* 2.5, pp. 933–963. URL: http://www.cscamm.umd.edu/centpack/publications/files/SLiMHDw_outCTJCP2008-centpack.pd.

M. Auweter-Kurtz, D. Haag amd, M. Fertig, and H. Kurtz (2005). "Development of an Applied Field Magnetoplasmadynamic Thruster Design Supported by Numerical Simulations at IRS". In: *IEPC Paper 2005-059*, pp. 1–14. URL: http://erps.spacegrant.org/uploads/images/images/iepc_articledownload_1988-2007/2005index/059.pdf.

Maecker, H. (1955). "Plasma jets in arcs in a process of self-induced magnetic compression". In: *Z. Phys.* 141, pp. 198–216.

Messerschmid, E. and S. Fasoulas (2011). *Raumfahrtsysteme*. Vol. 1. Springer-Verlag Berlin: Springer, pp. 43–74. DOI: 10.1007/978-3-642-12817-2.

Mikellides, G. P., J. P. Turchi, and F. N. Roderick (2000). "Applied-Field Magnetoplasmadynamic Thrusters, Part 1: Numerical Simulations Using the MACH2 Code". In: *Journal of propulsion and power* 16, pp. 887–893. DOI: 10.2514/2.5656.

Mikellides, P.G. (2004). "Modeling and Analysis of a Megawatt-Class Magnetoplasmadynamic Thruster". In: *Journal of Propulsion and Power* 20.2, pp. 894–901. DOI: 10.2514/1.9246.

Mikellides, P.G. and P.J. Tu (2000). "Applied-Field Magnetoplasmadynamic Thrusters, Part 2:Analytic Expressions for Thrust and Voltage". In: *Journal of Propulsion and Power* 16.5, pp. 894–901. DOI: 10.2514/2.5657.

Moukalled, F., L. Mangani, and M. Darwish (2016). *The Finite Volume Method in Computational Fluid Dynamics*. New York: Springer, pp. 103–137. DOI: 10.1007/978-3-319-16874-6.

Myers, R. M. (1990). "Geometric Effects in Applied-Field MPD Thrusters". In: *AIAA Paper 90-2669*. DOI: 10.2514/6.1990-2669.

Myers, R.M. and G.C. Soulas (1992). "Anode power deposition in applied-field MPD thrusters". In: *NASA Contractor Report 190790* AIAA-92-3463, pp. 1–26. URL: https://ntrs.nasa.gov/archive/nasa/casi.ntrs.nasa.gov/19930004095.pdf.

Nessyahu, H. and E. Tadmor (1990). "Non-oscillatory central differencing for hyperbolic conservation laws". In: *J. Comput. Phys.* 87.2, pp. 408–463. URL: http://www.cscamm.umd.edu/tadmor/pub/central-schemes/Nessyahu-Tadmor.JCP-90.pdf.

Niewood, E.H. (1989). "Transient One Dimensional Numerical Simulation of Magnetoplasmadynamic Thrusters". MA thesis. Massachusetts Institute of Technology, Cambridge, Massachusetts.

— (1993). "An explanation for anode voltage drops in an MPD thruster". PhD thesis. Massachusetts Institute of Technology, Cambridge, Massachusetts. URL: http://hdl.handle.net/1721.1/47320.

OpenFOAM version 2.3.0. openfoam.org/release/2-3-0. Accessed: 2014-04-01.

Picone, J. M. and R. B. Dahlburg (1990). *Numerical Simulation of the Compressible Orszag-Tang Vortex II. Supersonic Flow*. Tech. rep. URL: http://oai.dtic.mil/oai/oai?verb=getRecord&metadataPrefix=html&identifier=ADA224913.

Plok, J. E. et al. (1999). "Validation of the NSTAR Ion Propulsion System on the Deep Space One Mission". In: *AIAA*. URL: http://erps.spacegrant.org/uploads/images/images/iepc_articledownload_1988-2007/2001index/75_1.pdf.

Powell, K.G. (1994). "An approximate Riemann solver for magnetohydrodynamics (that works in more than one dimen- sion)". In: *NASA Contractor Report 194902*. URL: https://ntrs.nasa.gov/archive/nasa/casi.ntrs.nasa.gov/19940028527.pdf.

Powell, K.G. et al. (1999). "A Solution-Adaptive Upwind Scheme for Ideal Magnetohydrodynamics". In: *J. Comput. Phys* 154.2, 284–309. DOI: 10.1006/jcph.1999.6299.

Roe, P. L. (1981). "Approximate Riemann solvers, parameter vectors, and difference schemes". In: *J. Comput. Phys* 43.2, pp. 357–372. URL: http://www.sciencedirect.com/science/article/pii/0021999181901285.

Roe, P. L. and D. S. Balsara (1996). "Notes on the eigensystem of magnetohydrodynamics". In: *SIAM J. APPL. MATH.* 56.1, pp. 57–67. URL: https://www.jstor.org/stable/2102521?seq=1#page_scan_tab_contents.

Roe, P.L. (1986). "Characteristic-Based Schemes for the Euler Equations". In: *Annual Review of Fluid Mechanics* 18, pp. 337–365. DOI: 10.1146/annurev.fl.18.010186.002005.

Sankaran, K. (2005). "Simulation of MPD Flows Using a Flux-Limited Numerical Method for the MHD Equations". PhD thesis. Princeton University, Technology and Medicine, Princeton.

Sankaran, K., E. Y. Choueiri, and S. C. Jardin (2005). "Comparison of simulated Magnetoplasmadynamic Thruster Flowfields to Experimental Measurements". In: *Journal of Propulsion and Power* 21.1, pp. 129–138. DOI: 10.2514/1.5340.

Schaefer, M. (2006). *Computational Engineering — Introduction to Numerical Methods*. Vol. 1. Springer-Verlag Berlin: Springer, pp. 77–105. DOI: 10.1007/3-540-30686-2_4.

Shen, Y., G. Zha, and M. A. Huerta (2012). "E-CUSP scheme for equation of ideal MHD with high order WENO scheme". In: *J. comput. phys.* 231.19, pp. 6233–6247. URL: http://www.sciencedirect.com/science/article/pii/S0021999112001878.

Sleziona, P.C., M. Auweter-Kurtz, and H.O. Schrade (1992). "Numerical calculation of nozzle type and cylindrical MPD thrusters". In: 28^{th} *Joint Propulsion Conference and Exhibit, Joint Propulsion Conferences, Nashville, TN, July 6-8, AIAA 92-3296*. URL: http://dx.doi.org/10.2514/6.1992-3296.

— (1993). "Numerical calculation of a cylindrical MPD thruster". In: *Proceedings of* 23^{rd} *International Electric Propulsion Conference, Seattle, WA, USA, IEPC 93-072*, pp. 609–617. URL: http://erps.spacegrant.org/uploads/images/images/iepc_articledownload_1988-2007/1993index/IEPC1993-066.pdf.

Sod, G. A. (1978). "A survey of several finite difference methods for systems of nonlinear hyperbolic conservation laws". In: *Journal of computational physics* 27.01, pp. 1–31. URL: http://www.tat.physik.uni-tuebingen.de/~kley/lehre/bhydro/sod-paper.pdf.

Spitzer, L. (2006). *Physics of Fully Ionized Gases*. Dover Publications.

Spitzer, L. and R. Härm (1953). "Transport Phenomena in a Completely Ionized Gas". In: *Physical Review* 89.05, pp. 977–981. DOI: 10.1103/PhysRev.89.977.

Spurk, J. and N. Aksel (2007). *Strömungslehre*. 7^{th}. New York: Springer Verlag, pp. 39–47. DOI: 10.1007/978-3-642-13143-1.

Sterck, H. De, B.C. Low, and S. Poedts (1998). "Complex magnetohydrodynamic bow shock topology in field-aligned low-beta flow around a perfectly conducting cylinder". In: *Physic of Plasmas* 05.11, pp. 4015–4027. DOI: http://dx.doi.org/10.1063/1.873124.

Sutherland, W. (1893). "The Viscosity of Gases and Molecular Force". In: *Philosophical Magazine Series 5* 36, pp. 507–531. DOI: 10.1080/14786449308620508.

Sutton, G. P. and O. Biblarz (2010). *Rocket propulsion elements*. John Wiley and Sons, pp. 674–675.

Tang, H. et al. (2012). "Study of applied magnetic field magnetoplasmadynamic thrusters with particle-in-cell code with Monte Carlo collision. I. Computation methods and physical processes". In: *Physics of plasmas* 19. DOI: 10.2514/2.5656.

Tankara, M. and I. Kimura (1988). "Current Distribution and Plasma Acceleration in MPD Arcjets with Magnetic Fields". In: *Journal of Propulsion and Power* 4.5, pp. 428–436. DOI: 10.2514/3.23084.

Toro, E.F. (2009). *Riemann Solvers and Numerical Methods for Fluid Dynamics*. thrird. Vol. 1. Springer Berlin Heidelberg, pp. 413–487. DOI: 10.1007/b79761.

Touma, R. (2009). "Unstaggered Central Schemes for MHD and SMHD". In: *Proceedings of Symposia in Applied Mathematics* 67.2, pp. 967–976. URL: http://citeseerx.ist.psu.edu/viewdoc/download?doi=10.1.1.643.7537&rep=rep1&type=pdf.

Touma, R. and P. Arminjon (2006). "Central Finite Volume Schemes with Constraited Transport divergence Treatment for Three-Dimensional Ideal MHD".

In: *J. Comput. Phys.* 212.2, pp. 617–636. URL: http://www.sciencedirect.com/science/article/pii/S0021999105003487.

Valtonen, M. et al. (2016). "From Newton to Einstein: The Discovery of Laws of Motion and Gravity". In: *The Three-body Problem from Pythagoras to Hawking*. Cham: Springer International Publishing. DOI: 10.1007/978-3-319-22726-9_2.

Vanderlinde, J. (2005). *Classical Electromagnetic Theory*. Netherlands: Springer, pp. 182–186. DOI: 10.1007/1-4020-2700-1.

VanGilder, D. B. (2000). "Numerical simulations of the plumes of electric propulsion thrusters". PhD thesis. Cornell University, New York. URL: http://ngpdlab.engin.umich.edu/files/papers/VanGilder.pdf.

Villani, D.D. (1982). "Energy loss mechanisms in a magnetoplasmadynamic arcjet". PhD thesis. Princeton University, Princeton, New Jersey.

Waterson, N.P. and H. Deconinck (2007). "Design principles for bounded higher-order convection schemes – a unified approach". In: *J. Comput. Phys.* 224.1, pp. 182–207. DOI: 10.1016/j.jcp.2007.01.021.

White, F. M. (1991). *Viscous Fluid Flow*. 2nd edition. New-York, USA: Mcgraw-Hill Inc.

Winter, M. et al. (1997). "Experimental and Numerical Investigation of Steady State MPD Thrusters". In: *Proceedings of the Second European Spacecraft Propulsion Conference*, pp. 431–439. URL: http://adsbit.harvard.edu/cgi-bin/nph-iarticle_query?1997ESASP.398..431W&defaultprint=YES&filetype=.pdf.

Woods, L.C. (2007). *Physic of plasma*. New York: WILEY-VCH Verlag GmbH & Co. KGaA, pp. 1–222. DOI: 10.1002/9783527618064.

Xisto, C. M., J. C. Pascoa, and P. J. Oliviera (2013). "A pressure-based method with AUSM-type fluxes for MHD flows at arbitrary Mach numbers". In: *Int. J. Numer. Meth. Fluids* 72.11, pp. 1165–1182. URL: onlinelibrary.wiley.com/doi/10.1002/fld.3781/pdf.

— (2014). "A pressure-based high resolution numerical method for resistive MHD". In: *J. Comput. Phys* 175.3, pp. 323–345. URL: www.sciencedirect.com/sciencearticle/pii/S0021999114004896.

— (2015). "Numerical analysis of real gas MHD flow on two-dimensional self-field MPD thrusters". In: *Acta Astronautica* 112, pp. 89–101. DOI: 10.1016/j.actaastro.2015.03.009.

Xisto, C. M. et al. (2012). "A hybrid pressure-density-based algorithm for the Euler equations at all Mach numeber regimes". In: *Int. J. Numer. Meth. Fluids* 70.08, pp. 961–976. URL: http://onlinelibrary.wiley.com/doi/10.1002/fld.2722/pdf.